

DYNAMICS AND CHEMISTRY OF LAMINAR  
AND TURBULENT EXPANDING FLAMES

FUJIA WU

A DISSERTATION  
PRESENTED TO THE FACULTY  
OF PRINCETON UNIVERSITY  
IN CANDIDACY FOR THE DEGREE  
OF DOCTOR OF PHILOSOPHY

RECOMMENDED FOR ACCEPTANCE  
BY THE DEPARTMENT OF  
MECHANICAL AND AEROSPACE ENGINEERING

ADVISER: CHUNG K. LAW

NOVEMBER 2014

© Copyright by Fujia Wu, 2014. All rights reserved.

## Abstract

The present work consists of a series of experimental studies on expanding laminar and turbulent flames. The first goal is to use the laminar stable expanding flame to study laminar flame speed and flame chemistry. The second goal is to study the dynamics and stability of premixed flames with/without the presence of turbulence. A unique dual-chamber, high-pressure, fan-stirred, preheated combustion vessel was developed as the main experimental apparatus. The stretch extrapolation of laminar flame speeds from experimental raw data is a state-of-the-art practice. Its associated uncertainty was first quantified using numerical simulations of spherical expanding flames. Then laminar flame speeds of cyclo-alkanes, butanol isomers, toluene, *o*-xylene and mixtures of H<sub>2</sub> with C<sub>1</sub>-C<sub>4</sub> hydrocarbons were acquired for a wide range of pressures (1-20 atm). The molecular structure effects on the oxidation chemistry of cyclic alkanes and butanol isomers were studied. On the dynamics of premixed flames, the self-acceleration of expanding flames due to Darrieus-Landau and diffusional-thermal instabilities was quantified through experimentation on hydrogen flames. Results show that most cellular flames exhibit self-similar acceleration, which suggests that the wrinkled flame surface can be described by a fractal. Additionally, high pressure and high turbulent Reynolds number turbulent flames propagating in near isotropic turbulence were studied. Results show that the turbulent flame speeds can be scaled by a Reynolds number defined based on the properties of the corresponding laminar flame and the flow. Finally, spark ignition in turbulent flows was studied. Results showed that turbulence can enhance ignition for mixtures with sufficiently large Lewis number, which is contrary to the general belief that turbulence always renders ignition more difficult.

## Acknowledgments

Words cannot describe my gratitude to my wife, Jing Tao, who six years ago quit her job in China, married me, and came with me all the way to the United States. I would not have completed this dissertation without her sacrifice, support, encouragement, and endless love. I thank our two-year old daughter, Ashley Wu, for being healthy and bringing tremendous happiness to us.

I owe deep gratitude to my parents, Junpei Wu and Yuehua Yuan for their unconditional love. They raised me to be a healthy man, and provided me with the best care, education, support, and encouragement. Their hard work has afforded me the opportunity to achieve what I have achieved so far. They are always the source of my power and courage.

It is a great honor to be a graduate student of Professor Chung K. Law. I want to express my sincere gratitude and tremendous respect to him. His high standard of scholarship, constant pursuit of truth, and appreciation of beautiful science are always my sources of inspiration. I truly appreciate the stimulating and challenging research projects he suggested, the guidance he offered on a daily basis, and career long mentorship in the past and years to come.

I would achieve very little and end up exhausted without the enormous experimental support from Mr. Delin Zhu. He helped and looked after me all the time. Whenever I broke something apart, he always smiled and hours later walked out of the machine shop with his hands holding a manufactured replacement. I sincerely appreciate Mr. Zhu's patience and selfless help.

Many research projects would not be completed without the contribution from the students and staff in Professor Law's combustion group. Their fingerprints can be found all over this dissertation. Andrew Kelley and Grunde Jomaas patiently

passed on their knowledge on spherically expanding flames to me and established the ground for me to initiate the research in Chapters 4, 5 and 6. Swetaprovo Chaudhuri and Abhishek Saha have been true partners in conducting turbulent flame experiments for the research in Chapters 7, 8 and 9. I sincerely appreciate Wenkai Liang for his contribution to the numerical simulations in Chapter 3. The technical discussions with other members of the combustion group at Princeton are also very much appreciated.

I am truly grateful for the education offered by the MAE department of Princeton University. It is such an intellectually stimulating and nourishing place. I would like to thank all the faculty members and administrative staff of the department. Particularly, I am grateful to Professors Alexander Smits and Yiguang Ju for serving as my committee members. They both have provided great support, assistance and advice to the progress of my research and future career. I would particularly thank our graduate program administrator, Jill Ray. She is the unbelievably amazing that keeps us nerds in line, and always takes care of me and other graduate students.

My graduate school education was also immensely enriched through the daily interactions with the fellow students and staff around me. They constitute most of my friends in Princeton. Without them, my life for the past six years would not be so memorable. I also sincerely appreciate the technical discussions and friendship with many young researchers in the international combustion community during combustion conferences and the annual Princeton CEFRC summer school. The list would be too long if I enumerate all their names. I sincerely thank them all.

The dissertation was read by Professors Chih-Jen Sung, Michael Mueller and Swetaprovo Chaudhuri. Their insightful comments helped me a lot to improve the dissertation in many ways. I truly thank them for their effort, time and patience.

In my dissertation research, I also benefited a lot from the technical discussions with Professors John Bechtold, Fokion Egolfopoulos and Hai Wang. They have also shared valuable career advice to me.

My advisors, Jianxin Wang and Shijin Shuai, at Tsinghua University introduced me to the field of combustion. While working with them, I discovered the excitement of engine research, and started to appreciate the importance of fundamental combustion research. Their attitude and spirit toward academics are always inspiring me. I am truly grateful to them.

The research in this dissertation was supported by two sources of funding: the Air Force Office Scientific Research under the technical monitoring Dr. Julian M. Tishkoff and Dr. Chiping Li, and the Department of Energy through the Combustion Energy Frontier Research Center.

This dissertation carries the number T-3289 in the records of the Department of Mechanical and Aerospace Engineering.

To my wife Jing and our daughter Ashley

# Contents

Abstract . . . . .	iii
Acknowledgements . . . . .	iv
Contents . . . . .	viii
<b>1 Introduction</b>	<b>1</b>
1.1 Significance of Combustion Research . . . . .	1
1.1.1 Combustion and Our Civilization . . . . .	1
1.1.2 Need For Improvements . . . . .	6
1.2 Challenges of Combustion Science . . . . .	7
1.2.1 Nonlinearity . . . . .	10
1.2.2 Many Species and Reactions . . . . .	12
1.2.3 Large Range of Scales . . . . .	14
1.3 Motivations for the Present Work . . . . .	16
1.3.1 Laminar Flame Speeds and Flame Chemistry . . . . .	17
1.3.2 Dynamics of Premixed Flames . . . . .	20
1.4 Structure of Thesis . . . . .	29
<b>2 Experimental Design and Procedures</b>	<b>33</b>
2.1 Experimental Apparatus . . . . .	35

2.1.1	Vessel I . . . . .	35
2.1.2	Vessel II . . . . .	36
2.2	Visualization and Diagnostics . . . . .	42
2.2.1	Schlieren Imaging . . . . .	42
2.2.2	Mie Scattering and Particle Image Velocimetry . . . . .	43
<b>3</b>	<b>Error of Stretch Extrapolation of Flame Speeds</b>	<b>44</b>
3.1	Introduction . . . . .	44
3.2	Review of Extrapolation Equations . . . . .	48
3.3	Numerical Methods . . . . .	51
3.4	Computational Results . . . . .	54
3.4.1	Results For Hydrogen/air . . . . .	54
3.4.2	Burned Gas Density Effect . . . . .	57
3.4.3	Comparison With Experiments . . . . .	59
3.4.4	Results For <i>n</i> -Heptane/air . . . . .	61
3.5	Summary and Scaling of Uncertainties . . . . .	62
3.6	Concluding Remarks . . . . .	68
<b>4</b>	<b>Measured Laminar Flame Speeds</b>	<b>69</b>
4.1	Introduction . . . . .	69
4.2	<i>n</i> -Hexane . . . . .	72
4.3	Cyclo-alkanes . . . . .	75
4.3.1	Cyclohexane . . . . .	77
4.3.2	Methyl-cyclohexane . . . . .	79
4.3.3	Ethyl-cyclohexane . . . . .	82
4.4	Butanol Isomers . . . . .	83

4.4.1	<i>n</i> -Butanol . . . . .	86
4.4.2	<i>i</i> -Butanol . . . . .	89
4.4.3	<i>s</i> -Butanol . . . . .	92
4.4.4	<i>t</i> -Butanol . . . . .	94
4.5	Aromatic Fuels . . . . .	96
4.5.1	Toluene . . . . .	98
4.5.2	<i>o</i> -Xylene . . . . .	100
4.6	Mixtures of H <sub>2</sub> and C <sub>0</sub> -C <sub>4</sub> Hydrocarbons . . . . .	101
4.6.1	Hydrogen/Ethane Mixtures . . . . .	107
4.6.2	Hydrogen/Ethylene Mixtures . . . . .	108
4.6.3	Hydrogen/Acetylene Mixtures . . . . .	111
4.6.4	Hydrogen/Propane Mixtures . . . . .	112
4.6.5	Hydrogen/CO Mixtures . . . . .	113
4.7	Concluding Remarks . . . . .	117
<b>5</b>	<b>Flame Chemistry of Large Molecule Fuels</b>	<b>127</b>
5.1	Introduction . . . . .	127
5.2	C <sub>6</sub> -ring Cyclo-alkanes . . . . .	130
5.2.1	Comparison of Flame Speeds and Thermal Effects . . . . .	131
5.2.2	Analysis of Flame Chemistry . . . . .	138
5.3	Butanol Isomers . . . . .	150
5.3.1	Comparison of Flame Speeds and Thermal Effects . . . . .	151
5.3.2	Analysis of Flame Chemistry . . . . .	153
5.4	Concluding Remarks . . . . .	171

<b>6 Self-Acceleration Due to Flamefront Instabilities</b>	<b>173</b>
6.1 Introduction . . . . .	173
6.2 Review of Previous Works . . . . .	178
6.2.1 Experimental Studies . . . . .	178
6.2.2 Numerical Studies . . . . .	179
6.2.3 Fitting Formulas . . . . .	180
6.3 Present Experimental Considerations . . . . .	182
6.4 Experimental Results . . . . .	186
6.4.1 Propagation of Individual Flames . . . . .	187
6.4.2 Dimensionless Data . . . . .	191
6.5 Concluding Remarks . . . . .	204
<b>7 Turbulent Flame Speed Scaling For Expanding Flames</b>	<b>207</b>
7.1 Introduction . . . . .	207
7.2 Cold-flow Velocity Statistics . . . . .	210
7.3 Experimental Specifications . . . . .	214
7.4 Experimental Results . . . . .	220
7.4.1 Raw Data and Random Error . . . . .	220
7.4.2 Effective Turbulence Intensity . . . . .	222
7.5 Scaling of Turbulent Flame Speed . . . . .	226
7.5.1 Theoretical Considerations . . . . .	226
7.5.2 Scaling for Turbulence Intensity and Length Scale . . . . .	231
7.5.3 Scaling for Thermodiffusive Effects . . . . .	237
7.6 Concluding Remarks . . . . .	243

<b>8 Fuel Similarity and Local Extinction of Turbulent Flames</b>	<b>245</b>
8.1 Introduction . . . . .	245
8.2 Experimental Conditions . . . . .	247
8.3 Experimental Results . . . . .	248
8.3.1 Laminar Flame Speeds . . . . .	248
8.3.2 Turbulent Flame Speeds . . . . .	250
8.3.3 Stretch-induced Local Extinction . . . . .	253
8.4 Scaling of Turbulent Flame Speed . . . . .	258
8.5 Concluding Remarks . . . . .	260
<b>9 Spark Ignition in Turbulent Flows</b>	<b>264</b>
9.1 Introduction . . . . .	264
9.2 Experimental Considerations . . . . .	266
9.3 Experimental Results . . . . .	268
9.4 Explanation and Analysis . . . . .	274
9.5 Concluding Remarks . . . . .	279
<b>10 Conclusions and Recommendations</b>	<b>280</b>
10.1 Conclusions . . . . .	280
10.2 Recommendations . . . . .	282
10.2.1 Combustion Vessel Design . . . . .	283
10.2.2 Flame Speed Extrapolation . . . . .	283
10.2.3 Expanding Laminar Flames . . . . .	284
10.2.4 Flamefront Instabilities . . . . .	286
10.2.5 Expanding Turbulent Flames . . . . .	287
10.2.6 Flame Ignition Study . . . . .	288



# Chapter 1

## Introduction

### 1.1 Significance of Combustion Research

#### 1.1.1 Combustion and Our Civilization

The harnessing of fire was a pivotal milestone in our evolution history. As a cheap and effective energy conversion method, combustion of wood allowed early humans to cook food, obtain warmth and light, and protect themselves from wild animals. Recent anthropological theory ([Wrangham, 2010](#)) even suggests that the shift from consuming raw to cooked food one to two millions years ago was the key factor that allowed the brain of our ancestors to be substantially enlarged in comparison to those of the other mammals.

Another pivotal milestone of the human civilization was the industrial revolution, which started around two to three centuries ago. Large numbers of technological developments since industrial revolution, electrification and mechanization in particular, fundamentally changed human behavior. Since then the amount of food and consumer goods we produce, the distance we travel each year, the information

that we obtain in a day, and the number of babies that are born every year have increased significantly. However, at the same time, industrial revolution has also led to unprecedented energy consumption by our civilization to maintain this quality of life. As shown in Figure 1.1, the total world energy use has increased by more than 20 fold since the nineteenth century. Such a growth was caused by both the increase in total world population and the expansion of per capita energy consumption.

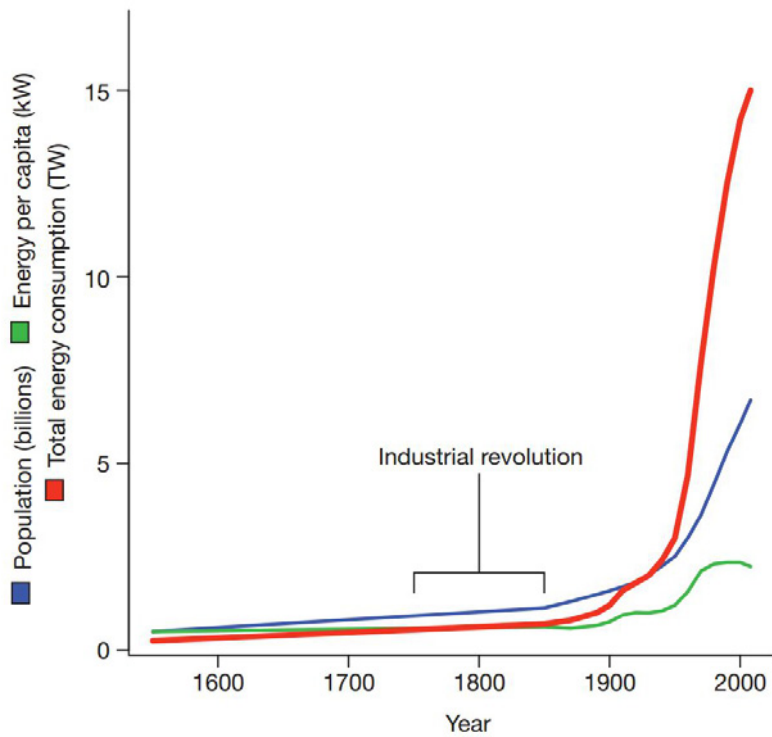


Figure 1.1: History of total and per capita human energy use and world population. The data and plot were collected and made by [Ehrlich \*et al.\* \(2012\)](#).

Where does this massive energy come from and go to? Figure 1.2 is an energy flow chart that shows the energy resources and end uses in the United States in 2013. It is seen that burning wood is no longer the primary means to acquire energy. The major energy resources today are fossil fuels, *i.e.*, coal, petroleum and natural gas, which constitute 80% of the total energy resource. However, what remains

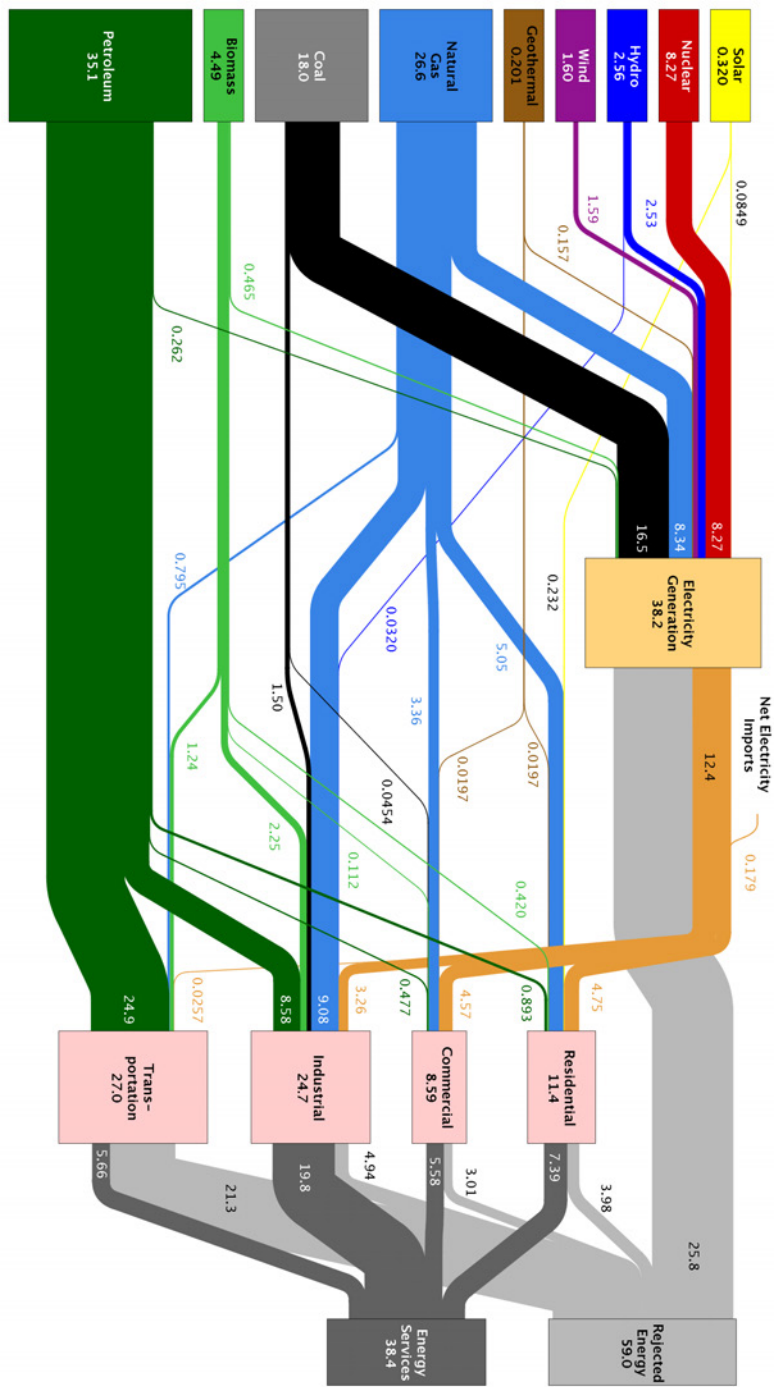


Figure 1.2: Energy flow charts show the relative size of primary energy resources and end uses in the United States in 2013, with fuels compared on a common energy unit basis. The chart is produced by Lawrence Livermore National Lab (<https://flowcharts.llnl.gov/>).

unchanged is that combustion is still the primary method for energy conversion: it converts 85% (fossil fuel + biomass) of the total world energy, which is the sum of the 95% in transportation, 67% in electricity generation and approximately 50% in all other sectors.

Fossil fuels are finite resources. According to the data from the US Central Intelligence Agency ([CIA, 2014](#)), if we continue using them at the current rate, the proven crude oil and natural gas reserves will be depleted in 50 and 60 years, respectively. While the actual fossil fuel resources maybe higher than the proven reserves as the exploration and extraction technologies improve ([Chu & Majumdar, 2012](#)), the global energy demand is also rapidly increasing as seen in Figure 1.1. Therefore, in the long term, alternative energy sources are necessary to reduce and eventually eradicate the worlds reliance on fossil fuel resources.

Energy sources such as wind, solar, hydroelectric, nuclear fusion, and bio-fuels are all possible renewable alternatives. Among them, bio-fuels and synthetic fuels from biomass present a viable and attractive energy option for the following reasons. First, as an energy storage medium, the energy density of liquid fuels is significantly higher than other types of energy storage. Figure 1.3 plots the energy density of various conventional fuels, alternative fuels and batteries. It is seen that the current bio-fuels in use, such as alcohols and bio-diesel, and Fischer-Tropsch (FT) synthetic fuels have significantly higher energy density compared to batteries. High energy density gives liquid fuels superior advantage in the transportation sector because of the need for a mobile power supply. Second, the energy transfer rate during vehicle or aircraft re-fueling is significantly higher than the electrical charging of battery based energy storage devices. For example, if a regular car is refueled in 2 minutes, the energy transfer rate is about 10,000 kilowatts, while that of a re-charging battery

is only about 50 kilowatts. Finally, bio-fuels are produced through photosynthesis. Therefore, potentially zero net carbon emission is possible. The above reasons indicate that, even after fossil fuels are depleted, the production and combustion of bio-based liquid fuels will still be one of the most viable energy solutions.

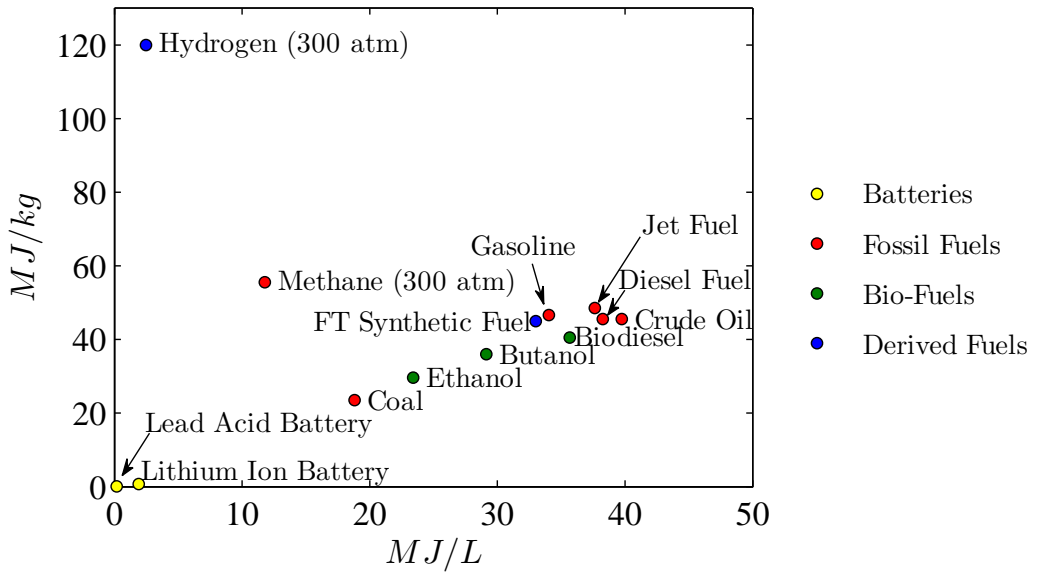


Figure 1.3: Energy density per mass plotted as a function of energy density per volume of various fuels and energy storage technologies. The plot was made by Andrew Kelley in his Ph.D. Thesis ([Kelley, 2011](#)). Data compiled from various sources.

In summary, combustion was, is and will continue to be an important energy conversion technology for our civilization. Currently, our civilization depends on the ability to exploit fossil fuels through combustion, and, in the future, bio-based liquid fuels, due to their high energy and power density, will most likely replace fossil fuels as the major energy source for ground and air transportation.

### 1.1.2 Need For Improvements

Although our civilization heavily relies on combustion, the current combustion technologies are still poor both in terms of efficiency and quality. The energy conversion efficiency of the current combustion systems is very low, leading to massive energy loss every day. It is seen from Figure 1.2 that less than 40% of the total energy is utilized to actually perform services. In electricity generation this is about 32%, while in the transportation sector the efficiency is only 20%. Typical spark-ignited gasoline engines deliver only 18% of the fuel energy to the drive train (Reitz, 2013), while the theoretical limit (Otto cycle) is 60-70% (Heywood, 1988) depending on the compression ratio and combustion temperature. Clearly, there is plenty of room to improve. Given the massive energy scale even small improvements in efficiency have a significant impact.

A major drawback of the combustion of carbon-based liquid fuels is the emission of carbon dioxide. The atmospheric concentration of carbon dioxide has increased 40% since the industrial revolution, and the main reasons are attributed to the burning of fossil fuels and the clearing of forests (IPCC, 2007; Chu & Majumdar, 2012). This continuous increase in atmospheric carbon dioxide has created significant climate-change risks. The fundamental fact is that the carbon in fossil fuels were accumulated in the time scale of millions of years but we are currently emitting all of them in the time scale of hundreds of years. Therefore, current combustion technologies need to be improved so that carbon dioxide emission is controlled. Carbon capture and storage (CCS) is a potential means for the ultimate mitigation of carbon dioxide emissions. However, current CCS technologies all come with large energy penalties, with 10-40% or more energy used if 85-95% of the CO<sub>2</sub> is expected to be captured (IPCC, 2011). Modified or more revolutionary combustion technolo-

gies have the potential to significantly reduce the cost of CCS, such as oxy-fuel combustion and chemical looping combustion ([Rubin \*et al.\*, 2012](#)).

In addition to carbon dioxide, combustion also emits air pollutants that directly harm human health, such as carbon monoxide, nitrogen oxides, particulates, sulfur oxides, unburned hydrocarbons, *etc.* Controlling these pollutant emissions again comes with additional cost and frequently emission requirement is the limitation for efficiency improvements ([Reitz, 2013](#)). It is clear that combustion technologies need to be improved so that the process of chemical energy utilization is both efficient and clean.

Finally, uncontrolled combustion can cause losses of human lives and wealth. Today, we still have many mine and building explosion accidents, vehicle and engine fires, forest fires, *etc.* Combustion technologies also need to be improved to increase the safety and reliability of existing and future combustion systems. All the improvements need investments in combustion research.

## 1.2 Challenges of Combustion Science

Given the energy and environmental challenges we face, it is our job to make the use of combustion as an energy conversion method more efficient, emit less carbon dioxide, cleaner and safer. Improvements in the combustion technology require qualitative and quantitative understanding of combustion science.

Combustion is an interdisciplinary subject by nature. Consider one of the simplest combustion phenomena, that of the candle flame. At the minimum the problem consists of fluid flow, chemical kinetics of fuels, and diffusive and radiative transport phenomena. For combustion of solid materials, large soot particle formation and

enhanced combustion by catalytic materials, the subject would involve material science. For spark ignition and plasma enhanced combustion, the subject also consists of the physics and chemistry of plasma. Nevertheless, as noted in Law (2006), the bulk of the field includes two subjects: fluid mechanics and chemical kinetics. As such a modern combustion researcher must be conversant in both.

The essential objective of modern fundamental combustion research is to progress towards a quantitatively predictive branch of science from the previously empirical and phenomenological one and ultimately develop tractable and predictive combustion models for the development and design of combustion-based energy conversion systems. The components constituting the investigation include computational fluid dynamics (CFD) models, combustion chemistry models, and models to describe other crucial physics in certain problems, such as plasma and interactions of gases with condensed phase materials.

Significant advances have been made in recent decades through the combined efforts of theory, experiment and computation. Today, we are reasonably confident in the qualitative understanding of the dynamics and structure of laminar flames (Law & Sung, 2000; Matalon *et al.*, 2003; Law, 2006, 2007; Buckmaster *et al.*, 2005), which provide guidelines for the modeling of complex flames, such as the flamelet modeling approach of turbulent combustion (Peters, 1984; Peters *et al.*, 2000). We are capable of computing laminar flames with high accuracy in a reasonable amount of time (Smooke, 2013) if the chemistry is accurate. Chemical kinetics of combustion have also improved substantially over recent years, as addressed in several reviews (Miller *et al.*, 2005; Pilling, 2009, 2013; Westbrook, 2013; Klippenstein *et al.*, 2014). We also have direct numerical simulation (DNS) capability to compute turbulent flames with detailed fuel chemistry and engine relevant Reynolds numbers (Chen,

[2011a](#)), so that the details revealed allowed us to understand the basic structure and features of turbulent flames as well as the complex interactions between turbulence, mixing and reactions.

However, we are still far from the goal of having tractable and predictive models to meet the needs of reliable design tools. The scientific challenges are formidable as evidenced by the persistent research efforts over the past many decades. Currently, we do not have computationally affordable models that can accurately predict even the key features of turbulent flames, such as the burning rate, before experimental data are in hand ([Lipatnikov & Chomiak, 2002, 2005; Driscoll, 2008](#)). Furthermore, while there are various reduced-order modeling approaches to describe turbulent combustion, such as those proposed by [Peters \(1984\)](#), [Pope \(2000\)](#) and [Poinsot & Veynante \(2005\)](#), we do not yet have predictive detailed chemistry models for the fuels used in engines, such as gasoline and diesel, recognizing nevertheless that progress is being made. We also do not have the capability to computationally track combustion instabilities and predict their consequences ([Law, 2006, 2007; Lieuwen, 2012](#)), and there are still unexplained sooting phenomena even in the simplest laminar flames ([Wang, 2011](#)).

As summarized by several recent plenary lectures at the biennial International Symposium on Combustion ([Buckmaster \*et al.\*, 2005; Miller \*et al.\*, 2005; Law, 2007; Peters, 2009; Pilling, 2009; Hanson, 2011; Pope, 2013; Smooke, 2013](#)), there are three principal scientific challenges for developing tractable and predictive combustion models: nonlinearity, many species and reactions, and large range of scales. They will be briefly discussed in the following.

### 1.2.1 Nonlinearity

The first principal challenge is that combustion is a highly nonlinear science. First, due to the need of large flow rate and thus burning rate, in almost all practical combustion systems the flow is turbulent. A turbulent flow itself is a nonlinear system. The source of the nonlinearity comes from the Navier-Stokes equations,

$$\rho \frac{\partial \vec{v}}{\partial t} + \rho (\vec{v} \cdot \nabla) \vec{v} = -\nabla p + \nabla \cdot \mathbf{T} + \mathbf{f} \quad (1.1)$$

where  $\vec{v}$  is the flow velocity vector,  $\rho$ ,  $p$ ,  $\mathbf{T}$  and  $\mathbf{f}$  are the density, pressure, stress tensor and body force, respectively, and  $\nabla$  represents the spatial gradient operator. The second term on the LHS,  $(\vec{v} \cdot \nabla) \vec{v}$ , is nonlinear convection that renders the Navier-Stokes equations nonlinear and devoid of general analytical solutions. It also causes chaotic, unsteady, three-dimensional eddies with a wide range of sizes ubiquitous in turbulent flows. These eddies cause fluctuations of all flow quantities at various magnitudes and frequencies, making all theoretical, numerical and experimental investigations challenging.

Second, chemical kinetics is also a highly nonlinear phenomenon. For an elementary reaction, the Arrhenius law states that the reaction rate has the following dependence on temperature,

$$k = BT^\alpha e^{-E_a/R^o T} \quad (1.2)$$

where  $k$  is the reaction rate,  $T$  the temperature,  $E_a$  the activation energy, the term  $BT^\alpha$  the pre-exponential factor with a temperature power exponent  $\alpha$ , and  $R^o$  is the universal gas constant. The activation energy  $E_a$  represents the barrier

energy required to initiate a reaction and is typically large for many important reactions in combustion. As a result, if the temperature of the reactive mixture is not high enough, the overall reaction will not proceed, while, if the temperature reaches the activation temperature, reactants will rapidly react to form products. This is the cause for the abrupt nature of the ignition and extinction phenomena in combustion. Furthermore, due to the high energy density of the fuels, reactions in combustion release a large amount of heat, which in turn induces gas motion. Therefore, fluid motion and chemical reactions are inherently coupled in flames of practical systems. The extent of coupling is aggravated by turbulence due to the fluctuations in various quantities, particularly temperature. For example, typical fluctuations in temperature are several hundred degrees ([Pope, 2013](#)). Thus if  $E_a$  is 20 kcal/mol (which is about the same to one of the most important reactions in combustion  $\text{H} + \text{O}_2 \rightarrow \text{HO} + \text{O}$ ), then a temperature variation from 1000 K to 1500 K will cause a factor of 30 change in the exponential term  $e^{-E_a/R^\circ T}$  and thus the reaction rate.

There are also nonlinear processes in diffusive and radiative transport. For example, the diffusion of multi-component gas mixtures without pressure gradient and body forces is governed by the following relation ([Williams, 1985](#)),

$$\nabla X_i = \sum_{j=1}^N \left( \frac{X_i X_j}{D_{i,j}} \right) (\vec{V}_j - \vec{V}_i) + \sum_{j=1}^N \left[ \left( \frac{X_i X_j}{\rho D_{i,j}} \right) \left( \frac{D_{T,j}}{Y_j} - \frac{D_{T,i}}{Y_i} \right) \right] \left( \frac{\nabla T}{T} \right) \quad (1.3)$$

where  $X_i$  and  $Y_i$  are the molar and mass concentration of species  $i$ ,  $\vec{V}_i$  the diffusion velocity of species  $i$ ,  $D_{i,j}$  the binary diffusion coefficient between species  $i$  and  $j$ ,  $D_{T,i}$  the Soret diffusion coefficient of species  $i$ , and  $\rho$  the density. The first term on the RHS represents the multi-component Fickian diffusion due to a concentra-

tion gradient, and the second term represents Soret diffusion due to a temperature gradient. It is seen that both terms are nonlinear.

Similarly, the governing equations of radiative transport are also highly nonlinear, which are integral and differential equations, and radiation effects can be strongly coupled with turbulence for sooty flames (Deshmukh *et al.*, 2008; Gupta *et al.*, 2013).

### 1.2.2 Many Species and Reactions

The second principal challenge is that the oxidation of fuels involves a large number of combustion intermediates and reactions. New discoveries in chemical kinetics are continuously being made over the past few decades, and as the molecular size of fuels increases the size of the chemical mechanisms reported also grow (Lu & Law, 2009). Depending on the fuel, the numbers of species and reactions can be as high as several thousands and tens of thousands, respectively.

Tracking each elementary reaction at a fundamental level is possible, and, by combining quantum chemistry theories and experiments, the quantitative information for many elementary reactions, *i.e.*, the rate constants and products yield, can be acquired with satisfactory accuracy (Miller *et al.*, 2005; Pilling, 2009, 2013; Klippenstein *et al.*, 2014). However, calculating or measuring these reaction rates one by one is an extremely time-consuming task. Methods for automatically determining the reaction pathways and calculating the associated rate constants have been developed (Mitsos *et al.*, 2008; Allen *et al.*, 2012); however, due to the unique specialties of individual reactions, these automatic methods still cannot fully replace the decisions made by well-trained chemists. Additionally, the current quantum chemistry theories and experimental measurement methods are not capable of determining the

rate constants of the reactions involving complex species, for example, the QOOH species in the low temperature combustion of hydrocarbons and alcohols (Zádor *et al.*, 2011), or reactions involving simple species at high pressure conditions, for example, HO<sub>2</sub> and H<sub>2</sub>O<sub>2</sub> at high pressures (Burke *et al.*, 2012).

As a result, we need to study the overall reaction systems, identify the reaction pathways, estimate reaction rate constants based on experience, and eventually form the entire reaction mechanisms, *e.g.*, those by Westbrook *et al.* (2009), Wang *et al.* (2010), Burke *et al.* (2012), Sarathy *et al.* (2012) and Ranzi *et al.* (2012). In these reaction mechanisms, only a small fraction of reactions have pre-calculated or measured rate constants available, and the other estimated reaction rate constants have large uncertainties. Therefore, there is always the need to validate reaction mechanisms indirectly by constraining these uncertainties against data obtained from well-controlled experiments.

Another problem is that, even if the rate constants of all the elementary reactions are known, the computational cost of tracking such large number of species and reactions in CFD is too large to be useful as design tools. Although computational power continuously increases, direct numerical simulation (DNS) of a laboratory flame, which resolves turbulent eddies in all scales, can only track less than 50 species using the most expensive computational resources (Chen, 2011a; Attili *et al.*, 2014). The number of species allowed in computations of combustion systems with complex geometry is significantly less (Gicquel *et al.*, 2012). If a detailed reaction mechanism for large-molecule fuels with thousands of species, such as those by Westbrook *et al.* (2009) and Sarathy *et al.* (2012), is to be used in CFD as design tool, substantial reduction of its size is necessary, and the current mechanism reduction methods cannot reduce the size lower enough to the need of industry (Lu & Law, 2009).

### 1.2.3 Large Range of Scales

The third principal challenge is that combustion is a multi-scale problem. The chemical and physical processes in combustion cover a wide range of length and time scales. At the smallest time scale, about  $10^{-12}$  seconds and shorter, quantum mechanics determines the electronic structure, chemical properties and reaction rates of gas molecules. Due to the fast and slow reactions, the residence time of combustion intermediates can vary from  $10^{-12}$  to  $10^{-4}$  seconds in reacting flow simulations ([Lu & Law, 2009](#)). In addition, radiation occurs at the speed of light. Therefore, the smallest time scale for radiation can be  $10^{-9}$  seconds for a system with length scale of 1 meter. From roughly  $10^{-6}$  to  $10^0$  second we have all the scales for continuous flow motion. The smallest scale in a turbulent flow in combustion is the Kolmogorov length scale ([Pope, 2000](#)), which can be as small as 100 nanometers, while the largest scale for a fire can be 10's or 100's of meters.

With such a large range of scales, it is impossible to resolve all of them in brute-force computations even with the most powerful computer, current and anticipated. Models have to be developed for various processes. Ideally, if different processes occur at different scales with minimum couplings, then in principle they can be treated separately. In all quantum chemistry computations the Born-Oppenheimer approximation is adopted, which assumes the time scale of the electron motion is much shorter than that of the nuclei. In all reacting flow simulations, when several rate constant parameters are used to represent chemical reactions, the underlying assumption is that the time scales of internal vibrations and molecular collisions are much shorter than the flow time scales, such that the gas flow is in thermodynamic equilibrium and all the energy levels follow the Boltzmann distribution. For turbulence or turbulent combustion computations, a popular method is large eddy

simulation (LES), which computes the large-scale motions based on first-principle equations, such as the Navier-Stokes equations and models the small-scale motion assuming they are universal.

It is essential that the models we develop are accurate, *i.e.*, the model constants are validated against experimental or full-fidelity computational results, and are also applicable to the problems of interests, *i.e.*, the assumptions still hold where we apply them. For chemical kinetics, the assumptions based on which we determine the elementary reaction constants generally holds well in real combustion systems; therefore, the major task is to make sure the model parameters, *i.e.*, the reaction rate constants are accurate. For turbulent combustion models, although the LES approach works well with reasonable success for non-reacting turbulent flows, we have not yet reached the consensus on the sub-grid modeling approaches for reacting flows. State-of-the-art approaches are flamelet modeling (Peters, 1992; Trisjono *et al.*, 2013; Knudsen *et al.*, 2013; Mittal *et al.*, 2012a), which assumes the flames are always thin compared to the flow eddies, thickened flame modeling (Poinsot & Veynante, 2005; Gicquel *et al.*, 2012), which artificially increases the flame thickness to be larger than the grid size, and approaches based on probability density function (PDF) (Pope, 2000, 2013), which models physical fluid properties with their joint PDFs. The primary reason for this inconsistency is that, as pointed out by Pope (2013), we lack understandings of the small-scale interactions between flames, gas motion and chemical reactions.

## 1.3 Motivations for the Present Work

Given the significance and challenges of combustion research, motivations for the present work are identified from the following considerations. First, as discussed above there are still many scientific challenges and knowledge gaps in the conventional subsonic gas-phase combustion. Therefore, in the present work, problems involving surface reactions, radiation, soot formation, catalytic combustion, plasmas, two-phase flow, detonation, thermoacoustics, *etc.*, are not considered.

Second, it is recognized that although the dynamics and structure of laminar flames are considered to be well understood (Law, 2007; Buckmaster *et al.*, 2005; Law & Sung, 2000) and stable laminar flames can also be computed accurately and efficiently (Smooke, 2013), the research of laminar flames have assumed its new roles. Laminar flames form the elemental unit of many complex combustion phenomena. Typical laminar flames have thicknesses in the range of dozens to hundreds of micro meters, and characteristic time in the range  $10^5$  to  $10^3$  seconds. Smaller than these scales are the complex fuel oxidation chemical kinetics, which are confined within the laminar flame thickness for most cases, and larger than them are the complex turbulent combustion, which in most cases are essentially the interactions between laminar flames and the associated turbulent flow. Therefore, laminar flame is the essential unit that connects chemical kinetics and turbulent combustion.

Third, as pointed out by Pope (2013), we specifically lack the understandings on flow, flame and chemistry interactions at small scales. Problems at small scales are challenging to study, but crucial to the development of sub-grid models such that large-scale problems can be modeled with the sub-grid models in hand. Examples are the intrinsic flamefront cellular instabilities and spark ignition, both of which

occur below the scale of resolution of numerical mesh of practical simulations, and are important.

Therefore, the present work will focus on two topics. The first topic is on the studies of fuel oxidation chemical kinetics by measuring laminar flame speeds. The second topic is on the dynamics and instabilities of premixed flames in various flow conditions (from quiescent to turbulent) and at various scales. The two topics are separately discussed in the following.

### 1.3.1 Laminar Flame Speeds and Flame Chemistry

As discussed above, the oxidation kinetics of both conventional and alternative fuels involve large numbers of species and reactions, many of which have large uncertainties causing inaccurate/erroneous predictions. This motivates the need to validate reaction mechanisms against controlled experimental measurements.

Currently, combustion phenomena used for validation purposes include homogeneous reactors and stable, laminar one-dimensional flames. The homogeneous reaction systems that are used extensively are shock tubes, flow reactors, jet-stirred reactors (JSR), and rapid compression machines (RCM). In these systems, all spatial dependencies are suppressed, reactions either start from, or extrapolated to, a given initial condition, and the system progress depends only on time. Therefore, the measured quantities are the ignition delay time and the evolution of the species concentrations and temperature. These data constitute the basis for studying kinetic pathways and sometimes for measuring the rate constants of the individual elementary reactions.

Laminar one-dimensional flames avoid multi-dimensional flow effects, and, compared to homogeneous systems, represent conditions close, to practical combustion

systems, *e.g.*, internal combustion engines, in which reactant consumption is through the agency of flames with the concomitant presence of heat and mass diffusion. As a result, the reaction pathways and sensitivities to reaction rate constants can be modified. As such, they constitute an additional class of minimum targets that a reaction mechanism has to meet in order to be considered predictive.

There are several types of laminar flames that have been used for kinetic studies, each of which is applicable in different pressure ranges. For pressures lower than 0.1 atm, burner-stabilized flat flames are used for measurements of species concentration profiles within the flame. These flames are thick enough to provide spatial resolution. They are also frequently combined with advanced synchrotron light source to conduct remarkable speciation measurements, *e.g.*, detection of radicals and identification of isomers ([Qi, 2013](#)). For pressures between 0.2 to 10 atm, stagnation flames (including both wall-stagnation flames and counterflow flames), burner-stabilized flat flames (heat flux method ([Bosschaart & de Goey, 2003](#))) and expanding spherical flames are used for to measure laminar flame speeds. Stagnation flames can also be used to measure ignition and extinction limits ([Liu \*et al.\*, 2011b](#); [Ji \*et al.\*, 2010](#)), as well as speciation profiles if high spatial resolution can be achieved ([Lefkowitz \*et al.\*, 2012](#)). For pressures higher than 10 atm, stagnation flames and burner-stabilized flames become unstable due to increased Reynolds number. Consequently, expanding spherical flame is the only method for high pressure one-dimensional flame studies. The advances and challenges of different flame configurations are discussed in the recent review paper by [Egolfopoulos \*et al.\* \(2014\)](#).

The present work will focus on the laminar flame speed measurements, particularly at elevated pressures, using the constant-pressure expanding spherical flame configuration. The laminar flame speed,  $S_u^0$ , is defined as the propagation speed

of a one-dimensional planar (unstretched), steady, adiabatic flame relative to the unburned gas. Accurate measurements of such a quantity is not a trivial task, because ideally the experiment needs to satisfy all the assumptions in its definition. What cannot be satisfied is the condition of planar unstretched flame because the flame speed of expanding spherical flames is subjected to flame stretch. The effects of stretch through the non-equildiffusion of heat and mass was not well established until the mid 1980s (Wu & Law, 1984; Matalon & Matkowsky, 1982; Pelce & Clavin, 1982), and since then the state-of-the-art procedure has been identifying the stretch effect from experimental raw data and then extrapolating it to zero stretch to determine the unstretched flame speed  $S_u^0$ , using various theoretically derived linear and nonlinear relations between stretched flame speed and stretch rate (Wu & Law, 1984; Dowdy *et al.*, 1990; Tien & Matalon, 1991; Kelley & Law, 2009; Chen, 2011b; Kelley *et al.*, 2011a). It is believed that the uncertainties associated with extrapolation are the largest sources of uncertainties, particularly at low pressures, compared to other effects, which have been studied previously, such as ignition (Chen & Ju, 2007; Chen *et al.*, 2009b; Kelley *et al.*, 2009; Kelley & Law, 2009), flow confinement (Chen *et al.*, 2009a; Kelley & Law, 2009; Burke *et al.*, 2009) and radiation (Chen, 2010; Santner *et al.*, 2014; Jayachandran *et al.*, 2014) effects. Therefore, the present work first assesses the uncertainties associated with stretch extrapolation.

Large number of measurements on  $S_u^0$  have been recently reported, with the number of related publications increased by a factor of three from 2007 to 2012. However, accurate data on large-molecule liquid fuels, especially at elevated pressures, are sparse (Kelley *et al.*, 2011c,b). For liquid hydrocarbon fuels, straight-chain and branched alkanes have been well studied (Kelley *et al.*, 2011c,b; Ji *et al.*, 2012b, 2010). The present work will mainly focus on cyclic alkanes and aromatics.

For alcohols, the present work will focus on butanol isomers, recognizing their potentials as bio-based alternative fuels. At the same time, it is known that all the oxidation chemistry of large fuels inevitably depend on H<sub>2</sub> and C<sub>1</sub>-C<sub>4</sub> foundation fuel chemistry. Therefore, the present study will also focus on the foundation fuels, particularly mixtures of H<sub>2</sub> with C<sub>1</sub>-C<sub>4</sub> hydrocarbons.

In addition to laminar flame speed measurements, it is equally important to study and understand the chemical structure of laminar flames and extract possible empirical rules between flame speeds and fuel molecule type and structure, which are useful to improve modeling approaches of their chemistry and develop surrogates for transportation fuels. First of all, from flame theory it is known that flame speeds do not only depend on the chemical reactivity of fuels (chemical effects) but also on the heat of combustion (thermal effects) and the transport properties of fuels (transport effects) ([Law, 2006](#)); therefore, the thermal and transport effects need to be understood or eliminated to elucidate the chemical effects. Second, the chemical reasons for one fuel to have higher flame speed than another are complex to analyze for large molecule fuels, such as the long-chain, branched and cyclic hydrocarbons and alcohols. Therefore, detailed reaction pathway and sensitivity analyses are needed in order to fully understand their oxidation chemistry.

### 1.3.2 Dynamics of Premixed Flames

The second topic of the present work is on the dynamics and instabilities of premixed flames in various flow conditions and at various scales. In particular, the focus will be on the flamefront cellular instabilities of laminar premixed flames, propagation of turbulent premixed flames and premixed flame kernel ignition in turbulent flows. The major goal of studying these problems is to understand the small-scale flame

dynamics and provide insights for sub-grid modeling.

A premixed flame is a flame in which fuel and oxidizer are well mixed before any diffusion and chemical reactions occur. Premixed flames are commonly seen or used in practical systems, such as gas appliance stoves, spark-ignited gasoline engines, lean premixed gas turbines and accidental mine explosions. Therefore, understanding their dynamics is crucial in seeking the appropriate modeling approaches for such systems.

Unlike non-premixed flames, a premixed flame is not constrained to follow the contour of stoichiometric composition, but instead propagates towards the unburned gas mixture. This gives it the possibility to reach almost anywhere in the flow field, propagate at various speeds, and even possibly transit to detonation, the supersonic combustion wave solution of RankineHugoniot relations ([Law, 2006](#)). Therefore, it is more difficult to predict the location and flame speed of premixed flames, especially for unstable and turbulent premixed flames.

Today we have a reasonably good understanding on the dynamics of laminar stable flames, particularly on the responses of flame speed to heat loss and stretch. The pioneering studies by [Karlovitz \*et al.\* \(1953\)](#) first suggested that local flame speed scales with the stretch experienced by the flame surface, which he defined as,

$$K = \frac{1}{A} \frac{dA}{dt} \quad (1.4)$$

where  $K$  is the stretch rate,  $A$  an arbitrary flame surface area and  $t$  the time. At the same time, [Markstein \(1951\)](#) empirically obtained the following relation between flame speed and curvature,

$$S_u = S_u^0 (1 + L\kappa) \quad (1.5)$$

where  $S_u$  is local flame speed,  $\kappa$  is the curvature of the flame surface and  $L$  is a characteristic length, which we shall refer to as the Markstein length. (Markstein, 1964) subsequently recognized that  $L$  depends on the Lewis number of the mixture, which is defined to be ratio of thermal diffusivity to mass diffusivity. In the 1980s, the stretch effect on flame speed was systematically identified using asymptotic analysis (Matalon & Matkowsky, 1982; Pelce & Clavin, 1982; Clavin & Williams, 1982; Clavin, 1985), resulting in the following relation,

$$S_u = S_u^0 - LK \quad (1.6)$$

The above relation was extended into a more general expression (Ronney & Sivashinsky, 1989; Bechtold & Matalon, 1999; Sun *et al.*, 1999; Sun & Law, 2000; Law & Sung, 2000),

$$\left(\frac{S_u}{S_u^0}\right)^2 \ln\left(\frac{S_u}{S_u^0}\right)^2 = -\frac{2LK}{S_u^0} \quad (1.7)$$

It is noted that the definition of  $L$  has changed from Equation 1.5 to Equations 1.6 and 1.7. The theoretical expression of the dependence of  $L$  on a series of flame parameters (such as Lewis number, thermal expansion ratio, activation energy, thermal conductivity, *etc.*) has also been refined as more details are taken into account in the analysis (Matalon & Matkowsky, 1982; Pelce & Clavin, 1982; Bechtold & Matalon, 2001; Matalon *et al.*, 2003; Clavin & Graña Otero, 2011). It should be realized that these theoretical results are still based on various assumptions, such as one-step or two-step overall reactions with large activation energy, weakly stretched flames, close to unity Lewis number, *etc.* Therefore, their accuracy could be compromised, and there are finite uncertainties if they are used for flame speed extrapolation, as will be addressed in Chapter 3. However, given the success of numerical simulations

of laminar flames (Smooke, 2013), currently we are always capable of obtaining the response of flame speed to stretch via numerical simulation.

What remain unsolved are the effects of the cellular flamefront instabilities and the dynamics of premixed flames in turbulent flows. Both problems heavily depend on the small-scale flame-flow interactions and are both beyond our typical computational capability, except peta-scale DNS (Chen, 2011a) which is extremely expensive.

Cellular instabilities have been observed in flames since the beginning of modern combustion research. Darrieus (1938) and Landau (1944) independently showed that hydrodynamic instabilities can always be induced by thermal expansion in the limit of an infinitely thin flame. Markstein (1951, 1964) subsequently demonstrated non-equidiffusion can induce a diffusional-thermal instability for flames with finite thickness, which can be either stabilizing or destabilizing, depending on the Lewis number. Subsequent theoretical (Sivashinsky, 1977a,b; Joulin & Clavin, 1979; Sivashinsky, 1979; Matkowsky *et al.*, 1980; Sivashinsky *et al.*, 1982; Sivashinsky, 1983; Clavin *et al.*, 1983; Frankel & Sivashinsky, 1983; Clavin, 1985; Williams, 1985; Clavin & Nicoli, 1985; Bechtold & Matalon, 1987; Addabbo *et al.*, 2002) and experimental (Manton *et al.*, 1952; Palm-leis & Strehlow, 1969; Groff, 1982; Kwon *et al.*, 1992; Bradley & Harper, 1994; Bradley *et al.*, 2000, 2001; Tse *et al.*, 2000; Kwon *et al.*, 2002; Law & Kwon, 2004; Tse *et al.*, 2004; Law *et al.*, 2005; Jomaas *et al.*, 2007b) studies systematically explained and experimentally confirmed that laminar premixed flames are subjected to two modes of cellular instability: hydrodynamic (Darrieus-Landau) and diffusional-thermal, with the former caused by thermal expansion and the latter caused by non-equidiffusion. Currently, we understand that, by decreasing the mixture's Lewis number, diffusional-thermal cellular instability

is promoted, *e.g.*, for lean H<sub>2</sub>/air and rich hydrocarbon/air mixtures, and similarly changing the inert bath gas from N<sub>2</sub> to He (Ar or CO<sub>2</sub>) can suppress (promote) cellular instability. We also understand that increasing pressure promotes hydrodynamic (Darrieus-Landau) instability mainly due to the reduced flame thickness. Furthermore, for expanding spherical flames, both linear stability analysis ([Sivashinsky \*et al.\*, 1982](#); [Bechtold & Matalon, 1987](#); [Addabbo \*et al.\*, 2002](#)) and experimental results ([Groff, 1982](#); [Bradley & Harper, 1994](#); [Kwon \*et al.\*, 2002](#); [Law & Kwon, 2004](#); [Jomaas \*et al.\*, 2007b](#)) indicate that cellular instabilities are initially suppressed at small flame radii due to the strong curvature-induced stretch. Reasonable agreement between theoretical predictions and experimental measurements on the onset of transition from stable smooth flames to unstable cellular flames has also been achieved ([Jomaas \*et al.\*, 2007b](#)).

However, an important unanswered question is how the flame speed is affected by the cellular instability. It is expected that the presence of instability increases the flame surface area and consequently the flame speed, but the rate and duration of acceleration is unknown. Since cellular instability is easily promoted in practical systems, *e.g.*, for lean H<sub>2</sub>/air and rich hydrocarbon/air mixtures at pressures above 5 atm, understanding the induced flame speed acceleration is necessary in order to properly model these premixed flames. Previous experimental studies ([Gostintsev \*et al.\*, 1988](#); [Bradley \*et al.\*, 2001](#); [Kwon \*et al.\*, 2002](#); [Gostintsev \*et al.\*, 2004](#); [Haq, 2005](#)) reported inconsistent results, and numerical studies ([Blinnikov & Sasorov, 1996](#); [Ashurst, 1997](#); [Liberman \*et al.\*, 2004](#); [Filyand \*et al.\*, 1994](#); [Aldredge & Zuo, 2001](#); [Galanti \*et al.\*, 1998](#); [Olami \*et al.\*, 1997](#); [Karlin & Sivashinsky, 2006, 2007](#); [Olami \*et al.\*, 1995](#); [Fur senko \*et al.\*, 2008](#); [Pan & Fur senko, 2008](#)) were neither rigorous nor conclusive, as will be reviewed in Chapter 6. The present work will provide

well-defined experimental data on flame acceleration due to cellular instabilities.

The ultimate goal for studying laminar flames and chemical kinetics is to quantitatively predict the behavior of flames in real applications, which are frequently turbulent. It is clear that turbulent combustion is an extremely challenging problem, as evidenced by persistent research efforts since the beginning of modern combustion research. The major challenge, as discussed early in this chapter and reviewed by several recent papers ([Bilger, 2000](#); [Lipatnikov & Chomiak, 2002](#); [Sivashinsky, 2002](#); [Bilger \*et al.\*, 2005](#); [Lipatnikov & Chomiak, 2005](#); [Driscoll, 2008](#); [Peters, 2009](#); [Pope, 2013](#)), is that the problem is multi-scale in nature and there is strong interactions between turbulent flows and chemical kinetics. In addition, it is widely agreed that premixed turbulent combustion is inherently more complex than non-premixed turbulent combustion because there is a much stronger coupling between chemistry and turbulence ([Bilger \*et al.\*, 2005](#)). The central problem of turbulent premixed combustion is to predict its burning rate or the turbulent flame speed.

The pioneering work on turbulent premixed combustion by [Damköhler \(1940\)](#) was based on the assumption that reactions occur in a thin front, which is not influenced by the flow. As a result, there are two limits: large-scale and small-scale turbulence. In large-scale turbulence, if the smallest flow eddy is still larger than the flame thickness (within which molecular diffusion and reactions occur) such that the local flame speed is unaffected (remains to be  $S_u^0$ ), then the turbulent flame speed  $S_T$  is entirely determined by the wrinkling of the flamefront by turbulence, and  $S_T$  is only related with the effective flame surface area via,

$$\frac{S_T}{S_u^0} = \frac{A_T}{A_L} \quad (1.8)$$

where  $A_T$  is the effective total flame surface area and  $A_L$  the projected area of  $A_T$  in the direct of flame propagation. For small-scale turbulence, if the largest flow eddy is smaller than the flame thickness so that  $A_T = A_L$ , but large enough such that the reaction rates are not affected, then the effect of turbulence is only to change the molecular diffusivity to turbulent diffusivity. Based on the scaling of laminar flame speed (Law, 2006), Damköhler (1940) argued that,

$$\frac{S_T}{S_u^0} = \left( \frac{D_T}{D} \right)^{0.5} \quad (1.9)$$

where  $D_T$  and  $D$  are the turbulent and molecular diffusivity, respectively.

Extensive efforts have been made over the last 50 years on the speed of turbulent premixed flames to validate, refine or extend the concepts by Damköhler (1940). This includes extensive analytical (Clavin & Williams, 1979; Yakhot, 1988; Kerstein *et al.*, 1988; Kerstein & Ashurst, 1992; Peters, 1992; Lipatnikov & Chomiak, 2007; Kolla *et al.*, 2010), experimental (Abdel-Gayed *et al.*, 1987; Bradley *et al.*, 2011; Filatyev *et al.*, 2005; Kobayashi *et al.*, 1996, 2005; Venkateswaran *et al.*, 2011), and computational (Bell *et al.*, 2005; Shim *et al.*, 2011) investigations. Because large-scale turbulence is more common in applications and laboratory flames, most studies followed the idea of Equation 1.8, and the interest is to seek a unified scaling for  $S_T$  with a small number of parameters, such as the turbulence intensity, turbulence length scale, Reynolds number, laminar flame thickness, Lewis number, *etc.* However, a unified scaling for turbulent flame speeds still does not exist.

One reason that simple turbulent flame speed scaling has not been identified, if it indeed exists, is perhaps the structure of turbulent premixed flames have been modified by turbulence so much such that the concept of Damköhler (1940) is not

appropriate any more. This leads to the studies on the internal structure of turbulent premixed flames and the identification of regimes for turbulent combustion. The most commonly referred regime diagrams are that of [Borghi \(1988\)](#) and [Peters et al. \(2000\)](#) and of [Libby & Williams \(1994\)](#). They are both two-dimensional planes with axes of  $u'/S_u^0$  versus  $L_I/\delta_L$ , and of  $Da = S_u^0 L_I / u' \delta_L$  versus  $Re = u' L_I / S_u^0 \delta_L$ , where  $u'$  is the turbulence rms-velocity,  $L_I$  the turbulence integral length scale,  $\delta_L$  the laminar flame thickness, and  $Da$  and  $Re$  the Damköhler number and Reynolds number. The idea is that, based on the time scale of the turbulent eddies relative to that of laminar flames, the internal structure of the turbulent flames can be classified as wrinkled/corrugated laminar flamelets, thin reaction zone flames, thickened/distributed reaction zone, well stirred reaction zone, etc. However, so far the regime diagrams are based on steady-state theoretical scaling arguments. There is no convincing experimental evidence (*e.g.*, three-dimensional measurements of OH and HCHO concentrations) that premixed flames are broadened for flames with Karlovitz number  $Ka = u' \delta_L / S_u^0 L_\eta$  significantly exceeding unity ([Driscoll, 2008](#)), where  $L_\eta$  is the Kolmogorov length scale. On the other hand, recent DNS simulations do suggest flame broadening for extremely high  $Ka$  flames ([Poludnenko & Oran, 2010](#); [Hamlington et al., 2011](#); [Aspden et al., 2011](#)). Recent studies by [Won et al. \(2014\)](#) showed that preheating the unburned gas mixture also change the turbulent premixed combustion regimes by changing the auto ignition time scale. This means a two-dimensional plane is not adequate to describe all the controlling physics, and a third dimension or more maybe needed to fully describe the regimes of turbulent premixed combustion.

Another reason that turbulent flame speed scaling has not been successful is that the flame wrinkling process by turbulent flows has very strong geometry de-

pendence, as suggested by Bilger *et al.* (2005) and Driscoll (2008). The flame that Damköhler (1940) considered, based on which turbulent flame speed is defined, is a statistically planar flame. Although it is a good reference flame, no laboratory flames are statistically planar. The canonical laboratory flames in use include Bunsen flames (Kobayashi *et al.*, 1996, 2005; Venkateswaran *et al.*, 2011), V-flames (Smith & Gouldint, 1979), flat-flames (including burner stabilized or stagnation/counterflow flames) (Shepherd & Cheng, 2001; Lawn & Schefer, 2006) and expanding flame (Abdel-Gayed *et al.*, 1987; Kido *et al.*, 2002; Bradley *et al.*, 2011). As suggested by Driscoll (2008), all these canonical flames have “memory” of the wrinkling process at upstream conditions. Therefore, it is not possible to reach a scaling without specific geometry information. Furthermore, it is recommended by Bilger *et al.* (2005) and Driscoll (2008) that any model validation or comparison of turbulent flame speeds should be restricted to a particular configuration with specific boundary conditions that the model or scaling is valid for.

Given the above mentioned status of research on turbulent premixed combustion, the present work focuses on the canonical configuration of expanding turbulent flames. One of the special characteristics of expanding turbulent flames is that the flame radius is continuously increasing. Therefore, the effective hydrodynamic length scale is also increasing. In addition, the present work mainly focuses on the conditions located in the wrinkled/corrugated flamelet and thin reaction zone regimes. Flames in such regimes not only are theoretically more traceable but are also directly relevant to applications, such as gasoline engines and explosions (Reitz, 2013). It is also relatively easier to explore high pressure conditions on expanding flames compared to other flame configurations.

The final topic on the dynamics of premixed flames that was studied is on the

spark ignition of a premixed mixture in turbulent flows. Ignition of a combustible mixture by a stimulus kernel is of relevance to many phenomena and applications, such as gasoline spark-ignited engines, gas turbines, prevention of accidental explosions, *etc.* The size of a spark is typically less than 2 mm, well below the computation mesh of typical engine CFD code (Reitz, 2013). Therefore, fundamental understandings and physics-based modeling of such a small-scale phenomenon are urgently needed. For a flame kernel of small radius  $R$ , the associated stretch rate  $K = (2/R) dR/dt$  is very large. According to Equation 1.7, the flame speed will be significantly modified and possibly extinguished by stretch. The dynamics of a small flame kernel in quiescent flow have been theoretically (Chen & Ju, 2007; Chen *et al.*, 2011) and experimentally (Kelley *et al.*, 2009) demonstrated. However, in all previous investigations on the spark ignition in turbulent flows, the dynamics of premixed flame kernels have not been considered (Ballal & Lefebvre, 1975, 1977; Kaminski *et al.*, 2000; Bradley *et al.*, 2004; Akindele *et al.*, 1982; Ahmed *et al.*, 2007; Ahmed & Mastorakos, 2006; Shy *et al.*, 2008b, 2010; Cardin *et al.*, 2013). The present work systematically investigates the problem of spark ignition of premixed mixtures in well-characterized turbulence, and for the first time demonstrate the importance of considering the dynamics of premixed flame kernels in spark ignition.

## 1.4 Structure of Thesis

This dissertation is organized as follows. Experimentation is the main research tool for the present work. In particular, laminar flame speeds, flamefront cellular instabilities, dynamics of turbulent expanding flames and spark ignition in turbulent flows are all studied using the constant-pressure, dual-chamber, fan-stirred combus-

tion vessel. Therefore, prior to presenting any results a detailed description of the experimental vessel, procedure and data analysis is given in Chapter 2.

The largest uncertainty of laminar flame speed measurements using expanding spherical flame technique is associated with the stretch extrapolation. Therefore, a systematic quantification of stretch extrapolation error by numerical simulations of laminar stable expanding flames is presented in Chapter 3. The resulting measurements of laminar flame speeds of various fuels and mixtures are presented in Chapter 4. Based on the experimental measurements, studies of flame chemistry of large-molecule liquid fuels using state-of-the-art chemical kinetic models are presented in Chapter 5.

Studies on the dynamics of premixed flames are presented in Chapters 6 to 9. Specifically, Chapter 6 presents the study on self-acceleration of expanding flames due to intrinsic flamefront cellular instabilities. Chapter 7 presents the study on turbulent flame speeds of various gaseous fuels and the scaling for expanding turbulent flames. Chapter 8 presents the study on turbulent flame speeds of liquid *n*-alkane fuels with focus on the fuel similarity and stretch-induced local extinctions. Chapter 9 presents the study on spark ignition in turbulent flows. Finally, in Chapter 10 the results of the present work are summarized and suggestions for future research are presented.

Majority of the material presented in this dissertation has been either previously published or submitted for publication considerations in the following articles:

- WU, F., LIANG, W., CHEN, Z., JU, Y. & LAW, C. K. 2014a Uncertainty in stretch extrapolation of laminar flame speed from expanding spherical flames. *Proceedings of the Combustion Institute* **35**, in press

- WU, F., KELLEY, A. P. & LAW, C. K. 2012 Laminar flame speeds of cyclohexane and mono-alkylated cyclohexanes at elevated pressures. *Combustion and Flame* **159**, 1417–1425
- WU, F. & LAW, C. K. 2013 An experimental and mechanistic study on the laminar flame speed, Markstein length and flame chemistry of the butanol isomers. *Combustion and Flame* **160**, 2744–2756
- WU, F., KELLEY, A. P., TANG, C., ZHU, D. & LAW, C. K. 2011 Measurement and correlation of laminar flame speeds of CO and C<sub>2</sub> hydrocarbons with hydrogen addition at atmospheric and elevated pressures. *International Journal of Hydrogen Energy* **36**, 13171–13180
- WU, F., JOMAAS, G. & LAW, C. K. 2013 An experimental investigation on self-acceleration of cellular spherical flames. *Proceedings of the Combustion Institute* **34**, 937–945
- CHAUDHURI, S., WU, F., ZHU, D. & LAW, C. K. 2012 Flame speed and self-similar propagation of expanding turbulent premixed flames. *Physical review letters* **108**, 044503
- CHAUDHURI, S., WU, F. & LAW, C. K. 2013 Scaling of turbulent flame speed for expanding flames with Markstein diffusion considerations. *Physical Review E* **88**, 033005
- WU, F., SAHA, A., CHAUDHURI, S. & LAW, C. K. 2014c Propagation speeds of expanding turbulent flames of C<sub>4</sub> to C<sub>8</sub> n-alkanes at elevated pressures: experimental determination, fuel similarity, and stretch-affected local extinction. *Proceedings of the Combustion Institute* **35**, in press

- WU, F., SAHA, A., CHAUDHURI, S. & LAW, C. K. 2014 *b* Facilitated ignition in turbulence through differential diffusion. *Physical Review Letters* **113**, 024503

# Chapter 2

## Experimental Design and Procedures

The present work adopted the expanding flame configuration to study both laminar and turbulent flames. For laminar flames, the expanding spherical flame is believed to be the most suitable for studying high-pressure flames ([Egolfopoulos \*et al.\*, 2014](#)). For turbulent flames, expanding flames are one of the canonical configurations to study turbulent premixed combustion ([Driscoll, 2008](#)).

The study of expanding spherical flame dates back to [Lewis & von Elbe \(1934\)](#), who used a constant-volume bomb to deduce laminar flame speeds from the recorded pressure history. This method was used until the 1980s ([Metghalchi & Keck, 1980](#)). The problem of such measurements is that the effects of stretch and a possible presence of flamefront instabilities at high pressure conditions are overlooked.

In the 1980s, the concept of flame stretch was understood and subsequent studies provided optical access to the constant-volume chamber such that the flame radius and stretch rate history can be obtained via Schlieren or shadowgraph techniques

(Dowdy *et al.*, 1990). Knowing the instantaneous stretch rate allows the effect of stretch to be accounted for. The major limitations of constant-volume combustion chamber are that: 1) the flame speed determination is complicated by the associated pressure rise and therefore only data at the very initial stage are not useful; 2) the factor of 7-10 pressure rise makes maintaining the integrity of the optical windows a challenge.

To achieve experiments at higher pressures and avoid pressure rise, Tse *et al.* (2000) adopted the dual-chamber design in which less than 2% pressure rise is achieved. In the design, a series of holes are installed on the wall of the inner chamber, which can be mechanically opened and closed to allow union and separation of the inner and outer chamber gases. The inner chamber is filled with the test combustible mixture and the outer chamber with inerts that balance the pressure of the gases in the inner chamber. Then ignition and opening union of gases is synchronized, resulting in an expanding flame that propagates in the inner chamber in essentially an isobaric environment. The flame is automatically quenched upon contacting the inerts in the outer chamber. This dual-chamber constant-pressure design allows measurements at pressures up to 60 atm (Tse *et al.*, 2000). Similar dual-chamber constant-pressure designs were adopted by Qin & Ju (2005) and recently by Kelley *et al.* (2011c) and Santner *et al.* (2013) to provide heating to the chamber in order to allow experiments with liquid fuels with higher boiling points.

The early work on expanding turbulent flames adopted the same constant-volume single-chamber combustion vessel design with optical access (Karpov *et al.*, 1959; Sokolik *et al.*, 1967). Stirring fans were installed in this design to create turbulent flows. This design is still be used in modern studies, using either a single spark ignition kernel (Bradley *et al.*, 2003; Kido *et al.*, 2002; Bradley *et al.*, 2009; Lawes

*et al.*, 2012) or double spark ignition kernels (Abdel-gayed & Bradley, 1977; Abdel-gayed *et al.*, 1984; Bradley *et al.*, 2013). The problem of using a constant-volume single-chamber design is the same as in the laminar spherical flame experiments, *i.e.*, the experiment cannot cover high-pressure conditions due to large pressure rise and flame speed measurement is compounded by pressure rise. Recently, Shy *et al.* (2008a) modified the double-chamber design of Tse *et al.* (2000) and implemented two stirring fans in the inner chamber such that turbulent expanding flames without pressure rise could be studied.

## 2.1 Experimental Apparatus

The present study successively adopted two constant-pressure dual-chamber vessels. The first vessel, designated Vessel I in this thesis, was developed for studying laminar flames of gaseous fuels at room temperature (Tse *et al.*, 2000). The present study uses Vessel I as it is. The second vessel, designated Vessel II in this thesis, was initially developed for studying laminar flames of liquid fuels (Kelley *et al.*, 2011c) at elevated temperatures. The present work installed stirring fans on Vessel II to study turbulent flames.

### 2.1.1 Vessel I

Details of Vessel I are given in Tse *et al.* (2000), Tse *et al.* (2004) and Jomaas (2008). Therefore, only a brief description is given here.

The combustion vessel is made up of two coaxial aluminum cylinders. The inner cylinder is 82.55 mm in inner diameter and 127 mm in length. The outer cylinder is 273.05 mm in inner diameter and 304.8 mm in length. Optical windows are mounted

at both ends of inner and outer chambers. The inner cylinder and its encasing sleeve have matching rows of holes on the lateral wall, which permits connection between the environments of the inner and outer chambers when the holes are aligned. The two chambers are isolated by offsetting the rows of holes, which then are sealed by O-rings. The apparatus has been tested to a maximum hydrostatic pressure of 95 atm (Tse *et al.*, 2004). Experiments have been performed at an operating pressure of 60 atm (Tse *et al.*, 2000, 2004; Rozencan *et al.*, 2002).

### 2.1.2 Vessel II

The geometry and general features of Vessel II were also previously described by Kelley (2011). Therefore, only a brief description and details of its stirring fans are given here.

The schematic of Vessel II are shown in Figures 2.1 and 2.2 at two different view angles, respectively. The plumbing diagram of the experimental setup of Vessel II is in Figure 2.3. The combustion vessel is also made up of two coaxial aluminum cylinders. The inner cylinder is 114.3 mm in inner diameter and 127 mm in length. The outer chamber consists of a cylindrical vessel, which is 273.05 mm in inner diameter and 322.58 mm in diameter, and four housings in which the motors for the inner chamber fans are encased. The walls of the inner chamber are fitted with a total of 32 holes of 5.613 mm diameter. The holes are arranged as eight sets of four, as shown in Figure 2.1. Each set of four holes has a circular disk that sits above the holes. The disk has a set of matching holes and can either seal the inner chamber walls via four o-rings, or rotate 45° to align the holes and connect the inner and outer chambers.

Four fans of 69.86 mm diameter are located at the walls of the inner chamber,

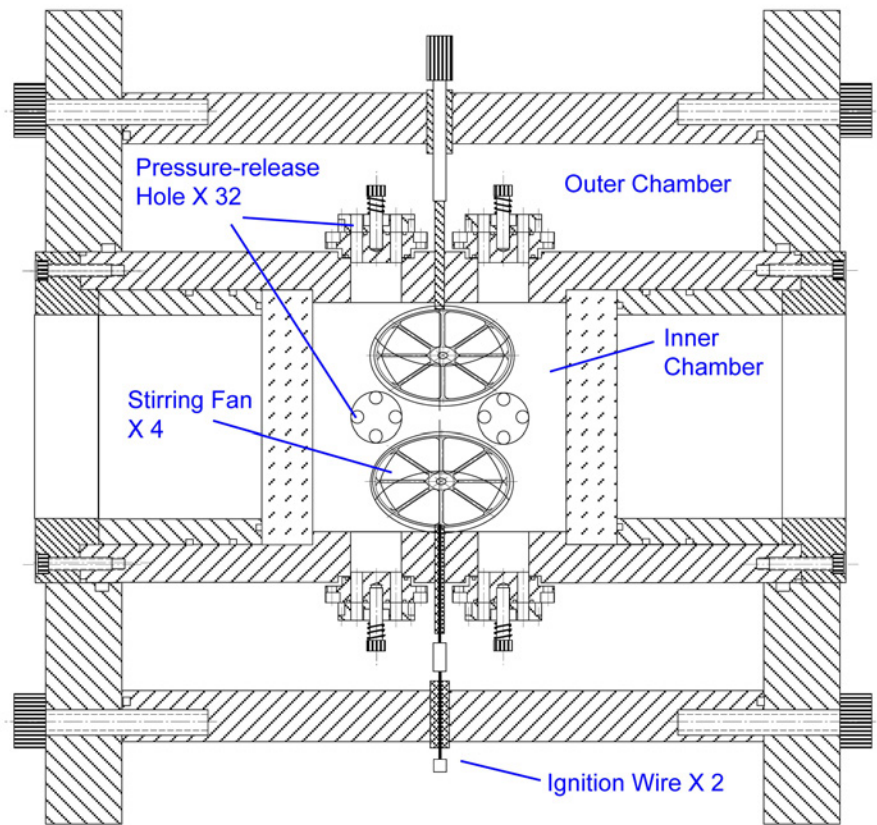


Figure 2.1: Schematic of Vessel II with line of sight perpendicular to pressure-release holes.

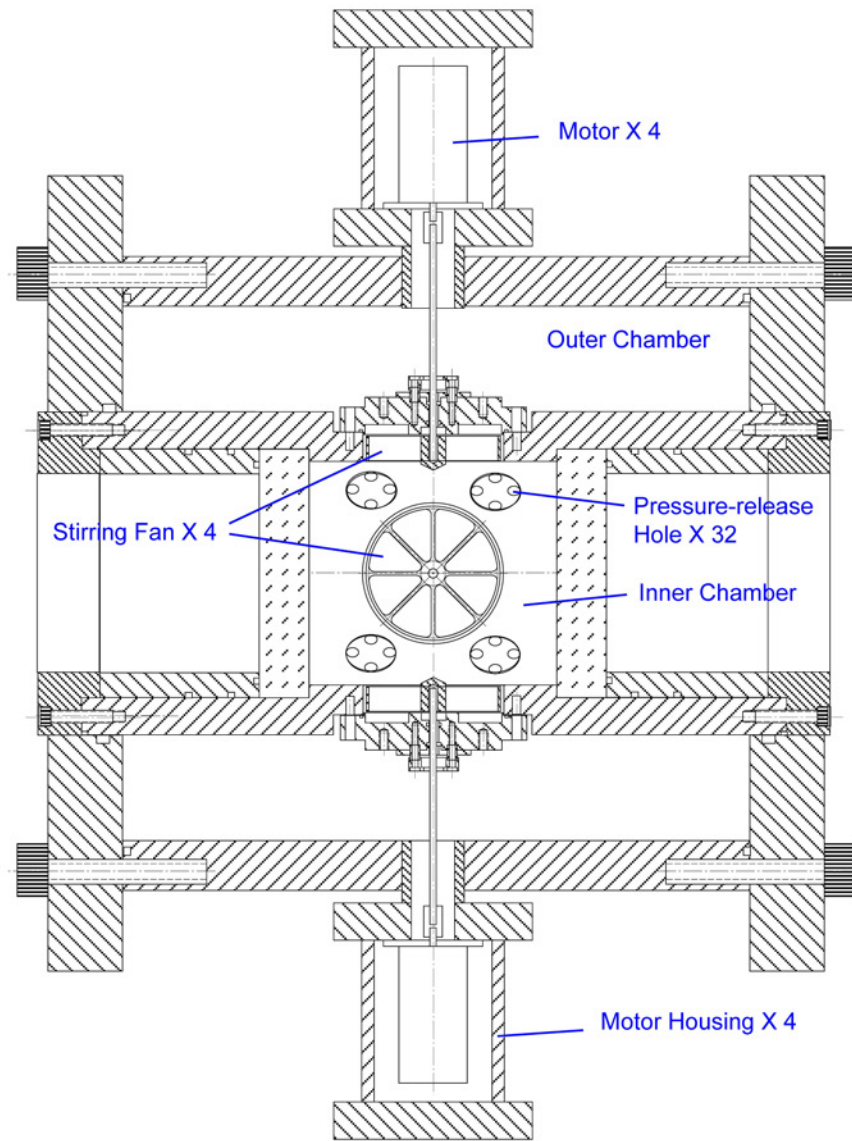
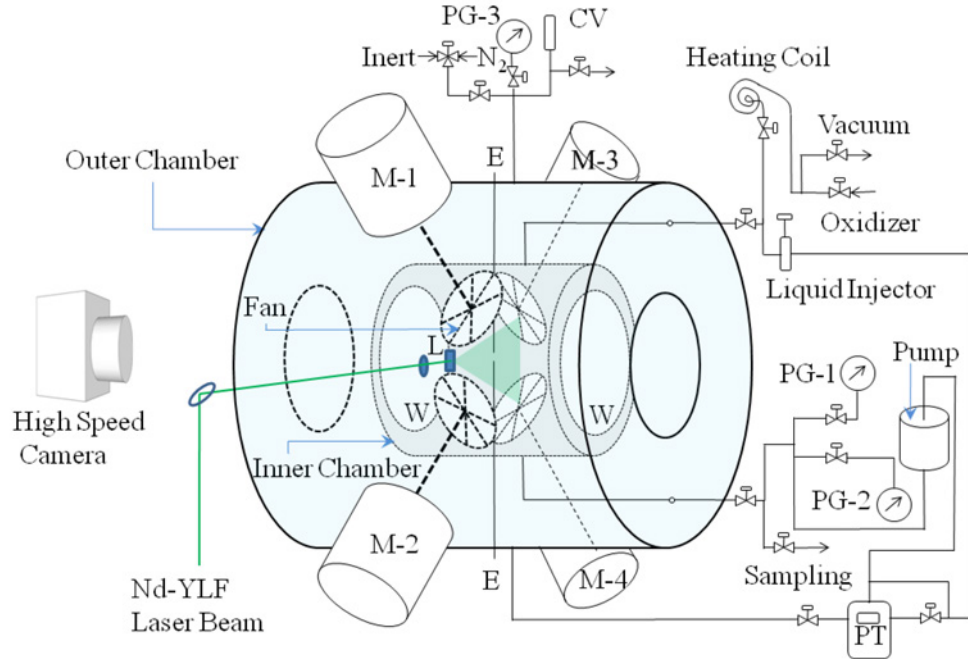


Figure 2.2: Schematic of Vessel II with line of sight perpendicular to stirring fans (45° turn to that of Figure 2.1).



CV: Check Valve, PG: Pressure Gauge, PT: Pressure Transducer, M: Fan Motor, L: Cylindrical Lens, E: Electrodes, W: Quartz Window

Figure 2.3: Plumbing diagram of the experimental setup of Vessel II.

as shown in Figure 2.2. They are radially located at  $90^\circ$  to one another and are centered axially in the chamber. The center line of each fan has a  $45^\circ$  shift to the plane in which pressure-release holes are fitted. These fans are driven by motors enclosed in the outer chamber, which are also shown in Figure 2.2. The photo and dimension of an individual fan is shown in Figure 2.4. The installment of the four fans relative to the inner chamber, in the center plane perpendicular to the center line of inner chamber, is shown in Figure 2.5. The speed of the stirring fans varies from 0 to 8000 rpm and is controlled by a closed-loop system. The accuracy of fan speed control is tested to be within 1%.

In order to study liquid fuels, the operating temperature needs to be increased to ensure that the liquid fuels remain in the gas phase. Heating of Vessel II is achieved

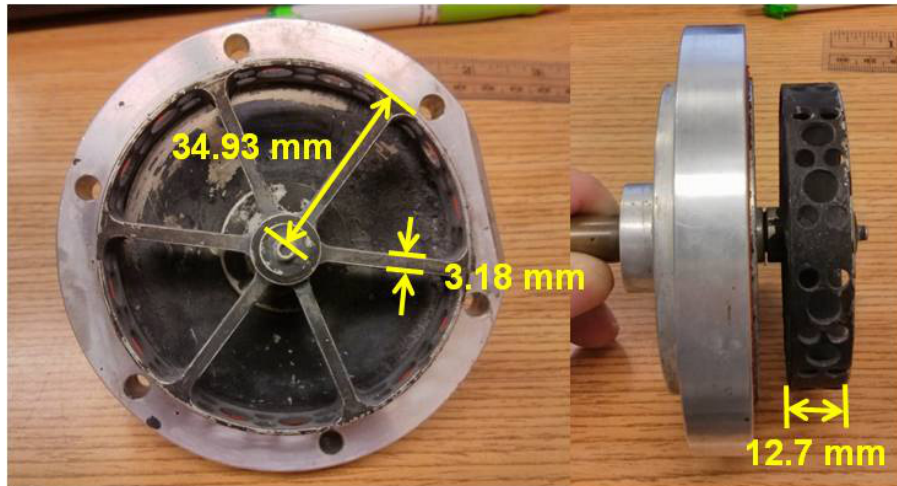


Figure 2.4: Photo and dimensions of the stirring fan of Vessel II.

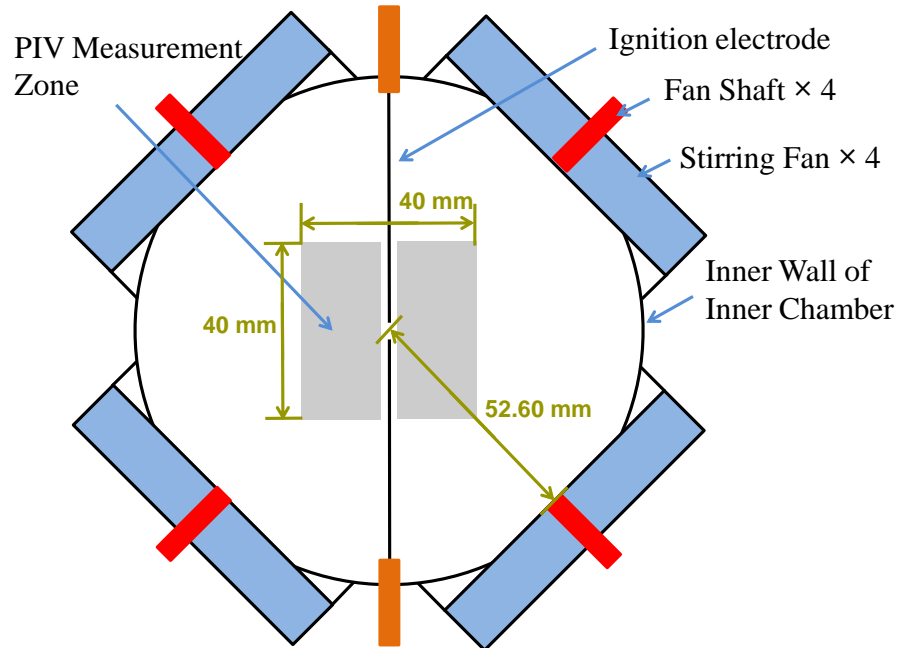


Figure 2.5: The installment of the four fans relative to the inner chamber in the center plane perpendicular to the center line of inner chamber. The PIV measurement zone is indicated in grey.

using silicon rubber heat sheets with adhesive backing. The temperature is maintained using four thermocouple controllers and additional eight thermocouples to monitor the temperature at various places of inner and outer chamber. The temperature can be maintained within  $\pm 2\text{K}$  for three hours after turning the heaters on. Due to the inevitable heat loss from the outer chamber to the laboratory, maintaining a slightly lower outer chamber temperature maintains the proper temperature gradient for heat loss from the outer chamber walls and heats the inner chamber nearly uniformly to the desired temperature.

As shown in Figure 2.3, both inner and outer chambers are connected with copper tubes to pressure gauges and transducers, gas/liquid filling ports, a heating coil for gas preheating, a gas sampling port, and a mixing pump. They form a closed loop with minimum dead ends to ensure adequate mixing by the mixing pump. All the copper tubes are also covered by heat insulators and tape heaters, to maintain the desired temperature.

Two  $250 \mu\text{m}$  tungsten wires are used as electrodes and are located inside the inner chamber. They are vertically oriented and centered axially. The electrodes have a gap that can be adjusted by a micrometer. The top electrode is grounded, and a high voltage is applied to the bottom electrode. The spark is generated by discharging a  $33 \mu\text{F}$  capacitor through an ignition coil with a 134:1 turns ratio. The ignition coil increases the voltage, which is then discharged across the electrodes resulting in a spark. The capacitor is charged with a voltage difference, which is variable to control the energy input of for the spark. Due to inevitable losses in the electrical wires and the ignition coil, the total energy stored in the capacitor should be higher than the energy that is used to ignite the mixture. In the present work, the ignition energy is not directly measured.

Designation	Manufacturer	Model	Full Scale (psia)	Accuracy (% Full Scale)
PG-1	Omega	PX409-005A5V	0 – 5	$\pm 0.08\%$
PG-2	CEComp	DPG1000AD15PSIA	0 – 15	$\pm 0.25\%$
PG-3	CEComp	DPG1000AD100PSIA	0 – 100	$\pm 0.25\%$
PG-4	CEComp	DPG1000AD1000PSIG	15 – 1015	$\pm 0.25\%$

Table 2.1: Pressure gauge specifications

Test mixtures with desired gas composition are ensured by the partial pressure method. The gas filling procedures are the same as those described in Kelley (2011). Four pressure gauges with different operating ranges and accuracies are used depending on the pressure. Their specifications are listed in Table 2.1. The pressure transducer (PT) measures the pressure differential between the inner and outer chambers. The pressure transducer used is model PX72-030GV from Omega and has a range of 0–30 psig pressure differential.

## 2.2 Visualization and Diagnostics

### 2.2.1 Schlieren Imaging

The flame surface is visualized using a Schlieren system (not shown in Figure 2.3) that allows visualization of the density gradient and thus temperature gradient in the inner chamber. The light source of the Schlieren system is given by a 100W mercury lamp (Newport Model 66902). The light is focused to a point and passes through a small hole to ensure that the light source closely represents a point source. It then passes through an achromatic plano-convex lens of focal length 250mm that creates a parallel light source. The parallel light passes axially through the inner chamber and then another plano-convex lens where it is focused. At the focal point, a pin-

hole or knife-edge is used to create the Schlieren effect. For pin-holes the Schlieren effect comes from the density gradient in the radial direction, and for knife-edge, it comes from the density gradient in the vertical direction. The resulting image is recorded via a Vision Research Phantom V7.3 high speed camera.

### 2.2.2 Mie Scattering and Particle Image Velocimetry

The two-dimensional flow field in the center plane perpendicular to the center line of inner chamber is measured using a time-resolved high-speed particle image velocimetry (PIV) system. The light source of the PIV system is provided by a double-beam Nd:YLF laser manufactured by Litron Lasers. The repetition rate of this laser can be as high as 10 kHz. In the present work, 4 kHz repetition rate is used, at which the energy output of the laser pulse of each beam is about 10 mJ. The two laser beams are directed and focused to the center of the inner chamber with a cylindrical lens through a window slot located between two stirring fans, as shown in Figure 2.3, resulting a diverging planar laser beam which covers a 20 mm × 20 mm area centered at the center of the inner chamber. The tracer particles for PIV are droplets of bis (2-ethylhexyl) sebacate ( $C_{26}H_{50}O_4$ ), which are generated by a self-made jet nebulizer. The size of these particles are estimated to be a few micrometers. The Mie scattering images are recorded via the same Phantom camera used for Schlieren imaging. To calculate the PIV velocity vectors, the two laser beams are shifted by a 30 ms time difference. The correlation of the resulting two-image pairs are analyzed by the DaVis Imaging Software from LaVision. In this work, velocity is measured in the 40 mm × 40 mm box centered in the inner chamber, as shown in Figure 2.5. The area close to the electrodes was excluded from the PIV measurement to minimize the error due to reflection.

# Chapter 3

## Error of Stretch Extrapolation of Flame Speeds

### 3.1 Introduction

Laminar flame speed,  $S_u^0$ , is defined to be the speed of the one-dimensional planar (unstretched), steady, adiabatic flame relative to the unburned gas. The speed of this flame relative to the burned gas is  $S_b^0$ . The two quantities are related by continuity,

$$S_b^0 = \Theta S_u^0 = \frac{\rho_u^0}{\rho_b^0} S_u^0 \quad (3.1)$$

where  $\Theta = \rho_u^0 / \rho_b^0$  is the thermal expansion ratio and  $\rho_u^0$  and  $\rho_b^0$  are the unburned and equilibrium burned gas density, respectively. The directly measured quantity from constant-pressure expanding spherical flames is the instantaneous burned gas velocity,  $S_b = dR_f/dt$ , where  $R_f$  is the flame radius. Here, it is assumed that the burned gas density  $\rho_b$  equals the equilibrium density  $\rho_b^0$ . This method is not a direct measurement of  $S_u^0$ . Therefore, the non-ideal effects need to be understood to make

corrections and then assess the uncertainties. Possible sources of uncertainties can come from ignition, flow confinement, radiation and stretch extrapolation. These effects can modify both  $S_b$  and  $\rho_b$ , and thus modify the measured  $S_u^0$ .

First, measurements of  $S_b$  maybe affected by the spark ignition energy and flow confinement by the chamber wall. A series of studies have investigated ignition (Chen & Ju, 2007; Chen *et al.*, 2009b; Kelley *et al.*, 2009; Kelley & Law, 2009) and flow confinement (Chen *et al.*, 2009a; Kelley & Law, 2009; Burke *et al.*, 2009) effects, and reasonably satisfactory understanding has been reached. The influence of ignition energy quickly diminishes as the flame radius increases, and the confinement by the chamber wall does not take significant effect until the flame radius reaches approximately 30% of the wall radius. For Vessel I and II, the range of experimental data that is independent of ignition energy and chamber confinement is in between radii of 1.0 to 1.8 centimeters (Jomaas, 2008; Kelley, 2011).

The value of  $S_b$  in experiments is also affected by radiation, especially the radiation of burned gas, which not only changes the flame speed but also the burned gas density, which in turn violates the assumption that burned gas is in equilibrium temperature and motionless. Radiation effects are difficult to quantify due to the complexity in radiation and re-absorption and the coupling with other effects, such as stretch. In the optically thin limit (a conservative estimate of uncertainty associated with radiation), radiation effects on the speed of expanding spherical flame were recently studied analytically and numerically (Chen, 2010; Santner *et al.*, 2014; Jayachandran *et al.*, 2014). Results showed that, at this limit, radiation can cause approximately 10% under prediction for flames at the flammability limit and less than 2% under prediction for regular flames.

Another major reason causing the difference between  $S_b$  and  $S_u^0$  is the preferential

diffusion of heat and mass characterized by non-unity values of the Lewis number ( $Le$ ), and the preferential diffusion between fuel and oxidizer (Law, 2006). The preferential diffusion modifies the flame temperature and thus the flame speed in the presence of flame stretch, which is characterized by the generalized stretch rate,

$$K = \frac{1}{A} \frac{dA}{dt} \quad (3.2)$$

where  $A$  is the flame surface area (Law, 2006). For expanding spherical flame,

$$K = \frac{2}{R_f} \frac{dR_f}{dt} \quad (3.3)$$

It is seen that a positive stretch rate is always present for expanding spherical flames and, as the  $R_f$  increases,  $K$  approaches 0, corresponding to  $S_b = S_b^0$ . If the relation between  $S_b$  and  $K$  is known, then  $S_b^0$  can be obtained by extrapolating a series of experimental data of  $S_b$  and  $K$  to the condition with  $K = 0$ . This extrapolation (or fitting) is a common practice for measuring laminar flame speeds from expanding spherical flames and other configuration such as counterflow flames.

Realizing the stretch effect on flame speed and the use of extrapolation largely advanced the accuracy of flame speed measurements in history. As an example, the historical measurements of the maximum laminar flame speed for methane/air mixtures at atmospheric pressure and temperature are shown in Figure 3.1. These measurements were obtained using a variety of experimental configurations. It is seen that, historically, the measurements varied by more than 25 cm/s. However, after 1980, the variations in the measurement were drastically reduced. This reduction was the result of Wu & Law (1984) recognizing that the measurement of the laminar flame speed must account for the influence of stretch.

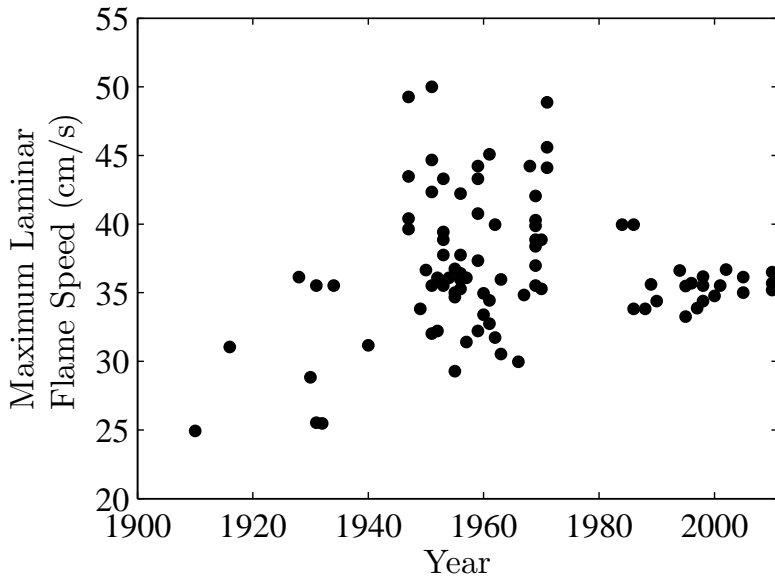


Figure 3.1: Historical measurements of the maximum laminar flame speed for methane/air mixtures at room temperature and pressure. The plot was made by Kelley (2011).

However, at the same time the uncertainties associated with extrapolation are still largely unknown. First of all, the current extrapolation equations (the relation between  $S_b$  and  $K$ ) in use were all derived from asymptotic analysis based on various assumptions, such as one-step chemistry scheme, weakly stretched flames, constant density, etc., which are not valid for flames of real fuels. In addition, depending on what assumptions are made in the asymptotic analysis, different extrapolation equations have been used (Wu & Law, 1984; Dowdy *et al.*, 1990; Tien & Matalon, 1991; Kelley & Law, 2009; Chen, 2011b; Kelley *et al.*, 2011a) in the past. Some previous studies have compared the difference among these equations on experimental data (Dowdy *et al.*, 1990; Kelley & Law, 2009; Chen, 2011b; Halter *et al.*, 2010). However, we still do not know what extrapolation equation gives the more accurate results and its error.

The work presented in this chapter investigated computationally the uncertain-

ties of different extrapolation relations for flame speed measurement using expanding spherical flames. A brief review of extrapolation equations is given first, followed by description of the numerical methods, results and conclusions. Finally, a formula for estimating extrapolation error is given, which is used throughout this thesis for quantify experimental uncertainties and make corrections.

The results presented in this chapter have been previously published in the following journal article ([Wu et al., 2014a](#)):

- WU, F., LIANG, W., CHEN, Z., JU, Y. & LAW, C. K. 2014a Uncertainty in stretch extrapolation of laminar flame speed from expanding spherical flames. *Proceedings of the Combustion Institute* **35**, in press

## 3.2 Review of Extrapolation Equations

[Wu & Law \(1984\)](#) first suggested the use of a linear relation between measured stretched flame speed and the stretch rate to extract the laminar flame speed from counterflow experiment. Later, such a relation has commonly been used for flame speed measurement using expanding spherical flames, such as [Dowdy et al. \(1990\)](#) and many others. The equation reads,

$$S_b = S_b^0 - L_b K \quad (3.4)$$

where  $S_b^0$  and  $L_b$  are the the unstretched laminar flame speed and Markstein length with respect to the burned mixture.  $S_b = dR_f/dt$  and  $K = (2/R_f)dR_f/dt$  are the stretched flame speed with respect to the burned mixture and the stretch rate of an expanding spherical flame, with  $R_f$  being the measured flame radius. Here it is

assumed that the burnt gas is motionless and in equilibrium. This linear model is just a first-order approximation of the relation, based on the assumption that the Lewis number is near unity and the flame is weakly stretched. Therefore, large error using this model in flame speed extrapolation is expected. Since the model assumes linear relation between flame speed and stretch, it is denoted as LS.

[Tien & Matalon \(1991\)](#) suggested that for counterflow flames nonlinear extrapolation should be used, and it has been shown experimentally ([Vagelopoulos \*et al.\*, 1994](#); [Davis & Law, 1998](#)) that linear and nonlinear extrapolations differ significantly for data at large strain rate. However, the nonlinearity considered in [Tien & Matalon \(1991\)](#) is not from the relation between stretched flame speed with stretch but rather comes from the location shift of the reference velocity and the velocity minimum, in counterflow flame measurement with stretch, which does not exist in expanding spherical flame method. [Kelley & Law \(2009\)](#) suggested using a nonlinear equation for flame extrapolation in expanding spherical flames,

$$\left(\frac{S_b}{S_b^0}\right)^2 \ln \left(\frac{S_b}{S_b^0}\right)^2 = -\frac{2L_b K}{S_b^0} \quad (3.5)$$

This equation has been derived by [Ronney & Sivashinsky \(1989\)](#), assuming quasi-steady flame propagation and large flame radius relative to the flame thickness. It allows arbitrary Lewis number ( $Le$ ), so it is expected to be more general than the linear model and can be applied for arbitrary mixtures. For the past few years, this model has been used extensively for extrapolating laminar flame speeds from expanding spherical flames. Improved accuracy and performance have been demonstrated in [Kelley & Law \(2009\)](#), [Chen \(2011b\)](#) and [Halter \*et al.\* \(2010\)](#). Since the nonlinear model is based on quasi-steady flame propagation, it is denoted as NQ in

this study.

In addition to Equation (3.5), Chen (2011b) suggested another nonlinear extrapolation equation,

$$S_b = S_b^0 - L_b \kappa = S_b^0 - \frac{2L_b}{R_f} \quad (3.6)$$

where  $\kappa = 2/R_f$  is the curvature of the flame surface. Since the model is actually a nonlinear relation between flame speed and stretch rate but a linear relation between flame speed and curvature, it is denoted as LC. This relation has been proposed empirically by Markstein (1951) and demonstrated analytically by Frankel & Sivashinsky (1983). It was demonstrated in Chen (2011b) that the difference between the extrapolated laminar flame speeds using Equation (3.6) and NQ is large for mixtures with  $Le > 1$  while they give almost the same results for mixtures with  $Le < 1$ . Chen (2011b) further showed that the extrapolation curve using Equation (3.6) agrees better with the results of numerically simulated methane flames than NQ, and, therefore, Equation (3.6) should be used instead of NQ, especially for mixtures with  $Le > 1$ .

To explain the apparent improved accuracy of LC over NQ, Kelley *et al.* (2011a) noted that, in the analysis of Ronney & Sivashinsky (1989), if the unsteady term is retained, the resulting relation reads,

$$\left(\frac{S_b}{S_b^0}\right)^2 \ln \left(\frac{S_b}{S_b^0}\right)^2 = \frac{2L_b}{S_b^0} \frac{dS_b}{dR_f} - \frac{2L_b K}{S_b^0} \quad (3.7)$$

which is expected to be more accurate than NQ; however, Equation (3.7) is numerically unstable, as demonstrated in Kelley *et al.* (2011a), due to the derivative term on the RHS thereby providing difficulty in its use for extrapolation. Kelley *et al.* (2011a) suggested using an equation resulting from the expansion of Equation (3.7)

in reverse powers of  $R_f$ ,

$$\frac{S_b}{S_b^0} \left[ 1 + \frac{2L_b}{R_f} + \frac{4L_b^2}{R_f^2} + \frac{16L_b^3}{3R_f^3} + O\left(\frac{L_b^4}{R_f^4}\right) \right] = 1 \quad (3.8)$$

This equation has been used in [Wu et al. \(2011\)](#), [Wu et al. \(2012\)](#) and [Wu & Law \(2013\)](#). Since Equation (3.8) comes from expanding (3.7), it is denoted as NE in this study. It was further noted in [Kelley et al. \(2011a\)](#) that by expanding Equations (3.4), (3.6), (3.5) and (3.7), the improved accuracy of LC over NQ can be explained, as seen in Table 3.1.

Finally, recognizing that difference among LS, LC, NQ and NE starts from the second-order inverse power of  $R_f$ , in this study an extrapolation equation with a free parameter on the second-order term was also considered,

$$S_b = S_b^0 - \frac{2L_b}{R_f} + \frac{C}{R_f^2} \quad (3.9)$$

This equation does not assume the curvature of the relation between flame speed and stretch; rather it relies on the experimental data to obtain the curvature, using the constant  $C$  as a fitting parameter. Since this nonlinear equation has three fitting parameters, it is denoted as N3P in this study. Table 3.1 summarizes all the five extrapolation equations evaluated in this study.

### 3.3 Numerical Methods

The one dimensional expanding spherical flame is simulated using the one dimensional, adaptive simulation of reactive flow (A-SURF) code ([Chen et al., 2009b](#)), which has been successfully used in a series of studies on spherical flame initiation

---

Model	References	Equations
LS	<a href="#">Wu &amp; Law (1984)</a>	$S_b = S_b^0 - L_b K$
NQ	<a href="#">Kelley &amp; Law (2009)</a>	$\left(\frac{S_b}{S_b^0}\right)^2 \ln\left(\frac{S_b}{S_b^0}\right)^2 = -\frac{2L_b K}{S_b^0}$
LC	<a href="#">Chen (2011b)</a>	$S_b = S_b^0 - \frac{2L_b}{R_f}$
NE	<a href="#">Kelley et al. (2011a)</a>	$\frac{S_b}{S_b^0} \left[ 1 + \frac{2L_b}{R_f} + \frac{4L_b^2}{R_f^2} + \frac{16L_b^3}{3R_f^3} + O\left(\frac{L_b^4}{R_f^4}\right) \right] = 1$
N3P	-	$S_b = S_b^0 - \frac{2L_b}{R_f} + \frac{C}{R_f^2}$

---

Table 3.1: Extrapolation Equations

and propagation, such as ([Chen et al., 2009a, 2007](#); [Burke et al., 2009](#)). A-SURF solves the conservation equations of one-dimensional, multi-component, reactive flow in a spherical coordinate using the finite volume method. The details on the governing equations, numerical schemes, and code validation can be found in ([Chen, 2010](#); [Chen et al., 2009b](#)). The second-order-accurate Strang splitting fractional-step procedure is utilized to separate the time evolution of the stiff reaction term from that of the convection and diffusion terms. To maintain adequate numerical resolution of the moving flame, a multi-level, dynamically adaptive mesh refinement algorithm has been used in A-SURF. In all simulations, it has been ensured that the confinement effect is negligible by using a large chamber radius (100 cm for the simulations of H<sub>2</sub>/air flame and 25 cm for those of *n*-heptane/air in this study) and only considering flame radius that is less than 30% of the wall radius ([Burke et al., 2009](#); [Chen et al., 2009a](#)).

The one-dimensional planar steady adiabatic flame is simulated using the PREMIX Code, which is part of the CHEMKIN package. PREMIX solves the conservation equations of one-dimensional, multi-component, reactive flow in Cartesian coordinates. Therefore, the solution is equal to that of A-SURF at very large flame radius. To be consistent, simulations with PREMIX and A-SURF use the same chemical kinetic model and transport formulations. For H<sub>2</sub>/air flame simulations both used multi-component model with Soret diffusion, and for *n*-heptane/air flame simulations both used mixture-averaged model without Soret diffusion. In addition, neither simulations includes a radiation model to eliminate the effects of radiation coupling.

From A-SURF simulations, the stretched flame speed relative to the burned gas,  $S_b = dR_f/dt$ , can be calculated by numerically differentiating the flame front history,  $R_f = R_f(t)$ , with  $R_f$  defined as the position of maximum heat release rate. The stretch rate can also be calculated from the flamefront history,  $K = (2/R_f)dR_f/dt$ . To consistently compare the results at different conditions, normalization is necessary. From PREMIX, the following quantities are determined: the flame speed relative to the burned gas  $S_{b,\text{premix}}^0$ , the flame thickness  $\delta_L$  of the one-dimensional planar flame, defined based on the maximum gradient of the temperature profile,

$$\delta_L = \frac{T_{\text{ad}} - T_u}{(dT/dx)_{\max}} \quad (3.10)$$

where  $T_{\text{ad}}$  is the adiabatic flame temperature, and  $T_u$  the unburned mixture temperature. With  $S_{b,\text{premix}}^0$  and  $\delta_L$ , the normalized flame speed  $S_b/S_{b,\text{premix}}^0$  and Karlovitz number  $Ka = K\delta_L/S_{b,\text{premix}}^0$  can then be computed.

## 3.4 Computational Results

### 3.4.1 Results For Hydrogen/air

$\text{H}_2/\text{air}$  mixtures are most suitable for error quantification for the following reasons. First, the chemistry is most well understood; therefore deviation from experiments is minimized. Second, since  $\text{H}_2$  has distinct transport properties from  $\text{N}_2$  and  $\text{O}_2$ , the variation of  $Le$  from lean to rich covers a wide range of values (0.3 - 2.4) and therefore can provide a conservative estimation of extrapolation error. Third, the simulation is efficient, and large-size flames can be computed within reasonable times.

Figure 3.2 plots  $S_b/S_{b,\text{premix}}^0$  versus  $Ka$  for various equivalence ratios for  $\text{H}_2/\text{air}$  at 1 atm and  $T_u = 298$  K. The updated high pressure  $\text{H}_2/\text{O}_2$  model by Burke *et al.* (2012) was used for both PREMIX and A-SURF simulations. As expected, for lean/rich mixtures the stretched flame speeds, calculated by A-SURF, start from high/low values at small radii (large  $Ka$ ), respectively. As the flame grows and  $Ka$  decreases, the flame speed calculated by A-SURF for lean/rich mixtures decreases/increases, respectively, approaching the solution of PREMIX for all equivalence ratios. This means that simulations using the two codes are consistent and can be used for error quantification of different extrapolation models.

To mimic the situations in real experiments, only the data in the range from  $R_f = 1.0$  cm to  $R_f = 2.0$  cm for extrapolation will be used. Figure 3.2 plots the corresponding extrapolation curves using the five equations in Table 3.1. It is seen that the extrapolated flame speeds for rich mixtures ( $Le > 1$ ) typically differ by less than 10% from the PREMIX solutions using all equations; however, those for lean mixtures ( $Le < 1$ ) for  $\phi < 0.7$  are substantially higher than the PREMIX solutions.

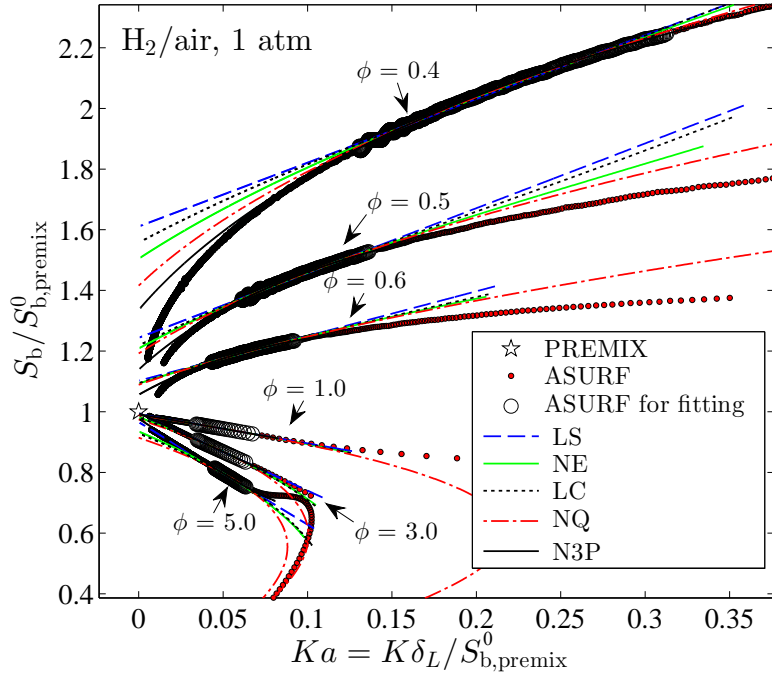


Figure 3.2: Comparison between results of various extrapolation models with numerical simulation for various equivalence ratios of  $\text{H}_2/\text{air}$  at 1 atm. Data used for fitting is for flame radius from 1 cm to 2 cm.

N3P model produces results closest to PREMIX solutions; however, the differences are still 10-35%. This large systematic error means none of the models are valid for mixtures with negative Markstein lengths and will cause significant over-prediction in practice. In addition, for very rich mixtures, for example  $\phi = 5.0$ , LS and N3P turn out to be more accurate than the other three nonlinear relations, which under-predicts the unstretched flame speed by 5-10%.

To investigate the cause of the failure of all equations for lean  $\text{H}_2/\text{mixtures}$ , the 95% confidence intervals ([Cox & Hinkley, 1974](#)) of all the fittings shown in Figure 3.3 is first computed. For all five models, the 95% confidence intervals for all fall within 99% to 101% of the estimates. This means the over-prediction of all models

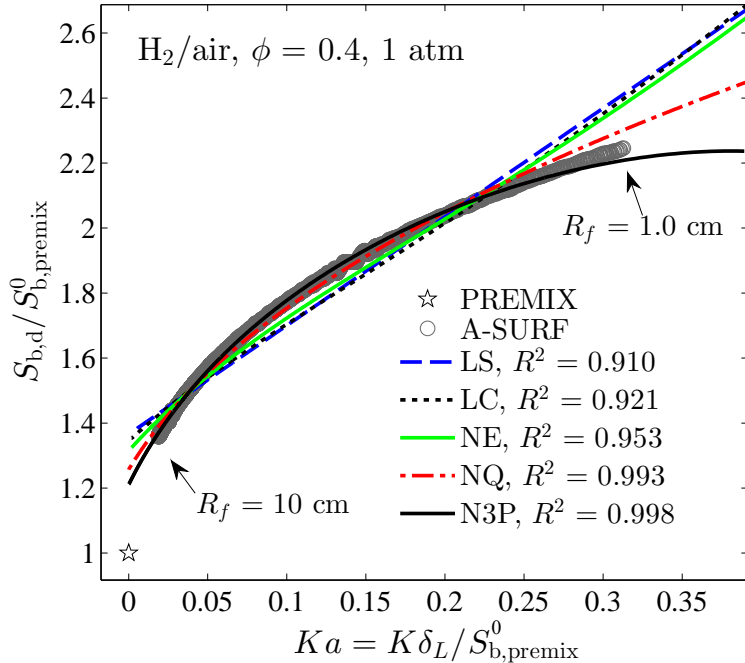


Figure 3.3: Comparison of various extrapolation models for  $\phi = 0.4$  of  $H_2/\text{air}$  at 1 atm using a large range of simulation data.

is not due to the statistic insignificance caused by inadequate data. Next, fittings on a wide range of data from  $R_f = 1.0 \text{ cm}$  to  $R_f = 10.0 \text{ cm}$  for  $Le = 0.4$  is conducted, and the results are shown in Figure 3.3. It is seen that the A-SURF data show a strong curvature, which none of the fittings can capture exactly. LS, LC and NE models have significant deviations from the A-SURF data. NQ model has a closer agreement. The N3P model has the closest agreement with the A-SURF data because it has another free parameter for the second-order term on RHS of Equation 6 for fitting. Even with this, the N3P still has noticeable deviation from A-SURF data, and its estimate is 20% higher than the PREMIX result.

### 3.4.2 Burned Gas Density Effect

Another influence of stretch that is frequently neglected is the change of burnt gas density due to the change in the flame temperature. The issue was recently raised in Bonhomme *et al.* (2013). Recognizing that since the stretch effect decreases with the progression of the expanding spherical flame, the burnt gas density would approach the equilibrium value. Consequently, the burnt gas density effect will modify the relation between local flame speed and stretch, and the induced error needs to be quantified. Using A-SURF simulations, it has been investigated in this study whether this effect is the cause of the failure of nonlinear extrapolations and quantified its effect on extrapolations.

As indicated in Bonhomme *et al.* (2013), the burnt gas density,  $\rho_b$ , of expanding spherical flames can deviate substantially from the equilibrium gas density,  $\rho_b^0$  due to the stretch effect on flame temperature. This will cause the displacement flame speed measured in experiment to differ from the consumption flame speed for non-unity  $Le$ . Based on the analysis in Bonhomme *et al.* (2013), the consumption speed relative to the burned gas,  $S_{b,c}$ , which is the speed of the flame if the burned gas density did not change, should be,

$$S_{b,c} = \frac{\bar{\rho}_b}{\rho_b^0} \frac{dR_f}{dt} + \frac{R_f}{3\rho_b^0} \frac{d\bar{\rho}_b}{dt} \quad (3.11)$$

where  $\bar{\rho}_b$  is the instantaneous spatially averaged burned gas density,

$$\bar{\rho}_b(t) = \frac{3}{R_f^3(t)} \int_0^{R_f(t)} r^2 \rho(r, t) dt \quad (3.12)$$

and  $\rho(r, t)$  is the instantaneous gas density, which is available from the A-SURF

simulations.

To quantify the effect of burned gas density on the local stretched flame speed as well as the extrapolation, the instantaneous consumption flame speeds are calculated from A-SURF simulations and extrapolations based on consumption flame speeds are performed. The results are shown in Figure 3.4. First, it is seen that for very lean or very rich mixtures, the displacement and consumption flame speeds differ significantly at small radii and large stretch. As expected, the consumption flame speed is lower and higher compared to the displacement flame speed,  $S_b$ , at lean and rich conditions, respectively.

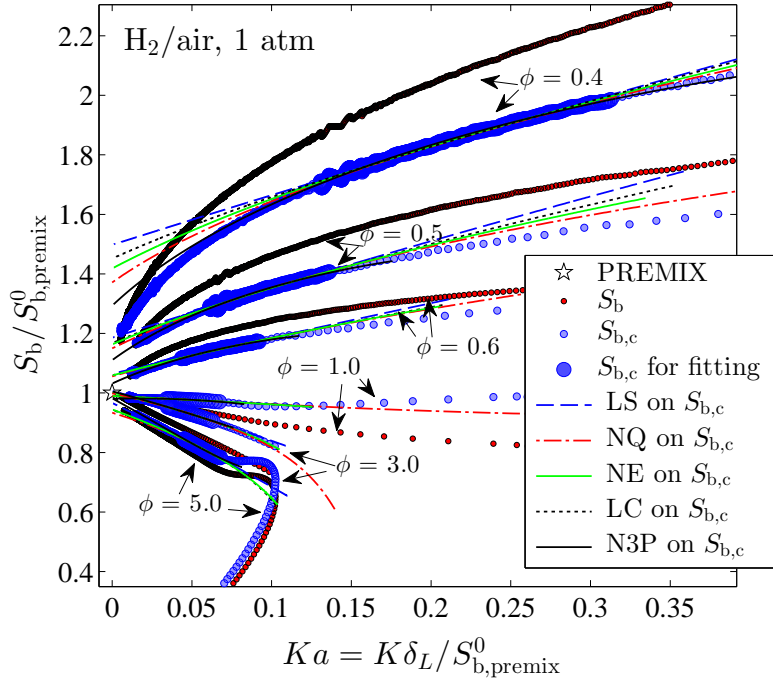


Figure 3.4: Extrapolation based on consumption flame speeds using various models at various equivalence ratios of H<sub>2</sub>/air at 1 atm. Data used for fitting is for flame radius from 1 cm to 2 cm.

Despite the difference, extrapolations based on the consumption flame speed do

not have much improvement compared to those based on the displacement flame speeds. The results are similar, *i.e.*, while the extrapolations for rich mixtures ( $Le > 1$ ) are slightly underpredicted, those for lean mixtures ( $Le < 1$ ) are significantly over-predicted. Although the consumption flame speeds differ substantially from the displacement flame speeds at small radii, the amount of difference decreases as flame radius increases. At large radii, the consumption and displacement flame speeds become almost the same. This leads to modified slopes, *i.e.*, Markstein lengths, and smaller differences in the extrapolated flame speeds than the difference at small radii between displacement and consumption flame speeds. In conclusion, the extrapolations based on consumption flame speeds show slight improvements, but the error is still large for very lean and rich mixtures.

### 3.4.3 Comparison With Experiments

Next the performance of extrapolation on experimental data is investigated. Experiments were conducted on expanding spherical flames, and the flamefront position was tracked from Schlieren luminosity which is proportional to the density gradient. A MATLAB program is written to track the location of maximum luminosity gradient of an image, which is defined as the flamefront position. This is consistent with the definition of flame radius in A-SURF simulations. Therefore, the experimental data corresponds to the flame speed relative to the burned gas.

Figure 3.5 plots the experimental data in comparison to the A-SURF simulations and the extrapolation results based on the experimental data. First, it is seen that the experimental data agree closely with the simulated flame speed at  $\phi = 0.5$ , 0.6, 1.0 and 3.0. Such agreement is much smaller than the difference between the extrapolated flame speeds and the PREMIX solutions. This supports the validity

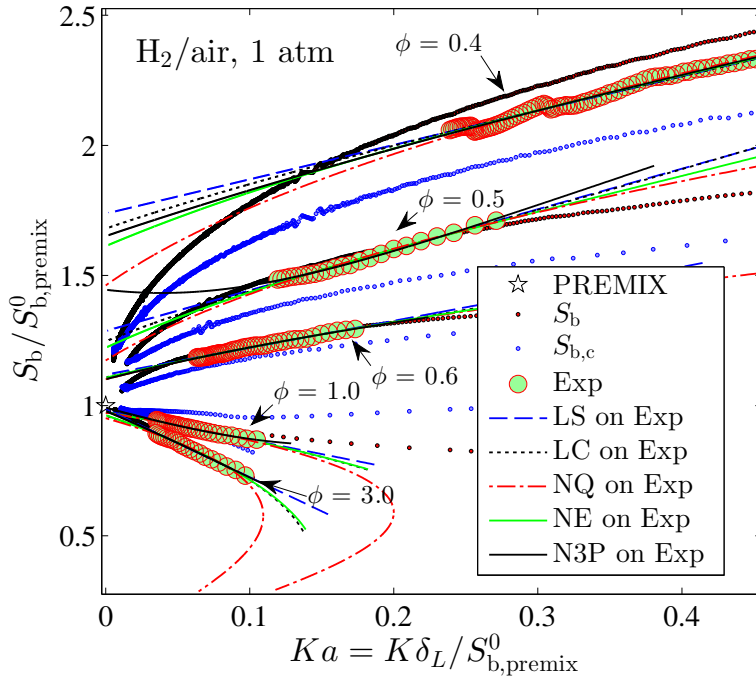


Figure 3.5: Extrapolation based on experimental data using various models at various equivalence ratios of H<sub>2</sub>/air at 1 atm. The flame speed  $S_b$ , and consumption flame speed  $S_{b,c}^0$ , are plotted for comparison.

of both the A-SURF simulations, experiments, and the kinetic model. At  $\phi = 0.4$ , the experimental data is slightly lower than the simulated flame speed, indicating influencing factors, such as radiation or chemistry. Second, the extrapolation results based on the experimental data are similar to those based on the flame speeds from A-SURF simulations, *i.e.*, there are still large over prediction and moderate under prediction for lean and rich H<sub>2</sub>/air flames. On the experimental data, the N3P model shows a different behavior compared to its performance on A-SURF data. While its estimates on  $S_b^0$  with A-SURF data have the closest agreement with PREMIX compared to other models, its performance on the experimental data is poor. This is because the three-parameter fitting largely relies on the curvature of the data,

while experimental data always has inevitable noise. For example, the N3P curve for  $\phi = 0.5$  is non-monotonic at small  $Ka$  which is clearly nonphysical.

### 3.4.4 Results For *n*-Heptane/air

Contrary to  $H_2$ , the diffusivity of heavy hydrocarbon fuels is much smaller than  $N_2$  and  $O_2$ . The resulting  $Le$  and Markstein lengths are also large but with opposite dependence on  $\phi$ . Simulations of *n*-heptane/air flames using the 88-species skeletal mechanism by [Yoo et al. \(2011\)](#) have also been conducted. Figure 3.6 plots the extrapolation results for *n*-heptane/air at 1 atm. It is seen that similar to  $H_2$ /air, the extrapolation results of all models are under predicted for  $\phi < 1.2$  with  $Le > 1$  and over predicted for  $\phi > 1.3$  with  $Le < 1$ . On the other hand, different from  $H_2$ /air, for mixtures with  $\phi > 1.5$  further increasing  $\phi$  does not result in increase of the slope of the flame speed dependence on stretch rate, *i.e.*, decrease in Markstein lengths. The A-SURF curves for  $\phi = 1.7$  and  $\phi = 2.0$  almost overlap. This is because in realistic hydrocarbon flames, fuel quickly decomposes into small fuel fragments before these fragments can be oxidized. Therefore, the sensitivity due to non-unity  $Le$  and preferential diffusion are controlled by the diffusion of the fuel fragment, rather than the fuel. Despite this, it is still seen that the error in the extrapolation can be 10% for very lean and rich mixtures, respectively. This error is expected to be higher for heavier fuels, such as *n*-dodecane, or fuels that do not decompose quickly in flames, such as trimethylbenzene.

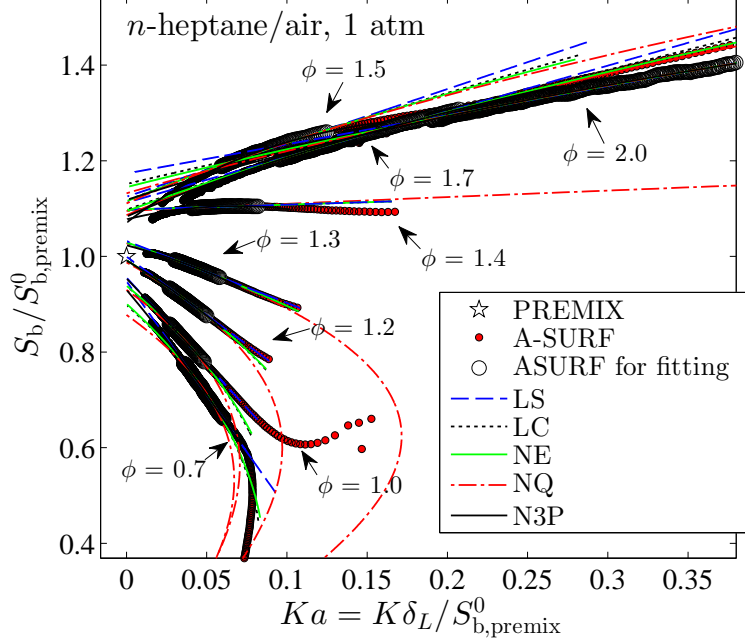


Figure 3.6: Comparison between results of various extrapolation models with numerical simulation for various equivalence ratios of *n*-heptane/air at 1 atm with unburned gas temperature  $T_u = 353$  K. Data used for fitting is for flame radius from 1 cm to 2 cm.

### 3.5 Summary and Scaling of Uncertainties

Figure 3.7 summarizes the errors in the extrapolation for H<sub>2</sub>/air and *n*-heptane/air. For clarity only results of part of the models are shown. For H<sub>2</sub>/air, it is seen that NE and N3P models yield results that are close to the PREMIX solutions, within 5% for  $\phi$  from 0.8 to 3. For  $\phi < 0.7$ , the over prediction sharply increases as  $\phi$  decreases and reaches 60% over prediction at  $\phi = 0.4$ , indicating failure of all models in predicting the relation between flame speed and stretch in such conditions. For  $\phi > 3.0$ , the extrapolation results also show under prediction (10% at the worst case) as  $\phi$  increases. Extrapolated results of NE and N3P models based on experimental data show similar dependence on  $\phi$ . However, it is worthwhile to note that while N3P has

better performance on A-SURF data, it does not give better results than the NE model when experimental data is used because N3P is too sensitive to experimental noise. Finally, it is clear to see that the difference between experiments and the predictions of the model by Burke *et al.* (2012) is mostly caused by extrapolation error. Indeed, from Figure 3.7 it is seen that the value  $S_{\text{Exp}}^0(\text{NE})/S_b^0(\text{NE})$  and  $S_{\text{Exp}}^0(\text{N3P})/S_b^0(\text{N3P})$  are much close to 1 for all  $\phi$ .

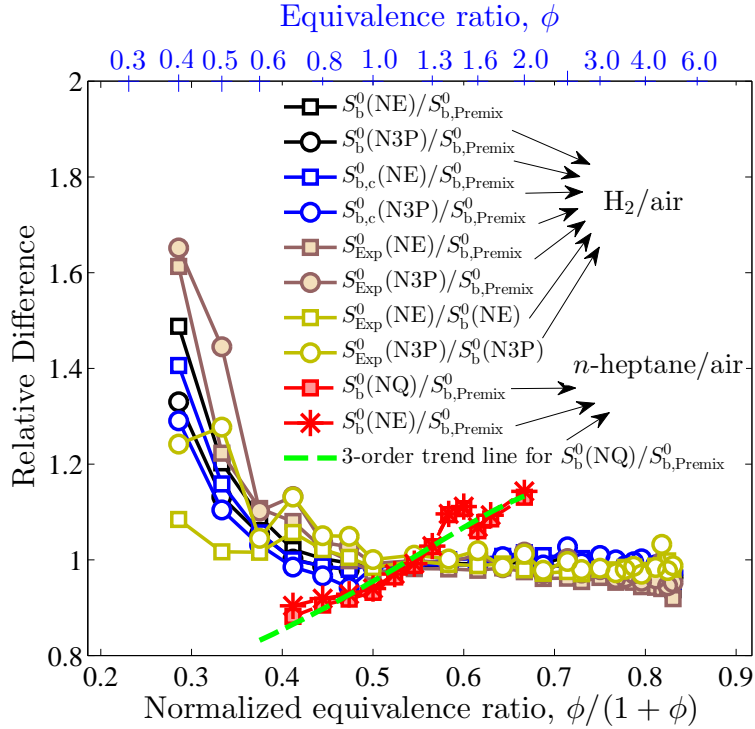


Figure 3.7: Extrapolated flame speeds using NE and N3P models in relative to PREMIX result for  $\text{H}_2/\text{air}$ , and extrapolated flame speeds using LS, NE and NQ models in relative to PREMIX result for  $n\text{-heptane}/\text{air}$

For  $n\text{-heptane}/\text{air}$ , the error shows opposite dependence on  $\phi$ , *i.e.*, extrapolation results in under predictions for lean mixtures and over predictions for rich mixtures. The maximum error is 10% for very lean and rich mixtures. The error is much smaller compared to lean  $\text{H}_2/\text{air}$  mixtures, but it may be sufficient to explain the

small discrepancies of recent atmospheric pressure hydrocarbon/air flame speed measurements, as will be shown in Chapter 4.

The present results show that the errors associated with extrapolation largely depend on the conditions. How do we proceed for future measurements and re-interpret existing ones? If the purpose of measurements is solely for validation of chemical kinetics, the straightforward solution is to compare simulation of spherical flames with experiments. Computationally assisted extrapolation are already used by Egolfopoulos and co-workers, when the counterflow twin flame technique is used for measuring laminar flame speeds (Wang *et al.*, 2009; Ji *et al.*, 2010), and the technique has been validated with detailed simulations (Mittal *et al.*, 2012b). Another solution is to dilute the mixture using inert to change the  $Le$  such that the extrapolation error is small. However,  $S_u^0$  for an arbitrary mixture is still a useful quantity in other contexts, such as study of turbulent combustion and thermal acoustics, that is worth our effort to measure it accurately. Therefore, solutions are needed to reconcile the extrapolation uncertainties.

Fundamentally, the variation of flame speeds on stretch comes from two sources (Law, 2006): the first one is the  $Le$  and preferential diffusion effects, which manifests them in terms of the Markstein number,  $Ma = L_b/\delta_L$ , while the second source is the normalized stretch rate, *i.e.*, the Karlovitz number  $Ka$ . The combined effect is the product of the two,  $MaKa$ . It is important to recognize that the nonlinearity of the relation between flame speed and stretch not only depends on the  $Le$  but also on  $Ka$ . This means that for data at different  $Ka$ , the nonlinearity is different. For example, although the flame radius history experimentally from  $R_f = 1$  to 2 cm for all equivalence ratios can be acquired, they correspond to different  $Ka$  at different equivalence ratios. If  $Ka$  is defined based on  $S_b$ , rather than  $S_b^0$ , *i.e.*,  $Ka = K\delta_L/S_b$ ,

then it can be easily shown that,

$$Ma_{\text{Linear}} Ka_{\text{mid}} = \frac{2L_b, \text{Linear}}{R_{f, \text{mid}}} \quad (3.13)$$

where  $Ma_{\text{Linear}}$  is the slope of the flame speed on stretch for a set of experimental data, *i.e.*, the Markstein length,  $L_b$ , here corresponding to the LS model, and  $Ka_{\text{mid}}$  is the normalized stretch rate at the middle point of the data. Equation 3.13 can be easily calculated in any experiments.

In Figure 3.8, the extrapolation errors of different models versus  $MaKa$  according to Equation 3.13 for both  $H_2$ /air and  $n$ -heptane/air mixtures are plotted. It is seen that for  $Ma_{\text{Linear}} Ka_{\text{mid}} < -0.05$  the extrapolations have significant over-prediction, while for  $Ma_{\text{Linear}} Ka_{\text{mid}} > 0.15$  the extrapolations have under predictions up to 10%. Future measurements should be conducted in the range of  $-0.05 < Ma_{\text{Linear}} Ka_{\text{mid}} < 0.15$  to minimize the extrapolation uncertainties (within 5%). The dependence of uncertainties on  $Ma_{\text{Linear}} Ka_{\text{mid}}$  can also be used to quantify the uncertainties of existing measurements and correct them. In practical spherical flame experiments, the flame radius range used in data processing is constrained by ignition and compression effects, so it is difficult to change the value of  $R_{f, \text{mid}}$  in Equation 3.13. The best way to minimize the extrapolation uncertainties is to set the mixture  $Le$  close to unity, for which  $|L_b|$  approaches zero.

It will very useful if it can be shown that all the results in Figure 3.8 can collapse on one line for one extrapolation equation. If that is the case, then this empirical curve can be used to correct the extrapolated flame speeds using that equation. In addition, Figure 3.8 only includes the results for  $H_2$ /air and  $n$ -heptane/air at 1 atm using data in the range  $R_f = 1.0 - 2.0$  cm for extrapolation. More calculations at

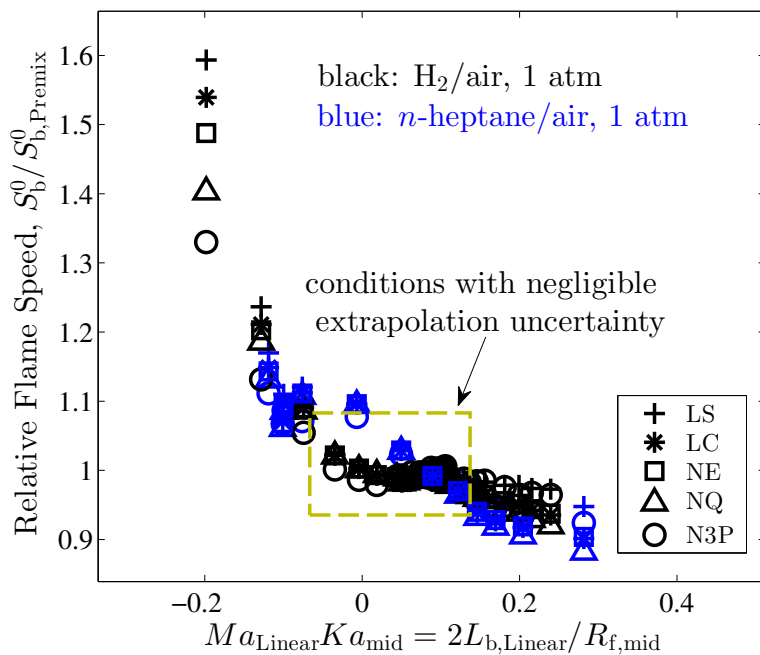


Figure 3.8: Extrapolation uncertainties versus  $Ma_{\text{Linear}}Ka_{\text{mid}}$  for  $H_2/\text{air}$  and  $n\text{-heptane}/\text{air}$  at 1 atm.

different conditions and data range with different  $R_f$ s need to be tested.

Figure 3.9 shows the extrapolation errors of the NE model versus  $MaKa$  according to Equation 3.13 for  $H_2/\text{air}$ ,  $n\text{-heptane}/\text{air}$  at 1 atm,  $H_2/\text{air}$  at 10 atm, and mixtures of  $H_2/O_2/N_2$  at 1 atm with  $O_2:N_2 = 1:9$  molar ratio. The use of high-pressure data and mixtures with lower  $O_2$  concentration is to vary the flame thickness  $\delta_L$  such that the ratio  $R_f/\delta_L$  can cover a wide range. At the same time, in Figure 3.8 the extrapolation errors using different ranges of  $R_f$  are used.

It is seen that the data for  $H_2/\text{air}$  at 10 atm has smaller extrapolation errors since both the flame thickness  $\delta_L$  and  $|L_b|$  decreases with pressure. Moreover, smaller errors can be achieved if the data used for extrapolation are at higher values of  $R_f$ .

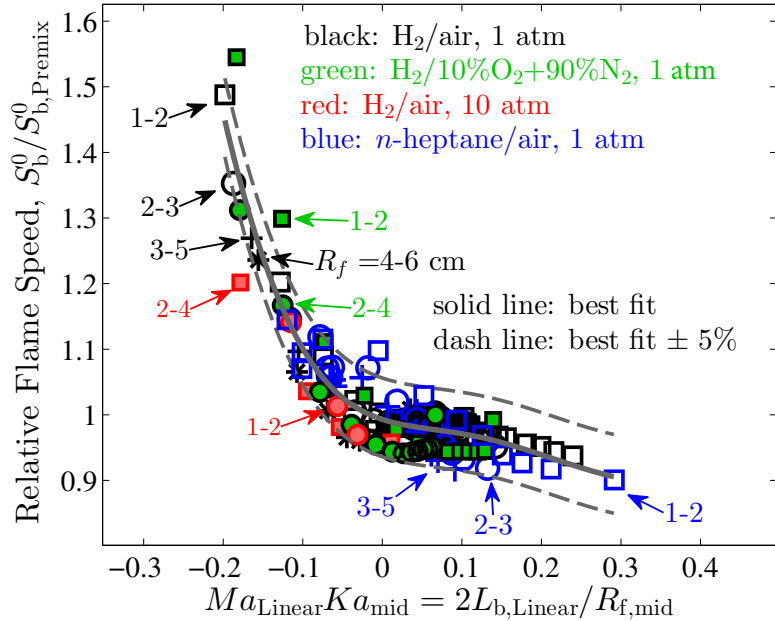


Figure 3.9: Extrapolation errors versus  $Ma_{\text{Linear}}Ka_{\text{mid}}$  for  $\text{H}_2/\text{air}$ ,  $n\text{-heptane}/\text{air}$  at 1 atm,  $\text{H}_2/\text{air}$  at 10 atm, and mixtures of  $\text{H}_2/\text{O}_2/\text{N}_2$  at 1 atm with  $\text{O}_2:\text{N}_2 = 1:9$  molar ratio.

Finally, the best fit of all data gives the following empirical relation,

$$\frac{S_{b,\text{extrapolated}}^0}{S_{b,\text{premix}}^0} = 1 - 0.4\chi + 4.0\chi^2 - 25.7\chi^3 + 36.2\chi^4 + 82.6\chi^5 - 178.4\chi^6 \quad (3.14)$$

where

$$\chi = Ma_{\text{Linear}}Ka_{\text{mid}} = \frac{2L_{b,\text{Linear}}}{R_{f,\text{mid}}}$$

All the extrapolation errors using the NE equation at all conditions reasonably locate in the band bounded by the  $\pm 5\%$  curves of Equation 3.14. Since all the laminar flame speeds presented in this thesis were previously published in journals (Wu *et al.*, 2011, 2012; Wu & Law, 2013), in which the NE equation was used for extrapolation, Equation 3.14 can be used to access the errors in those data and

make corrections.

## 3.6 Concluding Remarks

The systematic errors associated with the extrapolation of flame speed measurements using expanding spherical flames are quantified. The results show that none of the extrapolation equations in Table 3.1 is accurate enough and induce errors that are larger than the ignition, flow confinement and radiation effects. Larger errors are associated with conditions with small or large values of  $|Le - 1|$ . For very small  $Le$ , such as lean H<sub>2</sub>/air flames, the extrapolation errors are particularly large (up to 60% over predicted).

The burned gas density is also changed by the differential diffusion effects, causing a change in burned gas flame speed  $S_b$  relative to the consumption flame speed. The effects are strong particularly at small flame radii. However, including the burned gas density effect does not reduce the extrapolation error, since the difference between  $S_b$  and the consumption flame speed becomes smaller at large radii.

It is shown that, extrapolation errors mainly depend on the parameter  $MaKa = 2L_b/R_f$ , where the Markstein length  $L_b$  is proportional to the flame thickness  $\delta_L$  for fixed  $Le$  (or  $Ma$ ). Therefore, it is seen that extrapolation errors also decrease with the increase in flame radii of the data used for extrapolation and  $\delta_L$ , which decreases with pressure. A relation between the extrapolation error and  $2L_b/R_f$  is given by Equation 3.14. This is an empirical relation based on the simulation data computed in this chapter, and should be further tested with more fuels and conditions in future. Equation 3.14 is used to assess the uncertainties of measured laminar flame speeds, in Chapter 4.

# Chapter 4

## Measured Laminar Flame Speeds

### 4.1 Introduction

The laminar flame speeds,  $S_u^0$ , and Markstein lengths  $L_b$  were measured using Vessel I and Vessel II described in Chapter 2, and the results are presented in this chapter. Most of these data on  $S_u^0$  were previously published in journal publications ([Wu \*et al.\*, 2011, 2012; Wu & Law, 2013](#)), in which the nonlinear extrapolation equation, Equation 3.8 (the NE model), was employed. Therefore, to be consistent this equation is still employed in the extrapolation of all the experimental data in the present study and the obtained results are termed uncorrected  $S_u^0$ . However, as shown by the simulations presented in Chapter 3, Equation 3.8 still results in finite error, especially when  $Le$  and differential diffusion effects are strong. Therefore, to present the most accurate results possible, corrections for the extrapolation error are performed according to

$$S_u[\text{corrected}] = S_u[\text{uncorrected}] \left( \frac{S_{b,\text{extrapolated}}^0}{S_{b,\text{premix}}^0} \right)^{-1} \quad (4.1)$$

where the correction factor on the RHS of Equation 4.1 can be calculated from Equation 3.14 with the parameters  $R_{f,\text{mid}}$  and  $L_{b,\text{Linear}}$  experimentally determined. The resulting data is called corrected  $S_u^0$ . This chapter presents both the uncorrected and corrected  $S_u^0$ .

The error bar for the corrected  $S_u^0$  data is considered to have two contributions. First, the error is in part due to the validity of the correction formula Equation 3.14 for the extrapolation error, which can cover all the numerical simulation data discussed in Chapter 3 if a  $\pm 5\%$  uncertainty is allowed (Figure 3.9). The cause of this  $\pm 5\%$  fluctuation is believed to be due to the assumption that the parameter  $Ma_{\text{Linear}}Ka_{\text{mid}} = 2L_b/R_{f,\text{mid}}$  can account for the influences of pressure,  $Le$ , fuel, and the choice of  $R_f$  on extrapolation, which is a strong assumption considering the complexity and couplings in multi-step chemistry and differential diffusion between heat and mass, and between fuel and oxidizer. The second contribution of the error bar comes from the random error in the mixture composition during the preparation of the unburned gas mixture, due to the accuracies in pressure gauges ( $\pm 0.25\%$  of the span) and the mixture uncertainty of standard gas mixtures ( $\pm 2\%$  for  $N_2/O_2$  mixtures). Contribution of these errors depend on the sensitivity of flame speed on the mixture component at the particular measured conditions. For conditions presented in this chapter, this uncertainty is approximately  $\pm 1\%$ .

The error bar for the measured Markstein lengths  $L_b$  represents repeatability only, which is estimated to be  $\pm 0.02$  cm. This is due to the error in mixture composition as well as the scattering of  $S_b$  caused by the numerical differentiation process. The systematic uncertainty of  $L_b$  is much larger than  $\pm 0.02$ . The uncertainty of  $L_b$  is more difficult to quantify. The reason is that the theoretical definition of  $L_b$  is the sensitivity of  $S_b$  to  $K$  in the limit of  $K \rightarrow 0$  and  $R_f \rightarrow +\infty$ . However,

as shown by the numerical simulations in Chapter 3 the relation between  $S_b$  and  $K$  is highly nonlinear such that the slope at finite values of  $K$  (where we have experimental data) is very different from that at  $K \rightarrow 0$ . The best estimate, according to Kelley *et al.* (2011a), is to use the nonlinear model (NE model, Equation 3.8); however, it has been shown that even the NE model has significant errors. In addition, as shown in Section 3.4.2 and by Santner *et al.* (2014) and Jayachandran *et al.* (2014), it is also largely affected by stretch and radiation which affects the burned gas density. In this chapter, two Markstein lengths are reported for archival purpose:  $L_{b,\text{Linear}}$  extracted from experimental data using the LS model (Equation 3.4), and  $L_{b,\text{Nonlinear}}$  extracted from experimental data using the NE model (Equation 3.8). From the numerical simulations presented in Chapter 3 (Figures 3.2, 3.3 and 3.6), it is seen that for  $L_{b,\text{Linear}} > 0$ ,  $L_{b,\text{Linear}}$  is more accurate than  $L_{b,\text{Nonlinear}}$ , while for  $L_{b,\text{Linear}} < 0$ ,  $L_{b,\text{Nonlinear}}$  is more accurate than  $L_{b,\text{Linear}}$ , although both under predict.

For comparison with experimental data, predictions of laminar flame speeds by chemical kinetic models (mechanisms) were computed using the CHEMKIN code (Kee *et al.*, 1985) or the Open SMOKE code (Cuoci *et al.*, 2011). Both codes numerically solve the one-dimensional adiabatic planar flame. The computation grid of all calculations were refined until a grid-independent solution is found. All computations include Soret diffusion. The multi-component diffusion model was used in all computations except those for the butanol isomers, in which mixture-averaged diffusion model was used due to convergence difficulties.

The measurements of the key components of transportation fuels are presented first: *n*-hexane, cyclo-alkanes and aromatic fuels in Section 4.2, Section 4.3 and Section 4.5, respectively. These data are important targets for developing trans-

portation surrogate models. Next, the measurements of a series of potential biofuel, butanol isomers, are presented in Section 4.4. As will be shown in the analysis in Chapter 5, these larger fuel molecules rapidly break down into a pool of small molecule fragments, whose oxidation is slower compared to fuel cracking and thus dominates the overall heat release and burning rate. Therefore, some measurements of mixtures of H<sub>2</sub>, CO and C<sub>1</sub> to C<sub>3</sub> hydrocarbons are finally presented in Section 4.6.

The results presented in this chapter have been previously published in the following journal articles ([Wu et al., 2012](#); [Wu & Law, 2013](#); [Wu et al., 2011](#)):

- WU, F., KELLEY, A. P. & LAW, C. K. 2012 Laminar flame speeds of cyclohexane and mono-alkylated cyclohexanes at elevated pressures. *Combustion and Flame* **159**, 1417–1425
- WU, F. & LAW, C. K. 2013 An experimental and mechanistic study on the laminar flame speed, Markstein length and flame chemistry of the butanol isomers. *Combustion and Flame* **160**, 2744–2756
- WU, F., KELLEY, A. P., TANG, C., ZHU, D. & LAW, C. K. 2011 Measurement and correlation of laminar flame speeds of CO and C<sub>2</sub> hydrocarbons with hydrogen addition at atmospheric and elevated pressures. *International Journal of Hydrogen Energy* **36**, 13171–13180

## 4.2 *n*-Hexane

The chemistry of *n*-alkane combustion is important for the predictive modeling of practical and surrogate fuels. Laminar flame speeds of large *n*-alkanes from C<sub>5</sub>–

$\text{C}_{12}$  have recently been measured (Ji *et al.*, 2010; Kelley *et al.*, 2011c). In the present study, the flame speeds of *n*-hexane are measured again, first to check the repeatability with previous measurements and second to demonstrate the correction of extrapolation error.

Figure 4.1 plots the present measurements of the atmospheric laminar flame speeds of *n*-hexane/air at the initial temperature  $T_u = 353$  K, plotted against the measurements by Ji *et al.* (2010) and Kelley *et al.* (2011c) as well as the predictions by the JetSurF 2.0 mechanism (Wang *et al.*, 2010). The present measurements were conducted with Vessel II, same as those of Kelley *et al.* (2011c). The flame radii used for extrapolation in the present measurements were from 1.0 to 1.8 cm except for the condition at  $\phi = 0.7$ , at which the range 1.3 to 1.8 cm was used due to the large critical radius (Kelley *et al.*, 2009).

It is seen that the uncorrected  $S_u^0$  of the present data agrees well with the measurements by Kelley *et al.* (2011c), with less than 3% difference, indicating good repeatability. However, comparing them with the counterflow flame measurements of Ji *et al.* (2010), there seems to be a shift in equivalence ratio  $\phi$ , *i.e.*, on the lean side ( $\phi < 1.2$ ) the current measurements are lower and on the rich side ( $\phi > 1.3$ ) higher. Similar discrepancies are also found in other comparisons between the counterflow flame and spherical expanding flame data for  $\text{C}_5\text{-}\text{C}_8$  *n*-alkanes (Kelley *et al.*, 2011c; Ji *et al.*, 2010), cyclo-alkanes (Ji *et al.*, 2011; Wu *et al.*, 2012), butanols (Veloo & Egolfopoulos, 2011; Veloo *et al.*, 2010; Wu & Law, 2013) and dodecane (Ji *et al.*, 2010; Kim *et al.*, 2013).

On the other hand, the present measurements with the extrapolation corrected agree closely with the measurements by Ji *et al.* (2010), which suggests that the discrepancies in between previous counterflow flame measurements and spherical

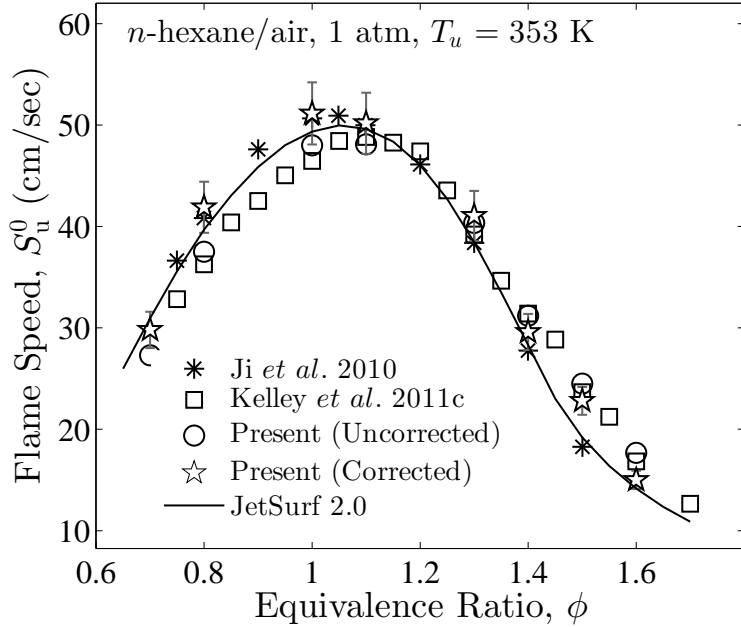


Figure 4.1: Present measurements of the atmospheric laminar flame speeds of *n*-hexane/air at unburned gas temperature  $T_u = 353$  K, plotted against the measurements by [Ji et al. \(2010\)](#), [Kelley et al. \(2011c\)](#) and the predictions by the JetSurF 2.0 mechanism ([Wang et al., 2010](#)).

expanding flame measurements ([Kelley et al., 2011c](#); [Ji et al., 2010, 2011](#); [Wu et al., 2012](#); [Veloo & Egolfopoulos, 2011](#); [Veloo et al., 2010](#); [Wu & Law, 2013](#); [Ji et al., 2010](#); [Kim et al., 2013](#)) can largely be explained by the extrapolation uncertainties.

Finally, the measured linear and nonlinear Markstein lengths and the calculated extrapolation correction factors are plotted in Figure 4.2. Here  $S_b^0$  in the correction factor equals  $S_{b,\text{extrapolated}}^0$  in Equation 4.1.  $L_{b,\text{Linear}}$  is obtained using the LS model (Equation 3.4).  $L_{b,\text{Nonlinear}}$  is obtained using the NE model (Equation 3.8). The error bar on  $L_b$  represents estimated random error only and does not include the systematic error. It is seen that the extrapolation correction factor varies from 0.9 to 1.2 at these atmospheric conditions.

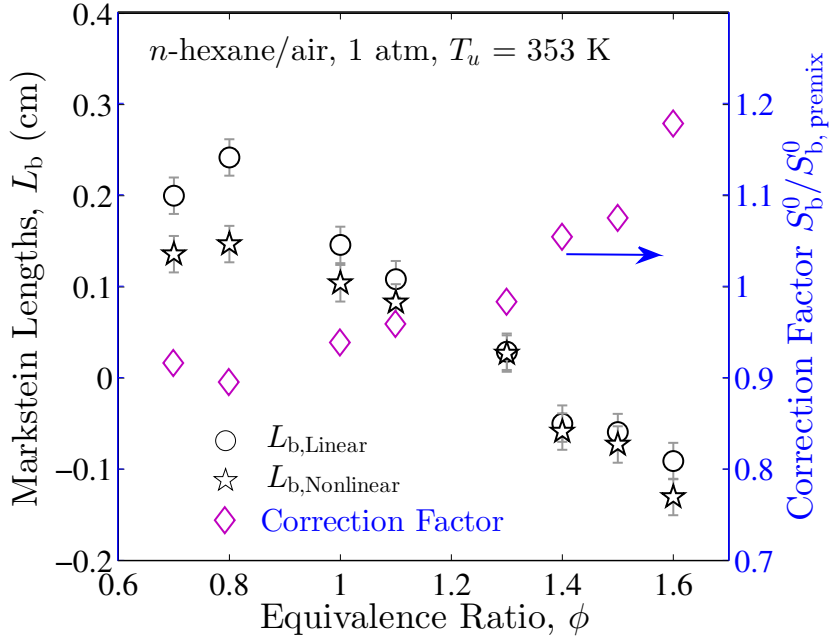


Figure 4.2: Present measurements of Markstein lengths and the calculated extrapolation correction factor based on Equation 3.14 corresponding to the  $S_u^0$  measurements plotted in Figure 4.1. Here  $S_b^0$  in the correction factor equals  $S_{b,\text{extrapolated}}^0$  in Equation 4.1. Same for all following figures involving the correction factor.

### 4.3 Cyclo-alkanes

Cyclo-alkanes are components of commercial fuels such as jet fuel which typically contains around 20% cyclo-alkanes by volume (Violi *et al.*, 2002). Some alternative fuels, particularly those derived from coal (Colket *et al.*, 2007), are almost entirely composed of cyclo-alkanes. However, the combustion characteristics and oxidation kinetics of cyclo-alkanes have not been studied as extensively as *n*-alkanes.

There are relatively few measurements of the laminar flame speeds for cyclo-alkanes. Most data were obtained at atmospheric or slightly elevated pressures. Specifically, Davis & Law (1998) measured the laminar flame speeds for cyclohexane and cyclopentane at atmospheric pressure and an unburned gas temperature

of 298 K; [Farrell \*et al.\* \(2004\)](#) measured those of cyclohexane, cyclopentane, and methylcyclopentane at 3 atm and 450 K; [Dubois \*et al.\* \(2009\)](#) measured those of *n*-propylcyclohexane at 403 K and atmospheric pressure; and [Ji \*et al.\* \(2011\)](#) measured those of cyclohexane, methyl-, ethyl-, *n*-propyl- and *n*-butyl-cyclohexanes at 353 K and atmospheric pressure.

Cyclohexane and its mono-alkylated derivatives have been selected as representative cyclo-alkane components of surrogate jet fuels ([Colket \*et al.\*, 2007](#)), gasoline ([Pitz \*et al.\*, 2007a](#)) and diesel ([Farrell \*et al.\*, 2007](#)). Several kinetic models have been proposed, such as the semi-detailed models for cyclohexane and methylcyclohexane by Ranzi and co-workers ([Granata \*et al.\*, 2003](#); [Cavallotti \*et al.\*, 2007](#); [Ranzi, 2006](#)), the kerosene model by Dagaut and co-workers ([Dagaut & Cathonnet, 2006](#)), which includes the kinetics of cyclo-alkanes, and models by Westbrook and co-workers for cyclohexane and methylcyclohexane ([Silke \*et al.\*, 2007](#); [Pitz \*et al.\*, 2007b](#)). Recently, another model, JetSurF 2.0 ([Wang \*et al.\*, 2010](#)), has been developed which includes the kinetics of cyclohexane and mono-alkylated cyclohexanes. The performance of JetSurF 2.0 in predicting the laminar flame speeds of cyclohexane and mono-alkylated cyclohexanes has been well validated at atmospheric pressure in [Ji \*et al.\* \(2011\)](#), however, its performance at elevated pressures has not been evaluated.

In the present study, the laminar flame speeds of cyclohexane, methyl-cyclohexane and ethyl-cyclohexane are determined at both atmospheric pressure and at elevated pressures up to 20 atm. The present measurements were conducted with Vessel II.

### 4.3.1 Cyclohexane

Figure 4.3 plots the measured laminar flame speeds of cyclohexane with air as oxidizer at pressures of 1, 2, 5, and 10 atm.

Experimental data of Ji *et al.* (2011) as well as the predictions of the JetSurF 2.0 mechanism (Wang *et al.*, 2010) are also plotted in Figure 4.3 for comparison. The flame radii used for extrapolation in the present measurements were from 1.0 to 1.8 cm except for:  $\phi = 0.7$  at 1 atm (1.3 to 1.8 cm were used due to large critical radius),  $\phi = 1.2$  at 5 atm and  $\phi = 0.9, 1.0$  at 10 atm (0.8 to 1.6 cm were used due to instabilities at large radii).

Comparing the present uncorrected measurements to those of Ji *et al.* (2011), it is seen that, similar to *n*-hexane and other *n*-alkanes (Ji *et al.*, 2010; Kelley *et al.*, 2011c), the measurements by Ji *et al.* (2011) are higher on the lean side ( $\phi < 1.2$ ) and lower on the rich side ( $\phi > 1.3$ ). Again, after the extrapolation correction, the present measurements agree closely with those of Ji *et al.* (2011).

Figure 4.4 plots the measured linear and nonlinear Markstein lengths and the calculated extrapolation correction factors for cyclohexane at 1, 2, 5, and 10 atm. At higher pressures, the Markstein lengths on the fuel rich conditions cannot be measured because of flamefront instabilities. First, it is seen that the Markstein lengths decrease significantly with pressure. As a result, the stretch extrapolation correction factor also decreases significantly with pressures. At 1 atm, the correction factor varies from 0.9 to 1.3, while from 2 to 10 atm, it varies from 0.96 to 1.04. This is why at higher pressures the difference between uncorrected and corrected  $S_u^0$  is smaller, as seen from Figure 4.3. It also means for measurements at higher pressures, there is no need to do extrapolation correction. The criterion can be Equation 3.14 or  $-0.05 < 2L_{b,\text{Linear}}/R_{f,\text{mid}} < 0.15$ .

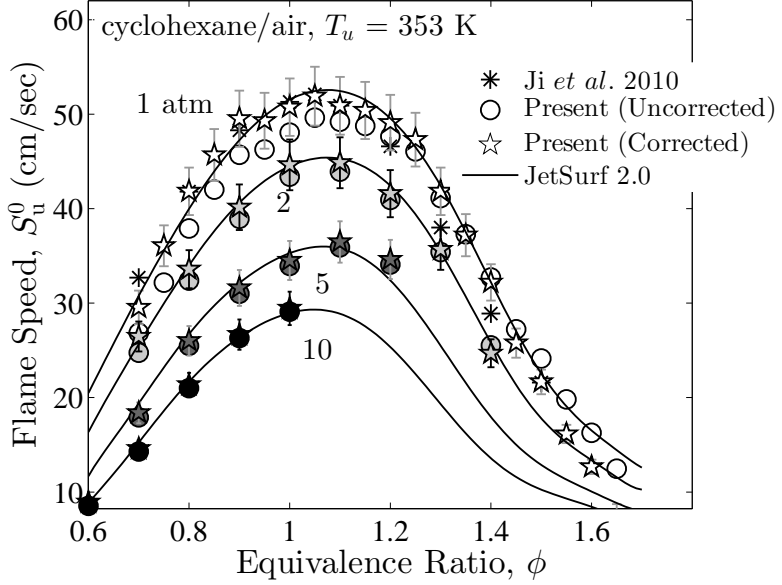


Figure 4.3: Present measurements of laminar flame speeds of cyclohexane at various pressures with air as the oxidizer and an unburned gas temperature  $T_u = 353$  K, plotted against the measurements by [Ji et al. \(2010\)](#) at 1 atm and the predictions by the JetSurF 2.0 mechanism ([Wang et al., 2010](#)).

In order to measure the flame speeds at even higher pressures, a mixture of 15 mol% O<sub>2</sub> with 85 mol% He was used as the oxidizer. The use of helium in place of nitrogen results in a larger Lewis number for the mixture such that diffusional-thermal instabilities are more readily suppressed. Additionally, decreasing the oxygen concentration results in an increase in the flame thickness. This tends to suppress the hydrodynamic instability which becomes progressively more prominent with increasing pressure. The laminar flame speeds of cyclohexane at 20 atm with this O<sub>2</sub>/He mixture as the oxidizer are plotted in Figure 4.5, and the the measured linear and nonlinear Markstein lengths and the calculated extrapolation correction factors are plotted in Figure 4.6. The flame radii used for extrapolation in the present measurements were from 1.0 to 1.8 cm for all conditions. Again, it is seen

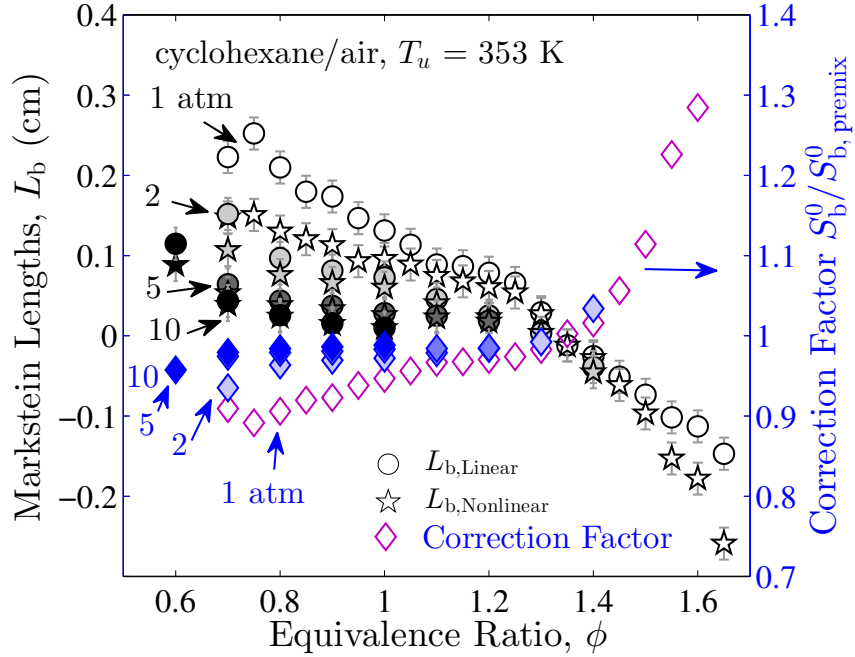


Figure 4.4: Present measurements of Markstein lengths and the calculated extrapolation correction factor based on Equation 3.14 corresponding to the  $S_u^0$  measurements plotted in Figure 4.3.

that since the flame thickness and Markstein lengths are significantly reduced with increasing pressure, the difference between uncorrected and corrected  $S_u^0$  is small.

Comparing the present measurements of cyclohexane at various pressures with the predictions of JetSurF 2.0 mechanism, it is seen that the mechanism generally predicts quite well the corrected laminar flame speeds. The differences are less than 3%, smaller than the estimated uncertainty of the experimental data. This indicates the adequate performance of the mechanism in predicting the laminar flame speeds.

### 4.3.2 Methyl-cyclohexane

Figure 4.7 plots the measured laminar flame speeds of methyl-cyclohexane with air as oxidizer at pressures of 1, 2, 5, and 10 atm. The experimental data of Ji

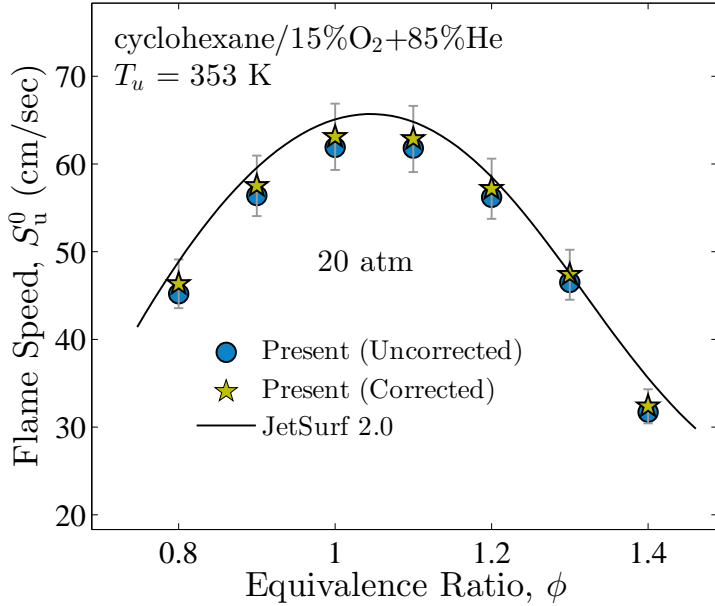


Figure 4.5: Present measurements of laminar flame speeds of cyclohexane at 20 atm with mixture of O<sub>2</sub> and He mixture with 15:85 molar ratio as the oxidizer and an unburned gas temperature  $T_u = 353$  K, plotted against the predictions by the JetSurF 2.0 mechanism ([Wang et al., 2010](#)).

*et al.* (2011) as well as the predictions using the JetSurF 2.0 mechanism ([Wang et al., 2010](#)) are also plotted in Figure 4.7 for comparison. The flame radii used for extrapolation in the present measurements were from 1.0 to 1.8 cm except for:  $\phi = 0.7$  at 1 atm (1.3 to 1.8 cm were used due to large critical radius),  $\phi = 1.2$  at 5 atm and  $\phi = 0.9, 1.0$  at 10 atm (0.8 to 1.6 cm were used duo to instabilities at large radii). Figure 4.8 plots the measured linear and nonlinear Markstein lengths and the calculated extrapolation correction factors.

The laminar flame speeds and Markstein lengths of methyl-cyclohexane at 20 atm with a mixture of 15 mol% O<sub>2</sub> with 85 mol% He as the oxidizer were also measured and plotted in Figures 4.9 and 4.10. The flame radii used for extrapolation in the present measurements were from 1.0 to 1.8 cm for all conditions.

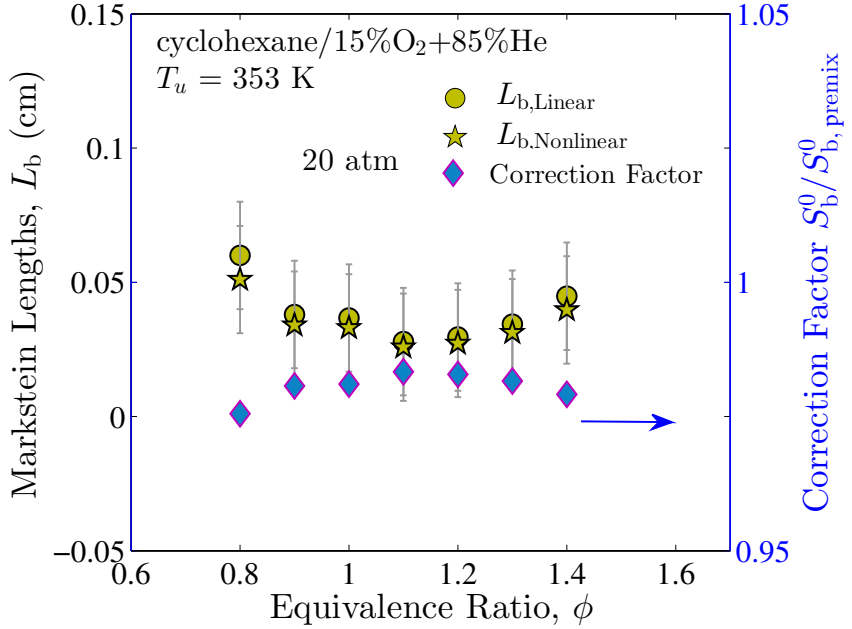


Figure 4.6: Present measurements of Markstein lengths and the calculated extrapolation correction factor based on Equation 3.14 corresponding to the  $S_u^0$  measurements plotted in Figure 4.5.

The agreement of the uncorrected and corrected  $S_u^0$  to those of [Ji et al. \(2011\)](#) is similar to cyclohexane, except in this case the measurements by [Ji et al. \(2011\)](#) is only slightly higher than the uncorrected  $S_u^0$  and as a result the corrected  $S_u^0$  is slightly higher than the measurements by [Ji et al. \(2011\)](#). Similar to cyclohexane, from Figure 4.8 it is seen the stretch extrapolation correction factor is from 0.9 to 1.3; however, since Markstein lengths decrease significantly with pressure, it becomes much closer to 1 and does not make a noticeable difference at 5, 10 and 20 atm. In addition, similar to cyclohexane, the predictions using JetSurF 2.0 mechanism agrees well with the present measurements.

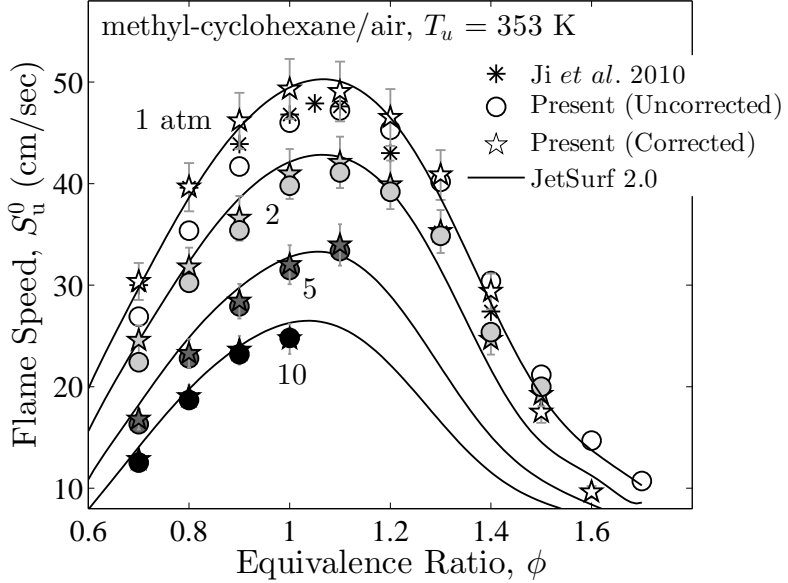


Figure 4.7: Present measurements of laminar flame speeds of methyl-cyclohexane at various pressures with air as the oxidizer and an unburned gas temperature  $T_u = 353$  K, plotted against the measurements by [Ji et al. \(2010\)](#) at 1 atm and the predictions by the JetSurF 2.0 mechanism ([Wang et al., 2010](#)).

### 4.3.3 Ethyl-cyclohexane

Figure 4.11 plots the measured laminar flame speeds of ethyl-cyclohexane with air as oxidizer at pressures of 1, 2 and 5 atm. The measurements at 10 atm were not possible due to the insufficiency of fuel vaporization at 353 K. The flame radii used for extrapolation in the present measurements were from 1.0 to 1.8 cm except for:  $\phi = 0.7$  at 1 atm (1.3 to 1.8 cm were used due to large critical radius),  $\phi = 1.2$  at 5 atm and  $\phi = 0.9, 1.0$  at 10 atm (0.8 to 1.6 cm were used due to instabilities at large radii). The experimental data of [Ji et al. \(2011\)](#) as well as the predictions using the JetSurF 2.0 mechanism ([Wang et al., 2010](#)) are also plotted in Figure 4.11 for comparison. Figure 4.12 plots the measured linear and nonlinear Markstein lengths and the calculated extrapolation correction factors. The error bar on  $L_b$  represents

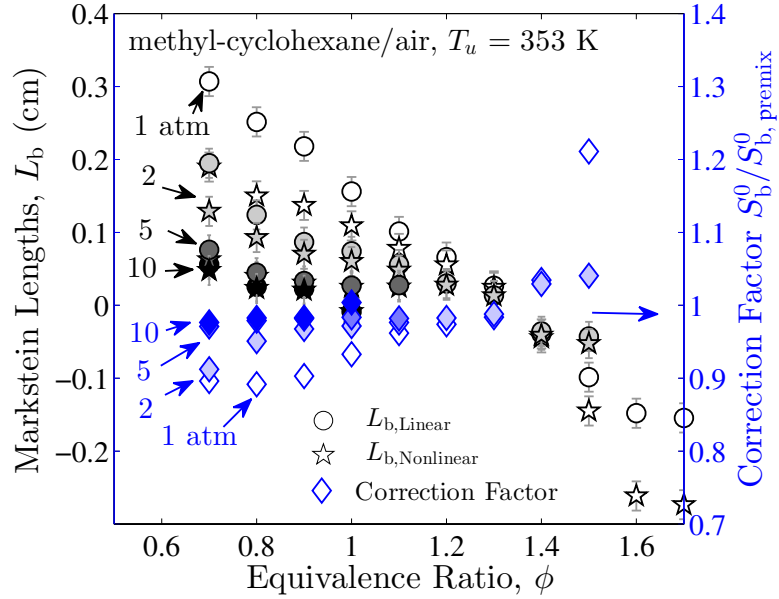


Figure 4.8: Present measurements of Markstein lengths and the calculated extrapolation correction factor based on Equation 3.14 corresponding to the  $S_u^0$  measurements plotted in Figure 4.7.

estimated random error only and does not include the systematic error.

The agreement of the uncorrected and corrected  $S_u^0$  to those of [Ji et al. \(2011\)](#) is similar to cyclohexane and methyl-cyclohexane. The predictions using JetSurF 2.0 mechanism also agrees well with the present measurements on ethyl-cyclohexane. Different from C<sub>5</sub>-C<sub>12</sub> *n*-alkanes, there are noticeable differences between the flame speeds between cyclohexane, methyl-cyclohexane and ethyl-cyclohexane. This will be discussed in Chapter 5.

## 4.4 Butanol Isomers

Butanol holds much potential as a significant alternative transportation fuel. Compared to methanol and ethanol, butanol not only has a diverse source of feedstock,

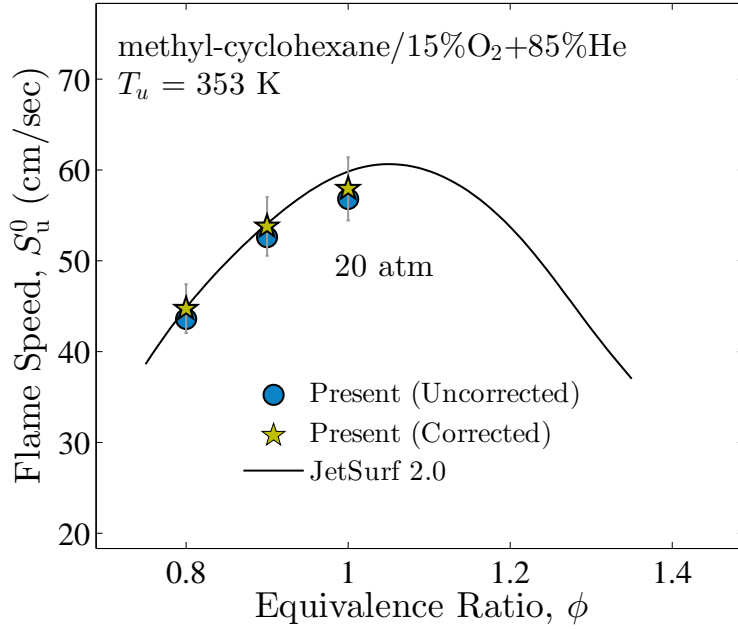


Figure 4.9: Present measurements of laminar flame speeds of methyl-cyclohexane at 20 atm with mixture of O<sub>2</sub> and He mixture with 15:85 molar ratio as the oxidizer and an unburned gas temperature  $T_u = 353$  K, plotted against the predictions by the JetSurF 2.0 mechanism ([Wang \*et al.\*, 2010](#)).

but it also has more desirable fuel properties such as higher energy density, miscibility with gasoline and diesel, and less corrosion.

There are four butanol isomers, namely normal butanol (*n*-butanol or 1-butanol), secondary butanol (*s*-butanol or 2-butanol), *iso*-butanol (*i*-butanol) and tertiary butanol (*t*-butanol). Most previous studies have focused on *n*-butanol, with *s*-butanol, *i*-butanol and *t*-butanol receiving considerably less attention. Not many data other than those of *n*-butanol have been reported, and most of the measurements were conducted only at atmospheric pressure. Specifically, the laminar flame speeds were reported by [Sarathy \*et al.\* \(2009\)](#) for *n*-butanol at 0.89 atm pressure and initial temperature of 350 K; by [Veloo \*et al.\* \(2010\)](#), [Veloo & Egolfopoulos \(2011\)](#) for the four

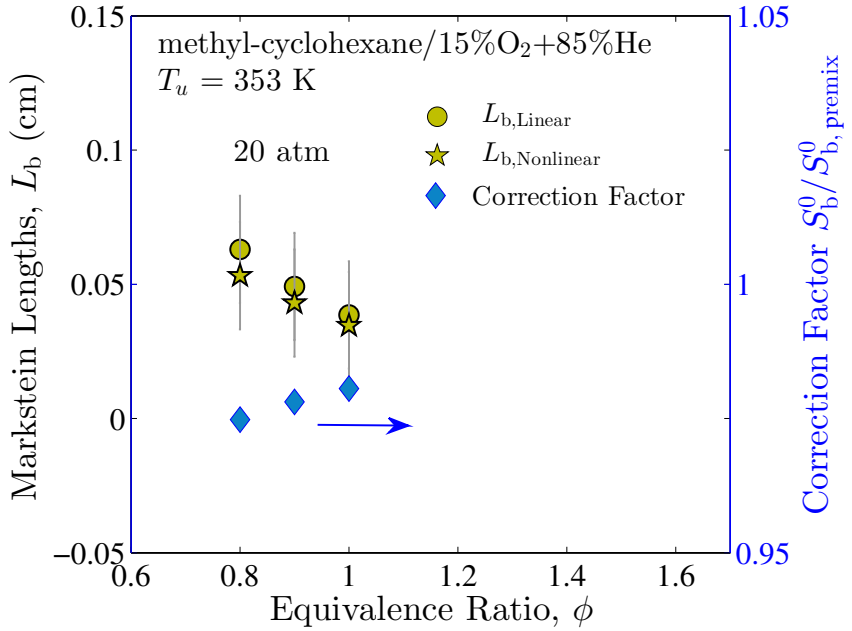


Figure 4.10: Present measurements of Markstein lengths and the calculated extrapolation correction factor based on Equation 3.14 corresponding to the  $S_u^0$  measurements plotted in Figure 4.9.

isomers at 1 atm and 343 K; by Liu *et al.* (2011a) for *n*-butanol and *i*-butanol at 1 atm and 2 atm and initial temperature of 353 K; and by Gu *et al.* (2009, 2010, 2011b,a) for *n*-butanol from 1 atm to 2.5 atm, *t*-butanol from 1 atm to 5 atm, and stoichiometric mixtures of the four isomers with air up to 7.5 atm, all at the initial temperature of 425 K.

Considerable effort has been devoted to model development of *n*-butanol (Harper *et al.*, 2011; Vranckx *et al.*, 2011; Black *et al.*, 2010; Hansen *et al.*, 2011), while models for other butanol isomers were also subsequently proposed. Van Geem *et al.* (2010) presented a high-temperature model for *n*-butanol, *s*-butanol and *t*-butanol, and Moss *et al.* (2008) presented an automatically generated mechanism for all four butanol isomers. Recently Sarathy *et al.* (2012) published a detailed model for all

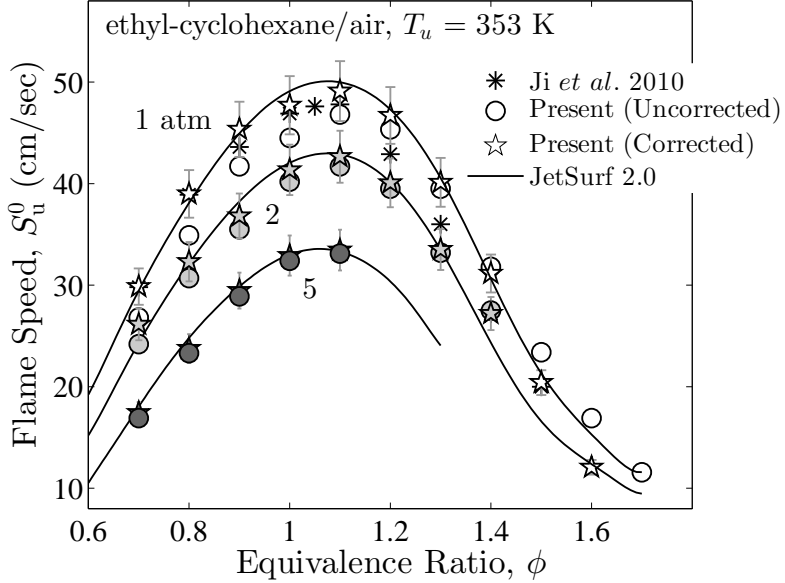


Figure 4.11: Present measurements of laminar flame speeds of ethylcyclohexane at various pressures with air as the oxidizer and an unburned gas temperature  $T_u = 353$  K, plotted against the measurements by [Ji et al. \(2010\)](#) at 1 atm and the predictions by the JetSurF 2.0 mechanism ([Wang et al., 2010](#)).

four butanol isomers, and [Ranzi et al. \(2012\)](#) also published an alcohol mechanism that includes the butanol isomers.

In the present study, the laminar flame speeds and Markstein lengths of *n*-butanol, *s*-butanol, *i*-butanol and *t*-butanol at 1, 2 and 5 atm are studied. The present measurements were conducted with Vessel II. The flame radii used for extrapolation in the present measurements were from 1.0 to 1.8 cm for all conditions.

#### 4.4.1 *n*-Butanol

The measured laminar flame speeds for *n*-butanol/air at 1 and 2 atm,  $T_u = 353$  K, are plotted in Figures 4.13 and 4.14. The corresponding Markstein lengths and stretch extrapolation correction factors are plotted in Figure 4.15. The original

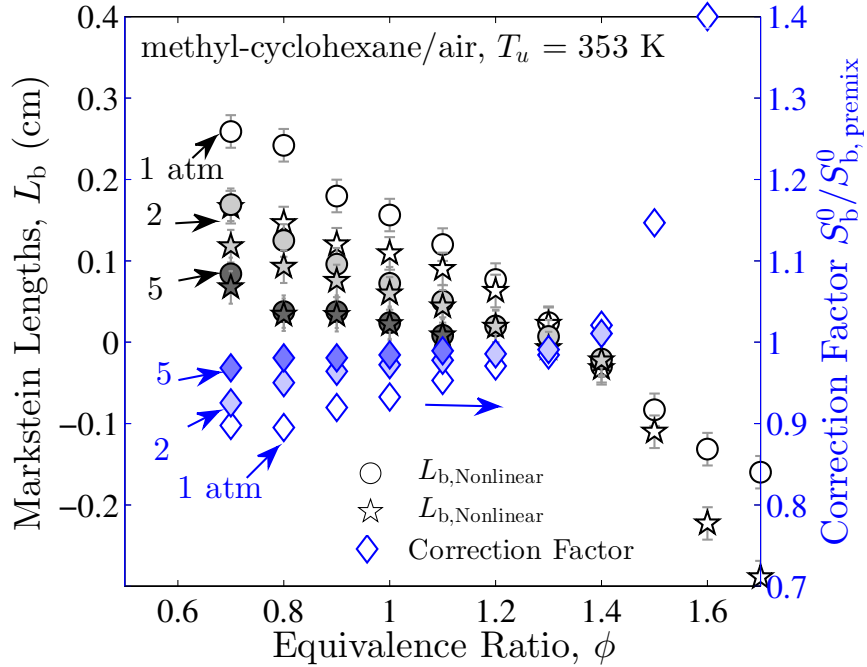


Figure 4.12: Present measurements of Markstein lengths and the calculated extrapolation correction factor based on Equation 3.14 corresponding to the  $S_u^0$  measurements plotted in Figure 4.11.

measurements, as well as empirical corrections, of [Veloo et al. \(2010\)](#) at  $T_u = 343$  K based on  $S_u^0 \sim T_u^{1.8}$  (to account for the 10 K difference in  $T_u$ ) are plotted.

Experimentation at higher pressures is limited by fuel condensation. To circumvent this difficulty, the unburned gas temperature is chosen to be 373 K, and an oxidizer with reduced oxygen concentration and a mixture of Ar and He as bath gas (molar ratio: O<sub>2</sub>%:Ar%:He% = 13%:38.1%:48.9%) was used. This renders the fuel vapor pressure as low as possible while the mixture also has a favorable effective  $Le$  for accurate extrapolation, noting that using pure Ar or He as bath gas will cause the  $Le$  to be either quite small or quite large. With these provisions, data up to 5 atm can be acquired. These data are plotted in Figure 4.16 and the corresponding Markstein lengths and extrapolation correction factors are plotted in Figure 4.17.

It is seen that all the conditions of the present measurements have positive Markstein lengths and stretch extrapolation correction causes increase in  $S_u^0$  (Correction Factor < 1). At 1 atm, it leads to a 10% increase which explains the previous discrepancies between the measurements by [Veloo et al. \(2010\)](#) and [Liu et al. \(2011a\)](#), *i.e.*, the uncorrected values of  $S_u^0$  are close to those of [Liu et al. \(2011a\)](#) while the corrected values of  $S_u^0$  are close to those of [Veloo & Egolfopoulos \(2011\)](#) after the  $T_u$  adjustment. The measurements by [Liu et al. \(2011a\)](#) were obtained using the same vessel as the present work and therefore a close agreement is expected.

For comparison, the measurements by [Liu et al. \(2011a\)](#) at 1 and 2 atm and [Veloo et al. \(2010\)](#) at 1 atm are also plotted in Figures 4.13 and 4.14. The measurements by [Veloo et al. \(2010\)](#) were obtained using the counterflow flame at unburned gas temperature of 343 K, 10 K lower in  $T_u$ . For reasonable comparison, empirical corrections of the measurements by [Veloo et al. \(2010\)](#) based on  $S_u^0 \sim T_u^{1.8}$  are also plotted. It is noted that the relation  $S_u^0 \sim T_u^{1.8}$  is not meant to be general. Instead, it simply provides a local approximation to give an estimate of the effect of the small difference in  $T_u$ .

The predictions using the Lawrence Livermore National Laboratory (LLNL) butanol model using [Sarathy et al. \(2012\)](#) (noted as LLNL model) and those by the mechanism developed at the Polytechnic University of Milan by [Ranzi et al. \(2012\)](#) (noted as PoliMi model) were also plotted in Figures 4.13, 4.14 and 4.16. It is seen that 1 and 2 atm, predictions of both models agree well with the experimental data. At 5 atm, predictions of the LLNL butanol model agree with experimental data while those of the PoliMi model are lower by 10%.

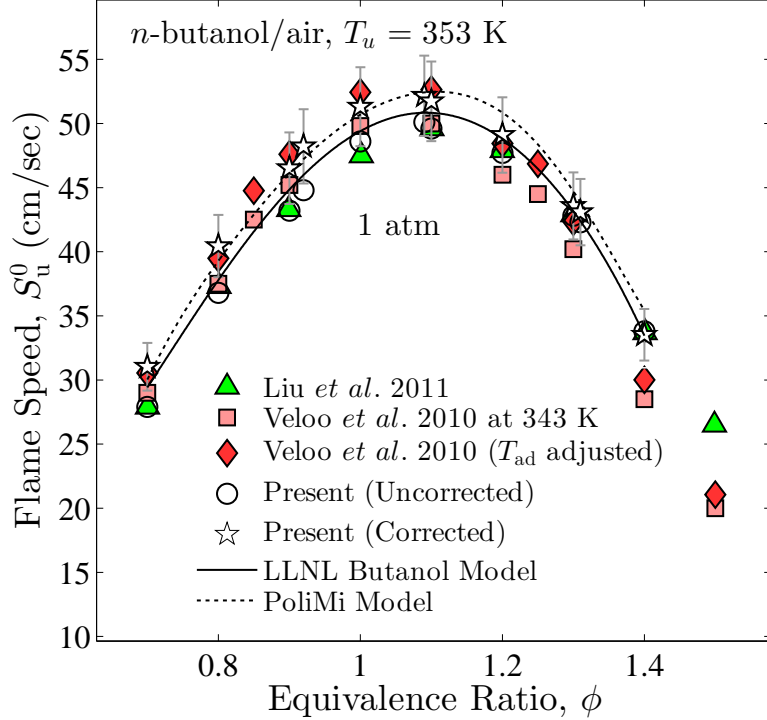


Figure 4.13: Present measurements of laminar flame speeds of *n*-butanol/air at 1 atm and unburned gas temperature  $T_u = 353$  K, plotted against the measurements by Liu *et al.* (2011a) and Veloo *et al.* (2010), and the predictions by the LLNL model (Sarathy *et al.*, 2012) and the PoliMi model (Ranzi *et al.*, 2012).

#### 4.4.2 *i*-Butanol

It is noted (Nigam & Singh, 2011) that *s*-butanol (2-butanol) and *i*-butanol (*iso*-butanol) are also produced in biological fermentation processes. This and the next subsection present measurements for these two fuels.

The measured laminar flame speeds for *i*-butanol/air at 1 and 2 atm and  $T_u = 353$  K, are plotted in Figures 4.18 and 4.19. The corresponding Markstein lengths and stretch extrapolation correction factors are plotted in Figure 4.20. The original measurements, as well as empirical corrections, by Veloo *et al.* (2010) at  $T_u = 343$  K based on  $S_u^0 \sim T_u^{1.8}$  (to account for the 10 K difference in  $T_u$ ) are plotted.

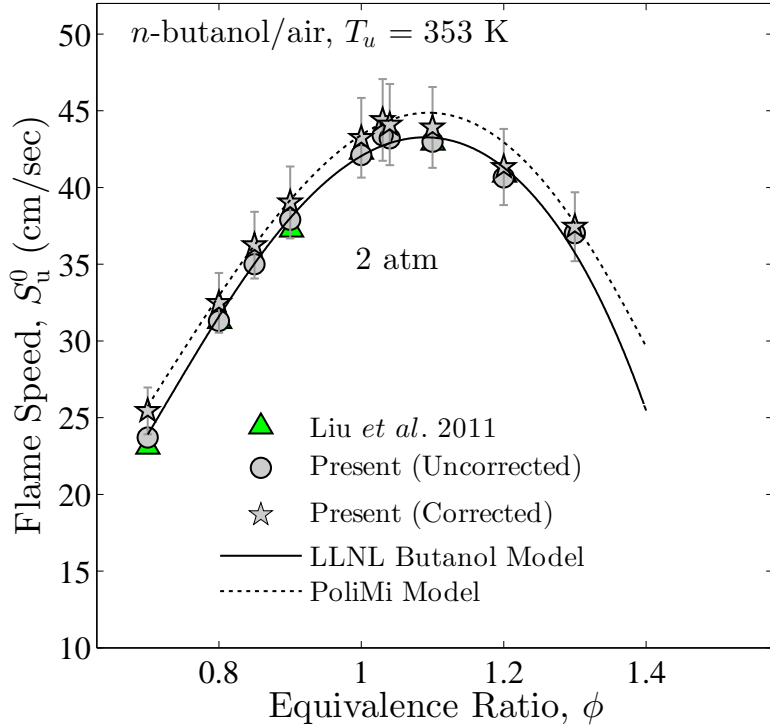


Figure 4.14: Present measurements of laminar flame speeds of  $n$ -butanol/air at 2 atm and unburned gas temperature  $T_u = 353$  K, plotted against the measurements by Liu *et al.* (2011a), and the predictions by the LLNL model (Sarathy *et al.*, 2012) and the PoliMi model (Ranzi *et al.*, 2012).

Similar to  $n$ -butanol, measurements at 5 atm were made with a mixture of  $O_2$ , Ar and He (molar ratio:  $O_2\%:Ar\%:He\% = 13\%:38.1\%:48.9\%$ ) as oxidizer and at unburned gas temperature 373 K. The measured laminar flame speeds, Markstein lengths and extrapolation correction factor were plotted in Figures 4.21 and 4.22. For comparison, the measurements by Liu *et al.* (2011a) at 1 and 2 atm and Veloo & Egolfopoulos (2011) at 1 atm and the predictions of LLNL butanol model (Sarathy *et al.*, 2012) and PoliMi model (Ranzi *et al.*, 2012) are also plotted in Figures 4.18 and 4.19. Again, the empirical corrections of the measurements by Veloo & Egolfopoulos (2011) based on  $S_u^0 \sim T_u^{1.8}$  are also plotted.

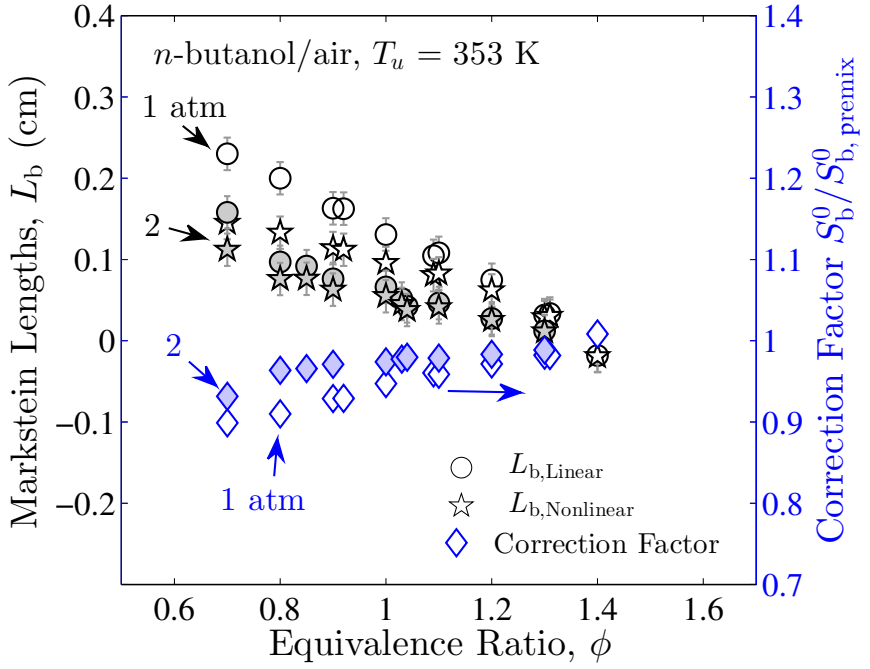


Figure 4.15: Present measurements of Markstein lengths and the calculated extrapolation correction factor based on Equation 3.14 corresponding to the  $S_u^0$  measurements plotted in Figures 4.13 and 4.14.

The larger discrepancies of the experimental measurements are at 1 atm than 2 atm. However, similar to *n*-butanol the uncorrected values of  $S_u^0$  are close to those of Liu *et al.* (2011a) while the corrected values of  $S_u^0$  are close to those of Veloo & Egolfopoulos (2011) after the  $T_u$  adjustment. For model predictions, it is seen that 1 and 2 atm, predictions of the LLNL butanol model are slightly lower than the present corrected  $S_u^0$  while those of the PoliMi model are slightly higher. At 5 atm, predictions of both models improved compared to 1 and 2 atm.

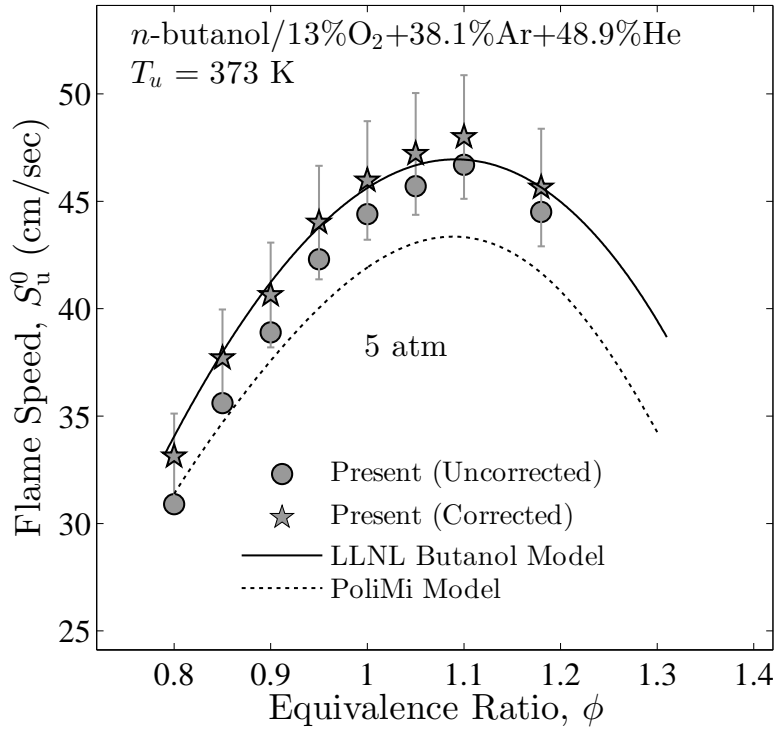


Figure 4.16: Present measurements of laminar flame speeds of *n*-butanol at 5 atm with mixture of O<sub>2</sub>, Ar and He mixture with 13:38.1:48.9 molar ratio as the oxidizer and an unburned gas temperature  $T_u = 373 \text{ K}$ , plotted against the predictions by the LLNL model (Sarathy *et al.*, 2012) and the PoliMi model (Ranzi *et al.*, 2012).

#### 4.4.3 *s*-Butanol

The measured laminar flame speeds, Markstein lengths and stretch extrapolation correction factors for *s*-butanol/air at 1 and 2 atm, and  $T_u = 353 \text{ K}$ , are plotted in Figures 4.23, 4.24 and 4.25. Measurements at 5 atm were made with a mixture of O<sub>2</sub>, Ar and He (molar ratio: O<sub>2</sub>%:Ar%:He% = 13%:38.1%:48.9%) as oxidizer and at unburned gas temperature 373 K were plotted in Figures 4.26 and 4.27. The measurements by Veloo & Egolfopoulos (2011) at 1 atm and the predictions of LLNL butanol model (Sarathy *et al.*, 2012) and PoliMi model (Ranzi *et al.*, 2012) are also plotted in Figures 4.23 and 4.24. Both the original measurements of Veloo

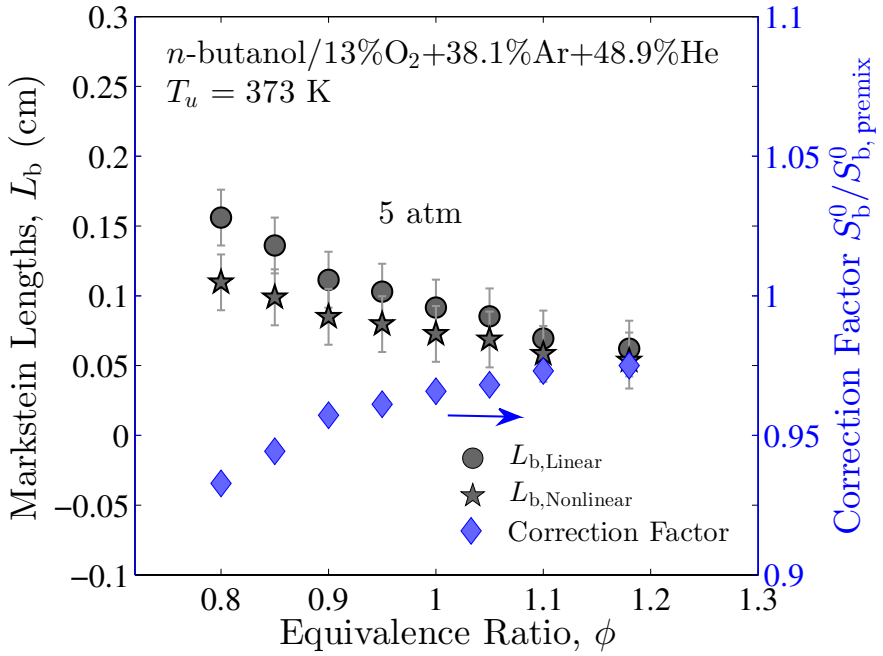


Figure 4.17: Present measurements of Markstein lengths and the calculated extrapolation correction factor based on Equation 3.14 corresponding to the  $S_u^0$  measurements plotted in Figure 4.16.

*et al.* (2010) at  $T_u = 343 \text{ K}$  as well as the empirical corrections of them based on  $S_u^0 \sim T_u^{1.8}$  (to account for the 10 K difference in  $T_u$ ) are plotted. The error bar on  $L_b$  represents estimated random error only and does not include the systematic error.

After stretch extrapolation correction, the present measurements have a closer agreement with the measurements by Veloo & Egolfopoulos (2011) at 1 atm. It is seen that for 1 and 2 atm, the predictions of both models (LLNL and PoliMi) agree well with experimental data. However, at 5 atm the predictions of the LLNL butanol model agree with experimental data while that of the PoliMi model are lower by 7-8%.

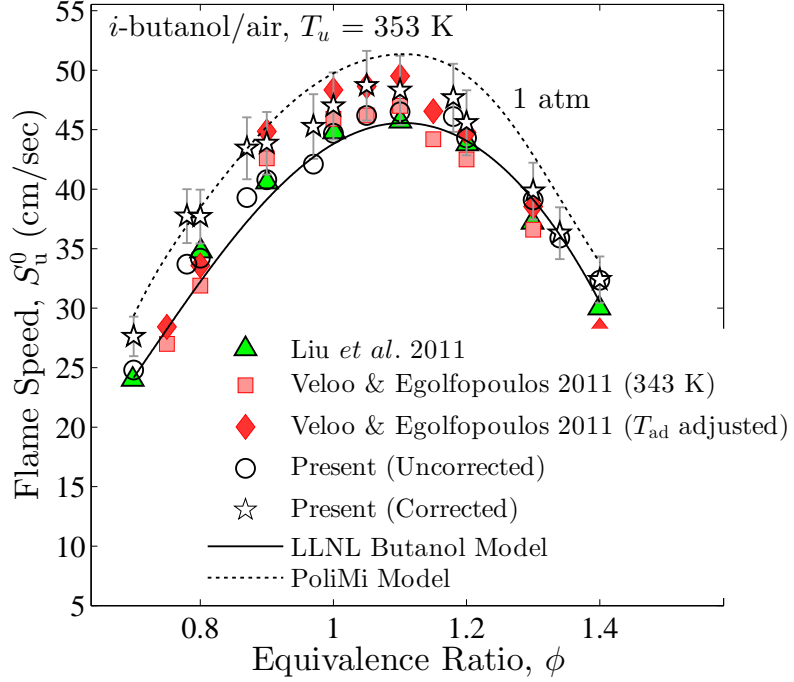


Figure 4.18: Present measurements of laminar flame speeds of *i*-butanol/air at 1 atm and unburned gas temperature  $T_u = 353$  K, plotted against the measurements by Liu *et al.* (2011a) and Veloo & Egolfopoulos (2011), and the predictions by the LLNL model (Sarathy *et al.*, 2012) and the PoliMi model (Ranzi *et al.*, 2012).

#### 4.4.4 *t*-Butanol

*t*-Butanol is a petrochemical product that has been used as an octane enhancer in gasoline for decades. Therefore, studying the combustion characteristics of all the four butanol isomers is useful and important.

The measured laminar flame speeds, Markstein lengths and stretch extrapolation correction factors for *t*-butanol/air at 1 and 2 atm,  $T_u = 353$  K, are plotted in Figures 4.28, 4.29 and 4.30. Measurements at 5 atm were made with a mixture of O<sub>2</sub>, Ar and He (molar ratio: O<sub>2</sub>%:Ar%:He% = 13%:38.1%:48.9%) as oxidizer and at unburned gas temperature 373 K were plotted in Figures 4.31 and 4.32. The measurements by Veloo & Egolfopoulos (2011) at 1 atm and the predictions of LLNL butanol

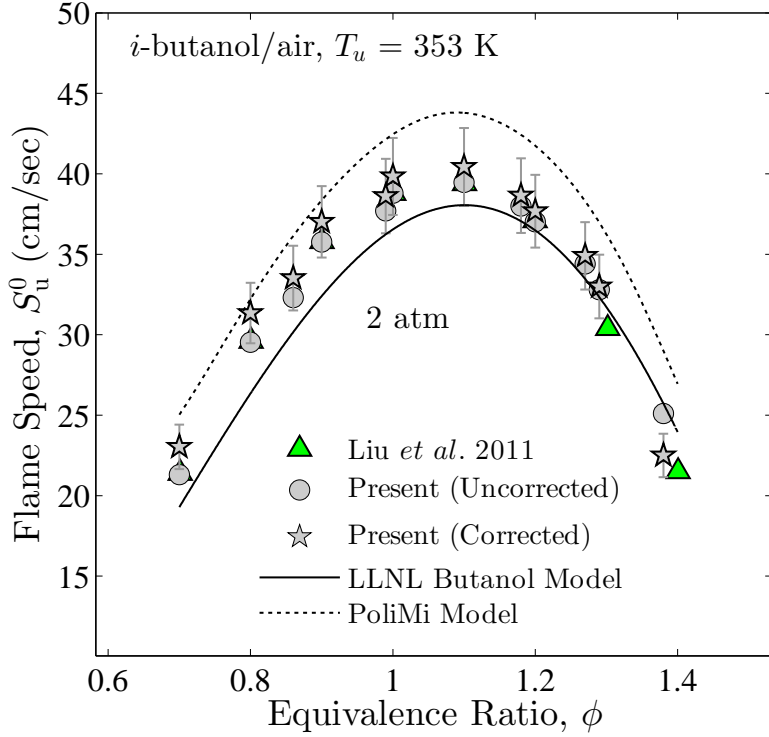


Figure 4.19: Present measurements of laminar flame speeds of *i*-butanol/air at 2 atm and unburned gas temperature  $T_u = 353$  K, plotted against the measurements by Liu *et al.* (2011a), and the predictions by the mechanism by the LLNL model (Sarathy *et al.*, 2012) and the PoliMi model (Ranzi *et al.*, 2012).

model (Sarathy *et al.*, 2012) and PoliMi model (Ranzi *et al.*, 2012) are also plotted in Figures 4.28 and 4.29. Both the original measurements of Veloo *et al.* (2010) at  $T_u = 343$  K as well as the empirical corrections of them based on  $S_u^0 \sim T_u^{1.8}$  (to account for the 10 K difference in  $T_u$ ) are plotted.

Different from the other three butanol isomers, the present measured uncorrected  $S_u^0$  agree closely with the measurements by Veloo & Egolfopoulos (2011) after temperature adjustment. As a result, the corrected  $S_u^0$  becomes higher than the Veloo & Egolfopoulos (2011) data by 10%. The predictions of both the LLNL butanol model and PoliMi model agree reasonably well with the present measurements on

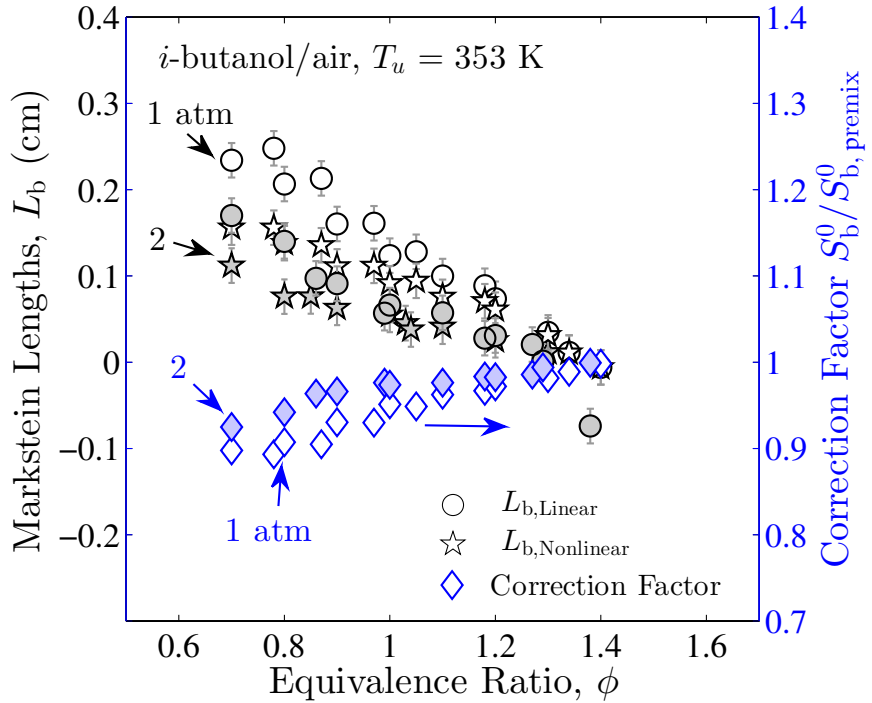


Figure 4.20: Present measurements of Markstein lengths and the calculated extrapolation correction factor based on Equation 3.14 corresponding to the  $S_u^0$  measurements plotted in Figures 4.18 and 4.19.

*t*-butanol, except at 1 and 2 atm where the LLNL butanol model slightly under predict the present corrected  $S_u^0$ .

## 4.5 Aromatic Fuels

Aromatics are also critical components of all practical hydrocarbon fuels, and benzene, toluene and other alkylated benzenes have been selected as key components of surrogate fuels (Violi *et al.*, 2002; Pitz *et al.*, 2007a; Farrell *et al.*, 2007). A aromatics are known to suppress auto-ignition and reduce the tendency of engine knock, and their chemistry is of importance also to fuel-rich combustion of all hydrocarbons. In

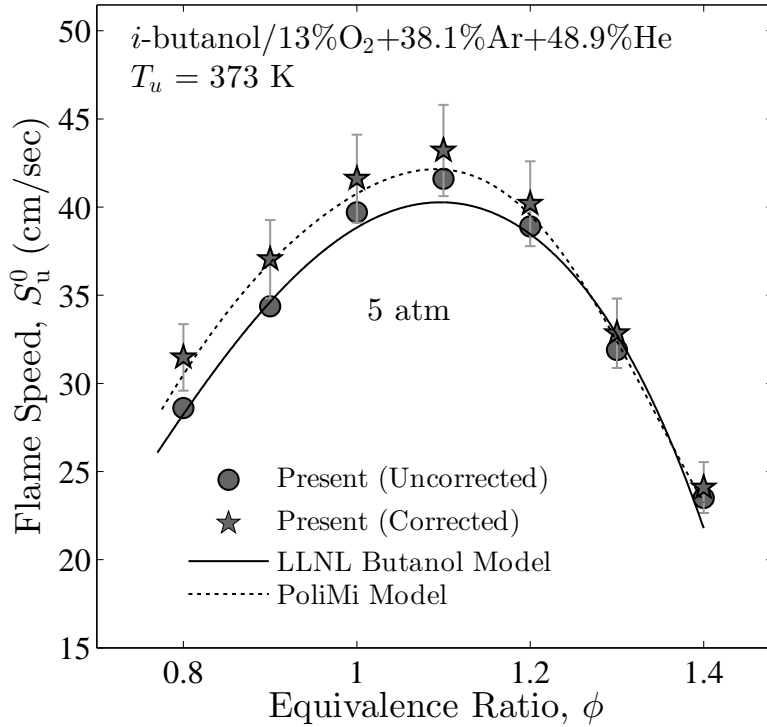


Figure 4.21: Present measurements of laminar flame speeds of *i*-butanol at 5 atm with mixture of O<sub>2</sub>, Ar and He mixture with 13:38.1:48.9 molar ratio as the oxidizer and an unburned gas temperature  $T_u = 373$  K, plotted against the predictions by the LLNL model (Sarathy *et al.*, 2012) and the PoliMi model (Ranzi *et al.*, 2012).

particular, polycyclic aromatic hydrocarbons are key precursors to soot formation (Wang, 2011). In the present study, archival experimental data were obtained for toluene and *o*-xylene. The present measurements were conducted with Vessel II. The flame radii used for extrapolation in the present measurements were from 1.0 to 1.8 cm, except for:  $\phi = 0.7$  at 1 atm (1.2 to 1.8 cm were used due to large critical radius).

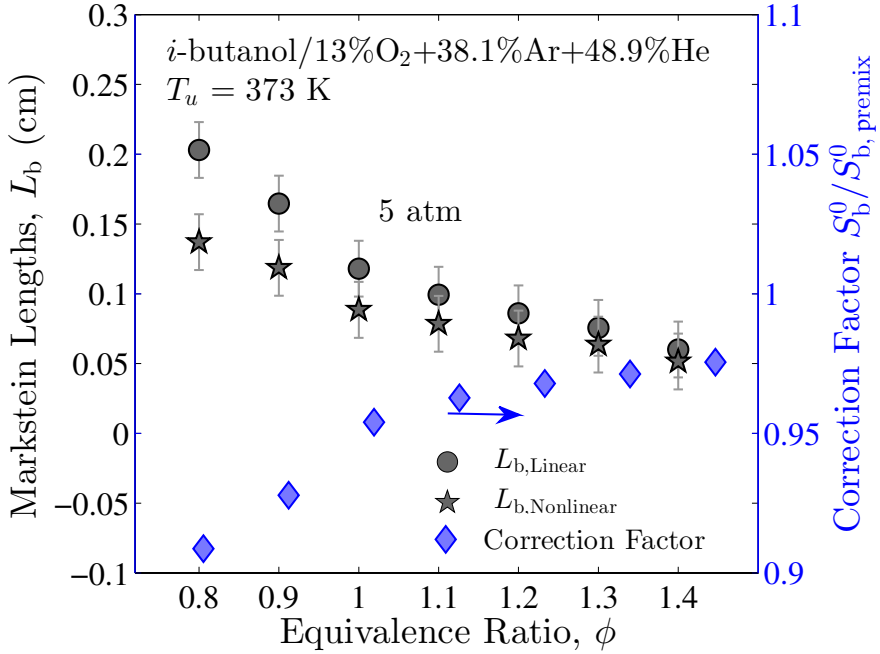


Figure 4.22: Present measurements of Markstein lengths and the calculated extrapolation correction factor based on Equation 3.14 corresponding to the  $S_u^0$  measurements plotted in Figure 4.21. The error bar on  $L_b$  represents estimated random error only and does not include the systematic error.

#### 4.5.1 Toluene

The measured laminar flame speeds, Markstein lengths and stretch extrapolation correction factors for toluene/air at 1, 2 and 5 atm,  $T_u = 353$  K, are plotted in Figures 4.33 and 4.34. The measurements by Ji *et al.* (2012a) and the predictions of toluene/air flame speeds by the model published in Metcalfe *et al.* (2011) are also plotted in Figure 4.33 for comparison.

Similar to data of other liquid fuels previously presented, the corrections of stretch extrapolation are the largest at 1 atm and decreases with pressure. The data by Ji *et al.* (2012a) at 1 atm agree well with the uncorrected  $S_u^0$  of the present measurements for  $\phi < 1.2$ . For  $\phi > 1.2$ , the data of Ji *et al.* (2012a) are lower. While

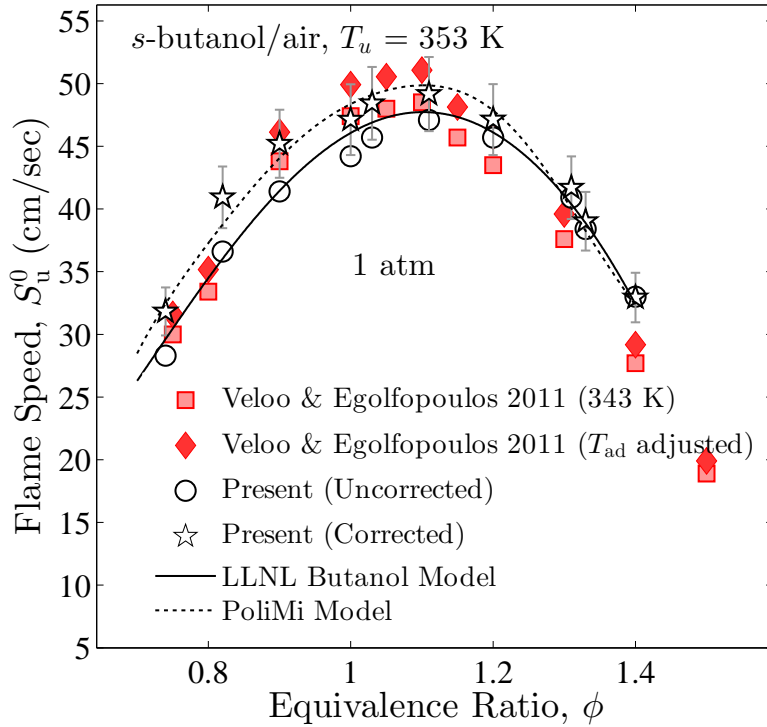


Figure 4.23: Present measurements of laminar flame speeds of *s*-butanol/air at 1 atm and unburned gas temperature  $T_u = 353$  K, plotted against the measurements by [Veloo & Egolfopoulos \(2011\)](#), and the predictions by the LLNL model ([Sarathy et al., 2012](#)) and the PoliMi model ([Ranzi et al., 2012](#)).

this discrepancies can be explained by stretch extrapolation uncertainty for other fuels previously presented, it is not the case here for toluene/air. The corrected  $S_u^0$  of the present measurements turn out to be higher than the measurements by [Ji et al. \(2012a\)](#) for  $\phi < 1.2$ . The reason for this difference needs to be investigated in future.

The predictions of the model by [Metcalfe et al. \(2011\)](#) in general agree well with the present measurements at 1 and 2 atm. At the 5 atm, the model predictions agree well with the present measurements for  $\phi < 1$  and are higher for  $\phi > 1$ .

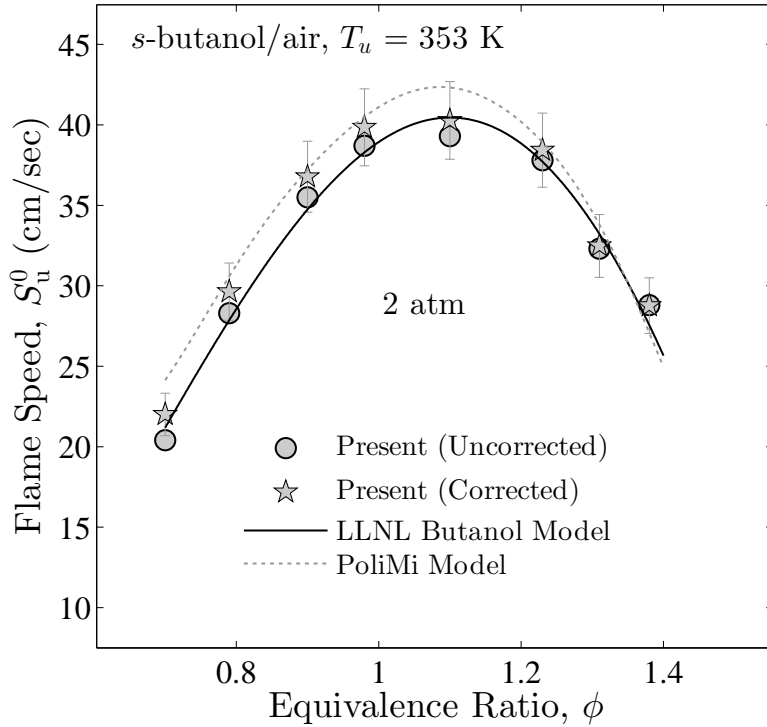


Figure 4.24: Present measurements of laminar flame speeds of *s*-butanol/air at 2 atm and unburned gas temperature  $T_u = 353$  K, plotted against the measurements by Liu *et al.* (2011a), and the predictions by the LLNL model (Sarathy *et al.*, 2012) and the PoliMi model (Ranzi *et al.*, 2012).

#### 4.5.2 *o*-Xylene

The measured laminar flame speeds, Markstein lengths and stretch extrapolation correction factors for *o*-xylene/air at 1 and 2 atm,  $T_u = 353$  K, are plotted in Figures 4.35 and 4.36. The measurements by Ji *et al.* (2012a) are also plotted in Figure 4.33 for comparison.

Similar to toluene, the error of the stretch extrapolation cannot fully explain the difference between the discrepancies of the present measurements with those by Ji *et al.* (2012a). The corrected  $S_u^0$  of the present measurements are noticeably higher than the measurements by Ji *et al.* (2012a) for  $\phi < 1.2$ . The reason for this

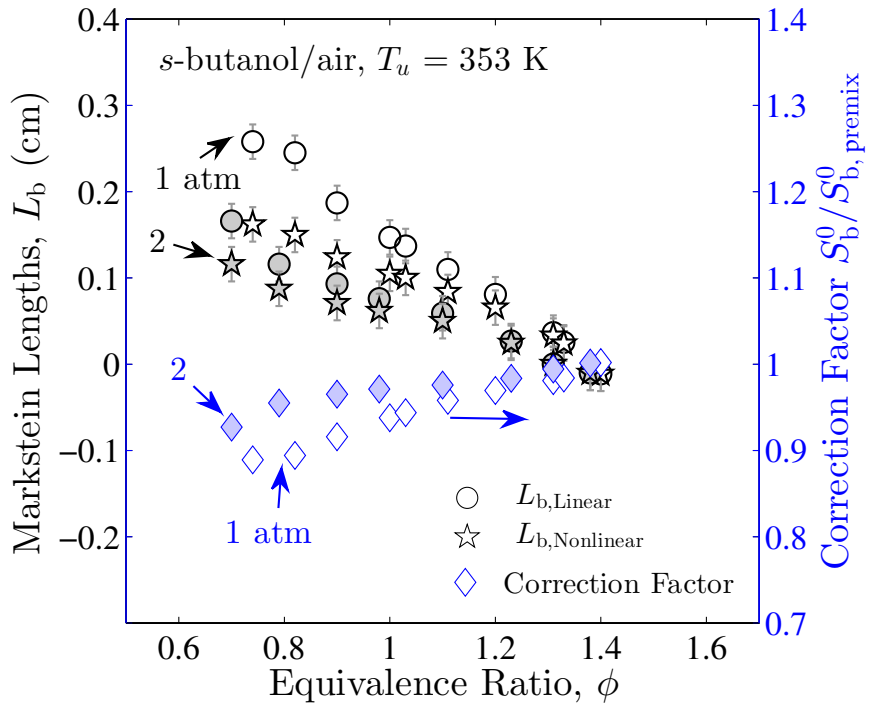


Figure 4.25: Present measurements of Markstein lengths and the calculated extrapolation correction factor based on Equation 3.14 corresponding to the  $S_u^0$  measurements plotted in Figures 4.23 and 4.24.

difference is yet unclear.

## 4.6 Mixtures of H<sub>2</sub> and C<sub>0</sub>-C<sub>4</sub> Hydrocarbons

As will be shown in the analysis in Chapter 5 as well as previous studies (You *et al.*, 2009; Wang *et al.*, 2010; Kelley *et al.*, 2011c), even for very large fuel molecules, such as cyclohexane, the majority of the chemical reactions which are typically rate controlling tend to involve reactions of small molecules with carbon numbers typically less than C<sub>4</sub>. Therefore, a fundamental understanding of the chemistry of small fuel molecules is necessary.

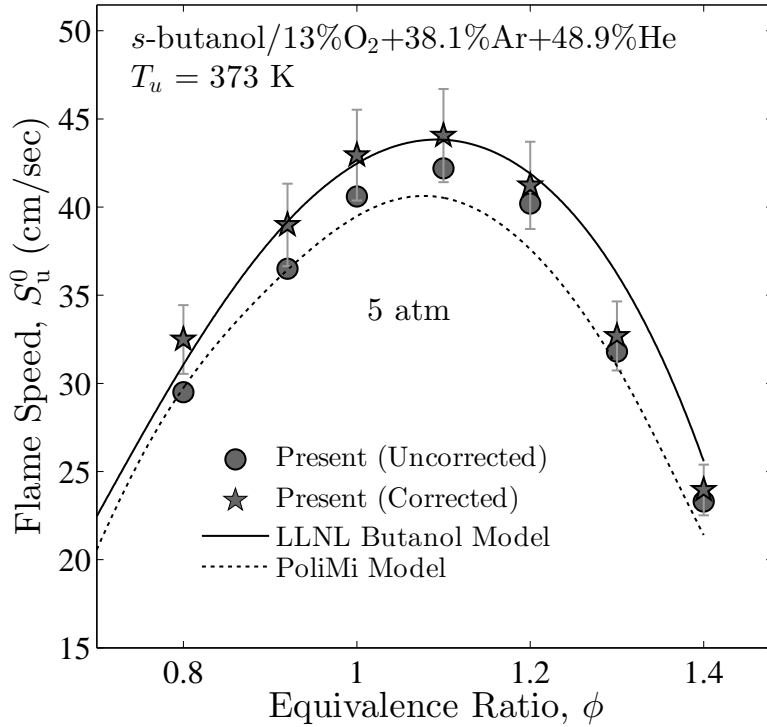


Figure 4.26: Present measurements of laminar flame speeds of *s*-butanol at 5 atm with mixture of O<sub>2</sub>, Ar and He mixture with 13:38.1:48.9 molar ratio as the oxidizer and an unburned gas temperature  $T_u = 373$  K, plotted against the predictions by the LLNL model (Sarathy *et al.*, 2012) and the PoliMi model (Ranzi *et al.*, 2012).

While there are extensive laminar flame speed data for pure fuels of H<sub>2</sub> and C<sub>0</sub>-C<sub>4</sub>, such as Tse *et al.* (2000), Jomaas *et al.* (2005), Sun *et al.* (2007), Kelley & Law (2009), Burke *et al.* (2010) and Zhao *et al.* (2014), data for mixtures of fuels are scarce. For the present work, the laminar flame speeds of mixtures of H<sub>2</sub> with CO and C<sub>1</sub>-C<sub>3</sub> hydrocarbons are investigated. Mixtures of H<sub>2</sub>, CO and small-molecule hydrocarbons are intermediates of large-molecule hydrocarbon oxidation. Therefore, predicting their flame speeds is also a minimum requirement for chemical kinetic models. Furthermore, the strong reactivity of H<sub>2</sub> renders it an attractive additive to enhance flame propagation and extend the flammability limits of fuel/air

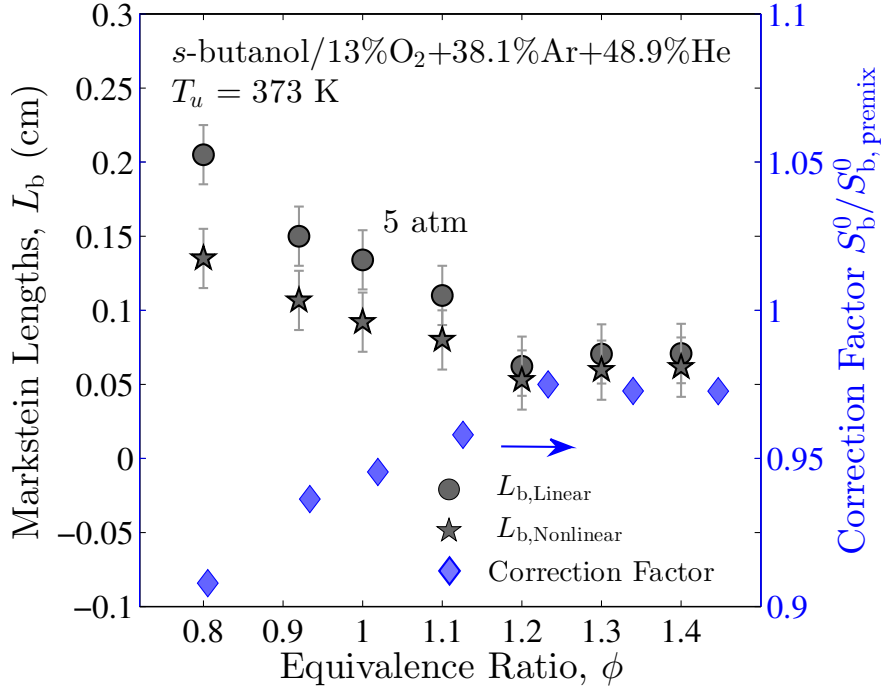


Figure 4.27: Present measurements of Markstein lengths and the calculated extrapolation correction factor based on Equation 3.14 corresponding to the  $S_u^0$  measurements plotted in Figure 4.26.

mixtures, and as such offers potential to combustion control. Therefore, it is useful to understand the effect of adding H<sub>2</sub> on flame speeds of CO and hydrocarbons.

To characterize the mixture composition of mixtures of H<sub>2</sub>, fuel and oxidizer, the following composition parameters to characterize the amount of hydrogen addition are adopted (Yu *et al.*, 1986),

$$R_H = \frac{C_H + C_H / (C_H/C_A)_{st}}{C_F + [C_A - C_H / (C_H/C_A)_{st}]} \quad (4.2)$$

$$\phi_F = \frac{C_F / [C_A - C_H / (C_H/C_A)_{st}]}{(C_F/C_A)_{st}} \quad (4.3)$$

where  $C_H$ ,  $C_F$  and  $C_A$  are the mole concentrations of the fuel (other than hydrogen),

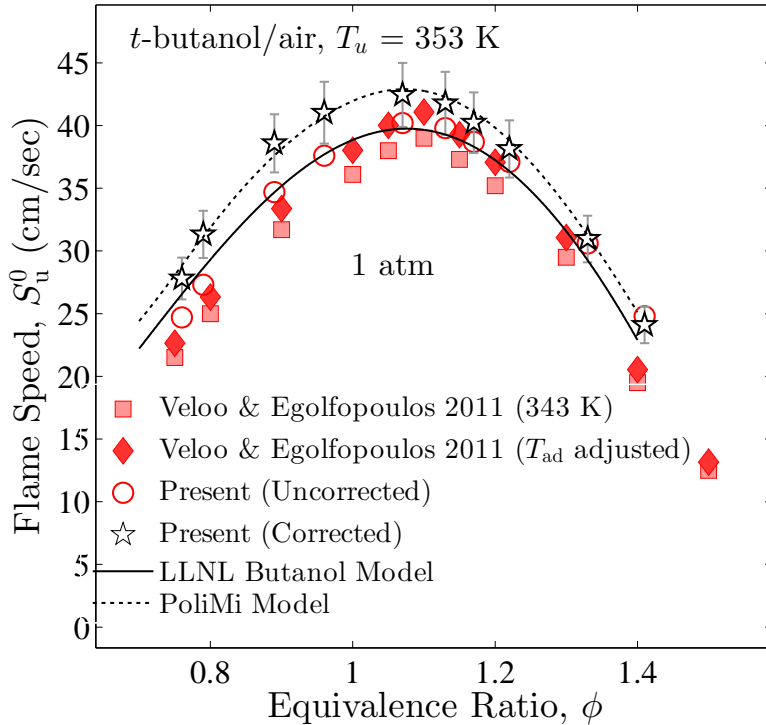


Figure 4.28: Present measurements of laminar flame speeds of *t*-butanol/air at 1 atm and unburned gas temperature  $T_u = 353$  K, plotted against the measurements by [Veloo & Egolfopoulos \(2011\)](#), and the predictions by the LLNL model ([Sarathy et al., 2012](#)) and the PoliMi model ([Ranzi et al., 2012](#)).

hydrogen and oxidizer (air or other mixtures of  $O_2$  and bath gases) respectively, and the subscript *st* designates the stoichiometric state. The parameter  $R_H$  is the ratio of the amount of hydrogen plus the stoichiometric amount of air needed for its oxidation, to the amount of fuel plus the remaining air left for its oxidation. Thus the numerator properly accounts for all the gases that participate in the oxidation of hydrogen. Consequently  $\phi_F$  represents an effective equivalence ratio of the fuel. Implicit in the adoption of these parameters is the anticipation that hydrogen is preferentially oxidized as compared to the fuel as its consumption is stoichiometric and hence complete, leaving the remaining oxygen to react with the fuel. Such

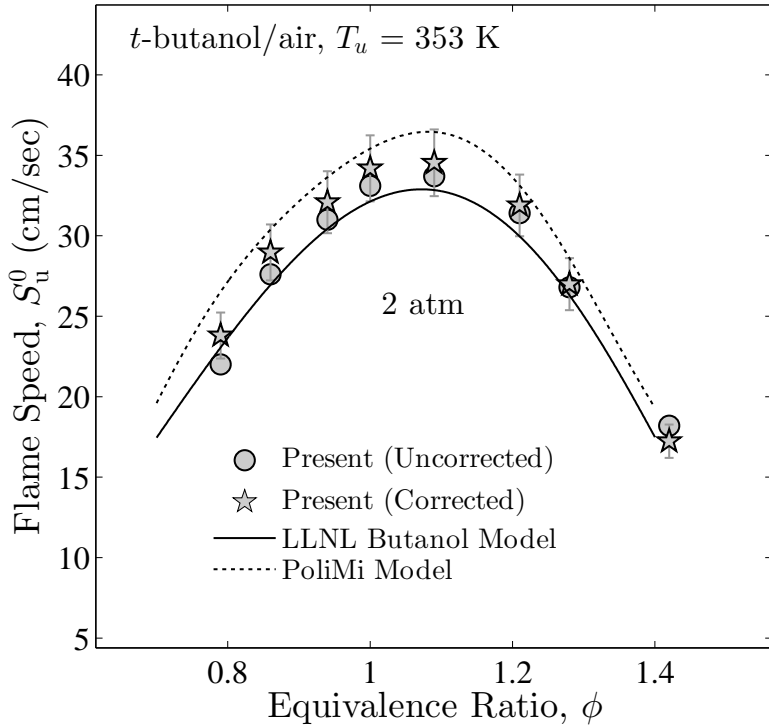


Figure 4.29: Present measurements of laminar flame speeds of *t*-butanol/air at 2 atm and unburned gas temperature  $T_u = 353$  K, plotted against the measurements by Liu *et al.* (2011a), and the predictions by the LLNL model (Sarathy *et al.*, 2012) and the PoliMi model (Ranzi *et al.*, 2012).

an assumption is reasonable considering the highly reactive and diffusive nature of hydrogen, as compared to the fuel, and the relatively small amount of hydrogen addition.

The results of Yu *et al.* (1986) showed that regardless of whether the mixture was lean or rich, the increase in the flame speed can be approximately linearly correlated with  $R_H$ . This simple correlation has generated substantial follow-on investigations. Specifically, Sher & Ozdor (1992) and Tang *et al.* (2011) measured the laminar flame speeds of *n*-butane/air mixtures with hydrogen addition, and found that the linear correlation again holds approximately. Recognizing that the

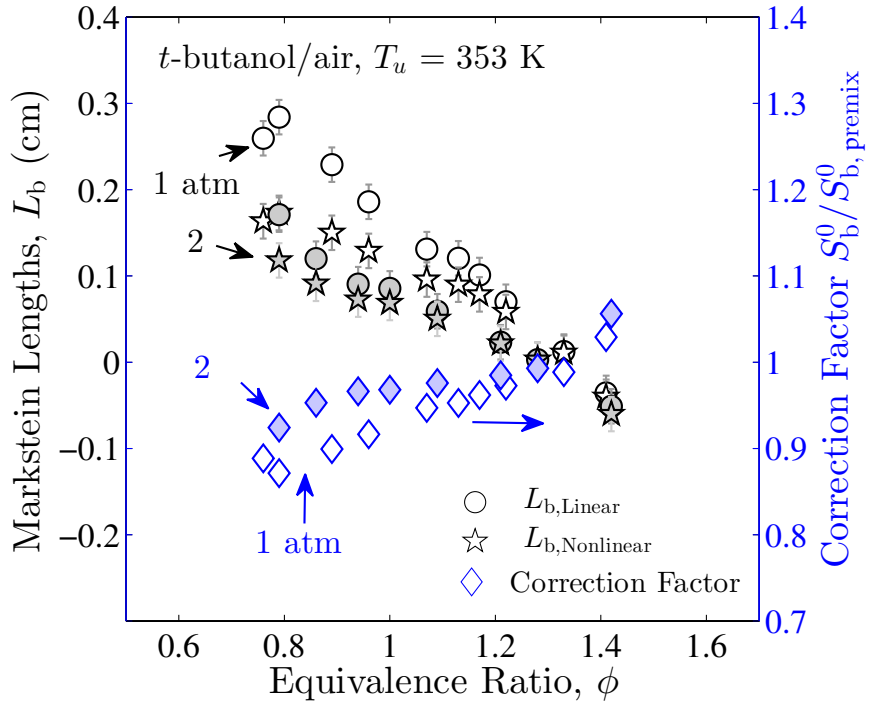


Figure 4.30: Present measurements of Markstein lengths and the calculated extrapolation correction factor based on Equation 3.14 corresponding to the  $S_u^0$  measurements plotted in Figures 4.28 and 4.29.

approximate linear correlation has been demonstrated for alkanes, namely, methane (Yu *et al.*, 1986), propane (Yu *et al.*, 1986) and *n*-butane (Sher & Ozdor, 1992; Tang *et al.*, 2011), the present work will investigate the effect of hydrogen addition on a range of fuels, including CO, alkane, alkene and alkyne fuels.

In the following, the effect of hydrogen addition on flame speeds of ethane, ethylene, acetylene, propane and CO will be studied. Measurements presented in this section were conducted with Vessel I. The flame radii used for extrapolation in the present measurements were from 1.0 to 1.8 cm.

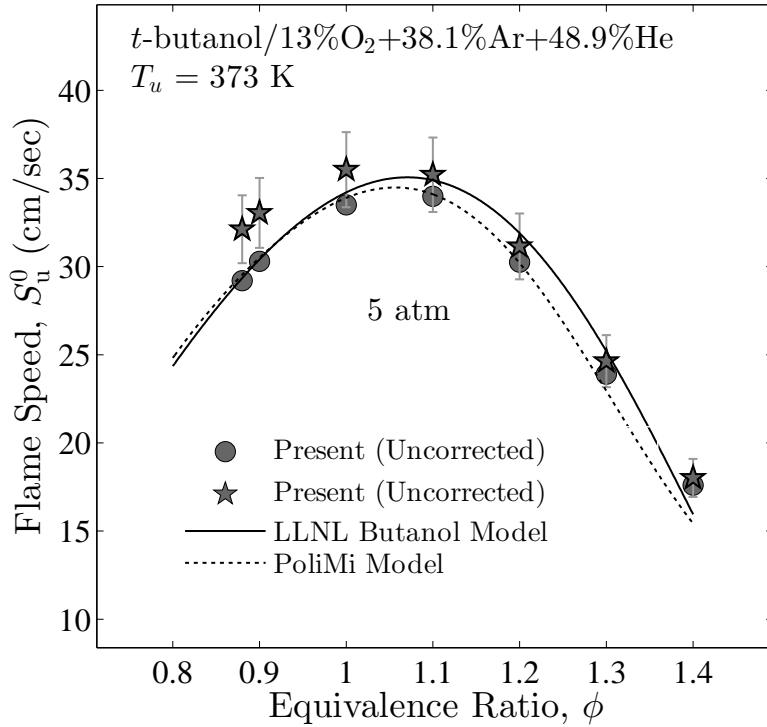


Figure 4.31: Present measurements of laminar flame speeds of *t*-butanol at 5 atm with mixture of O<sub>2</sub>, Ar and He mixture with 13:38.1:48.9 molar ratio as the oxidizer and an unburned gas temperature  $T_u = 373$  K, plotted against the predictions by the LLNL model (Sarathy *et al.*, 2012) and the PoliMi model (Ranzi *et al.*, 2012).

#### 4.6.1 Hydrogen/Ethane Mixtures

Figures 4.37 and 4.38 present the measurements of laminar flame speeds, Markstein lengths and extrapolation correction factors for hydrogen/ethane/air mixtures at 1 atm, plotted against the predictions by the USC Mech II kinetic mechanism by Wang *et al.* (2007). The results show that the relation between the laminar flame speeds and  $R_H$  for hydrogen/ethane/air mixtures at three different values of  $\phi_F$  are all approximately linear. In addition, it is seen from Figure 4.38 that the Markstein lengths and the stretch extrapolation correction factors are close to 0 and 1, respectively. As a result, the difference between the uncorrected and corrected  $S_u^0$

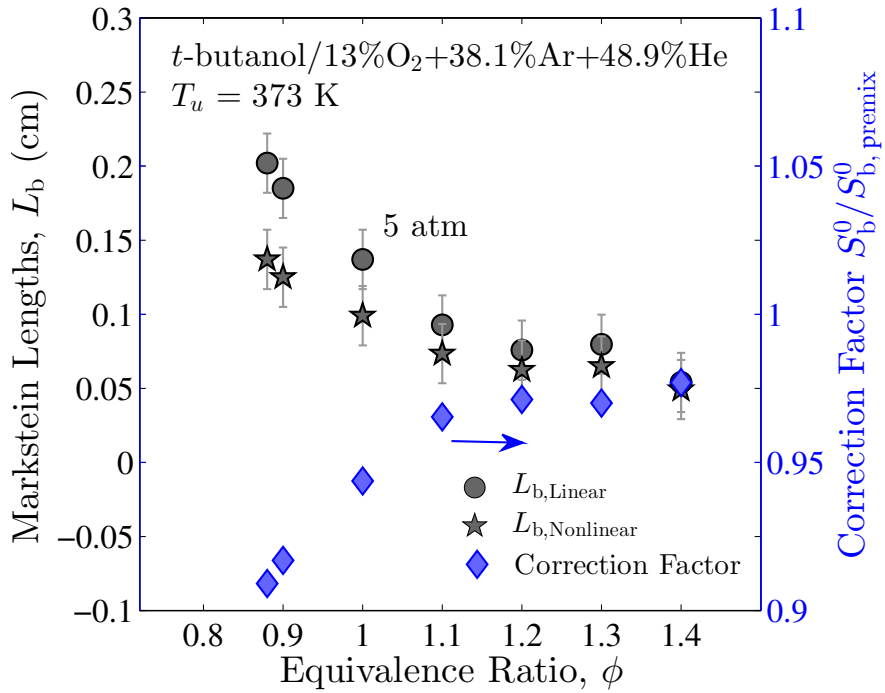


Figure 4.32: Present measurements of Markstein lengths and the calculated extrapolation correction factor based on Equation 3.14 corresponding to the  $S_u^0$  measurements plotted in Figure 4.31.

is small. This is expected because all the C<sub>2</sub> hydrocarbons have similar molecular weight as those of N<sub>2</sub> and O<sub>2</sub>. Therefore, their transport properties are close to those of air. Compared to the present measurements, the predictions using USC Mech II (Wang *et al.*, 2007) are mostly higher at lean, stoichiometric and rich conditions.

#### 4.6.2 Hydrogen/Ethylene Mixtures

Figures 4.39 and 4.40 present the measurements of laminar flame speeds, Markstein lengths and extrapolation correction factors for hydrogen/ethylene/air mixtures at 1 atm, plotted against the predictions by the USC Mech II kinetic mechanism by Wang *et al.* (2007). The results also show that the relation between the laminar

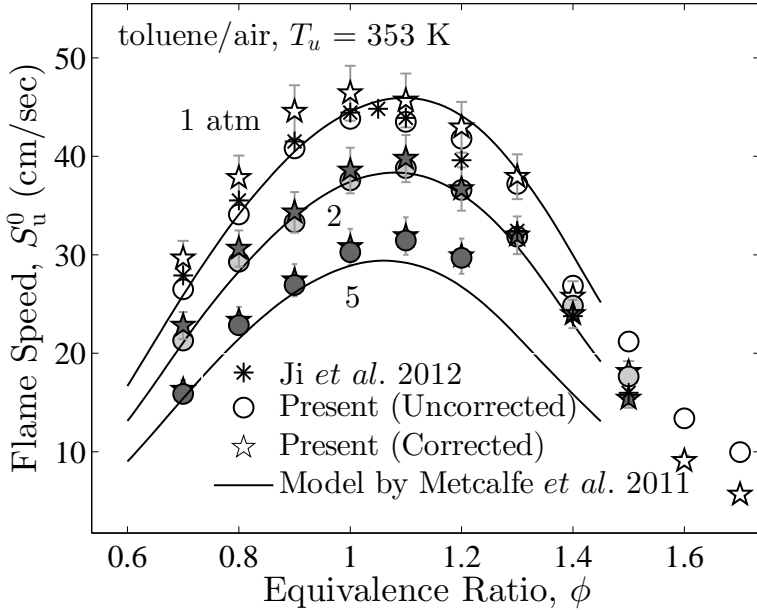


Figure 4.33: Present measurements of laminar flame speeds of toluene/air at 1, 2 and 5 atm and unburned gas temperature  $T_u = 353$  K, plotted against the measurements by [Ji et al. \(2012a\)](#), and the predictions by the model of [Metcalfe et al. \(2011\)](#).

flame speeds and  $R_H$  for hydrogen/ethane/air mixtures at three different  $\phi_F$ s are all approximately linear. Similar to ethane, the Markstein lengths and the stretch extrapolation correction factors are close to 0 and 1, respectively. Therefore, the difference between the uncorrected and corrected  $S_u^0$  is small. For ethylene at 1 atm, the predictions by USC Mech II ([Wang et al., 2007](#)) agree reasonably well with the present measurements.

Figures 4.41 and 4.42 present the measurements of laminar flame speeds, Markstein lengths and extrapolation correction factors for hydrogen/ethylene/air mixtures at 5 atm and  $\phi_F = 0.7$ , plotted against the predictions by the USC Mech II kinetic mechanism by [Wang et al. \(2007\)](#). Only results at  $R_H$  from 0 to 0.2 are shown because the flame speed measurement is only possible for small values of  $R_H$ ,

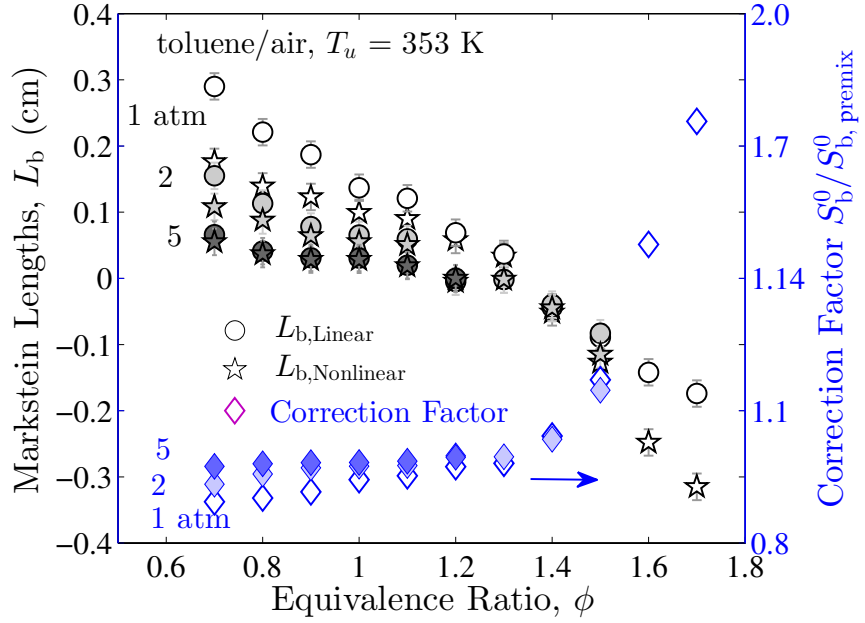


Figure 4.34: Present measurements of Markstein lengths and the calculated extrapolation correction factor based on Equation 3.14 corresponding to the  $S_u^0$  measurements plotted in Figure 4.33.

as further increasing  $R_H$  causes cellular instabilities to develop. The results also show that the relation between the flame speeds and  $R_H$  are approximately linear. Since flame thickness and Markstein length both decrease with pressure, the extrapolation correction factors at 5 atm are very close to 1. Therefore, the corrected  $S_u^0$ 's do not show any difference with uncorrected  $S_u^0$ . In addition, for ethylene with hydrogen addition at 5 atm, it is seen that the predictions by USC Mech II (Wang *et al.*, 2007) are higher than the present measurements at  $R_H = 0$ , but becomes smaller than the present measurements as  $R_H$  increases.

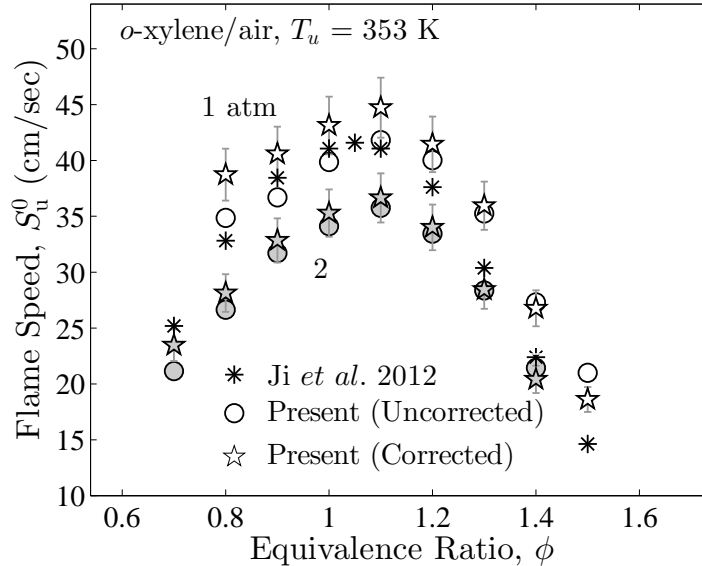


Figure 4.35: Present measurements of laminar flame speeds of *o*-xylene/air at 1 and 2 atm and unburned gas temperature  $T_u = 353$  K, plotted against the measurements by [Ji \*et al.\* \(2012a\)](#).

### 4.6.3 Hydrogen/Acetylene Mixtures

Figures 4.43 and 4.44 present the measurements of laminar flame speeds, Markstein lengths and extrapolation correction factors for hydrogen/acetylene/air mixtures at 1 atm, plotted against the predictions by the USC Mech II kinetic mechanism by [Wang \*et al.\* \(2007\)](#). The results show that the relation between the laminar flame speeds and  $R_H$  for hydrogen/ethane/air mixtures at three different  $\phi_F$  are all approximately linear, and that the Markstein lengths and the stretch extrapolation correction factors are close to 0 and 1, respectively. For acetylene at 1 atm, USC Mech II ([Wang \*et al.\*, 2007](#)) over-predicts the lean and stoichiometric flame speeds and under-predicts the rich flame speeds.

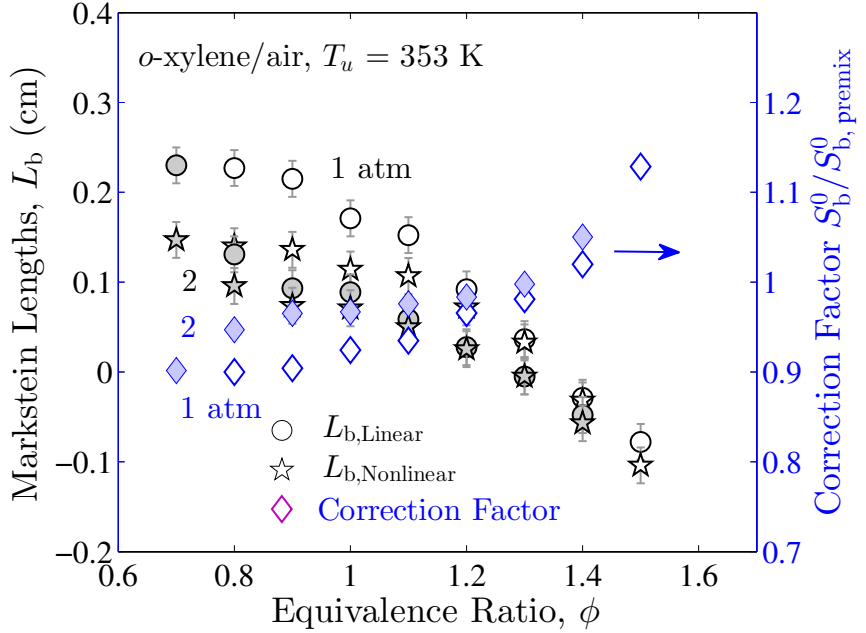


Figure 4.36: Present measurements of Markstein lengths and the calculated extrapolation correction factor based on Equation 3.14 corresponding to the  $S_u^0$  measurements plotted in Figure 4.35.

#### 4.6.4 Hydrogen/Propane Mixtures

Figures 4.45 and 4.46 present the measurements of laminar flame speeds, Markstein lengths and extrapolation correction factors for lean hydrogen/propane with oxygen/helium mixtures as oxidizer at 20 atm. The predictions by USC Mech II (Wang *et al.*, 2007) are also plotted for comparison. As pressure increases the flame again becomes harder to stabilize because of the decrease in the flame thickness. Therefore, to suppress cellular instabilities at 20 atm, helium is used to replace the nitrogen. It is seen that the USC Mech II (Wang *et al.*, 2007) largely under-predicts the flame speeds. The approximate linear correlation between the laminar flame speeds and  $R_H$  still holds for both experimental and computational data. Finally, the correction of stretch extrapolation is also very small at 20 atm.

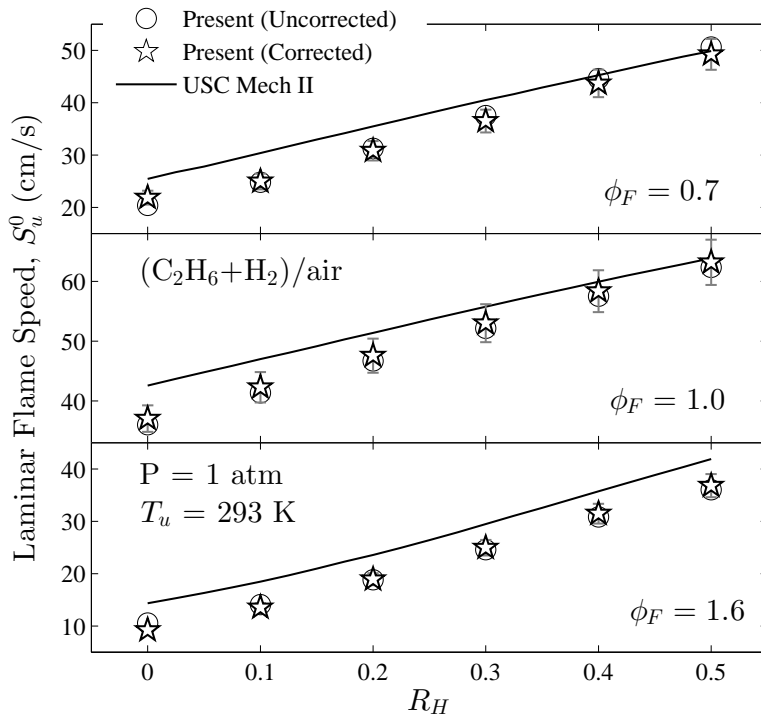


Figure 4.37: Present measurements of laminar flame speeds of hydrogen/ethane/air mixtures at 1 atm and unburned gas temperature  $T_u = 293$  K, plotted against the predictions by the USC Mech II mechanism ([Wang et al., 2007](#)).

#### 4.6.5 Hydrogen/CO Mixtures

From the above results, it is seen that for hydrocarbons (alkanes, alkenes and alkynes), flame speeds always correlate linearly with the hydrogen addition parameter  $R_H$ . It is not expected that the linear relationship will still hold for carbon monoxide with hydrogen addition, because hydrogen is known to have a strong catalytic effect on the oxidation of carbon monoxide.

Figures 4.47 and 4.48 present the measurements of laminar flame speeds, Markstein lengths and extrapolation correction factors for  $\text{H}_2/\text{CO}/\text{air}$  at 1 atm. The predictions by USC Mech II ([Wang et al., 2007](#)) are also plotted for comparison.

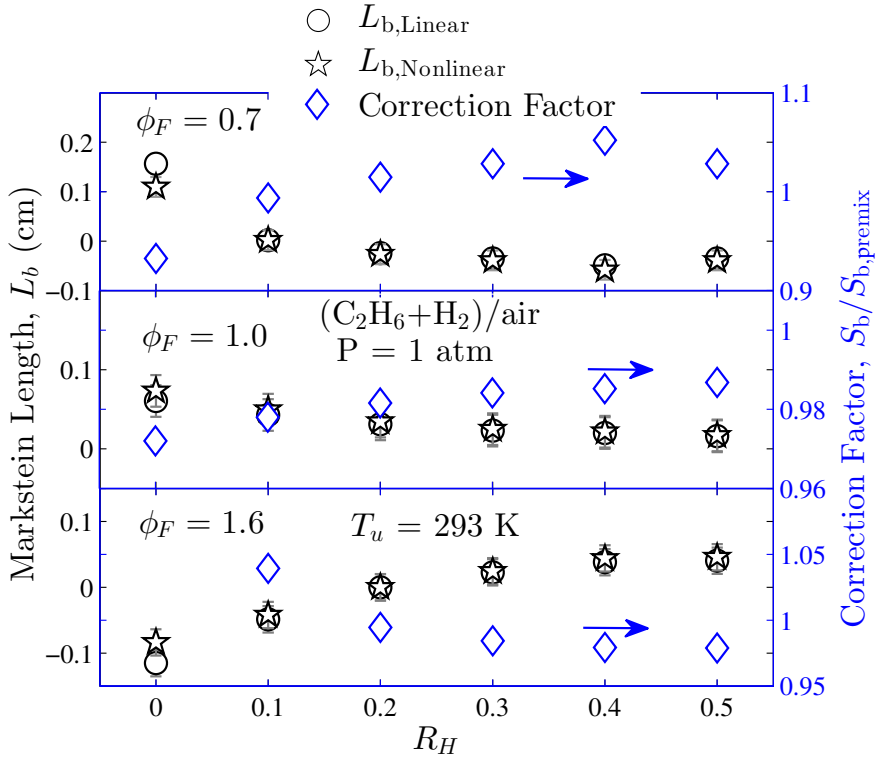


Figure 4.38: Present measurements of Markstein lengths and the calculated extrapolation correction factor based on Equation 3.14 corresponding to the  $S_u^0$  measurements plotted in Figure 4.37.

The laminar flame speeds of carbon monoxide/air mixture with hydrogen addition exhibit a highly nonlinear dependence on  $R_H$ . The laminar flame speed of pure carbon monoxide/air mixture is very close to zero. In fact, in experiments it was not possible to ignite a pure carbon monoxide mixture. The laminar flame speed increases rapidly as  $R_H$  increases from 0 to 0.1. Further increasing  $R_H$  beyond 0.1 results in a nearly linear relationship. Good agreement between calculation and experiment is seen for all values of  $\phi_F$ , both in the values of the laminar flame speeds and their dependence on hydrogen addition, hence demonstrating the satisfactory state of the oxidative mechanism of carbon monoxide.

From Figure 4.48, it is seen that the Markstein length decreases largely with

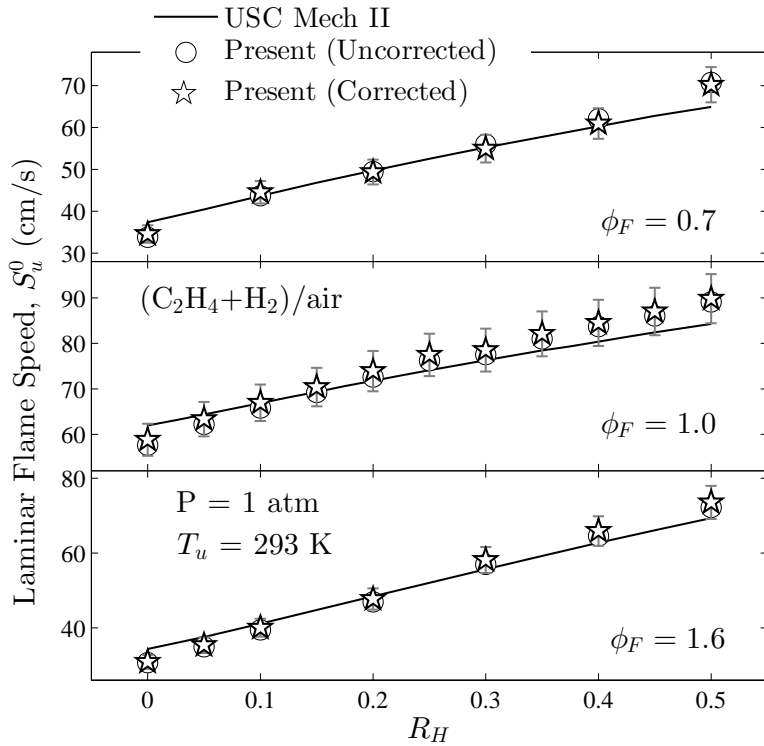


Figure 4.39: Present measurements of laminar flame speeds of hydrogen/ethylene/air mixtures at 1 atm and unburned gas temperature  $T_u = 293$  K, plotted against the predictions by the USC Mech II mechanism ([Wang et al., 2007](#)).

$R_H$ . This is due to the large flame thickness caused by weak reactivity and small flame speed. As a result, the stretch extrapolation correction factor increases from 0.95 to 1 as  $R_H$  increases. However, since the transport properties of CO are also close to those of  $N_2$  and  $O_2$ , the small corrections do not cause a noticeable change in  $S_u^0$  as seen from Figure 4.47.

Figures 4.49 and 4.50 present the measurements of laminar flame speeds, Markstein lengths and extrapolation correction factors for  $H_2/CO/O_2/He$  mixtures at  $\phi_F = 1.0$  at 20 atm. The predictions by USC Mech II ([Wang et al., 2007](#)) are also plotted for comparison. It is seen that while the calculation and experiment have

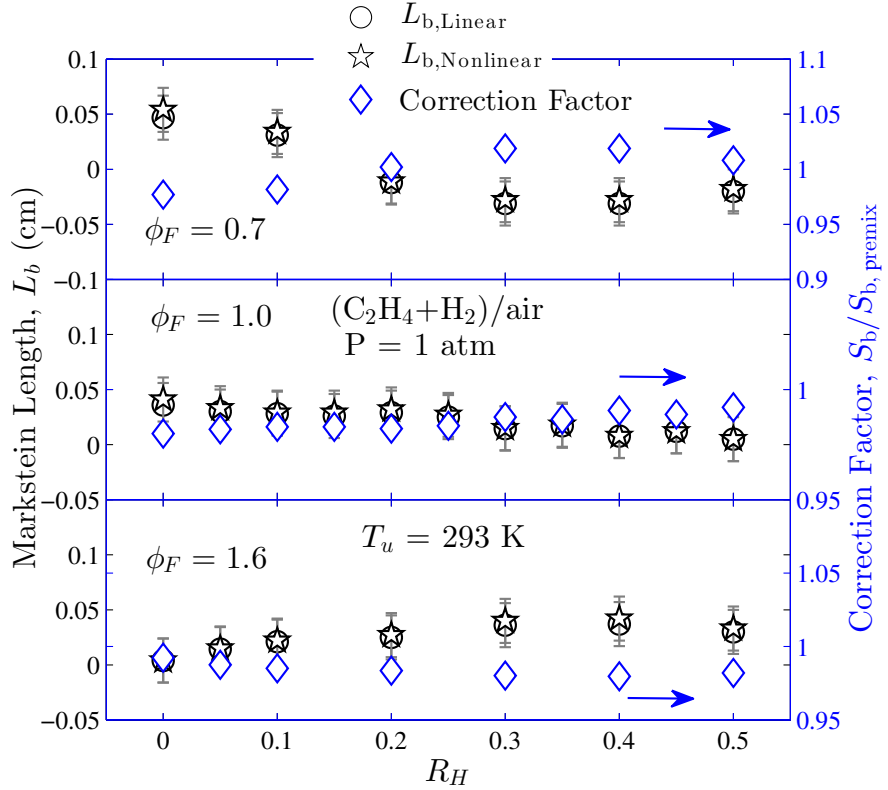


Figure 4.40: Present measurements of Markstein lengths and the calculated extrapolation correction factor based on Equation 3.14 corresponding to the  $S_u^0$  measurements plotted in Figure 4.39.

good agreement for small  $R_H$ , it under-predicts the flame speeds at higher hydrogen additions. The overall agreement between calculation and experiment is not as good as those at atmospheric pressure. In addition, the flame speeds in Figure 4.49 show a nonlinear dependence on  $R_H$ , which is similar in trend as the results at atmospheric pressure. This indicates that the influence of hydrogen addition on carbon monoxide oxidation is still characterized by the catalytic effect. Finally, the correction of stretch extrapolation is also very small at 20 atm.

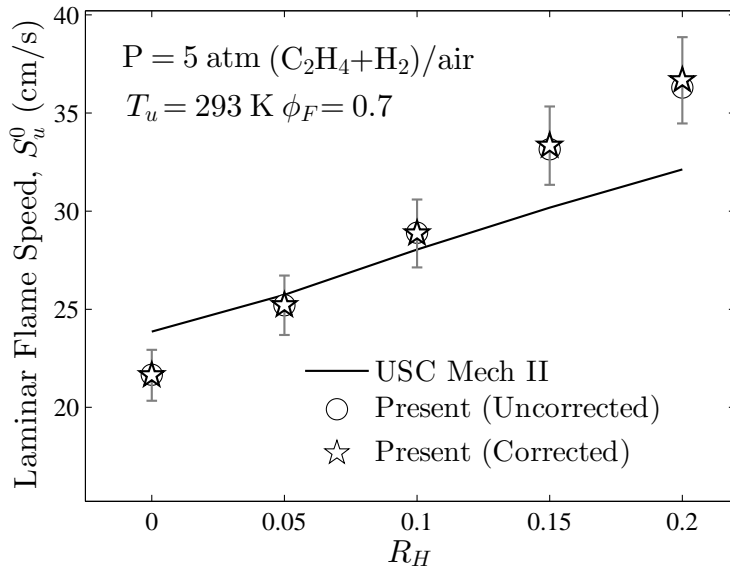


Figure 4.41: Present measurements of laminar flame speeds of hydrogen/ethylene/air mixtures at 5 atm and unburned gas temperature  $T_u = 293$  K, plotted against the predictions by the USC Mech II mechanism (Wang *et al.*, 2007).

## 4.7 Concluding Remarks

This chapter presented measured laminar flame speeds and Markstein lengths for a wide range of fuels: *n*-hexane, cyclic alkanes (with C<sub>6</sub> ring), butanol isomers, toluene, xylenes, and mixtures of H<sub>2</sub> with CO and C<sub>1</sub>-C<sub>3</sub> hydrocarbons. These archived data are useful for developing and validating chemical kinetic models.

Different from previously published data, the systematic error associated with stretch extrapolation is considered, and corrections based on the numerical computations presented in Chapter 3 were performed. These corrections cause the largest change for measurements at 1 atm, about 10%. Encouragingly, the corrected laminar flame speeds in many cases such as those on *n*-hexane, cyclo-alkanes and butanol isomers (except *t*-butanol at 1 atm) now agree well with previous measurements us-

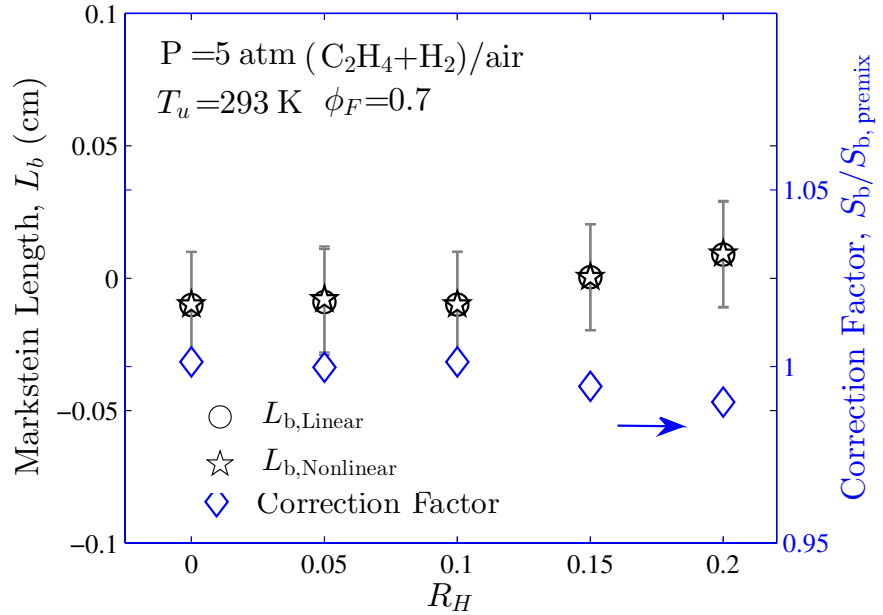


Figure 4.42: Present measurements of Markstein lengths and the calculated extrapolation correction factor based on Equation 3.14 corresponding to the  $S_u^0$  measurements plotted in Figure 4.41.

ing counterflow flames (Ji *et al.*, 2010, 2011; Veloo *et al.*, 2010; Veloo & Egolfopoulos, 2011).

This chapter discussed the comparison of the present measurements with previous ones and predictions of chemical kinetic models. The comparison of flame speeds between different fuels and the analysis of high-temperature flame chemistry of these fuels will be presented in Chapter 5.

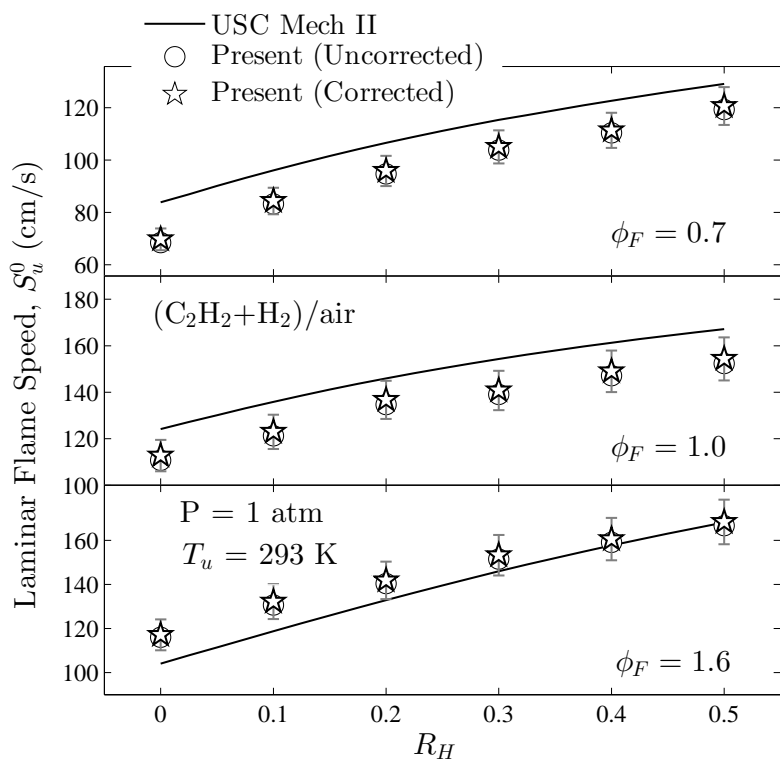


Figure 4.43: Present measurements of laminar flame speeds of hydrogen/acetylene/air mixtures at 1 atm and unburned gas temperature  $T_u = 293 \text{ K}$ , plotted against the predictions by the USC Mech II mechanism (Wang *et al.*, 2007).

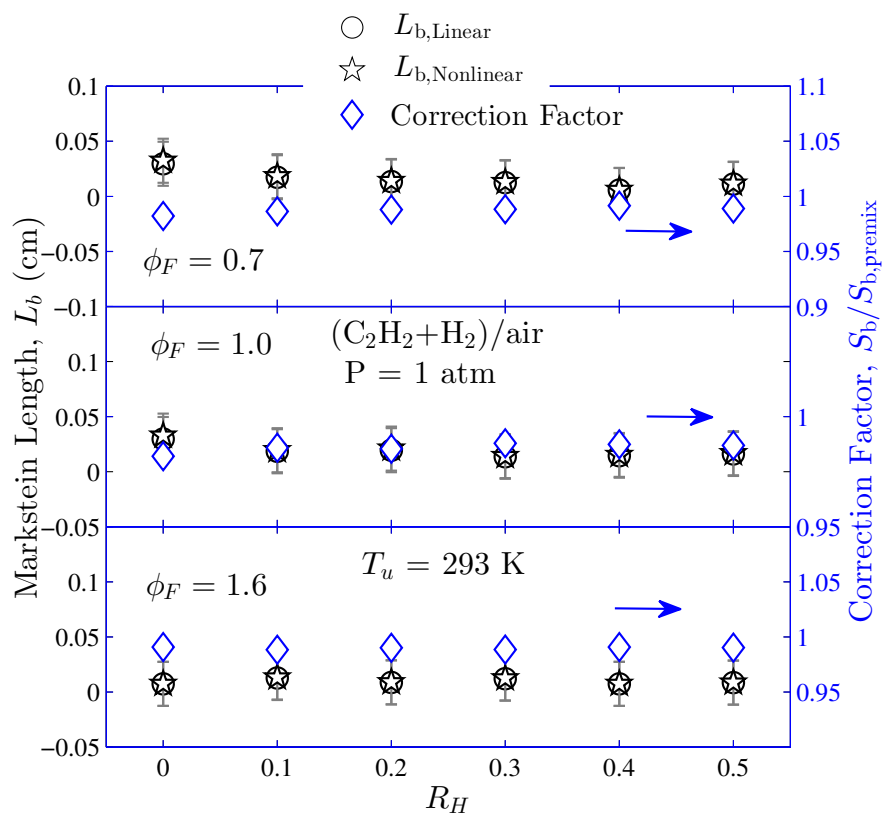


Figure 4.44: Present measurements of Markstein lengths and the calculated extrapolation correction factor based on Equation 3.14 corresponding to the  $S_u^0$  measurements plotted in Figure 4.43.

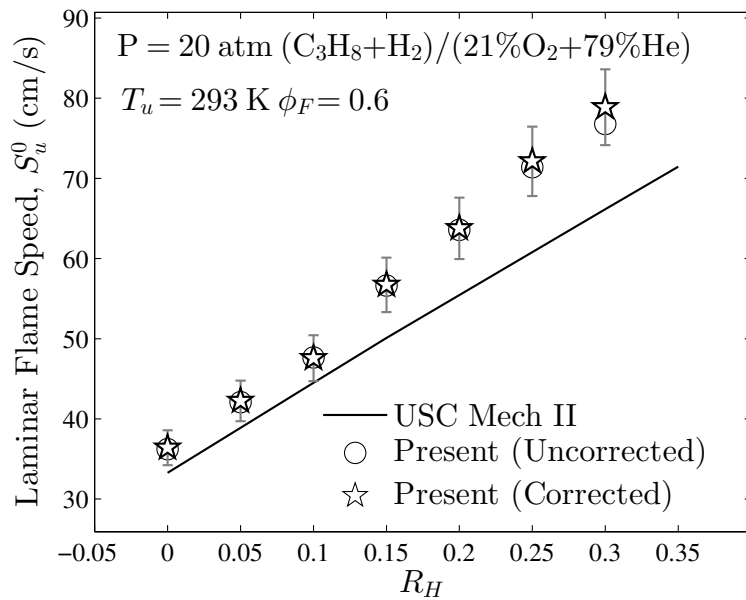


Figure 4.45: Present measurements of laminar flame speeds of lean hydrogen/propane/oxygen/helium mixtures at 20 atm and unburned gas temperature  $T_u = 293$  K, plotted against the predictions by the USC Mech II mechanism (Wang *et al.*, 2007).

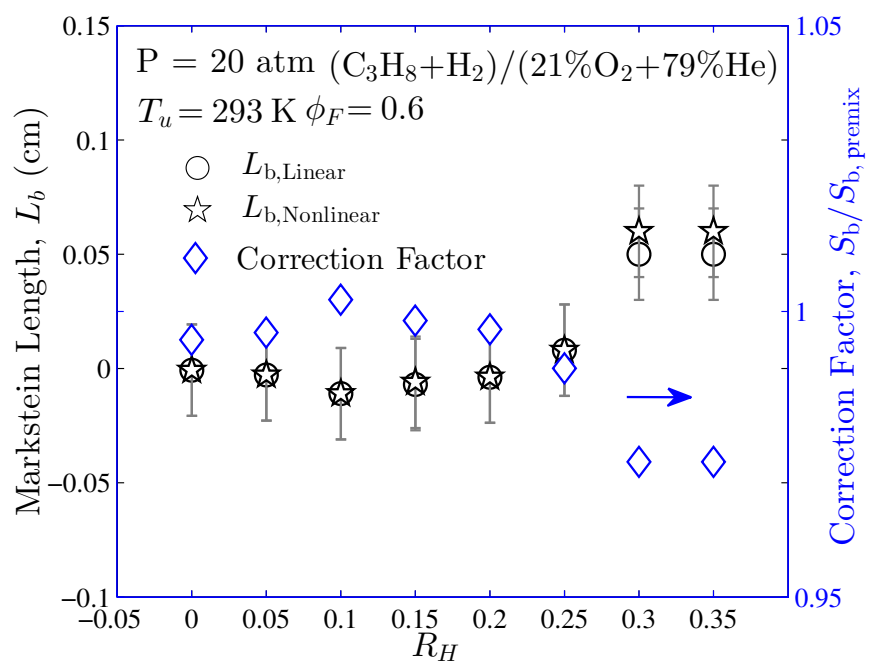


Figure 4.46: Present measurements of Markstein lengths and the calculated extrapolation correction factor based on Equation 3.14 corresponding to the  $S_u^0$  measurements plotted in Figure 4.45.

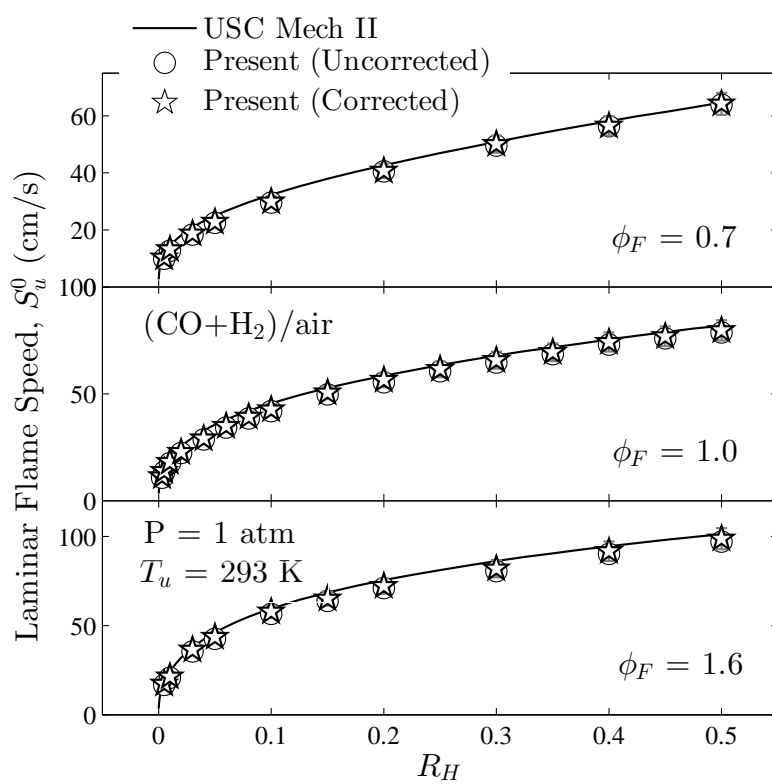


Figure 4.47: Present measurements of laminar flame speeds of  $\text{H}_2/\text{CO}/\text{air}$  mixtures at 1 atm and unburned gas temperature  $T_u = 293 \text{ K}$ , plotted against the predictions by the USC Mech II mechanism ([Wang \*et al.\*, 2007](#)).

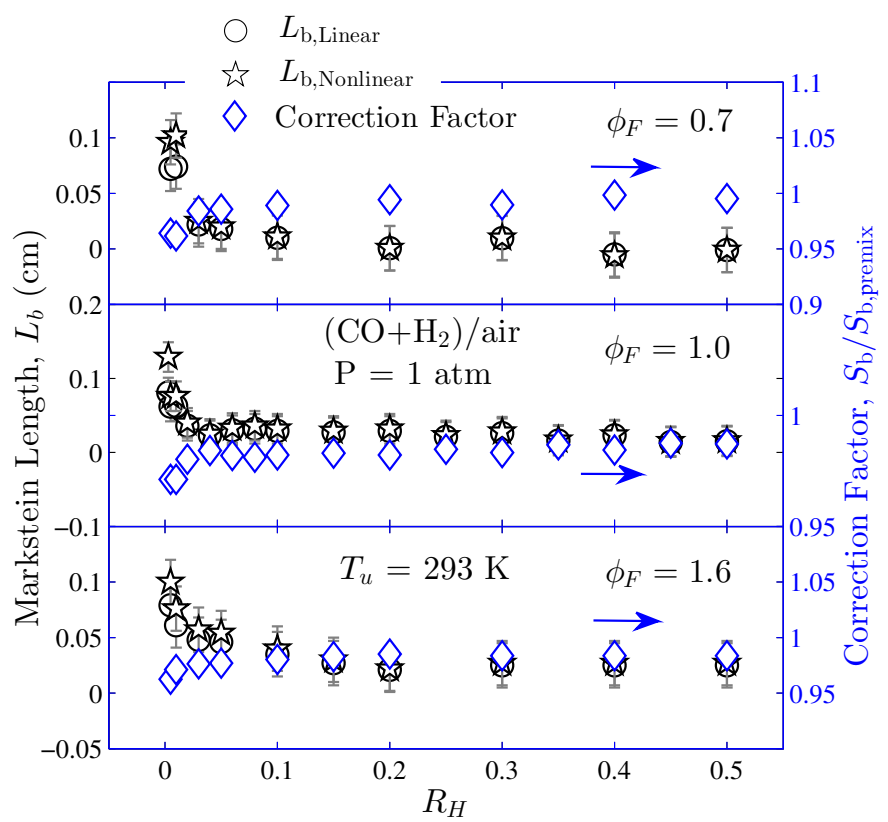


Figure 4.48: Present measurements of Markstein lengths and the calculated extrapolation correction factor based on Equation 3.14 corresponding to the  $S_u^0$  measurements plotted in Figure 4.47.

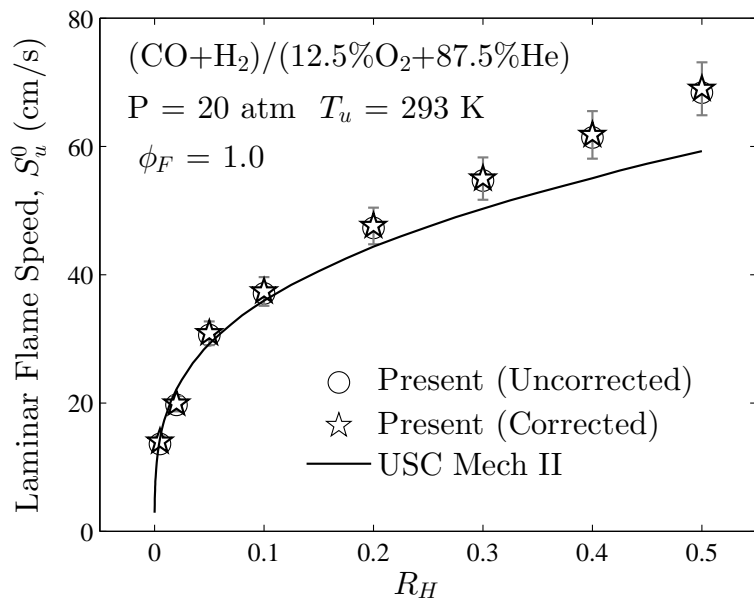


Figure 4.49: Present measurements of laminar flame speeds of lean  $H_2/CO/O_2/He$  mixtures at 20 atm and unburned gas temperature  $T_u = 293$  K, plotted against the predictions by the USC Mech II mechanism [Wang \*et al.\* \(2007\)](#).

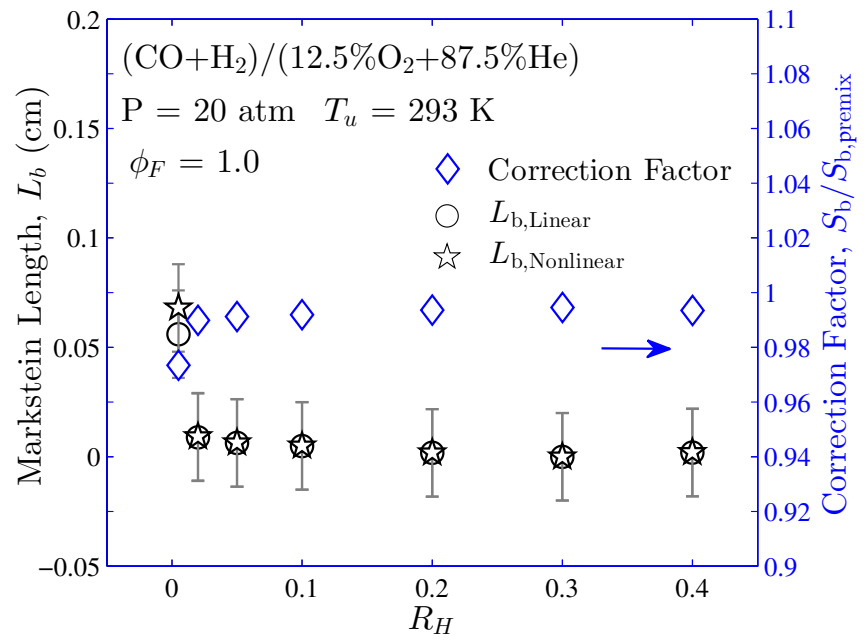


Figure 4.50: Present measurements of Markstein lengths and the calculated extrapolation correction factor based on Equation 3.14 corresponding to the  $S_u^0$  measurements plotted in Figure 4.49.

# Chapter 5

## Flame Chemistry of Large Molecule Fuels

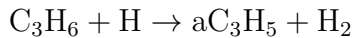
### 5.1 Introduction

The measured laminar flame speeds presented in Chapter 4 are useful for developing and validating the combustion chemistry of liquid hydrocarbon fuels and oxygenated biofuels. However, the combustion chemistry of large-molecule liquid fuels involves hundreds to thousands of intermediates and even larger numbers of reactions. It is a tedious and seemingly never-ending task to track all the reactions and pathways at a fundamental level. Therefore, it is equally important to study the chemical structure of these flames and then extract important insights and empirical rules for their flame chemistry, which are useful for the development of surrogates for practical transportation fuels and simplified modeling approaches.

A general feature of flames of large molecule fuels is that the fuel decomposes into intermediate fragments through H-abstraction followed by  $\beta$ -scission or direct

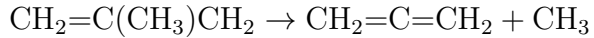
fuel decomposition reactions at rates much faster than the oxidation of these fuel fragments ([You et al., 2009](#)), which are mostly H<sub>2</sub>, CH<sub>4</sub> and C<sub>2</sub>-C<sub>4</sub> alkenes. As a result, large fuels do not enter the active oxidation zone directly, and it is the oxidation of the fuel fragments that determines the overall heat release rate and flame speed. In other words, the actual rates for the reactions describing the fuel cracking process are not important. Some recent reaction models for large molecule hydrocarbons have utilized this concept, which considered the detailed description of the oxidation of fuel fragments but only simplified description of the fuel cracking process which produces these fragments ([Zhang et al., 2007](#); [You et al., 2009](#); [Wang et al., 2010](#); [Ranzi et al., 2012](#)).

However, it is noted that although the rate of fuel cracking is not important in most cases, accurate predictions of the distribution of fuel fragments are still necessary, fuel fragments have very different reactivities in the oxidation process. For example, the CH<sub>4</sub> is stable due to its short C-H bond length while the C<sub>2</sub>H<sub>4</sub> is more reactive. In addition, as shown in USC Mech II ([Wang et al., 2007](#)) and [Ji et al. \(2012b\)](#), propene (C<sub>3</sub>H<sub>6</sub>) is also relatively stable compared to C<sub>2</sub>H<sub>4</sub> due to the following two reactions,



which is a termination mechanism for H radical. Furthermore, *iso*-butene (CH<sub>2</sub>=C(CH<sub>3</sub>)<sub>2</sub>) is more stable than 1-butene (CH<sub>2</sub>=CHCH<sub>2</sub>CH<sub>3</sub>) and 2-butene (CH<sub>3</sub>CH=CHCH<sub>3</sub>)

because the following two reactions,



result in  $\text{CH}_3$  (Wang *et al.*, 2007). Finally, acetone ( $\text{CH}_3\text{C}=\text{OCH}_3$ ) and *i*so-propenol ( $\text{CH}_2=\text{C}(\text{CH}_3)\text{OH}$ ) are also stable combustion intermediates in the oxidation of alcohols, for their further cracking produces propene ( $\text{C}_3\text{H}_6$ ) and  $\text{CH}_3$  (Sarathy *et al.*, 2012; Lefkowitz *et al.*, 2013).

Therefore, it is seen that, to understand the fuel molecule effects on flame speeds, it is important to analyze the distribution of the intermediate fragments that the fuel cracks into. For high temperature flame chemistry, the major fuel cracking pathways are direct single molecule decomposition and H-abstraction followed by  $\beta$ -scission. Therefore, it is relatively simple, and it is found in the present study that the geometry of the fuel molecule and the relative bond energies of C-H, C-C, C-O and O-H bonds play major roles.

In the present study, two groups of fuels were studied, *n*-hexane and the  $\text{C}_6$ -ring cyclo-alkanes (cyclohexane and mono-alkylated cyclohexanes) and the butanol isomers. These two groups of fuels are good candidates for studying flame chemistry because the fuels in each group have similar transport properties and almost equal heats of combustion such that the thermal and transport effects can be eliminated. The measured laminar flame speeds of each fuel in these two groups are presented in Chapter 4. In this chapter, these flame speeds will be first compared. Then the flame chemical structures are computed using the validated chemical kinetic models at the experimental conditions. Finally, the fundamental reason for the fuel

molecule effects on laminar flame speeds are discussed.

The results presented in this chapter have been previously published in the following journal articles ([Wu et al., 2012](#); [Wu & Law, 2013](#)):

- Wu, F., KELLEY, A. P. & LAW, C. K. 2012 Laminar flame speeds of cyclohexane and mono-alkylated cyclohexanes at elevated pressures. *Combustion and Flame* **159**, 1417–1425
- Wu, F. & LAW, C. K. 2013 An experimental and mechanistic study on the laminar flame speed, Markstein length and flame chemistry of the butanol isomers. *Combustion and Flame* **160**, 2744–2756

## 5.2 C<sub>6</sub>-ring Cyclo-alkanes

For *n*-alkanes, previous studies have shown that the laminar flame speeds of C<sub>5</sub>-C<sub>12</sub> alkanes ([Davis & Law, 1998](#); [Ji et al., 2010](#); [Kelley et al., 2011c](#)) are almost identical. The reason for this fuel similarity has been attributed ([Kelley et al., 2011c](#)) to the fact that *n*-alkanes all crack into similar small fragments (C<sub>0</sub>-C<sub>4</sub>) in flames due to their similar straight-chain molecular structure. For branched alkanes, it has been shown that the extent of fuel branching significantly reduces that laminar flame speeds ([Davis & Law, 1998](#); [Kelley et al., 2011b](#); [Ji et al., 2012b](#)), for branched alkanes crack into more stable intermediates such as CH<sub>4</sub>, propene and *iso*-butene. The effects of cyclic carbon chains in fuel molecule is yet to be studied.

In this section, the flame chemistry of the C<sub>6</sub> normal alkane, *i.e.*, *n*-hexane, and C<sub>6</sub>-ring cyclo-alkanes are compared and studied.

### 5.2.1 Comparison of Flame Speeds and Thermal Effects

Laminar flame speeds  $S_u^0$  determined in the present study (corrected for stretch extrapolation error, Chapter 4) of cyclohexane, methyl-cyclohexane and ethyl-cyclohexane determined from 1 to 20 atm in the present study are compared in Figures 5.1, 5.2 and 5.5. In order to compare with the straight chain C<sub>6</sub> counterpart, *n*-hexane, the measured  $S_u^0$ , uncorrected for stretch extrapolation error, are compared against the measurements of *n*-hexane by Kelley *et al.* (2011c) (which also does not have extrapolation error correction). The predictions of *n*-hexane, cyclohexane, methyl-cyclohexane and ethyl-cyclohexane at all these conditions by the JetSurF 2.0 mechanism (Wang *et al.*, 2010) are plotted in Figures 5.3, 5.4 and 5.5.

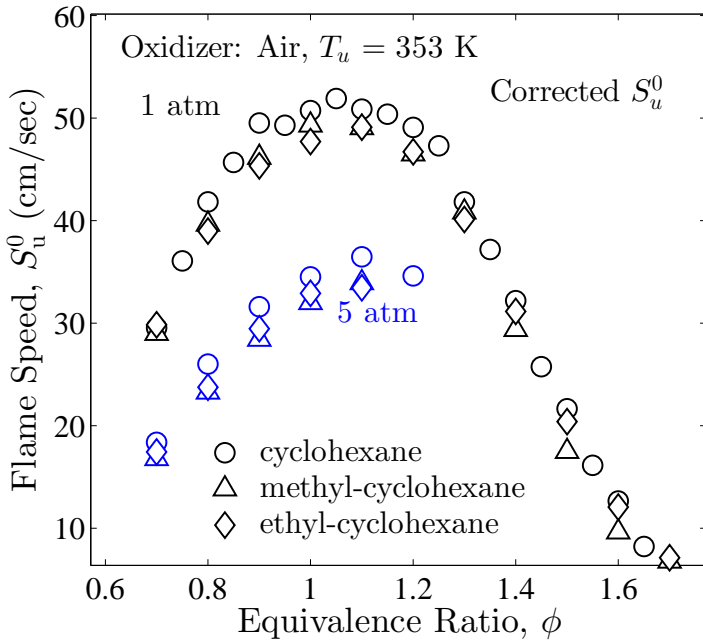


Figure 5.1: Comparison of measured  $S_u^0$  (corrected for extrapolation error) of cyclohexane, methyl-cyclohexane and ethyl-cyclohexane at 1 and 5 atm and an unburned gas temperature of 353 K. Experimental specifications are discussed in Chapter 4.

It is seen that while almost identical flame speeds were found for C<sub>5</sub>-C<sub>8</sub> alkanes

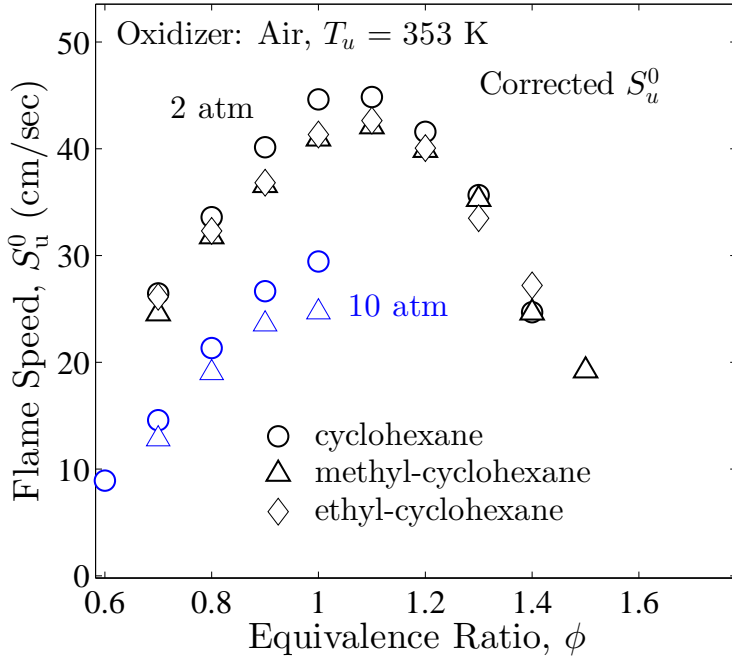


Figure 5.2: Comparison of measured  $S_u^0$  (corrected for extrapolation error) of cyclohexane, methyl-cyclohexane and ethyl-cyclohexane at 2 and 10 atm and an unburned gas temperature of 353 K. Experimental specifications are discussed in Chapter 4.

(Kelley *et al.*, 2011c), this is not the case for the cyclo-alkanes. Compared to *n*-hexane, the flame speeds of cyclohexane are uniformly higher, especially at elevated pressures. The laminar flame speeds of methyl-cyclohexane and ethyl-cyclohexane are almost identical to those of *n*-hexane. This result agrees with the trends found in Ji *et al.* (2011) at 1 atm.

As shown in Chapter 4 corrections for extrapolation error change  $S_u^0$  by approximately 10% at 1 atm depending on the equivalence ratio  $\phi$ . The corrections are much smaller at high pressures. Therefore, the corrections do not change the comparison of  $S_u^0$  for different fuels, *i.e.*, the trend discussed above is the same for corrected  $S_u^0$  and uncorrected  $S_u^0$ . In addition, from Figures 5.3, 5.4 and 5.5 it is

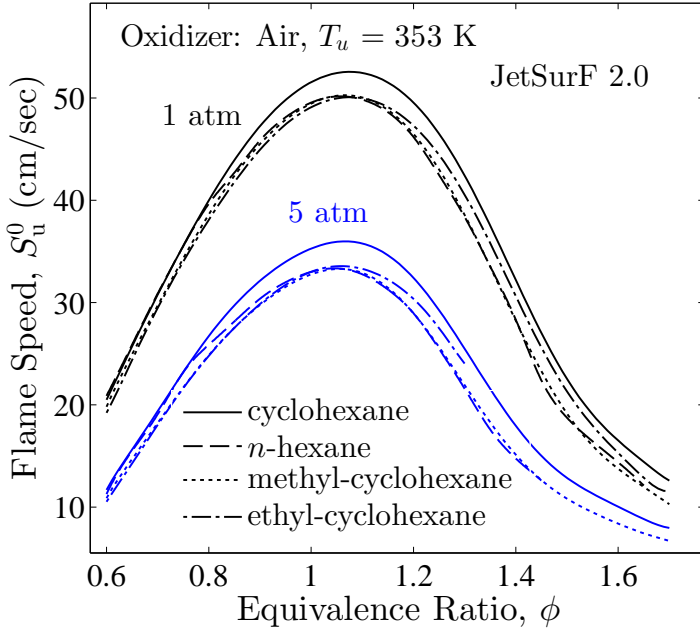


Figure 5.3: Predictions of  $S_u^0$  of  $n$ -hexane, cyclohexane, methyl-cyclohexane and ethyl-cyclohexane at 1 and 5 atm and an unburned gas temperature of 353 K by JetSurF 2.0 mechanism ([Wang \*et al.\* \(2010\)](#)).

seen that the same trend is also well captured by the predictions of JetSurF 2.0 mechanism.

To identify the pressure effects more clearly, the percentage difference in the maximum flame speed between different fuels in Figure 5.9 is plotted. It is seen that the difference in flame speeds between cyclohexane and  $n$ -hexane becomes larger as pressure increases. The percentage difference increases from approximately 2% to 10% as the pressure increases from 1 to 10 atm. The difference in flame speeds between  $n$ -hexane, methyl-cyclohexane and ethyl-cyclohexane, however, is insensitive to pressure, remaining at approximately 3% from 1 atm to 10 atm. Consequently, the difference in flame speeds between cyclohexane and its mono-alkylated counterparts increases from approximately 5% at 1 atm to 13% at 10

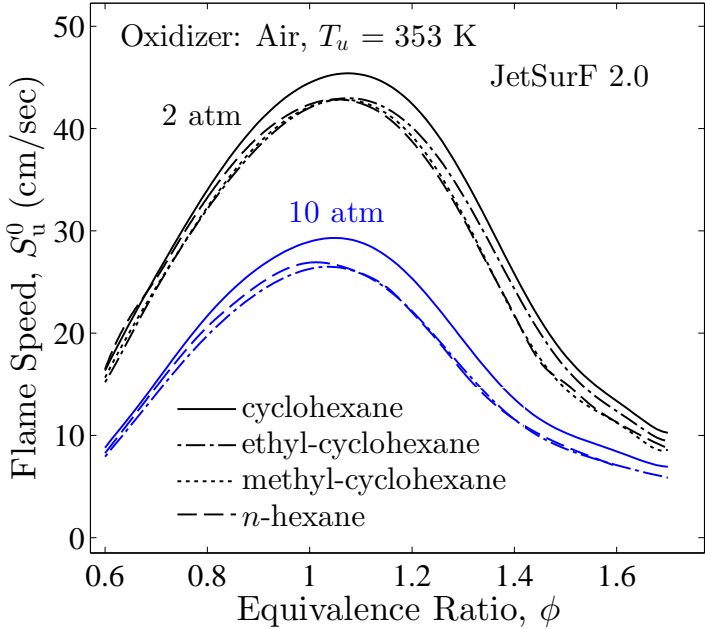


Figure 5.4: Predictions of  $S_u^0$  of  $n$ -hexane, cyclohexane, methyl-cyclohexane and ethyl-cyclohexane at 2 and 10 atm and an unburned gas temperature of 353 K by JetSurF 2.0 mechanism ([Wang \*et al.\* \(2010\)](#)).

atm.

To identify the effect of thermal properties of the fuels, Figure 5.10 plots the adiabatic flame temperature of the fuel/air mixtures at atmospheric pressure; the adiabatic flame temperatures at elevated pressures show the similar trend. It is seen that cyclohexane, methyl-cyclohexane and ethyl-cyclohexane have almost the same adiabatic flame temperature. However, the adiabatic flame temperature of  $n$ -hexane is lower than the other three fuels by approximately 10 K. This result is reasonable, for, while cyclohexane, methylcyclohexane and ethylcyclohexane have an C/H ratio of 0.5,  $n$ -hexane has the value of 0.43. Since all fuels in the present study do not have any double, C=C bond, the dominant parameter is then the C/H ratio, with flame temperature increasing with the C/H ratio.

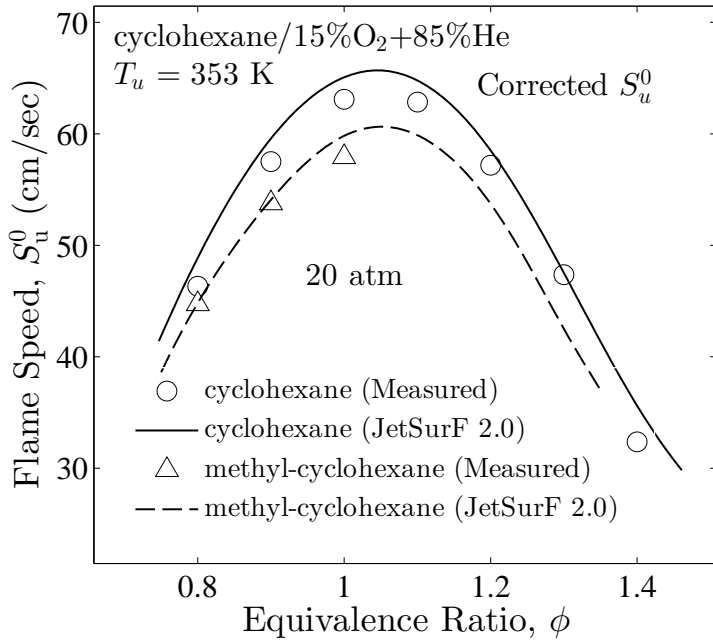


Figure 5.5: Comparison of measured  $S_u^0$  (corrected for extrapolation error) of *n*-hexane, cyclohexane, methyl-cyclohexane and ethyl-cyclohexane at 20 atm and an unburned gas temperature of 353 K. Experimental specifications are discussed in Chapter 4.

By numerically making the flame temperature of *n*-hexane equal to that of cyclohexane, achieved by substituting part of the inert, nitrogen, by argon, [Ji et al. \(2011\)](#) found that the resulting flame speed of *n*-hexane becomes basically the same as that of cyclohexane, hence implying that the cause of the difference in the flame speeds is thermal in nature. In view of this important insight, the investigation of [Ji et al. \(2011\)](#) are extended along two directions. First, the calculations using the same inert substitution method have been repeated, in which about 2.8 mole% of N<sub>2</sub> is substitute by Ar, and alternatively part of N<sub>2</sub> has also been replaced by O<sub>2</sub>, such that the O<sub>2</sub> concentration is increased from 21.0 to 21.2 mole%. Second, the investigation to pressures higher than 1 atm, which is the pressure studied in [Ji](#)

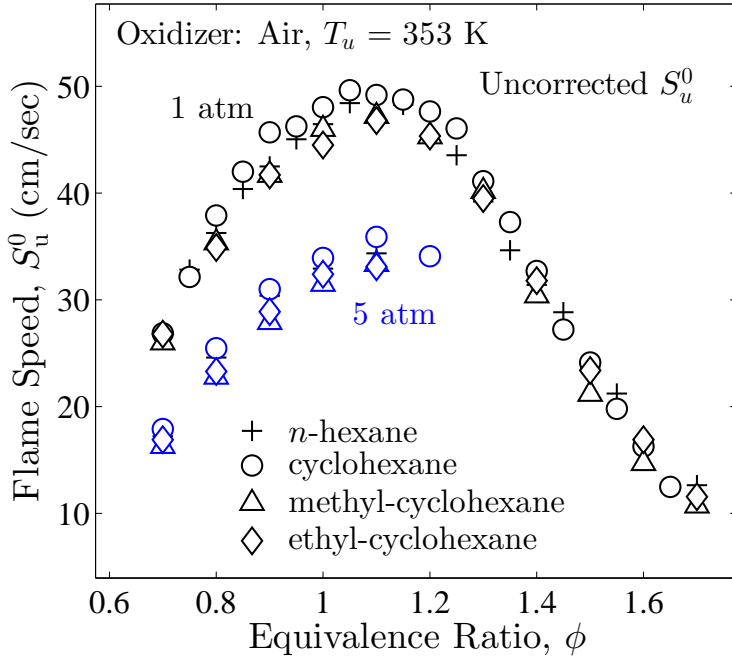


Figure 5.6: Comparison of measured  $S_u^0$  (uncorrected for extrapolation error) of cyclohexane, methyl-cyclohexane and ethyl-cyclohexane at 1 and 5 atm and an unburned gas temperature of 353 K plotted against the measurements of Kelley *et al.* (2011c) on *n*-hexane at the same condition. Experimental specifications are discussed in Chapter 4.

*et al.* (2011), have been performed.

Figure 5.9 shows that the increases in the flame speed using both methods of flame temperature matching are basically the same, providing mutual support to the validity of the two methods of flame-temperature matching. Furthermore, while the result substantiates that of Ji *et al.* (2011) at 1 atm, increasingly larger differences in the flame speeds of *n*-hexane and cyclohexane are observed as the pressure increases. For example, matching the flame temperatures at 10 atm increases the flame speed of *n*-hexane by only about 2%, such that the flame speed of cyclohexane is still 8% higher than that of *n*-hexane at this pressure. This result therefore suggests that

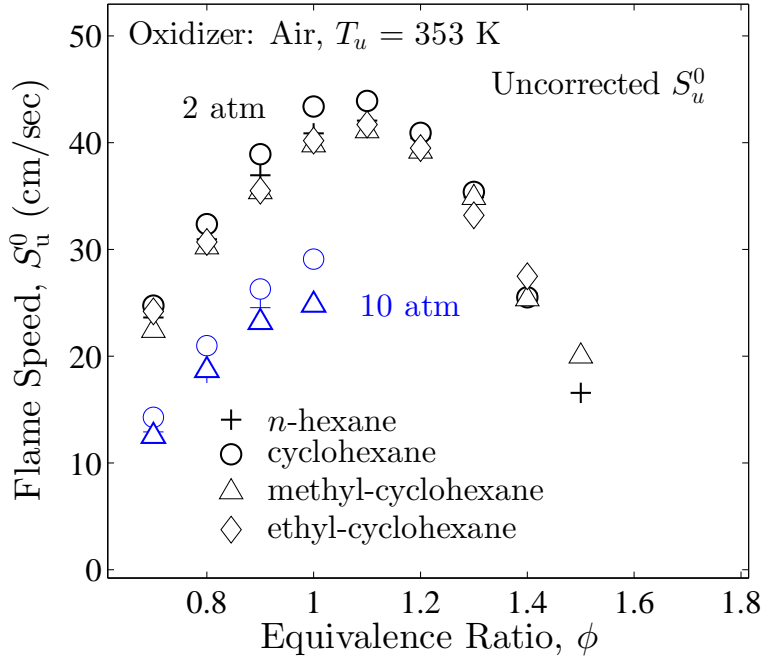


Figure 5.7: Comparison of measured  $S_u^0$  (uncorrected for extrapolation error) of cyclohexane, methyl-cyclohexane and ethyl-cyclohexane at 2 and 10 atm and an unburned gas temperature of 353 K plotted against the measurements of Kelley *et al.* (2011c) on *n*-hexane at the same condition. Experimental specifications are discussed in Chapter 4.

thermal effects cannot completely explain the difference in the flame speeds between *n*-hexane and cyclohexane.

It is also seen from Figure 5.10 that the difference in flame speeds between cyclohexane, methyl-cyclohexane and ethyl-cyclohexane is not caused by the thermal effect as these three fuels have almost identical adiabatic flame temperatures. All these results then lead us to investigate possible effects due to intrinsic chemical kinetics.

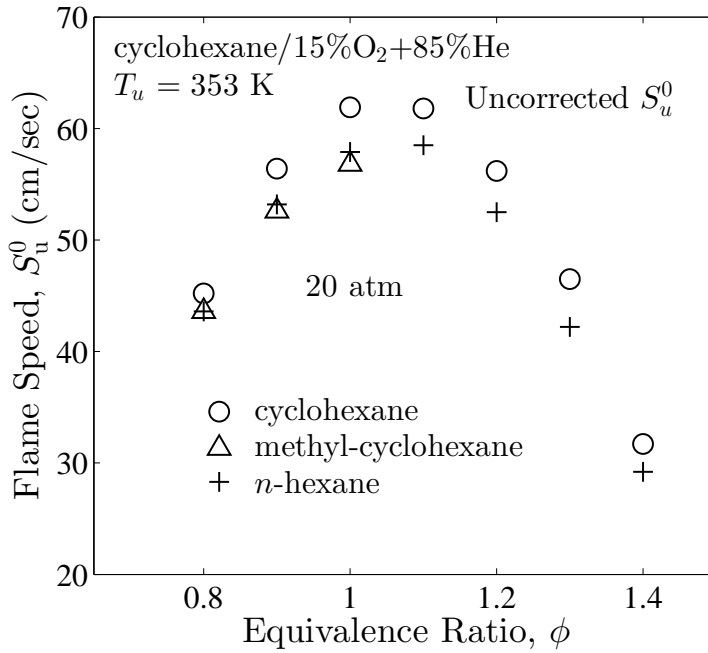


Figure 5.8: Comparison of measured  $S_u^0$  (uncorrected for extrapolation error) of cyclohexane, methyl-cyclohexane and ethyl-cyclohexane at 20 atm and an unburned gas temperature of 353 K plotted against the measurements of [Kelley et al. \(2011c\)](#) on  $n$ -hexane at the same condition. Experimental specifications are discussed in Chapter 4.

### 5.2.2 Analysis of Flame Chemistry

From the above analysis, it is seen that thermal effects cannot explain the higher flame speeds of cyclohexane compared to  $n$ -hexane, methyl- and ethyl-cyclohexane. In addition, the transport properties of the above fuels are similar to those of C<sub>6</sub>-C<sub>8</sub>  $n$ -alkanes, for which similar flame speeds have been found ([Kelley et al., 2011c](#)). Therefore, transport effects are also expected to be small. Consequently, chemical kinetics is expected to be the cause for the difference in flame speeds between fuels. Since JetSurf 2.0 mechanism yields fairly close agreement for different fuels in both the values and trends of the laminar flame speeds, it is justified to use the mechanism

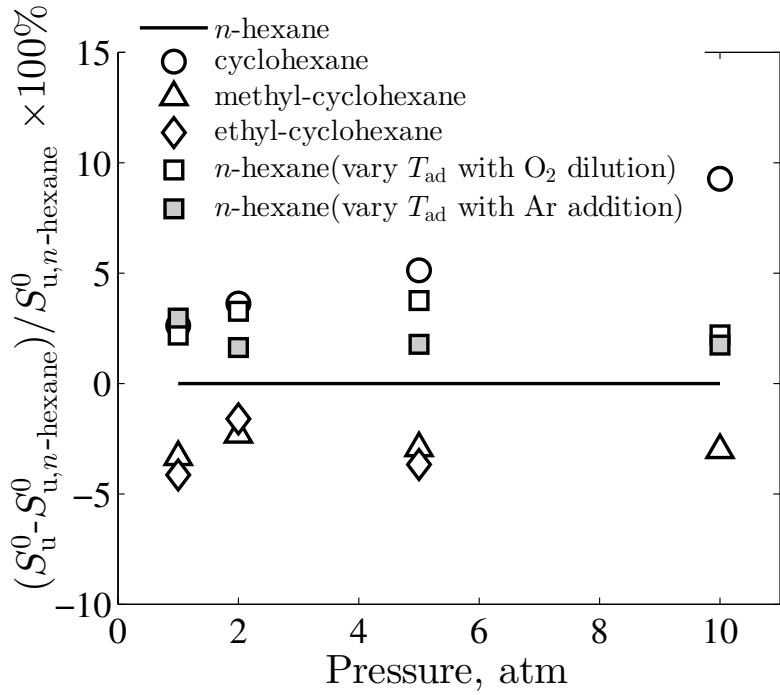


Figure 5.9: Difference in the maximum flame speed between *n*-hexane/air, cyclohexane/air, methyl-cyclohexane/air and ethyl-cyclohexane/air mixtures versus pressures with an unburned gas temperature of 353 K.

to examine the flame chemistry.

Figures 5.11 and 5.12 plot the temperature and heat release profiles for *n*-hexane, cyclohexane, methyl-cyclohexane and ethyl-cyclohexane for the 1-D premixed flames obtained from JetSurF 2.0 mechanism at 1 and 10 atm, and  $\phi = 1.0$ . It is seen that both the temperature and heat release profiles of *n*-hexane, methyl-cyclohexane and ethyl-cyclohexane are quite close, even though there is a slight difference in the flame temperatures at the equilibrium state. The temperature and heat release profiles of cyclohexane, however, deviate from those of the other three fuels. In particular, the temperature profile of cyclohexane is steeper than those of the other three fuels, corresponding to stronger heat release. In addition, the difference is intensified at 10 atm when compared to the case at 1 atm. As seen in Figures 5.11 and 5.12,

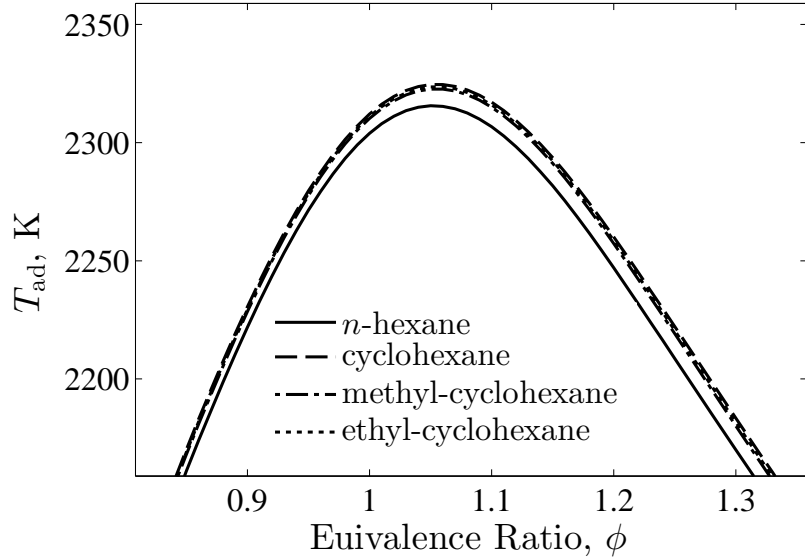


Figure 5.10: Comparison of adiabatic flame temperatures of *n*-hexane, cyclohexane, methyl-cyclohexane and ethyl-cyclohexane at atmospheric pressure. Thermodynamic data in JetSurF 2.0 mechanism ([Wang \*et al.\*, 2010](#)) was used in the calculation.

the heat release rate at 10 atm of cyclohexane is further increased. The maximum difference between the heat release rate of cyclohexane and the other fuels increases from 3% at 1 atm to 8% at 10 atm. With the adiabatic flame temperature being close, this difference in heat release clearly indicates a unique kinetic behavior of cyclohexane, compared to the other fuels.

As discussed at the beginning of this chapter, the initial fuel cracking process to form small fuel fragment, and the oxidation of these fuel fragments are largely decoupled. Furthermore, since the initial fuel cracking occurs much faster than the oxidation of the fuel fragments, the latter process mainly controls the heat release and eventually flame propagation. To verify this, sensitivity analysis of rate constants has been performed, and the results are shown in Figures 5.13, 5.14 and 5.15 for *n*-hexane/air, cyclohexane/air and methyl-cyclohexane/air mixtures at 1

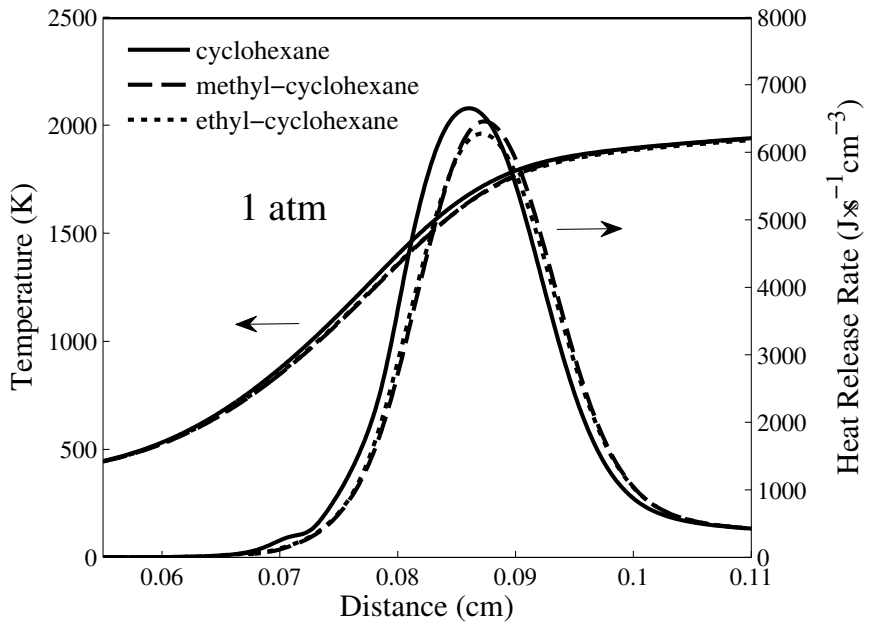


Figure 5.11: Temperature and heat release profiles for the 1-D planar flames of *n*-hexane/air, cyclohexane/air, methyl-cyclohexane/air and ethyl-cyclohexane/air at  $\phi = 1.0$ , 1 atm and an unburned gas temperature of 353 K, calculated with JetSurF 2.0 mechanism ([Wang \*et al.\*, 2010](#)).

and 10 atm. The normalized sensitivity coefficient  $k_i$  of a reaction  $i$  is defined as,

$$k_i = \frac{A_i}{S_u^0} \frac{\Delta S_u^0}{\Delta A_i} \quad (5.1)$$

where  $A_i$  is the pre-exponential factor of reaction  $i$ .

From Figures 5.13, 5.14 and 5.15 it is indeed seen that the flame speeds are mostly sensitive to the rate constants of those reactions involving the oxidation of C<sub>0</sub>-C<sub>4</sub> fuel fragments.

Using numerical simulation, [Ji \*et al.\* \(2011\)](#) attributed the difference between *n*-hexane and cyclohexane to thermal effects, *i.e.*, the small difference in the adiabatic

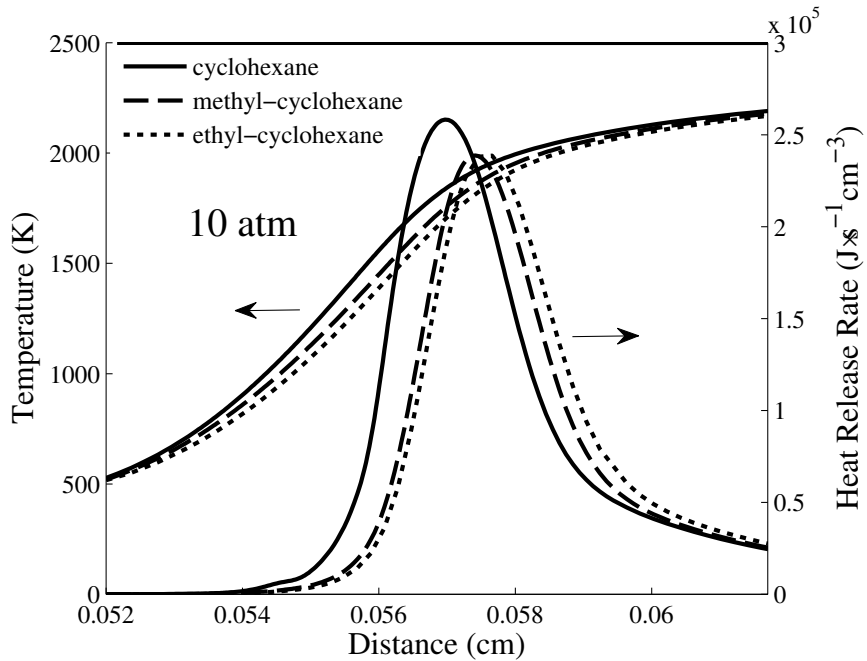


Figure 5.12: Temperature and heat release profiles for the 1-D planar flames of *n*-hexane/air, cyclohexane/air, methyl-cyclohexane/air and ethyl-cyclohexane/air at  $\phi = 1.0$ , 10 atm and an unburned gas temperature of 353 K, calculated with JetSurF 2.0 mechanism ([Wang et al., 2010](#)).

flame temperatures, and the difference between cyclohexane and its mono-alkylated derivatives to chemical kinetic effects caused by the change in the distribution of smaller molecules formed when the original fuel molecules decompose. In particular, mono-alkylated cyclohexane was found to form more propene while cyclohexane more 1,3-butadiene. The former would lead to chain terminating reactions while 1,3-butadiene would lead to chain branching, resulting in a lower flame speed for the mono-alkylated cyclohexanes compared to cyclohexane.

Figure 5.16 plots the profiles of the major C<sub>0</sub>-C<sub>4</sub> fuel fragments in the flames of stoichiometric *n*-hexane/air, cyclohexane/air and methyl-cyclohexane/air mixtures

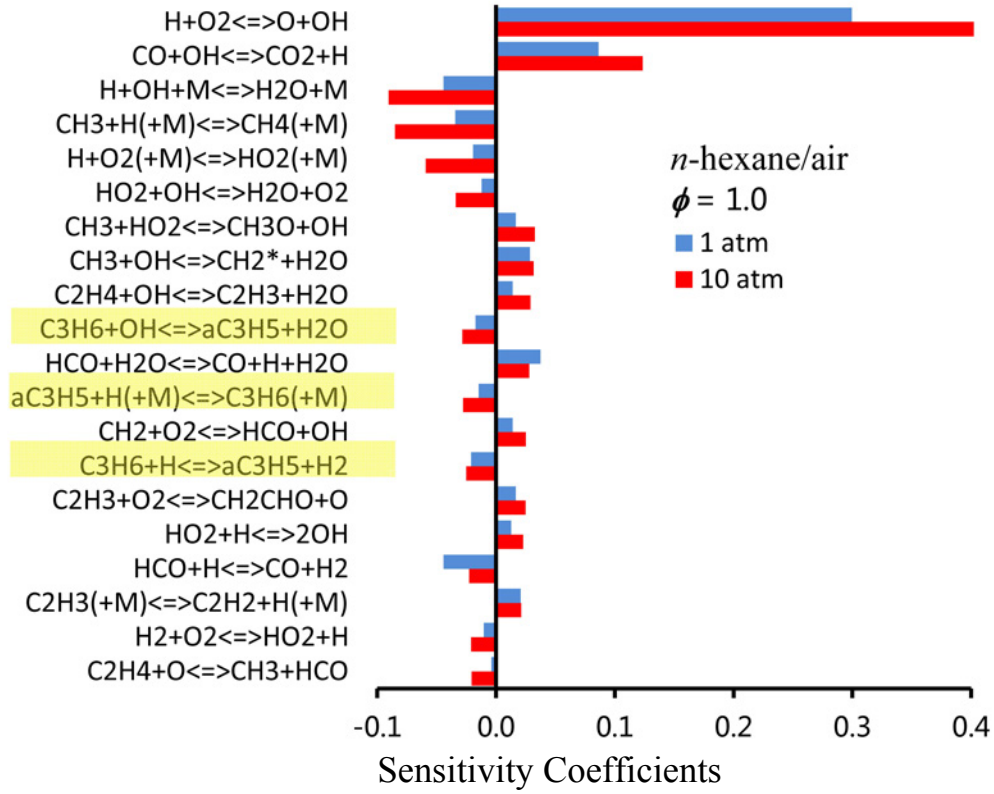


Figure 5.13: Normalized rate constant sensitivity coefficients on burning rate of *n*-hexane/air mixture, at  $P = 1, 10$  atm,  $\phi = 1.0$ , an unburned gas temperature of 353 K, calculated with JetSurF 2.0 mechanism (Wang *et al.*, 2010). The major different reactions from other fuels are highlighted in yellow.

at 10 atm. It is noted that the fragments not only have dominant concentrations but also participate in the important reactions identified through the sensitivity analysis. First, it is seen that the dissimilarity between different fuels increase as the carbon number of the intermediates increases from 0 to 4. In particular, the profiles of H, OH, O and CO of different fuels are very similar, while the profiles of  $CH_3$ ,  $CH_4$ ,  $C_2H_2$  and  $C_2H_4$  show some disparity but are still of the same order of magnitude. However, profiles of the major  $C_3$  and  $C_4$  intermediates, propene and 1,3-butadiene, show significant disparity between *n*-hexane, cyclohexane and methyl-cyclohexane.

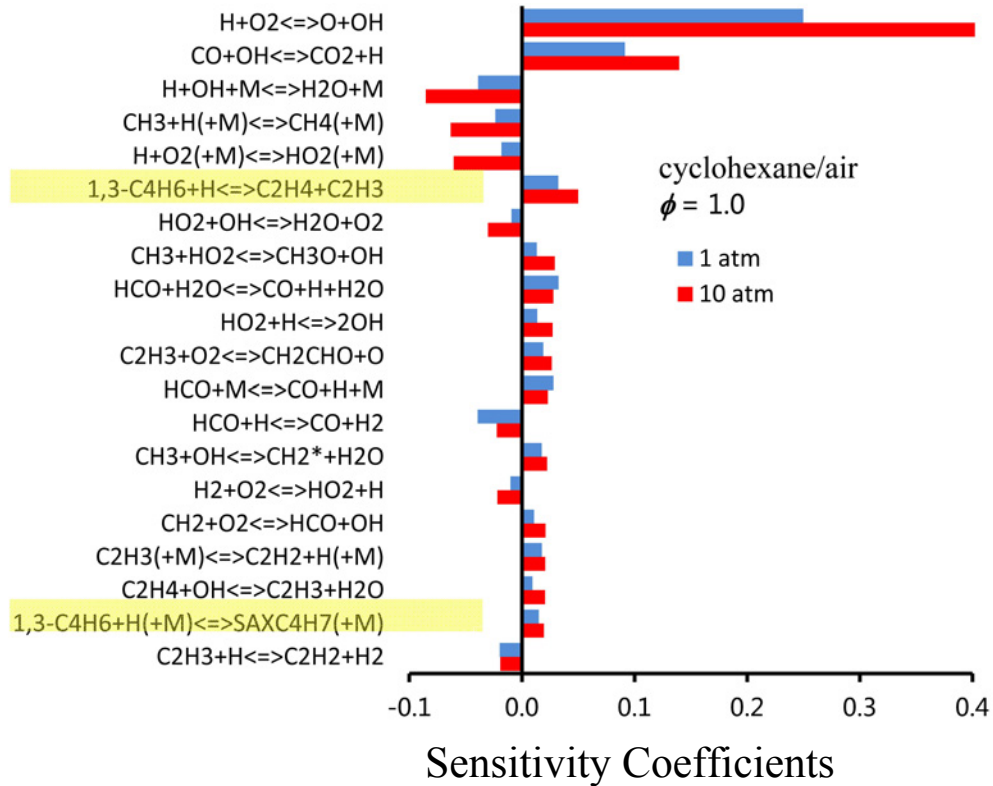


Figure 5.14: Normalized rate constant sensitivity coefficients on burning rate of cyclohexane/air mixture, at  $P = 1, 10 \text{ atm}, \phi = 1.0$ , an unburned gas temperature of 353 K, calculated with JetSurF 2.0 mechanism ([Wang et al., 2010](#)). The major different reactions from other fuels are highlighted in yellow.

Similar to what [Ji et al. \(2011\)](#) have found at atmospheric pressure, decomposition of cyclohexane forms considerably more 1,3-butadiene and less propene, compared to *n*-hexane and methyl-cyclohexane: the peak concentration of propene for cyclohexane is 30% and 40% of those for *n*-hexane and methyl-cyclohexane, while the peak concentration of 1,3-butadiene for cyclohexane is 19 and 2 times those for *n*-hexane and methyl-cyclohexane. This dominant difference between the fractions of 1,3-butadiene and propene is shown in the following discussion to be mostly responsible for the difference in the global burning rates observed both experimentally and

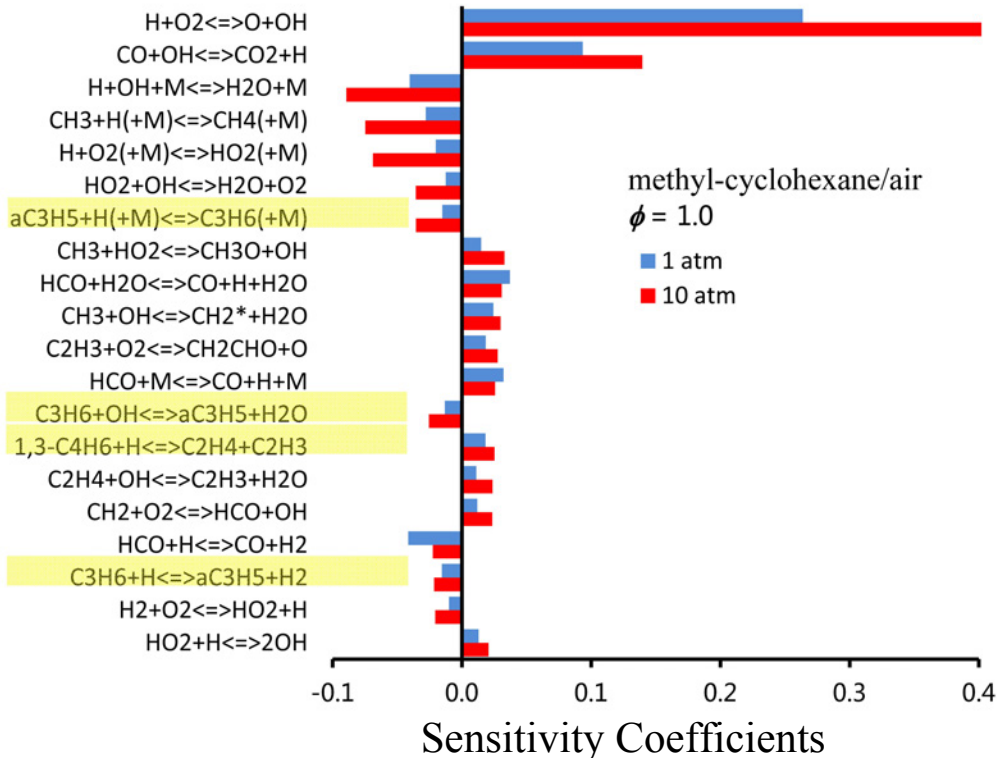
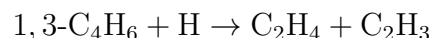


Figure 5.15: Normalized rate constant sensitivity coefficients on burning rate of methyl-cyclohexane/air mixture, at  $P = 1, 10$  atm,  $\phi = 1.0$ , an unburned gas temperature of 353 K, calculated with JetSurF 2.0 mechanism ([Wang et al., 2010](#)). The major different reactions from other fuels are highlighted in yellow.

numerically.

The intermediate 1,3-butadiene is reactive due to its subsequent decomposition breaks into  $C_2H_4$  and  $C_2H_3$  through



The reactivity of  $C_2H_4$  is high. The low reactivity of propene has already been

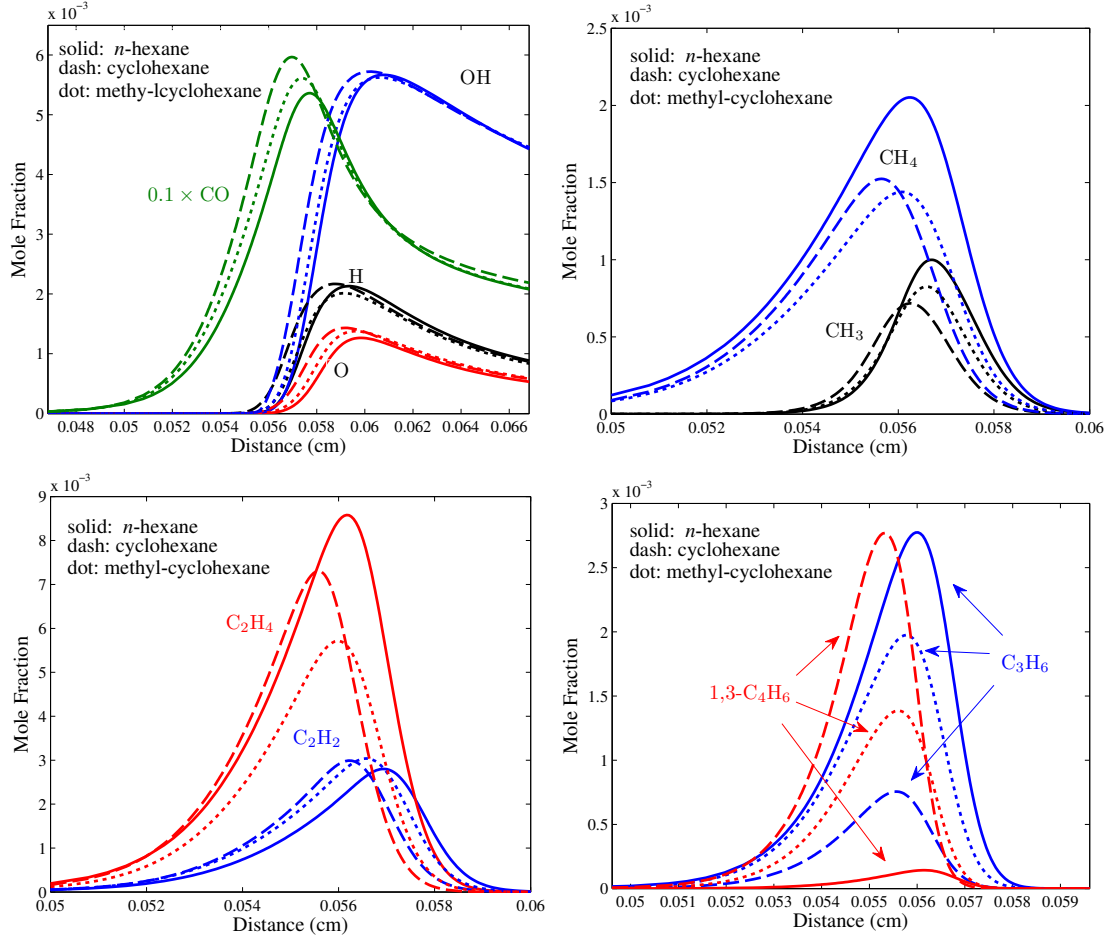
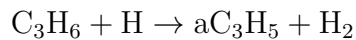


Figure 5.16: Profiles of major  $\text{C}_0\text{-}\text{C}_4$  intermediate fragments in the 1-D flames of *n*-hexane/air, cyclohexane/air and methyl-cyclohexane/air mixtures, at  $P = 10$  atm,  $\phi = 1.0$ , an unburned gas temperature of 353 K, calculated with JetSurF 2.0 mechanism ([Wang \*et al.\*, 2010](#)).

discussed at the beginning of this chapter, through the following two reactions:



The difference in the kinetic behavior between 1,3-butadiene and propene can also be seen from results of the sensitivity analysis in Figures 5.13, 5.14 and 5.15. Among the sensitivity coefficients for various reactions, it is seen that while, the reactions involving H, CO and C<sub>1</sub>-C<sub>2</sub> intermediates show similar importance for the three fuels, the major difference lies in the reactions involving 1,3-butadiene and propene. For *n*-hexane, the chain termination reactions involving propene and aC<sub>3</sub>H<sub>5</sub> exhibit a notable influence, and as expected the influence is negative. For cyclohexane, however, none of the important reactions involve propene and aC<sub>3</sub>H<sub>5</sub>. This is because, in the flames of cyclohexane, there are not as many C<sub>3</sub> intermediates as in the flames of *n*-hexane; therefore the corresponding propene and aC<sub>3</sub>H<sub>5</sub> reactions are not the rate-limiting steps anymore. Instead, the chain branching reactions involving 1,3-butadiene exhibit a notable positive influence, which is due to the high concentration of 1,3-butadiene in the flames of cyclohexane. Finally, for methyl-cyclohexane the sensitivity coefficients appear different from that for cyclohexane: the reactions involving propene and aC<sub>3</sub>H<sub>5</sub> become important again, corresponding to a relatively higher concentration of propene in the flames of methyl-cyclohexane. From the above results, it is therefore concluded that the higher flame speeds of cyclohexane as compared to those of the other fuels is due to its respectively higher and lower fractions of C<sub>3</sub> and C<sub>4</sub> species among all intermediates.

From Figures 5.13, 5.14, 5.15 and 5.16, it is also seen that the different dis-

tribution of C<sub>3</sub>-C<sub>4</sub> intermediates can explain the pressure effect seen in the heat release profiles and the laminar flame speeds. From sensitivity analysis, it is seen that the reactions involving C<sub>3</sub>-C<sub>4</sub> intermediates all have higher sensitivity coefficients at 10 atm compared to their values at 1 atm. This is because, as pressure increases, there are more chain terminating third-body reactions, such as  $a\text{C}_3\text{H}_5 + \text{H} + \text{M} \rightarrow \text{C}_3\text{H}_6 + \text{M}$ . This fact aggravates the sensitivity of the dependence of the overall burning rate on the fuel fragment distribution. For example, considering the reactions  $a\text{C}_3\text{H}_5 + \text{H} + \text{M} \rightarrow \text{C}_3\text{H}_6 + \text{M}$  and  $a\text{C}_3\text{H}_5 + \text{H} \rightarrow a\text{C}_3\text{H}_4 + \text{H}_2$ , calculation with JetSurF 2.0 shows that the ratio of the maximum reaction rates of the two reactions respectively increase from 7.2 at 1 atm, to 8.1 at 5 atm, and 8.5 at 10 atm.

By attributing the higher flame speeds of cyclohexane to the fact that it cracks into fewer C<sub>3</sub> intermediates, the reason as why it is so and why mono-alkylated cyclohexanes behave differently is discussed next. The phenomenon can be explained by the  $\beta$ -scission rule, which is largely applicable in the high-temperature decomposition of radicals. The rule states that the C-C bond that most likely breaks is one position removed from the radical site. Figures 5.17 and 5.18 show the reaction path for the ring opening and subsequent cracking of cyclohexane and methylcyclohexane under the dominant rule of  $\beta$ -scission. As shown in Figure 5.17, due to the symmetric structure of the cyclohexane molecule, ring opening of the cyclohexyl radical via  $\beta$ -scission occurs in two identical places, leading to the same intermediate: CH<sub>2</sub>=CH-CH<sub>2</sub>-CH<sub>2</sub>-CH<sub>2</sub>-CH<sub>2</sub>\*. According to the  $\beta$ -scission rule, the radical CH<sub>2</sub>=CH-CH<sub>2</sub>-CH<sub>2</sub>-CH<sub>2</sub>-CH<sub>2</sub>\* also undergoes chain breaking at only one position because the radical site is at the end, which produces C<sub>2</sub>H<sub>4</sub> and a CH<sub>2</sub>=CH-CH<sub>2</sub>-CH<sub>2</sub>\* radical. It is therefore seen that the decomposition of cyclohexane clearly

favors C<sub>2</sub> and C<sub>4</sub> over the C<sub>3</sub> fragments according to the  $\beta$ -scission rule.

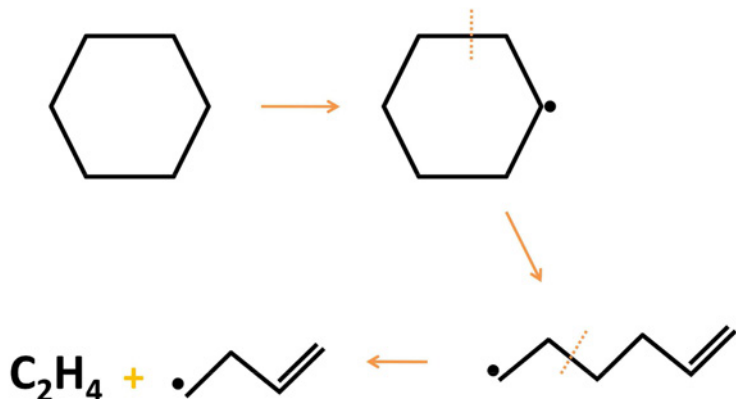


Figure 5.17: Initial ring opening and subsequent cracking of cyclohexane at high temperature assuming the rule of  $\beta$ -scission dominates fuel cracking.

On the other hand, the ring opening and subsequent cracking of methyl-cyclohexane and ethyl-cyclohexane is rather complicated because the presence of the alkyl group breaks the symmetry and leads to a branched carbon structure. For methyl-cyclohexane, there are five isomers of methyl-cyclohexyl radicals, differentiated by their positions relative to the methyl group. Having the five isomers, even assuming the dominant  $\beta$ -scission rule, as shown in Figure 5.18 there are still various possible ways of ring opening and subsequent cracking, leading to various C<sub>3</sub>, straight C<sub>4</sub> and branched C<sub>4</sub> fuel intermediates. Indeed, as shown in Figure 5.16, the distribution of C<sub>3</sub>-C<sub>4</sub> intermediates in the flames of methyl-cyclohexane is more balanced compared to those in the flames of *n*-hexane and cyclohexane.

Admittedly, there are reactions other than  $\beta$ -scission, such as isomerization, dehydrogenation, addition, *etc.* However, since the purpose here is to identify the dominant factor affecting the higher reactivity of cyclohexane, other type of reactions are not plotted in Figures 5.17 and 5.18. For example, the radical CH<sub>2</sub>=CH-CH<sub>2</sub>-CH<sub>2</sub>-

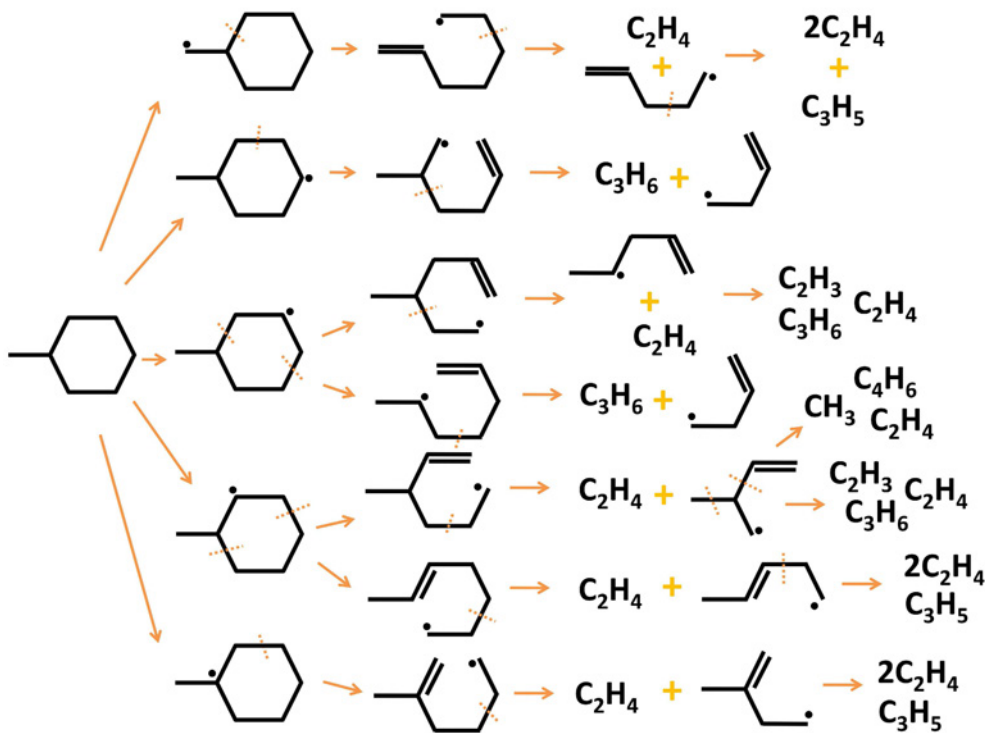


Figure 5.18: Initial ring opening and subsequent cracking of methylcyclohexane at high temperature assuming the rule of  $\beta$ -scission dominates fuel cracking.

$\text{CH}_2\text{-CH}_2^*$  can also undergo an important isomerization reaction, producing the  $\text{CH}_2=\text{CH-CH}^*\text{-CH}_2\text{-CH}_2\text{-CH}_3$  radical. However, the new radical  $\text{CH}_2=\text{CH-CH}^*\text{-CH}_2\text{-CH}_2\text{-CH}_3$  also has only one option for further  $\beta$ -scission due to the presence of the double bond, which produces 1,3-butadiene and  $\text{C}_2\text{H}_5^*$ . This further explains the higher reactivity of cyclohexane.

### 5.3 Butanol Isomers

The laminar flame speeds of all four butanol isomers were individually presented in Chapter 4. This is another set of fuels that is suitable for studying the effects

of fuel molecule geometry on their oxidation chemistry and laminar flame speeds since they are isomers and thus have similar transport and thermal properties. As will be shown next, the difference between the heat of combustion of butanol isomers is not enough to cause the large difference in their laminar flame speeds.

The goal here is to understand alcohol fuel molecule structure on flame chemistry from two recently updated butanol models, the LLNL model ([Sarathy et al., 2012](#)) and the PoliMi model ([Ranzi et al., 2012](#)), both of which agree reasonably well with the present experimental data. First, the differences in the reaction pathways between these two models are discussed. Next, the fundamental reasons for the differences between the flame speeds of butanol isomers are investigated, which are useful to arrive at empirical rules for the reactivities of alcohol fuels and seek simplified modeling approaches.

### 5.3.1 Comparison of Flame Speeds and Thermal Effects

Laminar flame speeds  $S_u^0$  determined in the present study (corrected for stretch extrapolation error, Chapter 4) for the four butanol isomers from 1 to 5 atm are compared Figures [5.19](#), [5.20](#) and [5.21](#).

It is seen that *n*-butanol has the highest flame speeds at all pressures, followed by *s*-butanol and *i*-butanol, and then *t*-butanol which has the lowest flame speeds. The experiments indicate that the flame speed difference between *s*-butanol and *i*-butanol is only 1% for all conditions, which is less than the experimental uncertainty. The flame speed difference between *n*-butanol and *i*-butanol (or *s*-butanol) is 7% at 1 atm and 11% at 5 atm, while the difference between *n*-butanol and *t*-butanol is 22% at 1 atm and 32% at 5 atm. The present experiment shows the following trend for the flame speeds of the four butanols:  $n\text{-butanol} > s\text{-butanol} \approx i\text{-butanol}$

$> t$ -butanol. This trend remains the same as pressure increases from 1 to 5 atm.

The predicted laminar flame speeds for the four butanol isomers by the LLNL butanol models (Sarathy *et al.*, 2012) at 1 atm are also compared in Figure 5.22. A similar trend is seen in the comparison with experimental data.

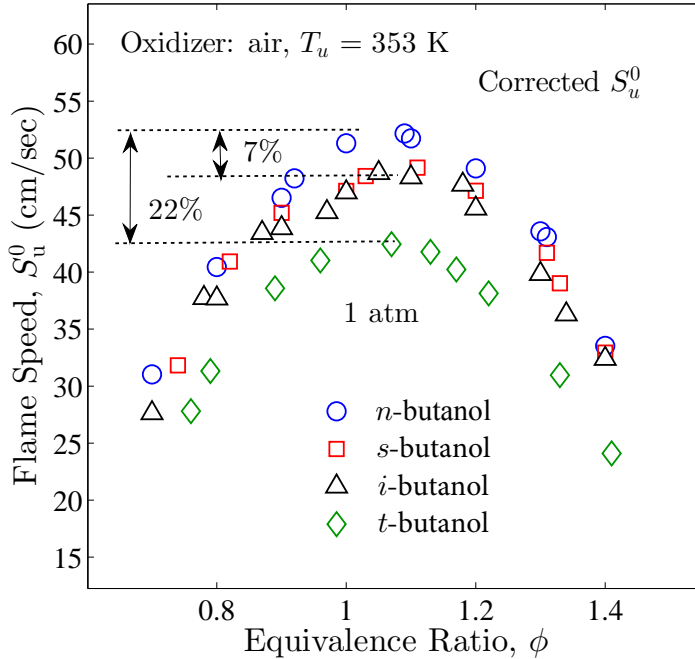


Figure 5.19: Comparison of measured  $S_u^0$  (corrected for extrapolation error) of four butanol isomers at 1 atm at an unburned gas temperature of 353 K with air as oxidizer. Experimental specifications are discussed in Chapter 4.

To investigate the contribution of heat of combustion, Figure 5.23 plots the adiabatic flame temperatures of the four isomers at 1 and 5 atm. It is seen that *n*-butanol has the highest adiabatic flame temperature, followed by *s*-butanol, *i*-butanol and then *t*-butanol. However, the differences among them are small. Specifically, the difference between *t*-butanol and *n*-butanol is around 20 K at lean and stoichiometric conditions and around 30 K on the rich side. To quantify the effect of such a difference, additional cases were calculated for *t*-butanol/air at 1 atm with the

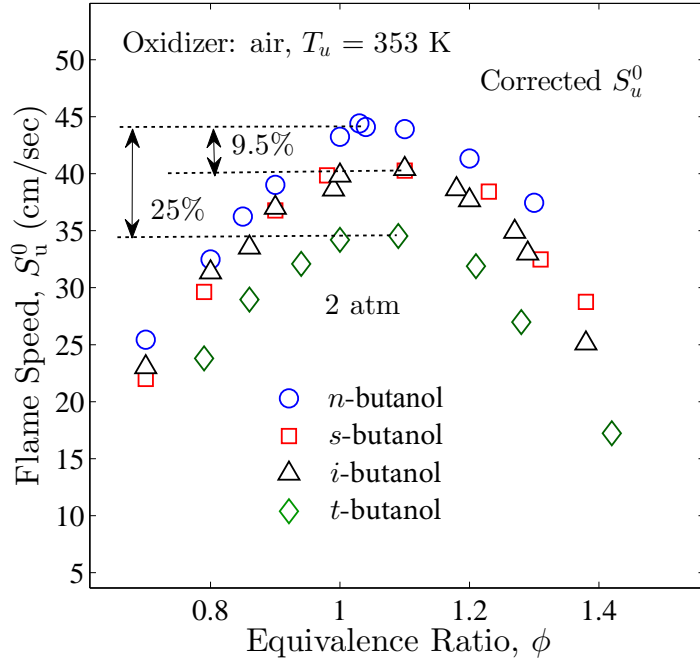


Figure 5.20: Comparison of measured  $S_u^0$  (corrected for extrapolation error) of four butanol isomers at 2 atm at an unburned gas temperature of 353 K with air as oxidizer. Experimental specifications are discussed in Chapter 4.

adiabatic flame temperature increased to that of *n*-butanol/air by slightly reducing the nitrogen concentration. The calculated results are plotted in Figure 5.22. It is seen that the increase in the flame speed by this temperature adjustment is about 2 cm/sec, which is only 1/5 of the difference between the calculated flame speeds of *n*-butanol and *t*-butanol. This indicates that flame temperature is not the main reason for the flame speed difference among the isomers.

### 5.3.2 Analysis of Flame Chemistry

From the above analysis, it is seen that the differences between the flame speeds of butanol isomers are clearly due to their chemical reactivities. Since both the LLNL butanol model ([Sarathy et al., 2012](#)) and the PoliMi model ([Ranzi et al.,](#)

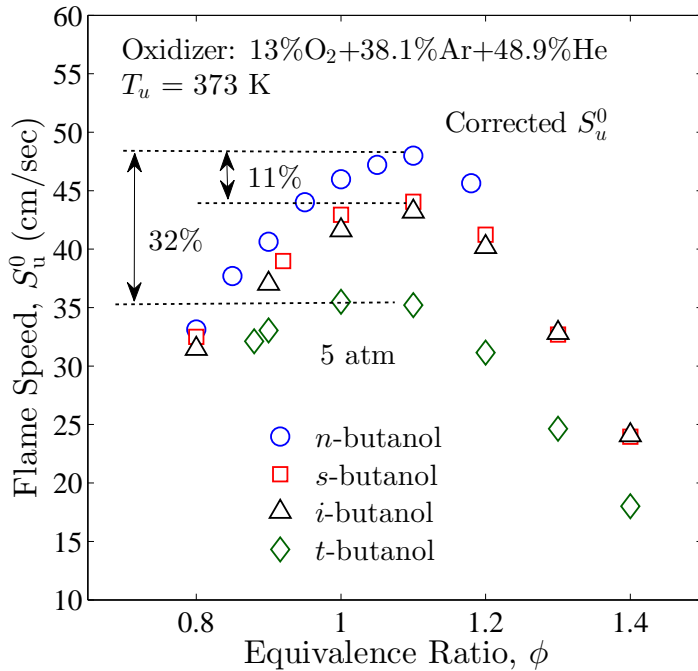


Figure 5.21: Comparison of measured  $S_u^0$  (corrected for extrapolation error) of four butanol isomers at 5 atm at an unburned gas temperature of 373 K a mixture of Ar and He as bath gas (molar ratio: O<sub>2</sub>%:Ar%:He% = 13%:38.1%:48.9%) as oxidizer. Experimental specifications are discussed in Chapter 4.

2012) yields fairly close agreement with the present experimental data in both the values and trends, they will be used to study their flame structure and examine the flame chemistry next.

Figures 5.24 and 5.25 plot the temperature and heat release profiles of the one-dimensional planar flames for the isomers at 1 and 5 atm, calculated by using the LLNL butanol model, respectively. It is seen from that the flame temperatures upstream and downstream of the flame zone for the four flames are almost identical while they differ significantly within the flame zone. This means that the total heat release is the same for all fuels while the heat release rate differs. It again indicates that the flame speed difference among the butanol isomers is not purely a thermal

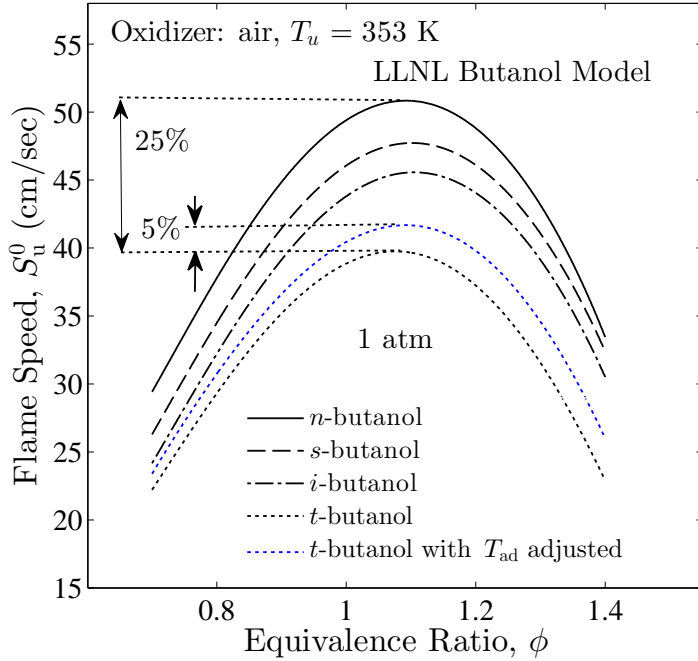


Figure 5.22: Predicted laminar flame speeds of four butanol isomers at 1 atm with air as oxidizer at an unburned gas temperature of 353 K by the LLNL butanol model (Sarathy *et al.*, 2012). “with  $T_{ad}$  adjusted” means the temperature of *t*-butanol has been adjusted to that of *n*-butanol by slightly reducing the nitrogen concentration from 79%.

effect. In addition, it is seen that with the LLNL butanol model, *n*-butanol has the highest heat release rate, followed by *s*-butanol, *i*-butanol and then *t*-butanol. The different ordering in the heat release profiles calculated with both mechanisms is consistent with their different predictions of the laminar flame speed. Finally, it is seen that, as pressure increases from 1 atm to 5 atm the difference among the heat release rates of different isomers also increases. This is also consistent with the pressure effect on the laminar flame speed.

To investigate the kinetic effects, sensitivity analysis of the rate constants is first conducted, recognizing that reactions with high sensitivity on the flame speed are rate limiting. Figures 5.26 and 5.27 plot the normalized rate constant sensitivity

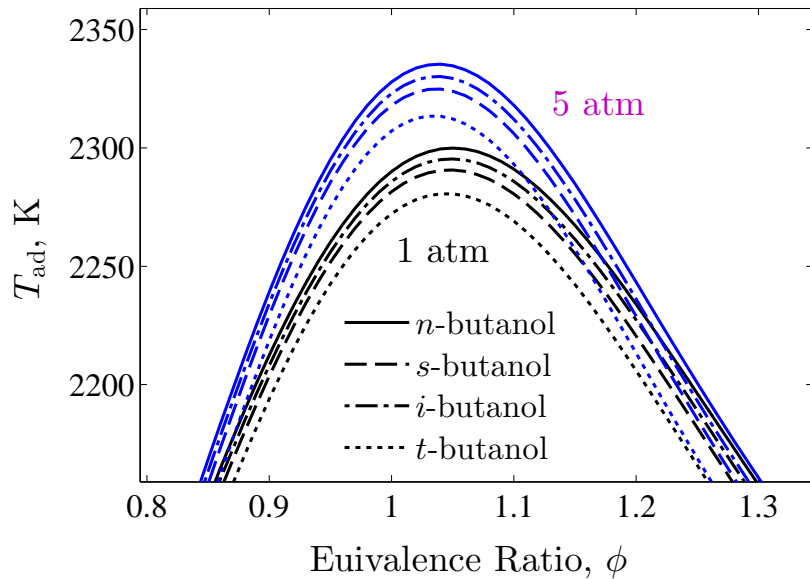


Figure 5.23: Computed adiabatic flame temperature  $T_{ad}$  of four butanol isomers at 1 and 5 atm, with air as oxidizer at an unburned gas temperature of 353 K. Thermal properties included in the LLNL butanol model ([Sarathy et al., 2012](#)) are used for the calculation.

coefficients (defined in Equation 5.1) for all isomers at 1 atm and 5 atm of the simulations using the LLNL butanol model and the PoliMi model, respectively. First, it is seen that in all cases for all isomers, the flame speed is most sensitive to the kinetics of hydrogen, carbon monoxide, and the small hydrocarbons. The fuel specific reactions are not rate limiting except for a few reactions for *t*-butanol. This heightened sensitivity on hydrogen and small hydrocarbon kinetics is similar to many other heavy hydrocarbons such as *n*-alkane and cyclo-alkanes, indicating that there is no fundamental difference between the kinetics of butanol isomers including *t*-butanol with that of the other heavy hydrocarbons. For *t*-butanol the reaction  $iC_4H_8 \rightarrow iC_4H_8 + H_2$  shows a small sensitivity at 1 atm in the the LLNL butanol model, and the *t*-butanol decomposition reactions show noticeable sensitivity at 5

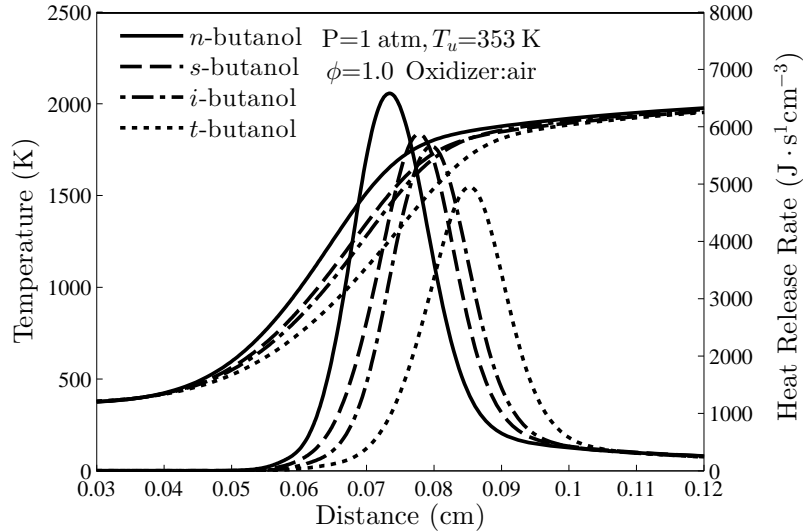


Figure 5.24: Computed temperature and heat release profiles of  $\phi = 1.0$  one-dimensional planar flame for the butanol isomers at 1 atm using the LLNL butanol model ([Sarathy et al., 2012](#)).

atm in the LLNL butanol model and at both 1 and 5 atm in the PoliMi model. This indicates the uniqueness of *t*-butanol kinetics.

Comparing the two mechanisms, it is seen that the H<sub>2</sub> and C<sub>1</sub>-C<sub>2</sub> reactions from the sensitivity analysis are largely the same for the two mechanisms, although they might have different sensitivity coefficients. The reactions C<sub>3</sub>H<sub>6</sub> = aC<sub>3</sub>H<sub>5</sub> + H and C<sub>3</sub>H<sub>6</sub> + OH = aC<sub>3</sub>H<sub>5</sub> + H<sub>2</sub>O show some sensitivity in the LLNL butanol model, especially for *i*-butanol and *t*-butanol; however, they do not have high sensitivity coefficients in the PoliMi model.

Finally, from the sensitivity analysis a strong pressure effect from 1 atm to 5 atm cannot be seen. The reactions with high sensitivity coefficients remain largely the same. Since third body reactions (+M) and reactions involving peroxide radicals (*e.g.*, HO<sub>2</sub>) are expected to become more sensitive at higher pressures, it

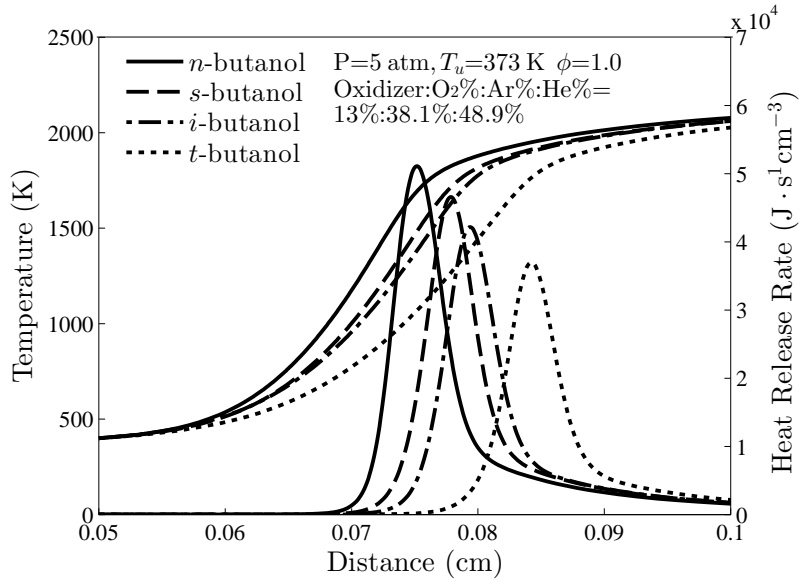


Figure 5.25: Computed temperature and heat release profiles of  $\phi = 1.0$  one-dimensional planar flame for the butanol isomers at 5 atm using the LLNL butanol model ([Sarathy et al., 2012](#)).

is nevertheless noted that such trends are not observed in Figures 5.26 and 5.27.

To investigate the cause of this pressure insensitivity, it is first recognized that 5 atm is still a relatively low pressure, and that the inert used at such conditions are argon and helium, instead of nitrogen. Thus to assess the high pressure and inert effects, using the LLNL butanol model the sensitivity coefficients of some representative third body reactions and reactions involving HO<sub>2</sub> for *n*-butanol at higher pressures with air as the oxidizer, have been computed and plotted in Figure 5.28. As expected, when the pressure increases from 1 to 20 atm, the magnitudes of the sensitivity coefficients of these reactions increase significantly, indicating the importance of third body reactions and peroxide radicals at higher pressures. On the other hand, at 5 atm using O<sub>2</sub>/Ar/He mixture as oxidizer these reactions do not show much sensitivity, primarily because the pressure is not high enough. In

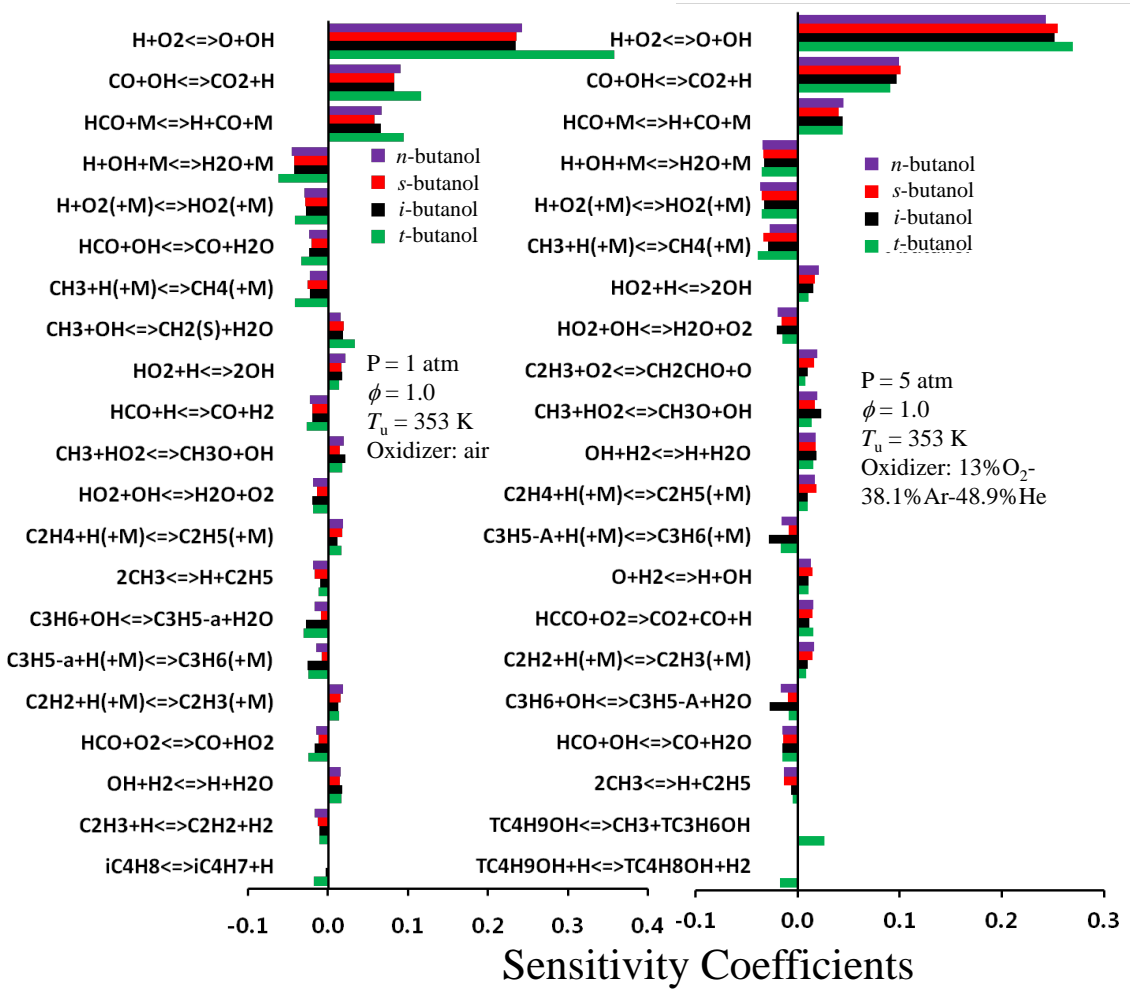


Figure 5.26: Normalized rate constant sensitivity coefficients,  $k_i$ , on the laminar flame speed  $S_u^0$  of the  $\phi = 1.0$  one-dimensional planar flame for the butanol isomers at 1 and 5 atm using the LLNL butanol model.

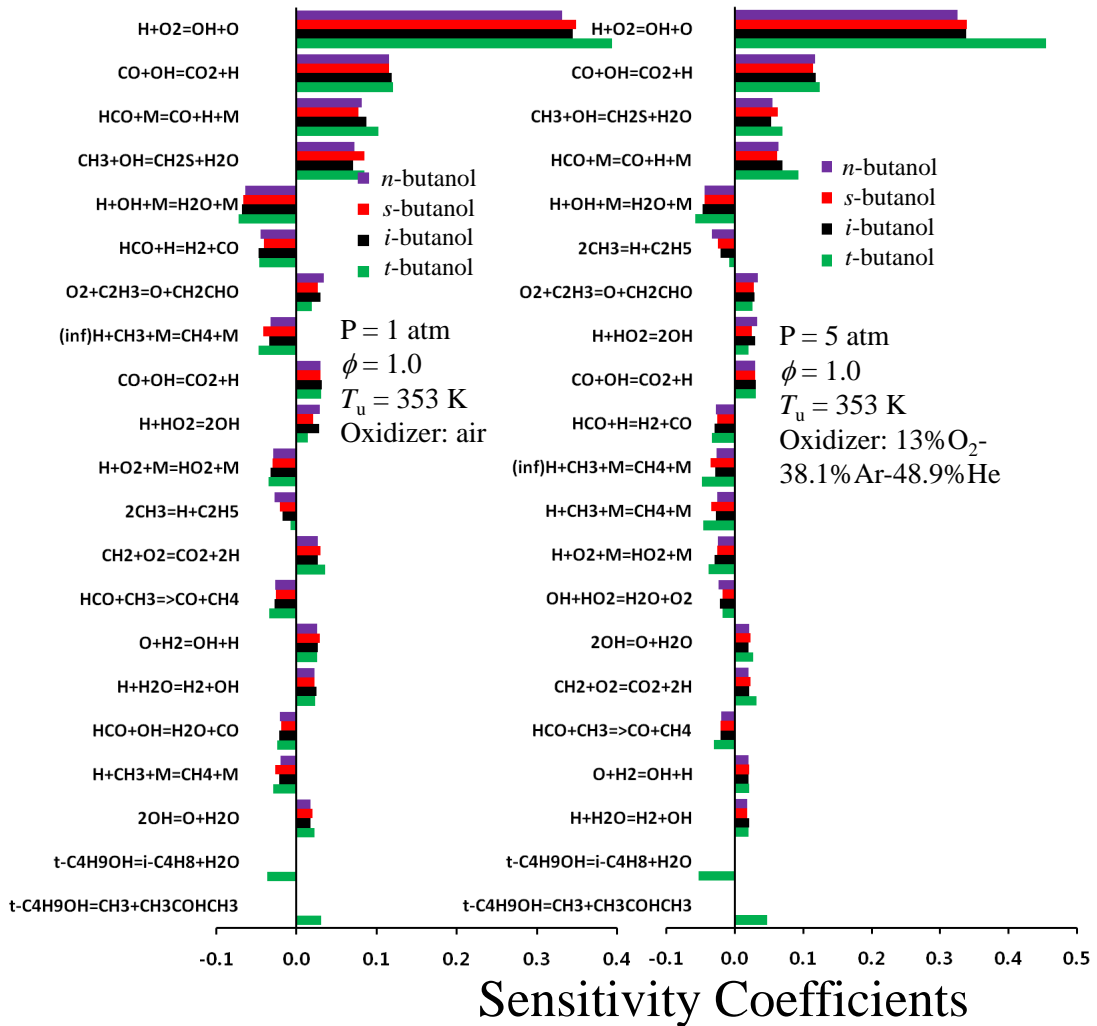


Figure 5.27: Normalized rate constant sensitivity coefficients,  $k_i$ , on the laminar flame speed  $S_u^0$  of the  $\phi = 1.0$  one-dimensional planar flame for the butanol isomers at 1 and 5 atm using the PoliMi model.

addition, for the reaction  $\text{H}+\text{O}_2+\text{M} \rightarrow \text{HO}_2+\text{M}$ , it is seen that at 5 atm using  $\text{O}_2/\text{Ar}/\text{He}$  mixture as oxidizer it has lower sensitivity than using air as the oxidizer. This means that using Ar/He as the inert reduces the importance of third body reactions.

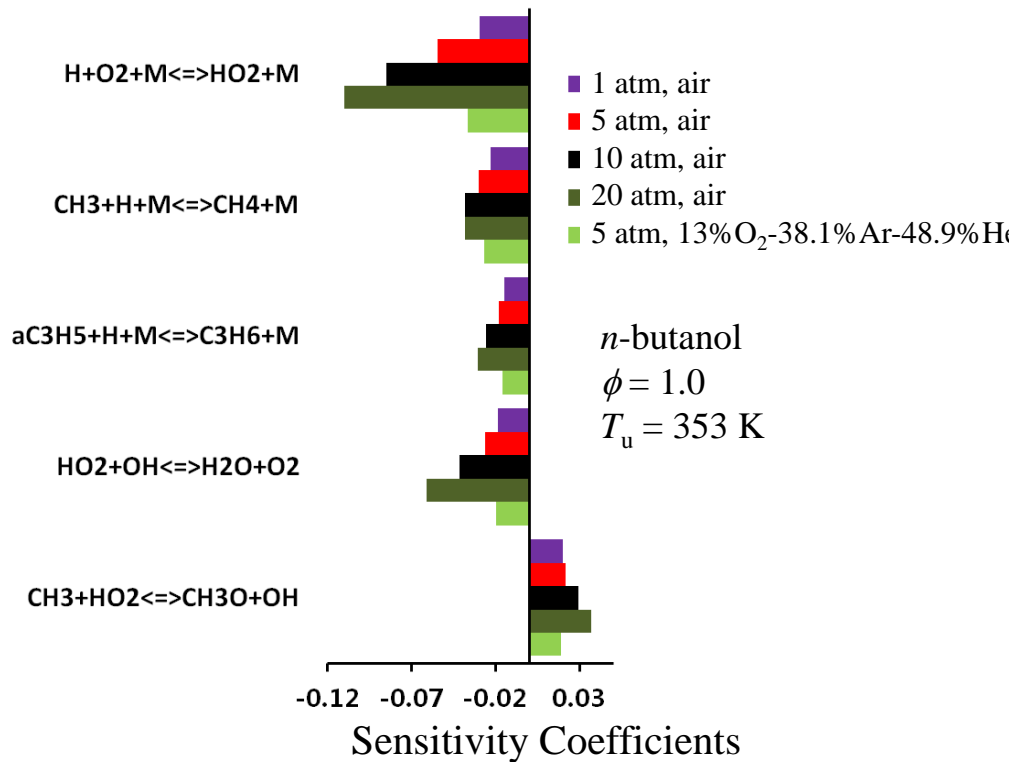


Figure 5.28: Normalized rate constant sensitivity coefficients,  $k_i$ , on the laminar flame speed  $S_u^0$  for some representative third body reactions and reactions involving  $\text{HO}_2$ , of the  $\phi = 1.0$  one-dimensional planar *n*-butanol flames at higher pressures with air as oxidizer using the PoliMi model.

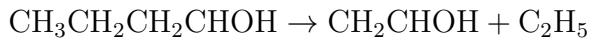
From the sensitivity analysis, it is seen that it is the oxidation of small fuel fragments that controls the total heat release and therefore the flame propagation. This means that the initial fuel cracking reactions are relatively fast and are not controlling the global rate. Such a rationale agrees with the discussion at the beginning of this chapter. Then the question is why the flame speeds of butanol isomers are

different. The reason lies in the fact that although the fuel-specific reactions are not the rate-limiting steps, they are completely different reactions due to the different molecular structure of the butanol isomers. These fuel specific reactions produce different fuel fragments, and therefore the distributions of intermediate species in the flames of different isomers are different. The reactivity of the intermediate species is different which finally leads to different global heat release.

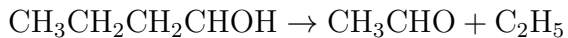
To confirm this explanation, reaction path analysis of the initial fuel cracking process up to a few reaction steps were performed. Figures 5.29, 5.30, 5.31 and 5.32 separately plot the initial fuel cracking reaction paths in the one-dimensional planar flames for all four isomers. To investigate the pressure effect and compare the difference between the LLNL butanol model and the PoliMi model, the conversion rates were calculated at 1 and 5 atm. It is seen that for each fuel, the main initial fuel cracking path is the H-abstraction reaction, forming various hydroxybutyl radicals that further crack into smaller species mostly following the  $\beta$ -scission rule, while there are also unimolecular fuel decomposition, fuel radical isomerization and enol-keto tautomerization reactions involved in the initial fuel cracking process.

From Figure 5.29, it is seen that, for *n*-butanol, the H abstraction reactions convert large percentages of the fuel into four hydroxybutyl radicals and a small portion of fuel into *n*-butoxy radicals. These five fuel radicals further decompose into smaller fragments, including alkenes, enols, aldehydes and ketones. Most of the fuel decomposition steps essentially follow the  $\beta$ -scission rule, and most of them occur at the  $\beta$  C-C bond and  $\beta$  C-O bond. Isomerization reactions between fuel radicals can also occur, for example, between 4-hydroxybutyl and *n*-butoxy. The fuel molecule can also directly decompose into smaller radicals or produce butene via the water elimination reaction. Comparing the two mechanisms, there are two major

differences. First, in the PoliMi model any enols produced from the fuel  $\beta$ -scission reactions are replaced by aldehydes or ketones. For example, for 1-hydroxybutyl radical the dominant pathway in the LLNL butanol model is:



which produces ethenol, while in the PoliMi model the dominant pathway is:



which produces acetaldehyde. Recent ab initio calculations showed that the dominant reaction channel is the one that produces ethenol (Zhang *et al.*, 2013). While enols are unstable and readily undergo enol-keto tautomerization producing aldehydes or ketones, the reaction is shown to have a high energy barrier and thus is slow in comparison to other reactions, such as the H abstraction of enols (Silva *et al.*, 2006). Therefore, the difference between replacing enols with aldehydes or ketones is not negligible. The conversion percentage from ethenol to acetaldehyde computed using the LLNL model is only 12% to 16%. The second difference between the two mechanisms is that the dominant reaction pathway of fuel radicals, *i.e.*, the  $\beta$ -scission reactions at C-C or C-O bond, has higher conversion percentage values in the LLNL model than those in the PoliMi model. In other words, in the PoliMi model the dominant  $\beta$ -scission pathways are attenuated by other pathways, such as isomerization and  $\beta$ -scission reactions at the C-H bond. For example, 100% of the 3-hydroxybutyl radicals in the LLNL model produce propene and  $\text{CH}_2\text{OH}$  radicals, while in the PoliMi model it is also converted into *n*-butoxy via isomerization and 3-buten-1-ol ( $\text{CH}_2=\text{CHCH}_2\text{CH}_2\text{OH}$ ) via the  $\beta$ -scission reaction at the

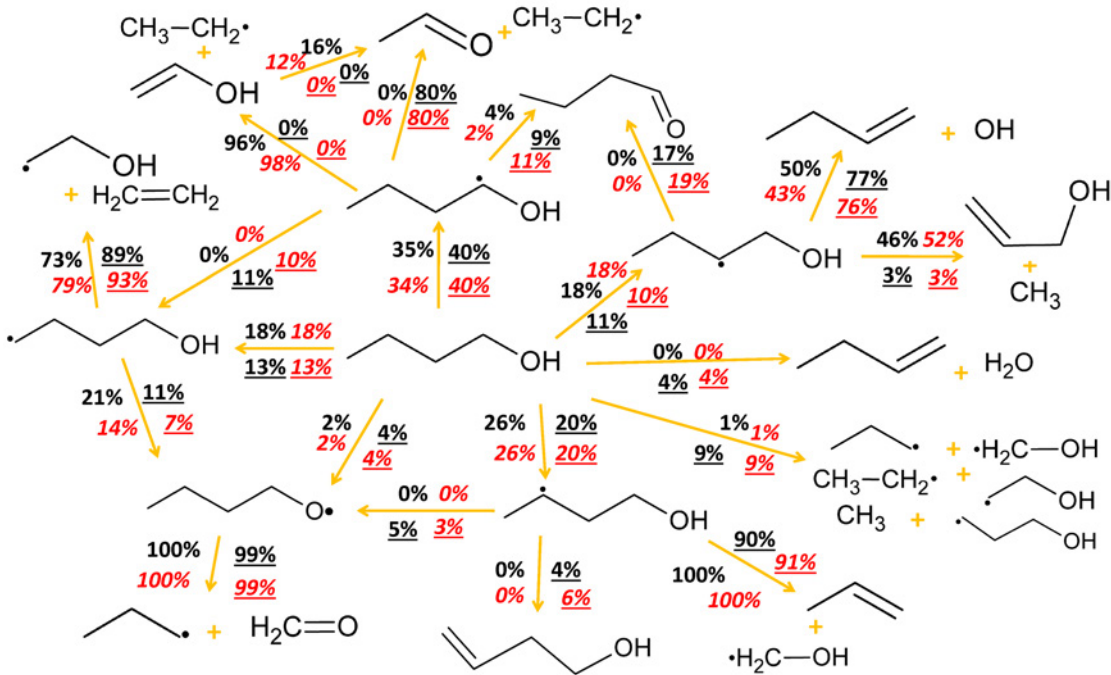


Figure 5.29: Fuel cracking path of the stoichiometric one-dimensional planar flame of *n*-butanol at 1 and 5 atm, calculated using the LLNL butanol model and the PoliMi model. The numbers indicate the conversion percentage (regular: 1 atm with air as oxidizer; italic: 5 atm with 13%O<sub>2</sub>-38.1%Ar-48.9%He as oxidizer; text without underline: LLNL butanol model; text with underline: PoliMi model).

C-H bond. The only fuel radical isomerization reaction that is not negligible in the LLNL model is the one between 3-hydroxybutyl radicals and *n*-butoxy. In addition, in the PoliMi model the direct fuel decomposition and water elimination also have higher conversion percentages than those in the LLNL model.

Similar to *n*-butanol, H abstraction reactions converted most of the *s*-butanol into hydroxybutyl radicals of *s*-butanol and a small portion into *s*-butoxy radicals, as shown in Figure 5.30. There are also four hydroxybutyl radicals for *s*-butanol: 1-hydroxybutyl, 2-hydroxybutyl, 3-hydroxybutyl and m-hydroxybutyl. They mostly undergo  $\beta$ -scission producing smaller alkenes, enols, aldehydes and

ketones species. Different from *n*-butanol which only produces straight-chain fragments, *s*-butanol flames also have branched intermediates, such as *iso*-propenol (*i*C<sub>3</sub>H<sub>5</sub>OH), acetone (CH<sub>3</sub>COCH<sub>3</sub>) and 2-butanone (C<sub>2</sub>H<sub>5</sub>COCH<sub>3</sub>). The differences between the two kinetic models shown for the case of *n*-butanol are also the same for *s*-butanol. In the PoliMi model, enols produced from fuel radicals  $\beta$ -scission reactions are replaced by aldehydes or ketones. For example, in the decomposition of m-hydroxybutyl, 1-hydroxybutyl and 2-hydroxybutyl, the products ethenol, *iso*-propenol and 1-propen-1-ol (CH<sub>3</sub>CH=CHOH) are replaced by acetaldehyde, acetone and propanal (C<sub>2</sub>H<sub>5</sub>CHO). Similar to *n*-butanol, the direct fuel decomposition, water elimination and fuel radical isomerization reactions in the *s*-butanol flames also have higher conversion percentages in the PoliMi model than those in the LLNL model. In addition, the PoliMi model does not distinguish isomers of some intermediate species. For example, 1-butene and 2-butene are treated as one species “NC4H8” in PoliMi model. Furthermore, 3-buten-1-ol (CH<sub>2</sub>=CHCH<sub>2</sub>CH<sub>2</sub>OH), 2-methyl-2-propen-1-ol (CH<sub>2</sub>=C(CH<sub>3</sub>)CH<sub>2</sub>OH) and 3-buten-2-ol (CH<sub>2</sub>=CHCH(CH<sub>3</sub>)OH), which respectively come from the decomposition of hydroxybutyl radicals of *n*-butanol, *s*-butanol and *i*-butanol, are also treated as a single species, C<sub>4</sub>H<sub>7</sub>OH, in the PoliMi model.

The initial cracking of *i*-butanol follows similar steps as *n*-butanol and *s*-butanol, although the resulting fuel fragments are different. There are three hydroxybutyl radicals for *i*-butanol: 1-hydroxybutyl, 2-hydroxybutyl and 3-hydroxybutyl, which again are the main products of H-abstraction of the fuel, leaving *iso*-butoxy radicals only as a small percentage. The decomposition of 1-hydroxybutyl and 3-hydroxybutyl radicals produces mostly straight-chain intermediates, such as propene and propenols, while 2-hydroxybutyl radicals produce all branched intermediate

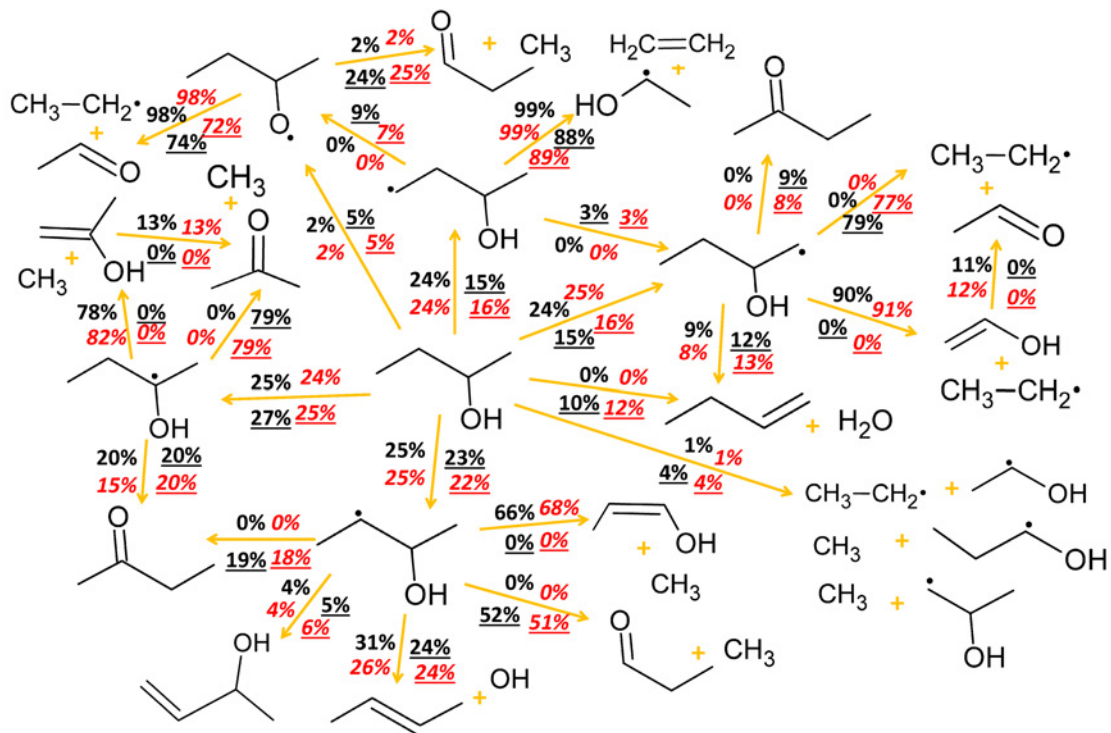


Figure 5.30: Fuel cracking path of the stoichiometric one-dimensional planar flame of *s*-butanol at 1 and 5 atm, calculated using the LLNL butanol model and the PoliMi model. The numbers indicate the conversion percentage (regular: 1 atm with air as oxidizer; italic: 5 atm with  $13\%\text{O}_2$ - $38.1\%\text{Ar}$ - $48.9\%\text{He}$  as oxidizer; text without underline: LLNL butanol model; text with underline: PoliMi model).

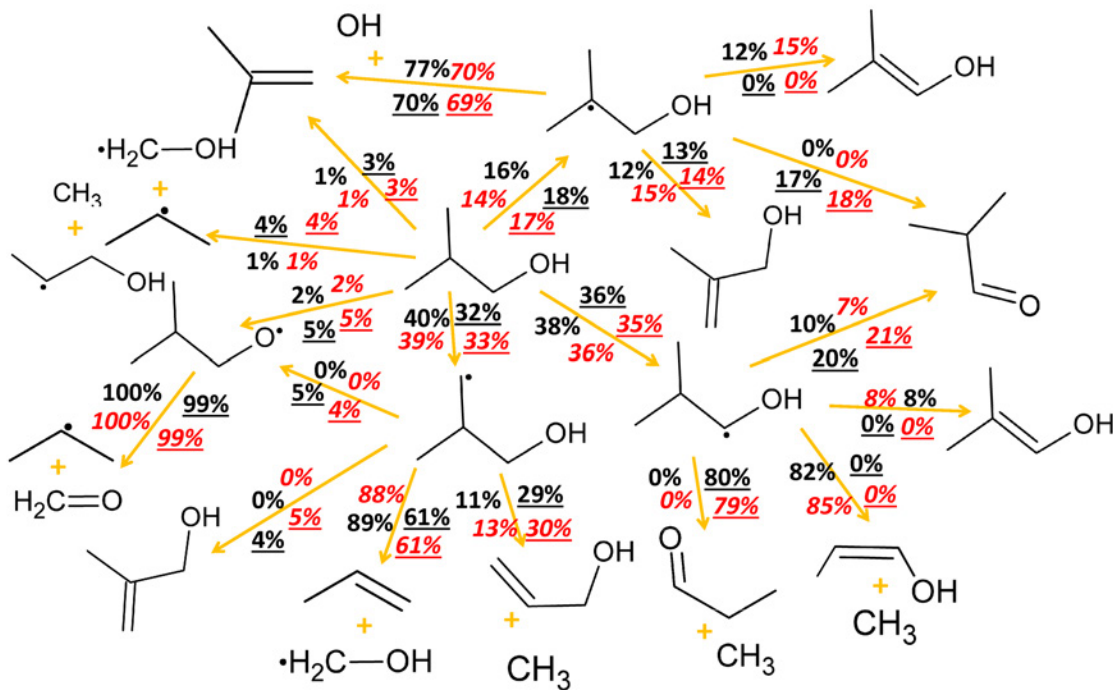


Figure 5.31: Fuel cracking path of the stoichiometric one-dimensional planar flame of *i*-butanol at 1 and 5 atm, calculated using the LLNL butanol model and the PoliMi model. The numbers indicate the conversion percentage (regular: 1 atm with air as oxidizer; italic: 5 atm with 13% O<sub>2</sub>-38.1% Ar-48.9% He as oxidizer; text without underline: LLNL butanol model; text with underline: PoliMi model).

species that contain a C<sub>4</sub> alkanyl group, such as *iso*-butene, 2-methyl-1-propen-1-ol ((CH<sub>3</sub>)<sub>2</sub>C=CHOH) and 2-methyl-2-propen-1-ol. From Figure 5.31 it is seen that for *i*-butanol the PoliMi model also directly replaces enols in the products of hydroxybutyl radical decomposition by aldehydes or ketones, such as 1-propen-1-ol replaced by propanal in the decomposition reaction of 1-hydroxybutyl *i*-butanol radical. Similar to *n*-butanol and *s*-butanol, direct fuel decomposition, water elimination and fuel radical isomerization reactions have higher conversion percentages in the PoliMi model by than that in the LLNL model.

Lastly, for *t*-butanol, it is seen from Figure 5.32 that the reaction path is much simpler than those of the other butanol isomers. Since the ternary C atom in

the *t*-butanol molecule does not have an H atom connected to it and the three other C atoms are symmetric, there is only one *t*-butanol hydroxybutyl radical:  $(CH_3)_2(CH_2)COH$ . The dominant path of the H-abstraction reaction of *t*-butanol is the one producing  $(CH_3)_2(CH_2)COH$ ; only a small portion produces tert-butoxy radical ( $(CH_3)_3CO$ ). In addition, *t*-butanol can also undergo a water elimination reaction, which produces *iso*-butene, or directly decomposes into  $CH_3$  and  $(CH_3)_2COH$  radicals. Similar to other isomers, the water elimination reaction and direct fuel decomposition reaction have much higher conversion percentages in the PoliMi model than in the LLNL model. The  $(CH_3)_2(CH_2)COH$  radical undergoes two  $\beta$ -scission reactions producing *iso*-butene and *iso*-propenol respectively. In the PoliMi model there is no *iso*-propenol species, which is replaced by acetone directly. The  $(CH_3)_2COH$  radical mostly undergoes  $\beta$ -scission producing acetone, with a small portion of it producing *iso*-propenol in the LLNL model. In any case, the reaction path of *t*-butanol has to go through *iso*-butene, *iso*-propenol or acetone.

In general, there is not a strong pressure effect between 1 atm and 5 atm on the initial fuel cracking pathways and conversion rates. For most of the reactions in the reaction path of *n*-butanol, *s*-butanol and *i*-butanol, the conversion percentages at 5 atm are very close to the values at 1 atm. The pressure effect on the reaction path of *t*-butanol is a little stronger. From Figure 5.32, it is seen that with both mechanisms increasing pressure tends to reduce the conversion percentages of H abstraction reactions while increasing the percentages of water elimination and fuel decomposition reactions. In the LLNL model, increasing pressure also causes  $(CH_3)_2COH$  radicals to decompose more *iso*-propenol.

From the above reaction path analysis for all isomers, it can be concluded that while *n*-butanol all cracks into straight-chain species (oxygenated or not), *s*-butanol,

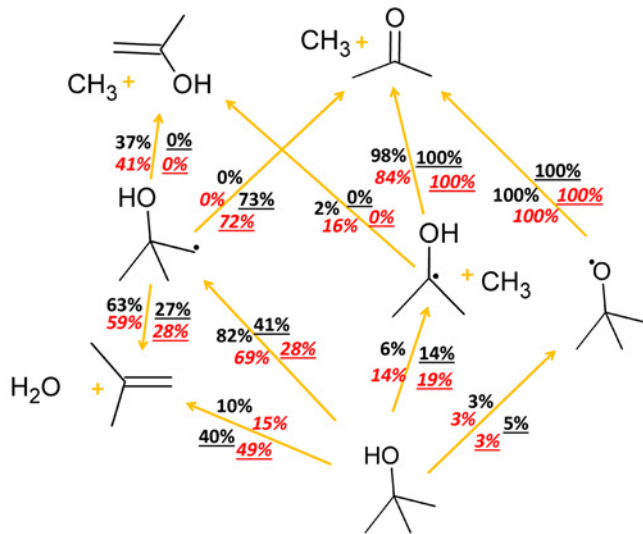


Figure 5.32: Fuel cracking path of the stoichiometric one-dimensional planar flame of *t*-butanol at 1 and 5 atm, calculated using the LLNL butanol model and the PoliMi model. The numbers indicate the conversion percentage (regular: 1 atm with air as oxidizer; italic: 5 atm with 13% $\text{O}_2$ -38.1%Ar-48.9%He as oxidizer; text without underline: LLNL butanol model; text with underline: PoliMi model).

*i*-butanol and *t*-butanol crack into significantly more branched species. Specifically, in the flames of *i*-butanol a significant amount of fuel is converted to *iso*-butene and oxygenated species with similar branched carbon structure, such as 2-methyl-2-propen-1-ol. *iso*-Butene is a notably stable species and has slow flame speeds as discussed at the beginning of this chapter. In the *s*-butanol flame, *iso*-butene is not formed; however, there is considerably more acetone ( $\text{CH}_3\text{COCH}_3$ ) and *iso*-propenol ( $\text{iC}_3\text{H}_5\text{OH}$ ). Acetone and *iso*-propenol can exchange through tautomerization reaction or isomerization reactions with radicals, and they both are relatively stable intermediate species, as discussed at the beginning of this chapter. This therefore explains the lower flame speed of *s*-butanol relative to *n*-butanol. Finally, in *t*-butanol flames all the fuel is converted to branched species: *iso*-butene, acetone and *iso*-propenol. Therefore, the combined effect of the low reactivity of these three

branched species causes *t*-butanol to have the lowest flame speeds.

It is noted that many previous studies have shown that branched hydrocarbons has slower flame speed compared to their straight chain counterparts, such as *iso*-butane versus *n*-butane (Davis & Law, 1998), *iso*-butene versus 1-butene and 2-butene (Kelley, 2011), and *iso*-octane versus *n*-octane (Ji *et al.*, 2012b; Kelley *et al.*, 2011b). Now it is seen that this rule can also be applied to alcohols, which contains not only C-C, C-H bonds but also C-O and O-H bonds. The fundamental reason for this similarity lies in the bond energies. The calculation by Gu *et al.* (2010) shows the following ordering of bond dissociation energies in the butanol fuel molecules: O-H bond (104-107 kcal/mol) > terminal C-H bond (100-103 kcal/mol) > inner C-H bond (97-99 kcal/mol) > C-O bond (93-96 kcal/mol) > C-C bond (85-90). For hydroxybutyl radicals, the bond energies at the  $\beta$  position will be different but the ordering remains approximately the same. It is seen that the C-O bond has a similar bond energy to the C-C bond, while the O-H bond has a similar bond energy to the C-H bond. In hydrocarbon fuels,  $\beta$ -scission at C-C is usually the dominant reaction path because it has lower bond energy than that of the C-H bond. Whereas for alcohols  $\beta$ -scission at both C-C and C-O are the dominant pathways because they have similar bond energies, which in turn are lower than the energies of C-H bonds and O-H bonds. In other words, in high temperature chemistry where H abstraction followed by  $\beta$ -scission is the dominant reaction pathway, the role of the O atom is similar to the C atom when the extent of branching of a fuel is considered. In this sense, if the chain structure formed by the C-C and C-O bonds is considered, only *n*-butanol has the straight chain structure, whereas *s*-butanol, *i*-butanol and *t*-butanol all crack into various amount of branched intermediate species, which are kinetically more stable.

## 5.4 Concluding Remarks

Using state-of-the-art chemical kinetic models, whose laminar flame speed predictions reasonably agree with the present measurements, high temperature flame chemistry of two groups of fuels have been studied. The first group is C<sub>6</sub> straight-chain alkane (*n*-hexane) and C<sub>6</sub> carbon ring cyclo-alkanes, *i.e.*, cyclohexane, methyl- and ethyl-cyclohexanes. The second group is the butanol isomers, *i.e.*, *n*-butanol (1-butanol), *s*-butanol (2-butanol), *i*-butanol (*iso*-butanol) and *t*-butanol (tertiary-butanol). Both groups are suitable to study the fuel molecule structure effects on their reactivities since the fuels in each group have very small differences in the thermal and transport properties.

In light of the understanding and confirmed by sensitivity analysis that large fuel molecules decompose into C<sub>1</sub>-C<sub>4</sub> fuel fragments rapidly before a significant amount of these fragments are oxidized, the fuel cracking process, which are mainly the H-abstraction/ $\beta$ -scission and direct fuel decomposition, is analyzed and compared.

For the C<sub>6</sub> carbon ring cyclo-alkanes, it is found that because cyclohexane has symmetric molecule structure, its ring opening always results in a radical site at the two ends of the carbon ring. This effect causes the fuel molecule to decompose into C<sub>2</sub> (C<sub>2</sub>H<sub>4</sub>) and C<sub>4</sub> (1,3-butadiene) fragments, which have higher reactivity than the C<sub>1</sub> (CH<sub>4</sub>), C<sub>3</sub> (propene) fragments and *iso*-butene. This explains the higher flame speeds of cyclohexane compared to all other fuels in the group.

For butanol isomers, it is found that since the C-O bond energy in alcohols is close to the C-C bond energy, and the O-H bond energy is close to C-H bond energy, the fuel decomposition depends on the C-C-O molecule structure. Therefore, the general rule that fuel branching reduces the flame speed for hydrocarbons can also

be applied to alcohols.

# Chapter 6

## Self-Acceleration Due to Flamefront Instabilities

### 6.1 Introduction

In Chapters 3, 4 and 5, the expanding flames were studied under the condition for which the flame surface is smooth such that the flame is one-dimensional and spherical. Under such a condition, the flame radius  $R_f$  and the stretch rate  $K = (2/R_f)dR_f/dt$  are the only parameters that characterize the flame under the ideal conditions (*i.e.*, the effects of ignition, flow confinement, radiation and buoyancy are negligible). Therefore, once the effect of stretch is eliminated (Chapters 3), the resulting quantity  $S_u^0$  does not depend on the flow any more but only on the properties of the combustible mixture. Consequently, smooth expanding spherical flames are suitable to study combustion chemistry (Chapters 4 and 5).

However, unfortunately and fortunately, propagation of laminar premixed flames is frequently subjected to the excitation of flamefront cellular instabilities due to

the hydrodynamic instabilities induced by the thermal expansion across the flame (Darrieus, 1938; Landau, 1944), and diffusional-thermal instabilities induced by the non-equidiffusion of heat and species (Markstein, 1951, 1964; Sivashinsky, 1977a). The historical perspectives on cellular flamefront instabilities have been presented in Chapter 1. For expanding flames, since these flamefront cellular instabilities are suppressed by viscous diffusion and aerodynamic stretch at small flame radius, they are only excited when the flame radius reaches some critical value (named onset of cellularity  $R_{oc}$ , to be differentiated from the critical radius in the flame initiation problem (Kelley & Law, 2009; Chen *et al.*, 2011)). This critical radius has been studied theoretically by Bechtold & Matalon (1987), Addabbo *et al.* (2002) and experimentally by Jomaas *et al.* (2007b). Both theory and experiments verified the following expression for the onset of cellularity,

$$Pe_{oc} \equiv \frac{R_{oc}}{\delta_L} = Pe_1(\Theta) + Ze(Le - 1)Pe_2(\Theta) \quad (6.1)$$

where  $Pe$  is the Peclet number, defined as the normalized flame thickness in this case,  $\Theta$  is the thermal expansion ratio, and  $Ze$  the Zel'dovich number. Equation 6.1 indicates that the cellularity onset radius  $R_{oc}$ , if normalized by the flame thickness  $\delta_L$ , is induced by two sources, namely the hydrodynamic part  $Pe_1$  and the diffusional-thermal part  $Ze(Le - 1)Pe_2(\Theta)$ , which is largely dominated by the value of the Lewis number  $Le$ . The specific expressions for  $Pe_1$  and  $Pe_2$  are given in Addabbo *et al.* (2002).

What remains unknown is what happens to flame propagation after the cellularity onset. The presence of instability cells over the flame surface increases its surface area and consequently also the global propagation speed of the flame. Furthermore,

since new cells continuously evolve as the flame propagates, it is reasonable to expect that the flame speed will also continuously increase, leading to the possibility of self-acceleration. The phenomenon is of particular interest for the propagation of the globally spherical flame because of the well-defined, yet continuously increasing flame radius, which yields a characteristic dimension and the dynamic parameters against which excitation of the various instability modes evolve. Specifically, during the initial stage of flame propagation when the flame radius is small, the small-scale diffusional-thermal instability is expected to dominate. As the flame becomes larger and its thickness is small compared to its radius, the hydrodynamic, Darrieus-Landau (DL) instability sets in, progressively dominating the flame morphology and the accelerative dynamics.

This self-acceleration can be quantified, and an assessment of the propagation mode made, by determining the history of the average flame radius,  $R_{av}$ , through a power-law expression,  $R_{av} \sim t^\alpha$ , where  $t$  is the time. There has been considerable interest in the specific values that  $\alpha$  can assume. That is, if  $\alpha$  is a constant, then the flame acceleration is either self-similar in  $t$ , if it holds for all  $t$ , or locally similar if it holds only for a specific period of  $t$ .

Furthermore, it has been suggested ([Bychkov & Liberman, 1996](#); [Blinnikov & Sasorov, 1996](#); [Gostintsev \*et al.\*, 1997](#)) that, if  $\alpha$  is not an integer, then the wrinkled flame front can be considered as a fractal surface with the total surface area of the front given by  $A_f \sim R_{av}^{2+d}$ , where the constant  $d = 1 - 1/\alpha$  is the fractal excess. An example of such a fractal surface is the Koch snowflake as shown in Figure 6.1.

In the limit of an infinitesimally thin flame, diffusional-thermal effects are suppressed, and the local flame speed over the wrinkled flame surface is that of the laminar flame speed,  $S_u^0$ , and is as such a constant. The fractal hypothesis can then

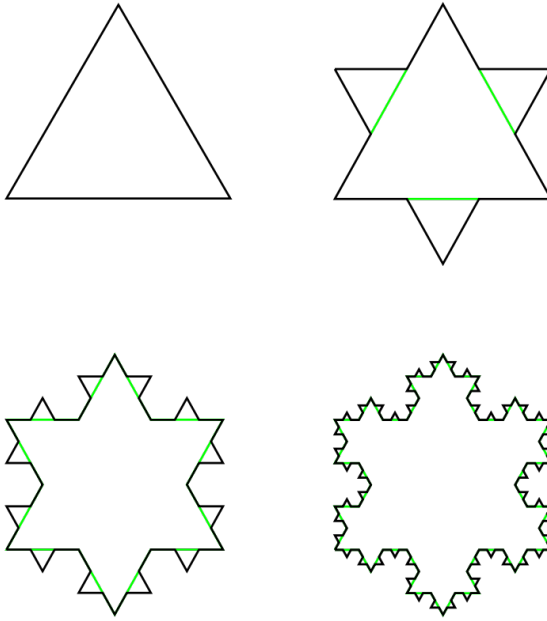


Figure 6.1: The first four iterations of the Koch snowflake ([http://en.wikipedia.org/wiki/Koch\\_snowflake](http://en.wikipedia.org/wiki/Koch_snowflake)).

be related to the self-similar propagation of the flame front through

$$4\pi R_{av}^2 \frac{dR_{av}}{dt} \approx \Theta S_u^0 A_f \propto \Theta S_u^0 R_{av}^{2+d} \quad (6.2)$$

Thus, we have

$$\frac{dR_{av}}{dt} \propto R_{av}^d \quad (6.3)$$

Finally, for fully-developed Kolmogorov turbulence it has been suggested by Mandelbrot (1974, 1975) that the iso-surfaces (e.g., iso temperature) also have a fractal character, and the fractal dimension  $2 + d$  has been theoretically estimated by Sreenivasan *et al.* (1989) to be  $7/3$  based on Reynolds number similarity. Exper-

imental values by [Sreenivasan & Meneveau \(1986\)](#) and [Sreenivasan & Prasad \(1989\)](#) for a variety of turbulent flows fall in the range of  $2.35 \pm 0.05$ , in close agreement with the theoretical prediction of  $7/3$ . Consequently, if  $\alpha$  assumes the value of 1.5 for the case of expanding laminar flames under hydrodynamic instability, then  $2+d = 7/3$ , and the flame has possibly undergone self-turbulization and thereby assumed the character of turbulence.

Considerable experimental and computational studies on laminar flames have been conducted, aiming to demonstrate the possible attainment of  $\alpha = 1.5$  and hence self-turbulization, although with inconclusive results. In fact, in the interest of demonstrating such an attainment, interpretations of the results have been conducted rather loosely, causing considerable confusion in the rigorous understanding of the fundamental phenomena.

In view of the above considerations, the present study aims to perform a well-controlled experimental investigation, to provide reliable data to answer the following three increasingly demanding claims on  $\alpha$ , namely:

- Does the flame self-accelerate, *i.e.*, is  $\alpha > 1$ ?
- Is  $\alpha$  a constant such that the propagation is self-similar?
- Is  $\alpha$  approximately equal to 1.5 such that the wrinkled laminar flame has undergone self-turbulization?

Before doing so, it is necessary to first present a brief assessment of the state of the determination of  $\alpha$  in order to demonstrate the various subtleties involved in conducting an unambiguous determination.

The results presented in this chapter have been previously published in the following journal article ([Wu \*et al.\*, 2013](#)):

- WU, F., JOMAAS, G. & LAW, C. K. 2013 An experimental investigation on self-acceleration of cellular spherical flames. *Proceedings of the Combustion Institute* **34**, 937–945

## 6.2 Review of Previous Works

### 6.2.1 Experimental Studies

Lind & Whitson (1977) conducted large-scale explosion experiments in quiescent conditions at atmospheric pressure with various mixtures including H<sub>2</sub>/air, H<sub>2</sub>/O<sub>2</sub>, C<sub>3</sub>H<sub>8</sub>/air, CH<sub>4</sub>/air, C<sub>4</sub>H<sub>6</sub>/air, C<sub>2</sub>H<sub>2</sub>/air. These experimental data were later analyzed by Gostintsev *et al.* (1988) using  $\alpha = 1.5$  for all mixtures studied and concluded that this value is consistent with the data. However, the data analysis was not clearly described, and, more significantly, the original reported value of 1.5 was lowered to 1.25  $\sim$  1.5 in two later publications (Gostintsev *et al.*, 1999, 2004). Most of the subsequent studies by others have either justified or focused their investigations on the presumed validity of  $\alpha = 1.5$ .

Bradley (1999); Bradley *et al.* (2001) experimented with large-scale flames at atmospheric pressure, and allowed the outwardly propagating flames to grow to radii as large as 3 meters so that hydrodynamic cells could be developed. A constant  $\alpha$  of 1.5 was again used in their data analysis. However, due to strong buoyancy with typical Froude numbers, being around 2, the experimental flame was largely hemispherical, as shown in Bradley *et al.* (2001). This severe lack of spherical symmetry fundamentally complicates the data interpretation and analysis.

Haq (2005) conducted experiments for atmospheric CH<sub>4</sub>/air flames in a combustion vessel. It was shown that the data obtained at small radii could be blended

with those of [Lind & Whitson \(1977\)](#) at large radii, with good match. Furthermore, the results showed that  $\alpha$  is 1.24 for the horizontal radii and 1.32 for the vertical radii; the difference could be due to buoyancy effects. The primary concern with this series of experiments is whether mature hydrodynamic cells were developed for flames of such small dimension at atmospheric pressure, at which the flame thickness would require cells of large dimension, recognizing that the flame of [Bradley \*et al.\* \(2001\)](#) required 3 meters to develop.

[Kwon \*et al.\* \(2002\)](#) experimented with  $H_2/O_2/N_2$  flames, using a constant and high-pressure dual-chamber vessel at a pressure of 15 atm. It is noted that the elevated pressure reduces the flame thickness and thereby the hydrodynamic cell size, hence allowing the development of hydrodynamic cells for the small, laboratory-scale flames. The reported values of  $\alpha$  are 1.26, 1.36 and 1.23 for  $\phi = 0.50, 1.00$  and 1.50, respectively.

### 6.2.2 Numerical Studies

A number of numerical investigations ([Blinnikov & Sasorov, 1996](#); [Ashurst, 1997](#); [Liberman \*et al.\*, 2004](#); [Filyand \*et al.\*, 1994](#); [Aldredge & Zuo, 2001](#); [Galanti \*et al.\*, 1998](#); [Olami \*et al.\*, 1997](#); [Karlin & Sivashinsky, 2006, 2007](#); [Olami \*et al.\*, 1995](#); [Furserenko \*et al.\*, 2008](#); [Pan & Furserenko, 2008](#)) have been conducted with focus on the issue of self-acceleration of expanding wrinkled flames. Due to the high computational cost, almost all studies were performed for 2-D cylindrical flames. Because the power-law exponent  $\alpha$  for the 2D and 3D flames are necessarily different, as noted by ([Blinnikov & Sasorov, 1996](#)), caution is needed in drawing direct comparison for values of  $\alpha$  obtained from 2D and 3D flames. Furthermore, most simulations were also conducted using simplified models, such as the Sivashinsky equation or

Frankel equation. Finally, there were studies that not only claimed  $\alpha_{2D} = 1.5$  from calculations obtained by using 2D cylindrical flames, but the relevant slopes were also determined from results exhibiting various degrees of nonlinearity ([Ashurst, 1997](#); [Filyand \*et al.\*, 1994](#); [Aldredge & Zuo, 2001](#)).

### 6.2.3 Fitting Formulas

In addition to disagreement in the values of  $\alpha$ , there is also inconsistency among different studies in the extraction of  $\alpha$ . The early studies of [Gostintsev \*et al.\* \(1988\)](#) and [Bradley \*et al.\* \(2001\)](#) simply assumed  $\alpha = 1.5$  and applied the following self-similar law:

$$R = R_0 + At^{1.5} \quad (6.4)$$

where  $R$  is the flame radius,  $t$  the time after ignition, and  $R_0$  and  $A$  are the parameters for best linear fitting. Obviously, such a fitting automatically assigns  $\alpha = 1.5$  although an examination of the reported data shows that a plot of  $R-t^{1.5}$  is not exactly linear.

To evaluate  $\alpha$  directly from data, other experimental and numerical studies ([Kwon \*et al.\*, 2002](#); [Ashurst, 1997](#); [Liberman \*et al.\*, 2004](#)) treated all  $R$ ,  $A$  and  $\alpha$  as fitting parameters,

$$R = R_0 + At^\alpha \quad (6.5)$$

where  $R$  is the flame radius and  $t$  is either the time after ignition in experiments or the time after calculation starts in the simulation. This formula allows determination of the acceleration exponent,  $\alpha$ , directly from the data. However, because of the definition of  $t$ , the fitting result will automatically depend on the instant of ignition, or the simulation starting point. For example, as shown in Figure 6.2, when a

set of experimental data is artificially shifted in time (which in real experiments can be caused by the different ignition conditions), different values of  $\alpha$  are obtained.

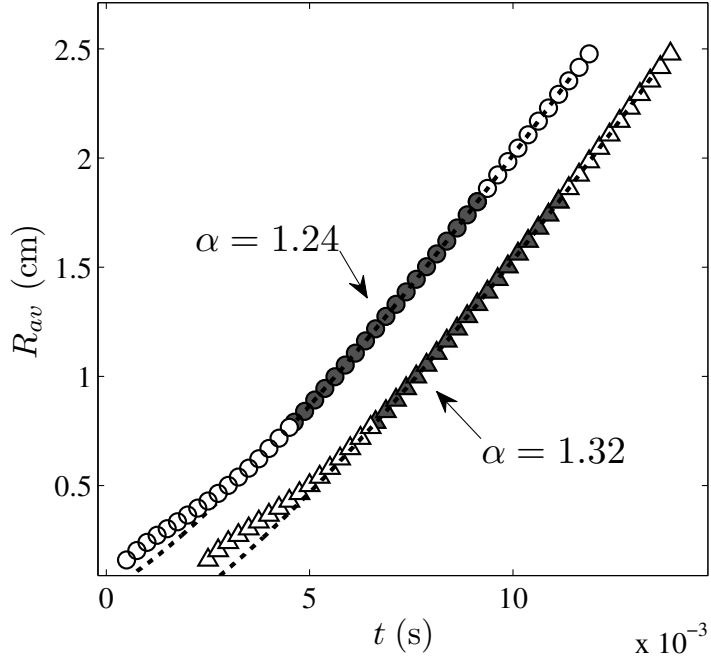


Figure 6.2: A set of experimental data from the present study; Circles: original data, Triangles: same set of data after an artificial time shift  $\Delta t = 2$  ms. Filled markers indicate data used for fitting. The dot lines are fitting curves.  $R_{av}$  is defined by Equation 6.9.

Other studies (Filyand *et al.*, 1994; Aldredge & Zuo, 2001) set  $R_0$  to be the visual onset of the transition from a smooth to a wrinkled flame, and consider the following formula:

$$R = R_0 + A(t - t_0)^\alpha \quad (6.6)$$

where  $R_0$  and  $t_0$  are the radius and time of the onset of wrinkling. This method avoids the influence of the ignition condition; however, it introduces two other concerns. First, the determination of the onset of cellularity from experimental or

numerical flame images can be quite subjective. The fitting result are very sensitive with respect to the values of  $R_0$  and  $t_0$ , especially for the range of data points that immediately follow the onset since both  $R - R_0$  and  $t - t_0$  are close to zero. Second, since there is possibly a transitional period after the onset of cellularity but before the acceleration reaches a saturated self-similar regime (Lberman *et al.*, 2004; Galanti *et al.*, 1998; Karlin & Sivashinsky, 2006), using this formula still depends on the transitional period, as shown herein.

Some numerical studies (Galanti *et al.*, 1998; Karlin & Sivashinsky, 2006, 2007) fitted the calculated propagation velocity,  $U = dR/dt$ , by a power-law

$$U = Bt^{\alpha-1} \quad (6.7)$$

where  $B = A\alpha$  is another constant, while others (Haq, 2005) ignored the constant  $R_0$  or  $t_0$  and directly considered the power-law

$$R = At^\alpha \quad (6.8)$$

However, the influence of the initial condition still exists as  $t$  is still defined as the time after ignition in experiments or the time after the calculation starts in simulations.

### 6.3 Present Experimental Considerations

Most of the data presented in this chapter were acquired using Vessel I, which has been described in Chapter 2 and in Tse *et al.* (2004) and Jomaas (2008). It allows very high pressure experiments up to 60 atm. The data at stoichiometric H<sub>2</sub>/air

( $\phi = 1.0$ ) were repeated using Vessel II, and the results agree closely with the data obtained on Vessel I.

The key consideration for the present experiment is to reduce the flame thickness such that hydrodynamic cells can be readily excited and rapidly grow to maturity in accordance with the Landau limit of flame-sheet propagation. This goal was achieved by employing two unique features. First, the high pressure conditions substantially reduce the flame thickness  $\delta_L$ , such that the Peclet number  $Pe = R/\delta_L$  achieved is quite high. Second, the flame thickness was further reduced by using hydrogen as the test fuel because of its high flame speed. In particular, lean hydrogen flames were observed to almost immediately exhibit cellular instabilities after initiation of propagation because of the simultaneous excitation of the diffusional-thermal cellular instability ([Law et al., 2005; Jomaas et al., 2007b](#)). Consequently, they are particularly suitable for the present investigation, with their cellular propagation period taking place over 102 to 103 times of the flame time in the present investigation. This provides ample time and space for the development of the cell and exploration of the possible existence of the self-similar propagation mode.

Figure 6.3 shows three typical sequences of the images of propagating hydrogen/air flames. Specifically, it is seen that, at a pressure of 5 atm, the flame surface is wrinkled for lean but not rich mixtures, hence demonstrating the stabilizing effect of the diffusional-thermal instability on rich hydrogen/air mixtures whose  $Le$  is greater than unity. Flames of these rich mixtures, however, also become wrinkled at the higher pressure of 25 atm, demonstrating the manifestation of hydrodynamic instability as the flame becomes progressively thinner with increasing pressure.

Accurate tracking of the flame front from Schlieren cine images is crucial, especially for a subject like this current study with high sensitivity. Due to the fact

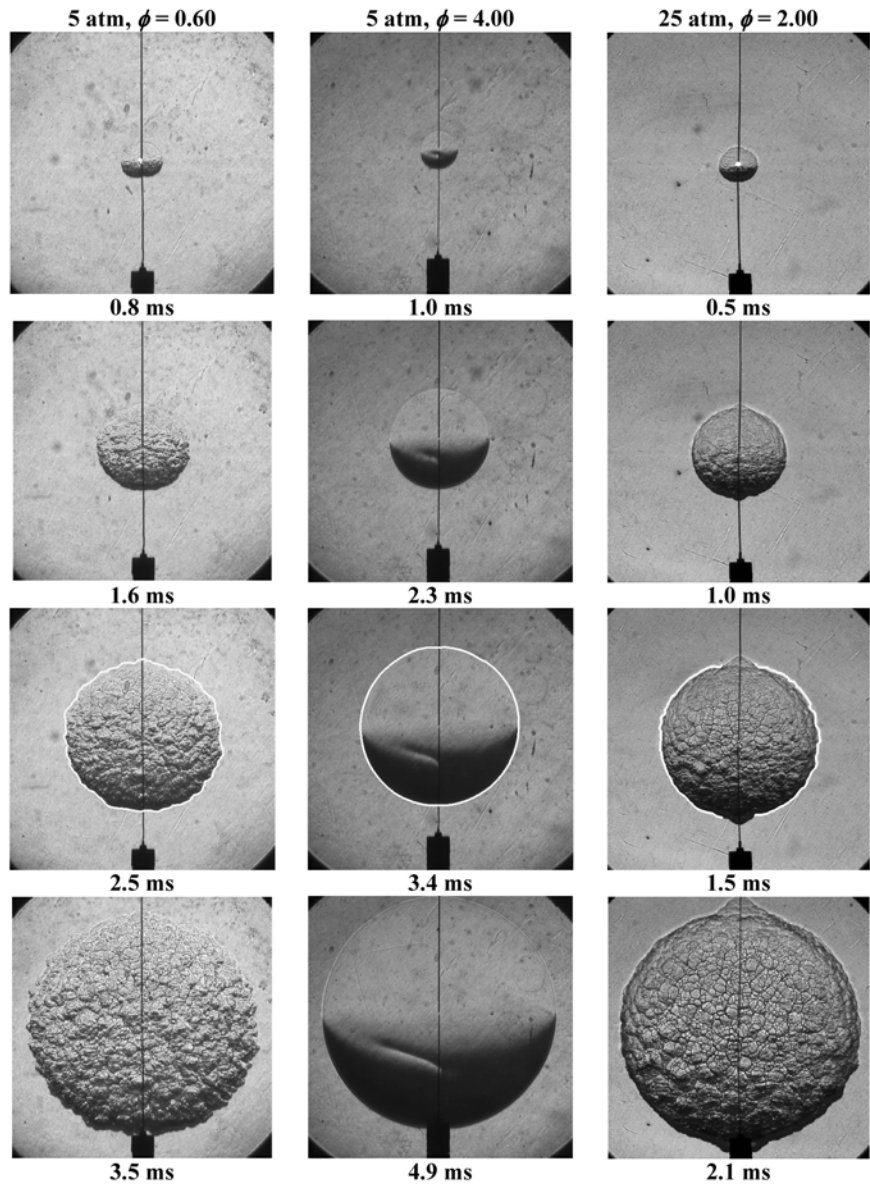


Figure 6.3: Sequences of flame propagation in hydrogen/air mixtures, showing the development of cellular flamefront instability is promoted for  $Le < 1$  mixtures and in high pressure environments. The images were obtained from the experiments conducted by [Jomaas \(2008\)](#) and also published in [Wu \*et al.\* \(2013\)](#).

that wrinkled flame fronts contain many troughs and cusps, only an averaged flame radius of the entire flame front has statistical meaning. This was applied on the Schlieren flame images and the flame radius,  $R(\theta, t)$ , was determined as a function of time,  $t$ , and angle,  $\theta$ . The tracked lines are plotted in the third row of each column in Figure 6.3. From the tracking results, the average flame radius of a wrinkled flame front is defined as,

$$R_{av}(t) = \frac{1}{\Lambda} \int_0^\Lambda R(\theta, t) d\theta \quad (6.9)$$

where  $\Lambda$  is the angle that the selected portion of flamefront encompasses.  $\Lambda$  is slightly less than  $2\pi$  most of the time for the cases where the disturbances by the ignition wires become visible, for example, the flame shown in the third column of Figure 6.3. If  $\Lambda = 2\pi$ , this definition of  $R_{av}$  is equivalent to the one defined based on the area, *i.e.*,  $R_{av} = \sqrt{A_S/\pi}$ , where  $A_S$  is the surface area covered by the flame image.

Realizing the inconsistency in the fitting methods in previous studies, it is noted that the fundamental hypothesis on the self-similar propagation is applied to the velocity instead of the radius ([Bychkov & Liberman, 1996](#); [Blinnikov & Sasorov, 1996](#)).

$$U_{av} = \frac{dR_{av}}{dt} = BR_{av}^d \quad (6.10)$$

where  $B = \alpha A^{1/\alpha}$  is a constant that only depends on the properties of the mixture. This relation directly comes from the fractal description of the flame propagation. Therefore, this formula is employed in the present study, treating  $B$  and  $d$  as parameters for optimal fitting. As a result, the current fitting method removes the influence of initial conditions through the removal of  $t$  in the fitting equation, and

the issues in the determination of  $R_0$  or  $t_0$ .

The concern remaining is then the accuracy in the numerical differentiation of  $R_{av}$  to obtain  $U_{av}$ . For any discrete data, a straightforward numerical differentiation, such as the central differencing, will introduce additional random errors. This is either because the time step in the differentiation is too small to acquire a statistically meaningful quantity, or the poor performance of the flame front tracking technique. To suppress the random error introduced by numerical differentiation, smoothing techniques are frequently employed. However, these techniques, such as the spline-fit or moving average, use a much longer range of the  $R-t$  data than central differencing and can thus potentially produce artificial effects, especially considering that the influences of ignition and wall confinement are to be eliminated. With these considerations in mind, no curve smoothing technique was used; rather,  $U_{av}$  was calculated by taking central difference on  $R_{av}-t$ . Owing to the quality of flamefront tracking and the averaging technique used when calculating  $R_{av}$ , the local spatial effects caused by each cusp or trough approximately cancel out. From Figure 6.4, it is seen that, the averaged velocity of the entire flamefront  $U_{av}$  is much smoother in comparison to the velocity based on the flame diameter in the horizontal direction, which was used for smooth spherical flame tracking in Kelley (2011).

## 6.4 Experimental Results

It is interesting to assess if the propagation of wrinkled flames indeed self-accelerates, and if the acceleration follows a self-similar law. In other words, if the velocity data is fitted with a power-law formula, not only should the exponent  $\alpha$  be greater

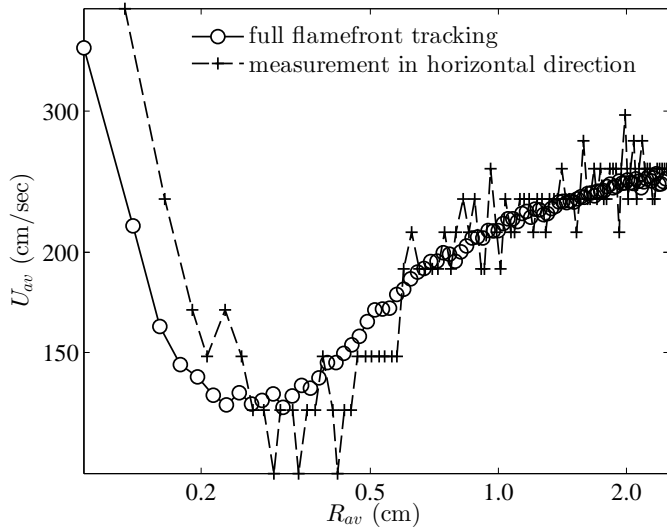


Figure 6.4: Comparison of velocity curves calculated from full flamefront tracking and that measured in the horizontal direction.

than unity but it should also be a constant, at least within a certain range of the propagation. This question is important in its own right, and needs to be addressed before conclusion on the specific values of  $\alpha$  is made. Therefore, in the following the results on individual experiments is first presented, and then present the overall characteristics of accelerated flames by looking at the dimensionless data and scaling.

#### 6.4.1 Propagation of Individual Flames

Figures 6.5a and 6.5b are logarithmic plots of the propagation velocity versus the flame radius for two experimental runs with the same mixture compositions ( $\phi = 0.60$  and 1.00, respectively) but with different ignition energies. Experiments with different ignition energies were conducted to quantify the effects of ignition and cell development on flame acceleration. It is seen that the two curves overlap after certain transition periods. In the overlapping region, the slope of the  $\log(U_{av})$  vs.

$\log(R_{av})$  remains a constant until chamber confinement starts to have an influence, at about  $R_{av} = 2.0$  cm. This result suggests that a self-similar regime does exist for wrinkled laminar flame propagation, after an initial transition period. Note that in the transition period the slope is higher than that in the self-similar regime, which agrees with numerical results ([Galanti \*et al.\*, 1998](#); [Karlin & Sivashinsky, 2006](#)).

The same phenomenon was also observed for other conditions.

In Figure 6.6 the experimentally measured acceleration exponent  $\alpha$  for hydrogen/air mixtures as a function of the fuel equivalence ratio,  $\phi$ , for various pressures are plotted. Three trends are observed. First, the values of  $\alpha$  for the lean mixtures as a group are higher than those for the rich mixtures. It is reasonable to suggest that this is due to the effect of the diffusional-thermal instability, which is cellularly de-stabilizing for lean mixtures and stabilizing for rich mixtures, and as such can lead to stronger and weaker wrinkling for these mixtures, respectively. The second trend is that, for the strongly burning mixtures, with  $\phi$  ranging from 0.60 to 1.20, increasing the pressure results in larger values of  $\alpha$ , which implies more wrinkling. This is in agreement with the anticipation in that, for a given  $\phi$ , increasing pressure reduces the flame thickness and thereby increases the propensity of the flame to become hydrodynamically unstable, leading to earlier onset, and possibly more wrinkling. It is noted, however, that for safety reasons the highest pressure studied for these flames was 10 atm. Therefore, additional experiments at higher pressures and thus thinner flames in this range of  $\phi$  are needed. Third, in the range of  $\phi = 1.4 - 2.0$ , increasing the pressure does not change the value of  $\alpha$ , within the experimental uncertainty. This can be interpreted as a sign that the maximum value of the acceleration exponent has been reached, as using flames that become unstable at an earlier point does not change the value of the acceleration exponent. It is

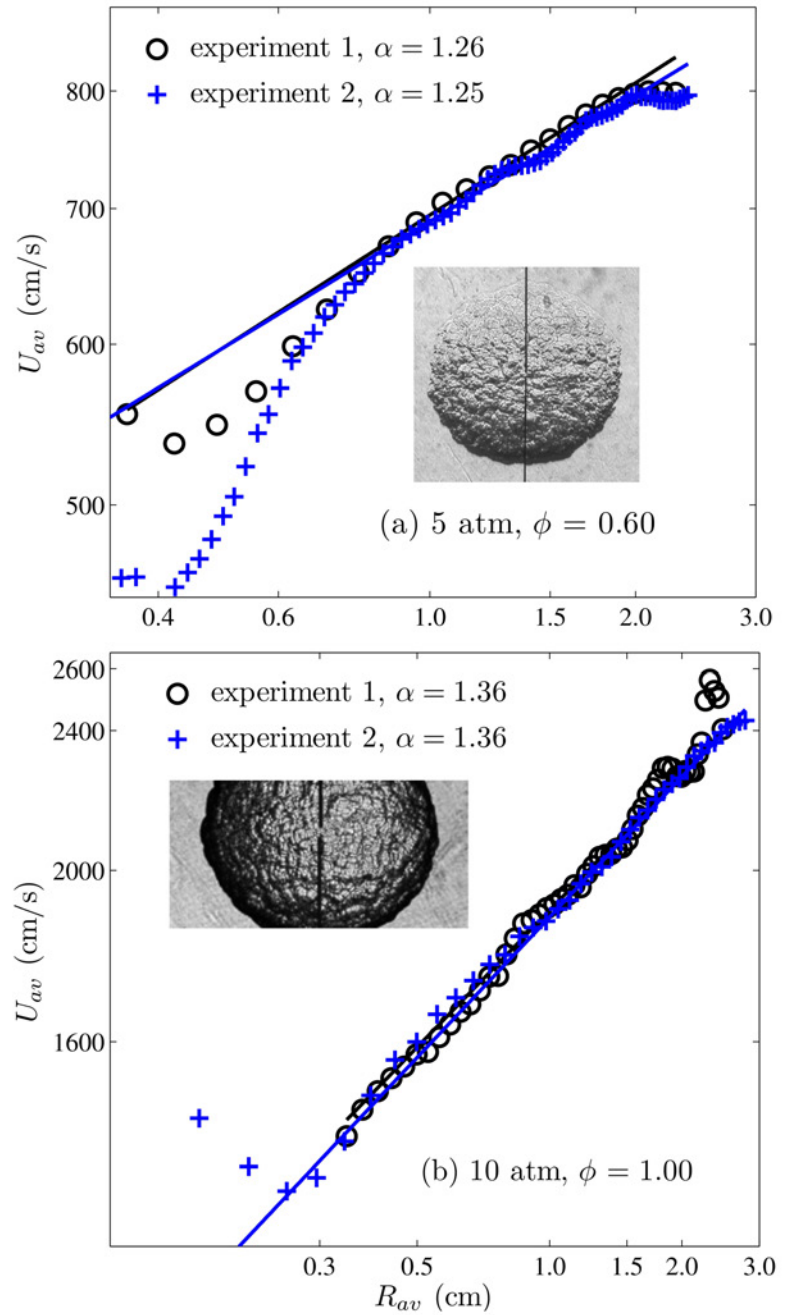


Figure 6.5: Propagation velocity for two experiments for  $H_2/air$ , at (a) 5 atm,  $\phi = 0.60$ , and (b) 10 atm,  $\phi = 1.00$ . Experiments 1 and 2 are runs with the same mixture but different ignition energies.

noted that, while the diffusional-thermal cellular instability is suppressed for the rich cases ( $Le > 1$ ), pulsating instability (Jomaas *et al.*, 2007*a*; Jomaas & Law, 2010) is activated, and its coupled effects with the hydrodynamic cells have yet to be understood. As such, inclusion of detailed chemistry in the modeling would be beneficial, in order to capture potential subtle effects associated with high-pressure chemistry.

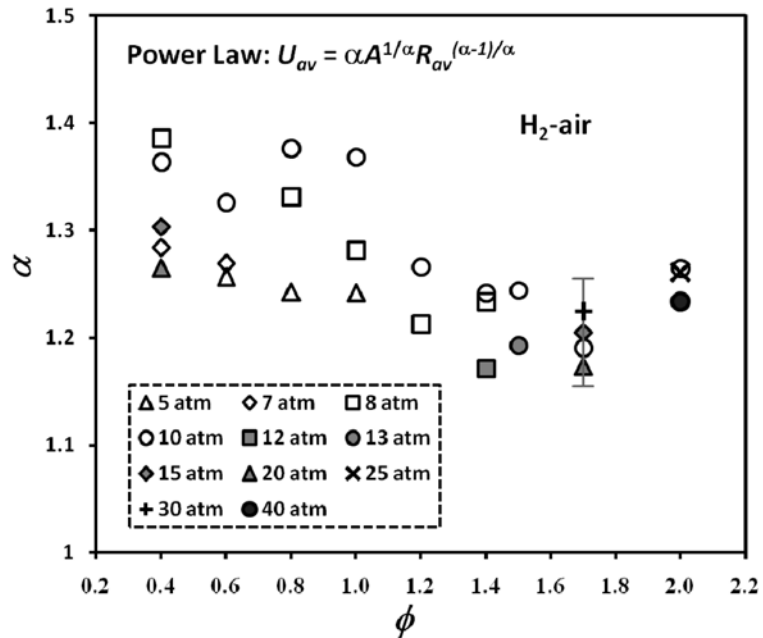


Figure 6.6: Experimental acceleration exponents for H<sub>2</sub>/air at various pressures and equivalence ratios. All data points are estimated to have uncertainty  $\pm 0.05$  which is based on the repeatability and sensitivity to the range of data selected for fitting; however, error bar is indicated only at one point for display clarity.

The promoting effect of pressure is also less conclusive for the ultra-lean case of  $\phi = 0.40$ , for which a consistent trend is not observed. Recognizing that the lean flammability limit for hydrogen/air mixtures at atmospheric pressure is about  $\phi = 0.17$ , and that increasing pressure could elevate this limit due to enhanced three-body termination reactions, it is reasonable to anticipate the possible occurrence

of local extinction and re-ignition, which would introduce additional factors in the flame propagation that are not amenable to direct interpretation.

Recognizing the potential complications due to diffusional-thermal effects in the interpretation of hydrodynamic instability on the self-similar propagation, it is prudent to consider equidiffusive mixtures for which these effects are suppressed. For hydrogen/air mixtures this is close to the stoichiometric value of  $\phi = 1.00$ . Figure 6.6 then shows that the acceleration exponent for such mixtures assumes a maximum value of about  $\alpha = 1.37$ , occurring at 10 atm pressure. This value, determined in a manner that can be considered to be rigorous based on the current understanding and state-of-the-art investigation, is close to, but still sufficiently smaller than  $\alpha = 1.5$ , the value purportedly related to the concept of self-turbulization.

Having determined the acceleration exponents of the laminar flames, the fractal excess,  $d = 1 - 1/\alpha$ , is plotted in Figure 6.7, showing the approach to  $d = 1/3$  for the high-pressure, stoichiometric mixture.

#### 6.4.2 Dimensionless Data

The acceleration exponents and fractal excess extracted from individual data have large uncertainty. As a result, it is difficult to draw firm conclusions on their dependence on experimental variables, such as pressure and equivalence ratios. The major reason  $\alpha$  has large uncertainty is that, in the fitting formula Equation 6.10, the value of  $d$  heavily depends on the “curvature” of experimental  $U_{\text{av}}-R_{\text{av}}$  data, *i.e.*, the second derivative,  $d^2U_{\text{av}}/dR_{\text{av}}^2$ . Individual experimental data are always affected by random noise. In addition, it is not clear whether the large values of  $\alpha$  (or  $d$ ) indicate strong self-acceleration caused by flamefront cellular instabilities because from Equation 6.10 it is seen that  $U_{\text{av}}$  also depends on the value of the

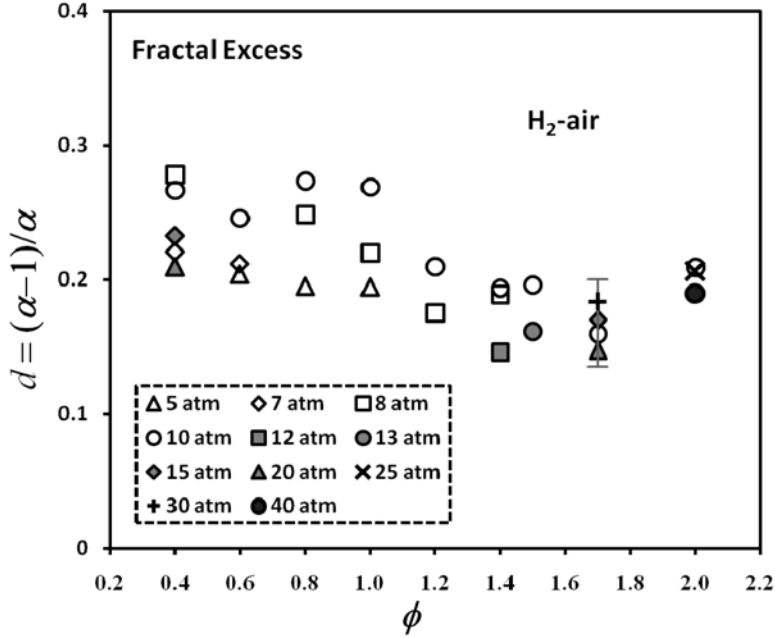


Figure 6.7: Experimental fractal excess for H<sub>2</sub>/air at various pressures and equivalence ratios. All the data points are estimated to have uncertainty  $\pm 0.03$ , which is based on the repeatability and sensitivity to the range of data selected for fitting; however, error bar is indicated only at one point for display clarity.

pre-exponential factor  $B$ .

Therefore, a reasonable comparison of self-acceleration at different experimental conditions is to compare their flame speeds directly, rather than only looking at the value of  $\alpha$  (or  $d$ ). However, the dimensional data  $U_{\text{av}}$  and  $R_{\text{av}}$  are not suitable for comparison because they also include information about the chemical reactivity of mixtures at different conditions. In particular,  $U_{\text{av}}$  and  $R_{\text{av}}$  in Figure 6.5 are dimensional, and should be appropriately normalized by the length scale and time scale of a reference flame. From the fractal hypothesis of cellular flame and Figure 6.1, it is seen that the self-acceleration mechanism is purely a geometry problem, *i.e.*, the increase in the global flame speed is due to the increase in total flame surface area  $A_f$ . As demonstrated by [Liberman \*et al.\* \(2004\)](#), the fractal structure

of a flamefront can be described as a cascade of cusps, similar to the Koch Flake (Figure 6.1). From the definition of fractal, the ratios of length scale and total surface area (in Koch Flake, the total length since it is 2-D) are fixed. Then we have,

$$\frac{A_{\max}}{A_{\min}} = x^N \quad (6.11)$$

$$\frac{\lambda_{\max}}{\lambda_{\min}} = y^N \quad (6.12)$$

where  $A_{\max}$ ,  $A_{\min}$  are the maximum and minimum surface area among all the generations, which correspond to the Nth and 1st generations;  $\lambda_{\max}$ ,  $\lambda_{\min}$  are the maximum and minimum characteristic length scale among all the generations, which correspond to the 1st and Nth generations; and  $x$  and  $y$  are constants. From Equations 6.11 and 6.12, we have,

$$\frac{A_{\max}}{A_{\min}} = \left( \frac{\lambda_{\max}}{\lambda_{\min}} \right)^d \quad (6.13)$$

with

$$d = \frac{\log x}{\log y}$$

For expanding cellular flames,  $A_{\max} = A_f$ ,  $A_{\min} = 4\pi R_{\text{av}}$ ,  $\lambda_{\max} = R_{\text{av}}$  and  $\lambda_{\max} = \delta_L$ , where  $\delta_L$  is the flame thickness. If the flame speed for unit surface area is assumed constant and equal to  $S_b^0$ , we have,

$$\frac{U_{\text{av}}}{S_b^0} = \frac{A_f}{4\pi R_{\text{av}}} = \left( \frac{R_{\text{av}}}{\delta_L} \right)^d \quad (6.14)$$

It is seen from Equation 6.14 that to compare the self-acceleration of flames at different conditions, the flame speed and radius should be normalized by  $S_b^0$  and  $R_{\text{av}}$ ,

respectively. For the present experimental conditions, since the flames are cellular  $S_b^0$  cannot be measured from experiments. To compute the values of  $S_b^0$  and  $\delta_L$ , the recent H<sub>2</sub>-O<sub>2</sub> chemical kinetic model by Burke *et al.* (2012) was used. The method for calculating the flame thickness  $\delta_L$  is based on Equation 3.10. Figures 6.8 and 6.9 plot the calculated  $S_u^0$ ,  $S_b^0$ , burning flux  $f = S_u^0 \rho_u$  and  $\delta_L$ , respectively. As expected, although the burning flux increases with pressure,  $S_b^0$  reduces with pressure due to the density effect. From Figure 6.9 it is seen that  $\delta_L$  reduces at a much higher slope than  $S_b^0$  with pressure, a factor of 7 from 1 to 5 atm. As a result, the Peclet number  $Pe = R_{av}/\delta_L$  largely increases from 80 at 1 atm to approximately 2500 at 40 atm.

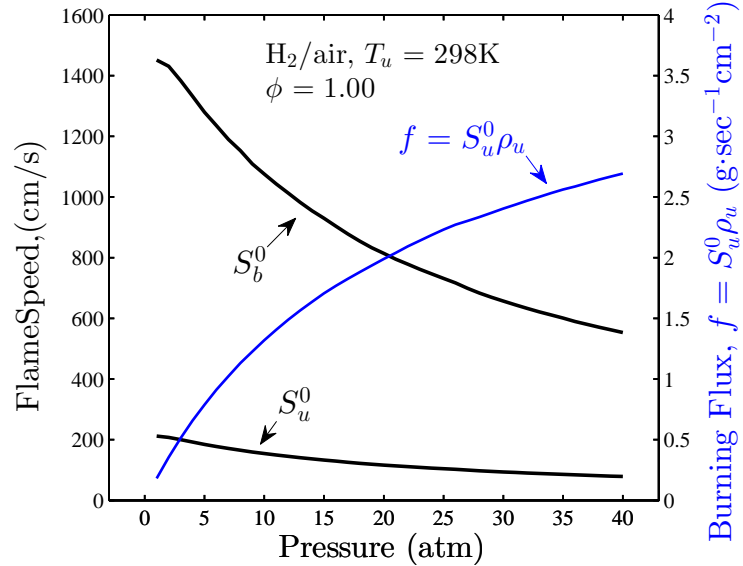


Figure 6.8: Calculated flame speeds  $S_u^0$ ,  $S_b^0$  and burning flux  $f = \rho_u S_u^0$  for stoichiometric H<sub>2</sub>/air mixture at various pressures (where  $\rho_u$  is the density of the unburned gas). The recent H<sub>2</sub>-O<sub>2</sub> chemical kinetic model by Burke *et al.* (2012) was used.

The data for  $\phi = 1.00$  at different pressures are first investigated. At  $\phi = 1.00$ , the Lewis number ( $Le$ ) is close to unity (1.1, calculated using Chemkin Transport package). Therefore, the thermodiffusive effect ( $Le$  effect) is negligible and the result

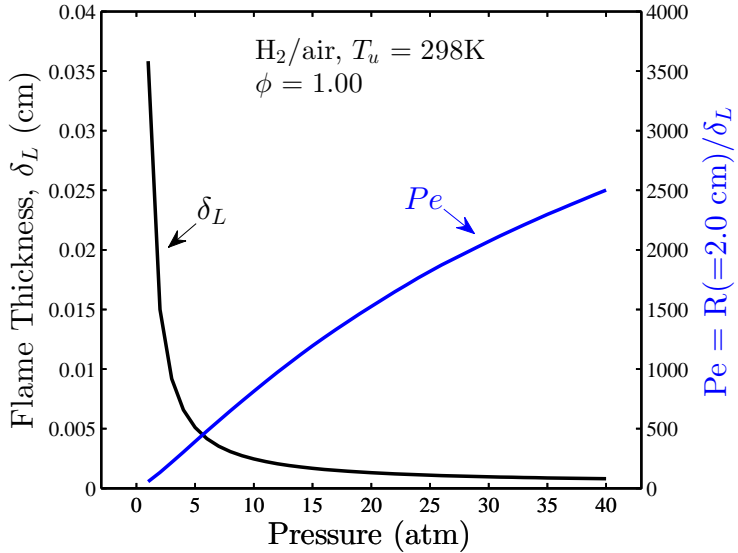


Figure 6.9: Calculated flame thickness  $\delta_L$  and Peclet number  $Pe = R/\delta_L$  for stoichiometric  $H_2$ /air mixture at various pressures. The value of  $R$  is set to be 2.0 cm in this plot as it is approximately the size of a typical flame. The recent  $H_2$ - $O_2$  chemical kinetic model by [Burke et al. \(2012\)](#) was used.

is only affected by the hydrodynamic (Darrieus-Landau) instability. Figures 6.10 and 6.11 plot  $U_{av}$ - $R_{av}$  data at  $\phi = 1.00$  from 1 to 10 atm in linear and log-log scale, respectively. It is seen that the data at 1 atm show very weak acceleration (with fitting result  $d = 0.06$ ). This is reasonable because there is no instability formed at such low pressure and the change in flame speed is only due to the stretch effect on stable flames, which is relatively weak. At 2 atm, it is seen that the flame acceleration for  $R_{av} < 2.0$  cm is also weak ( $d = 0.06$ ). However, there is a sudden increase in flame speed at around  $R_{av} < 2.2$  cm, when the instability occurs. It is seen that although the flame speed is affected by the chamber confinement effect at this radius, which reduces the flame speed, the acceleration is still very strong ( $d = 0.65$ ). At 3 atm, the sudden increase in flame speed occurs at smaller radius around

$R_{av} = 1.2$  cm. At 5 atm and higher, the onset of instability occurs at smaller radius and the effect is mixed with the effect of spark ignition. Nevertheless, it is seen that the flame acceleration progresses with nearly constant slope with  $d = 0.25 \sim 0.27$  throughout the observation range. From these dimensional data it is therefore seen that the flame self-acceleration is non-monotonic with pressure, with  $d=0.06, 0.65, 0.25\sim0.27$  at 1, 2 and 7~10 atm.

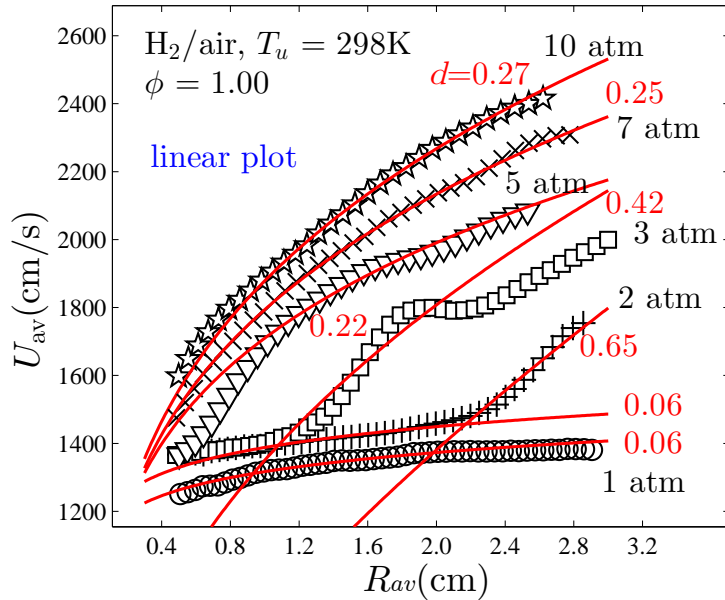


Figure 6.10: Experimental data  $U_{av}$ - $R_{av}$  for  $H_2$ /air at  $\phi=1.00$  from 1 to 10 atm, plotted in linear scale.

Figures 6.12 and 6.13 plot  $U_{av}/S_b^0$ - $R_{av}/\delta_L$  data at  $\phi = 1.00$  from 1 to 10 atm in linear and log-log scale, respectively. It is seen that the normalized data at different pressures approximately collapse on a single curve. Considering the uncertainty in the calculation of  $S_b^0$  and  $\delta_L$  based on chemical kinetic mechanism, a perfect collapse of data at all pressures is not expected. Since the normalized data collapse on one curve, the non-monotonic self-acceleration behavior can now be explained. That

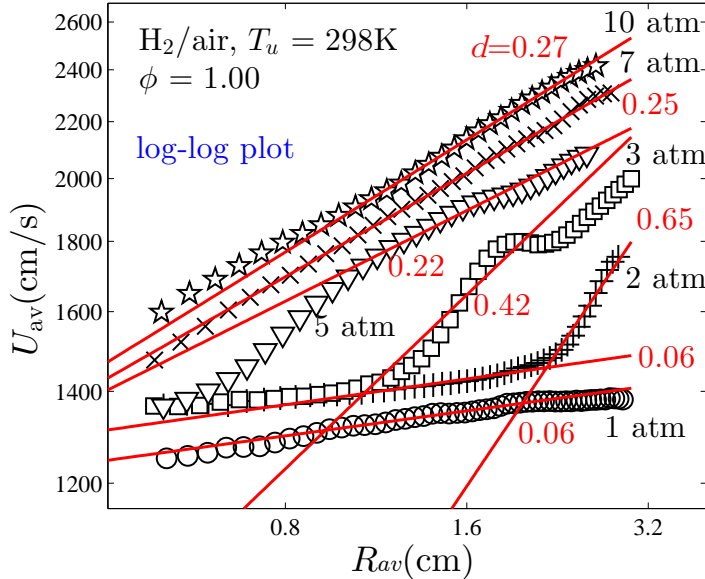


Figure 6.11: Experimental data  $U_{av}$ - $R_{av}$  for  $H_2$ /air at  $\phi=1.00$  from 1 to 10 atm, plotted in log-log scale.

is, the self-acceleration have three stages. When  $Pe < 150$ , there is no cellular instability and the weak acceleration ( $d \sim 0.06$ ) is only due to the global stretch effect. For  $150 < Pe < 300$ , cellular instability occurs and suddenly increases the flame speed. The acceleration is very strong ( $d \sim 0.65$ ,  $\alpha = 1/[1-d] \sim 2.85$ ) in this transient period. For  $Pe > 300$ , the self-acceleration reaches a constant slope in the log-log plot with  $d \sim 0.28$  and  $\alpha \sim 1.38$ . The result here further suggests that the propagation of cellular flames is self-similar for a wide range of  $Pe$  (300-1000). However, before the acceleration becomes self-similar there is a transient period during which the acceleration is much stronger.

At  $\phi = 1.00$ , the Lewis number  $Le$  and the Markstein number  $Ma$  are close to 1 and 0, respectively. However, it is not the case for other equivalence ratios. Figure 6.14 plots the calculated and experimentally determined  $Le$  and the burned gas Markstein number  $Ma_b$  for  $H_2$ /air at 1 atm for different equivalence ratios. It

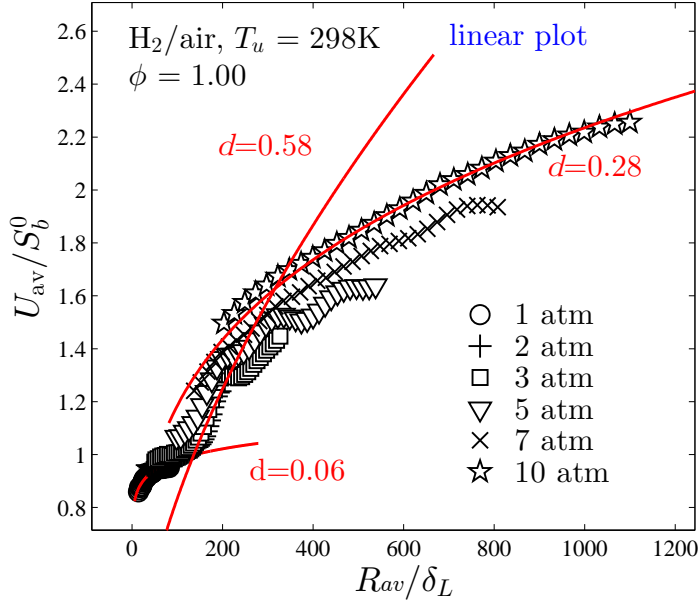


Figure 6.12: Experimental data  $U_{av}/S_b^0$ - $R_{av}/\delta_L$  for  $H_2/\text{air}$  at  $\phi=1.00$  from 1 to 10 atm, plotted in linear scale.

is seen that both  $Le$  and  $Ma_b$  increase monotonic with  $\phi$ . At  $\phi = 1.00$ , their values are both close to unity. The value of  $Le$  and  $Ma_b$  can represents the propensity of diffusional-thermal (DT) instability. The smaller the  $Le$  and  $Ma_b$ , the less stable the flame. Another pertinent parameter that has strong dependence on  $\phi$  is the thermal expansion ratio  $\Theta$ . Thermal expansion is the reason for hydrodynamic (Darrieus-Landau) instability. Therefore, stronger hydrodynamic instability is expected for flames with higher  $\Theta$ . Figure 6.14 also plot the dependence of  $\Theta$  on  $\phi$ . It is seen that  $\Theta$  peaks at  $\phi = 1.05$  and decreases as  $\phi$  deviates from unity on the two sides.

Figures 6.15 and 6.16 plot all the  $U_{av}/S_b^0$ - $R_{av}/\delta_L$  data at various  $\phi$  and pressure in linear and log-log scale, respectively. The data for  $\phi$  from 1.7 to 2.0 are re-plotted in a smaller scale for clarity in Figures 6.17 and 6.18. Two observations can be made here. First, the normalized flame speed  $U_{av}/S_b^0$  substantially decreases with  $\phi$  for the

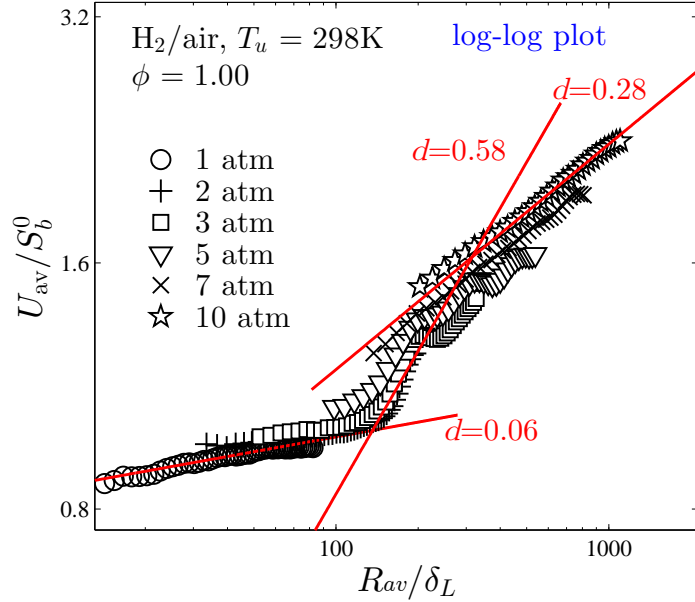


Figure 6.13: Experimental data  $U_{\text{av}}/S_b^0$ - $R_{\text{av}}/\delta_L$  for H<sub>2</sub>/air at  $\phi=1.00$  from 1 to 10 atm, plotted in log-log scale.

same value of  $R_{\text{av}}/\delta_L$ . This means the diffusional-thermal effect is strong on flame propagation. At  $\phi = 0.60$ ,  $U_{\text{av}}/S_b^0$  reaches 4.0 at 10 atm and  $Pe = R_{\text{av}}/\delta_L = 200$ . While at  $\phi = 2.00$ ,  $U_{\text{av}}/S_b^0$  is less than 1.5, even at 40 atm and  $Pe = R_{\text{av}}/\delta_L = 3000$ . Noticing the since  $Le$  and  $\text{Ma}_b$  both increases with  $\phi$  monotonically, it means the propensity of diffusional-thermal instability decreases with  $\phi$  monotonically. On the other hand,  $\Theta$  increases with  $\phi$  for  $\phi < 1.05$  but decreases with  $\phi$  for  $\phi = 1.05$ , so the propensity of hydrodynamically also increases with  $\phi$  for  $\phi < 1.05$  and decreases with  $\phi > 1.05$ . Consequently, for rich conditions both the  $Le$  and  $\Theta$  effects tend to suppress instability and reduce flame propagation speed. It is not clear which one has the stronger influence. For lean conditions, as  $\phi$  becomes smaller the  $Le$  effect tends to promote cellular instability while the  $\Theta$  effect tends to suppress cellular instability. However, from the experimental data, it is seen that the  $Le$  effect has

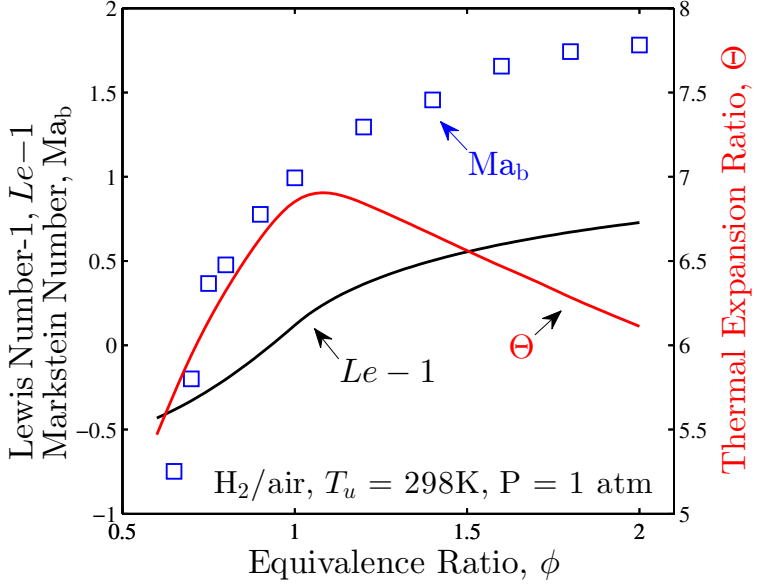


Figure 6.14: Calculated Lewis number  $Le$  (plotted as  $Le-1$ ), thermal expansion ratio  $\Theta$  using the Chemkin II package and experimental determined burned gas Markstein number  $Ma_b$  for  $H_2/air$  at 1 atm for different equivalence ratios.  $Ma_b$  is extracted from the experimental  $R(t)$  data for stable flames using the NE extrapolation formula, (Equation 3.8). The theoretically derived formula for the effective Lewis number of a mixture of two reactants by Matalon *et al.* (2003) is used for calculating  $Le$ .

the dominant influence over  $\Theta$ .

The second observation that can be made from Figures 6.15 and 6.16 is that, for rich conditions ( $\phi > 1.00$ ), *i.e.*,  $\phi = 1.00, 1.40, 1.70$  and  $2.00$ , the data at different pressures approximately fall on a single curve. This indicates that the influence of pressure is only through the decrease in the flame thickness  $\delta_L$ , which is the lower cutoff length scale for the fractal description of cellular flames. However, for lean conditions ( $\phi < 1.00$ ), *i.e.*,  $\phi = 0.80$  and  $0.60$ , although the individual  $U_{av}/S_b^0 \cdot R_{av}/\delta_L$  data at fixed pressure still show a good power-law dependence, the data at different pressures do not fall on a single curve. Specifically, at lean conditions the

value of  $U_{av}/S_b^0$  is higher at higher pressures for the same value of  $R_{av}/\delta_L$ . This indicates that the influence of pressure is not only through the decrease in  $\delta_L$  but also some other effects which is not captured in the fractal description. Such a difference at lean and rich conditions is consistent with the recent numerical studies by Mukaiyama *et al.* (2013), whose results suggest that hydrodynamically unstable flames exhibit fractal character but diffusional-thermally unstable flames do not.

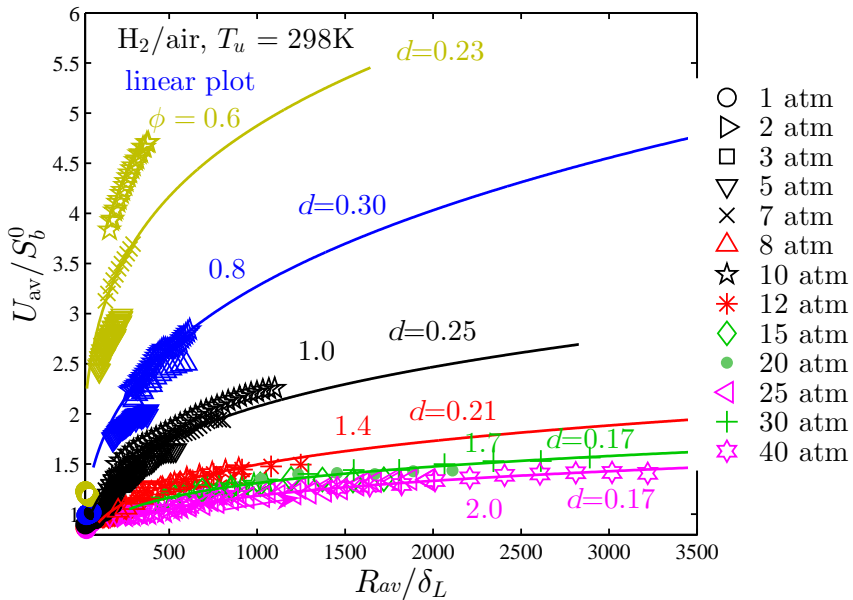


Figure 6.15: Experimental data  $U_{av}/S_b^0$ - $R_{av}/\delta_L$  for  $H_2/\text{air}$  for various pressures and  $\phi$  from 0.6-2.0, plotted in log-log scale.

From the above results, it is seen that the normalized flame speed  $U_{av}/S_b^0$  increases with  $Pe = R_{av}/\delta_L$ . However, there is substantial dependence on  $\phi$ . It might be of interest if the  $\phi$  can be explained by some simple mechanism. It is seen from Chapter 3 that the Markstein length  $L_b = \text{Ma}_b \delta_L$  (where  $\text{Ma}_b$  is defined to be burned gas Markstein number) is the only length scale to describe the stable stretched flame speed, as seen from the equations listed in Table 3.1. Figure 6.19

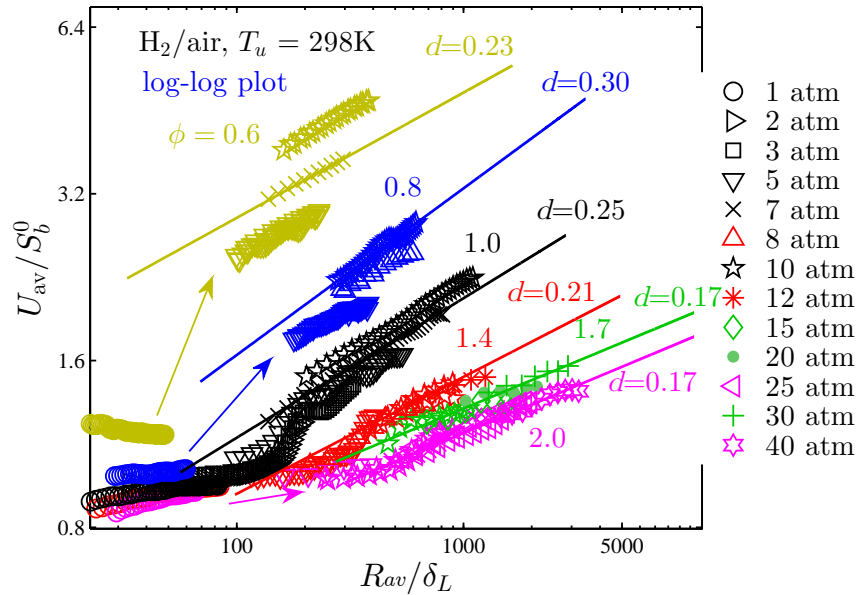


Figure 6.16: Experimental data  $U_{av}/S_b^0$ - $R_{av}/\delta_L$  for  $H_2$ /air for various pressures and  $\phi$  from 0.6-2.0, plotted in log-log scale.

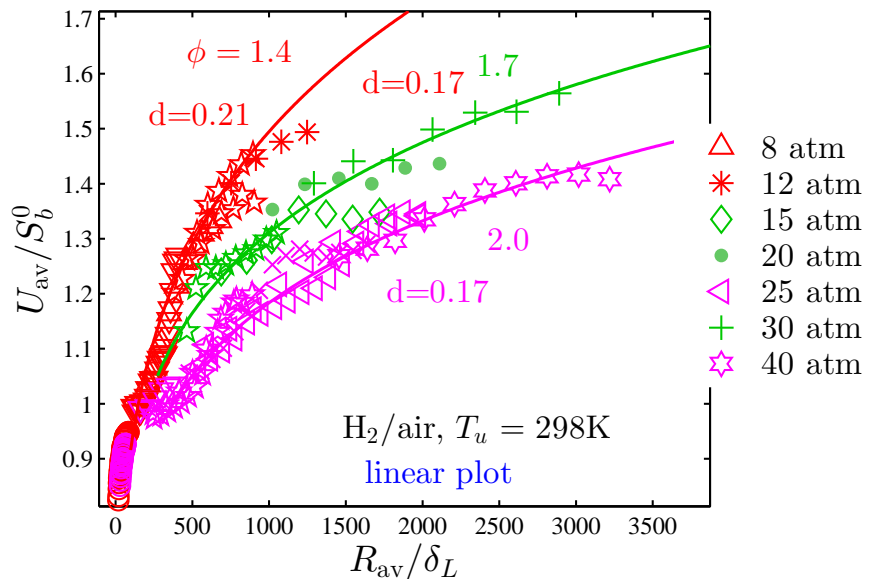


Figure 6.17: Experimental data  $U_{av}/S_b^0$ - $R_{av}/\delta_L$  for  $H_2$ /air for various pressures and  $\phi$  from 1.7-2.0, plotted in log-log scale.

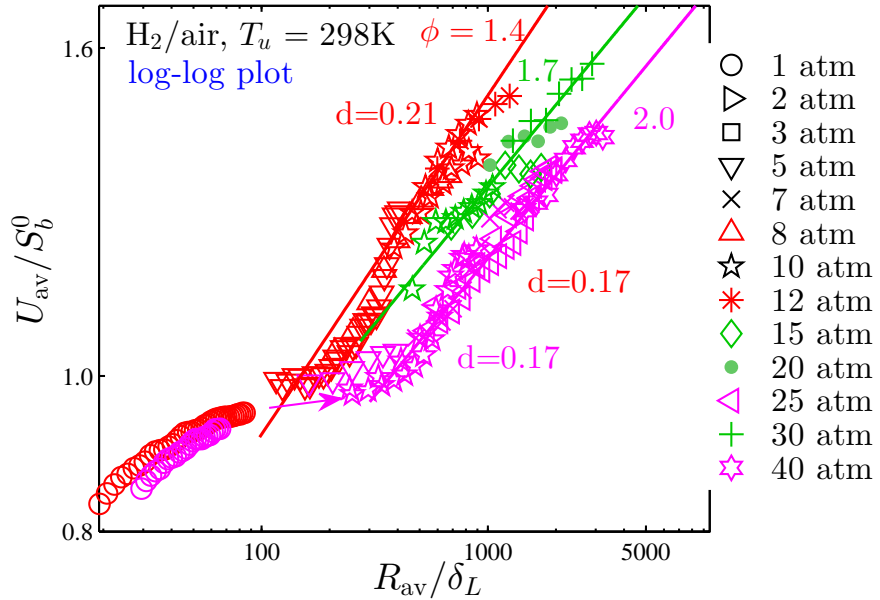


Figure 6.18: Experimental data  $U_{av}/S_b^0$ - $R_{av}/\delta_L$  for H<sub>2</sub>/air for various pressures and  $\phi$  from 1.7-2.0, plotted in log-log scale.

plots all the data from  $\phi = 0.80$  to  $2.00$  ( $L_b < 0$  at  $\phi = 0.60$ ) with  $\delta_L$  replaced by  $L_b$ , *i.e.*, the  $U_{av}/S_b^0$  versus  $R_{av}/L_b$  plot. It is seen that although the difference between data for different  $\phi$  is smaller compared to Figure 6.16, they still do not fall on a single curve. This means the dependence of cellular flame propagation on  $\phi$  is stronger than the  $Ma_b^{-1}$  dependence. More investigations are needed to explain the  $\phi$  dependence.

Finally, Figure 6.20 plots additional data on H<sub>2</sub>/O<sub>2</sub>/He and H<sub>2</sub>/O<sub>2</sub>/Ar mixtures at  $\phi = 1.00$ . By holding  $\phi$  unchanged and using He and Ar, it can be ensured that the combustion chemistry and thermal expansion ratio are not altered since He and Ar have almost the same specific heat and thus the same adiabatic flame temperature. However, the mixtures with He as the inert have significantly higher  $Le$  due to the small molecular weight of He. From Figure 6.20 it is seen that the

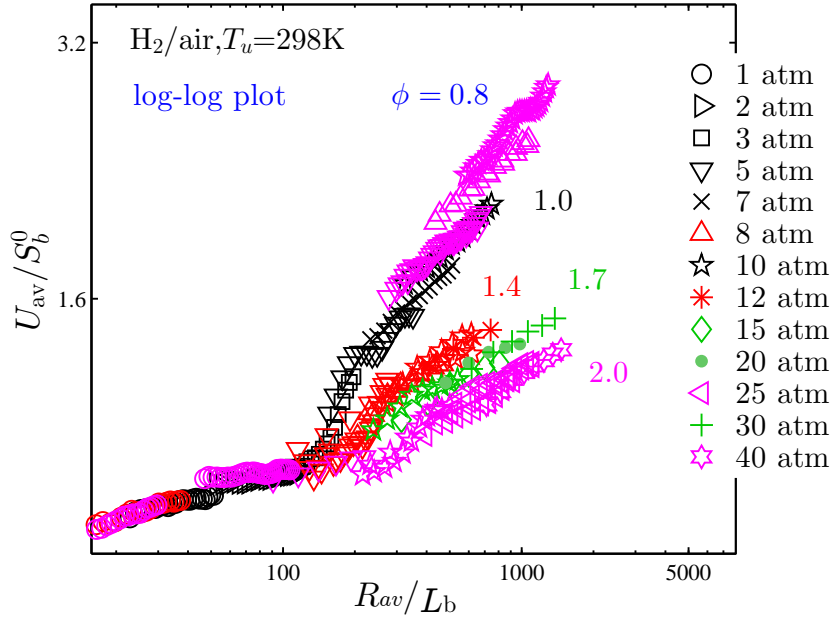


Figure 6.19: Experimental data  $U_{av}/S_b^0$ - $R_{av}/L_b$  for  $H_2$ /air for various pressures and equivalence ratios, plotted in log-log scale.

$U_{av}/S_b^0$ - $R_{av}/\delta_L$  data also exhibit the three-stage propagation regimes, *i.e.*, stable flame propagation, transient period after instability onset with strong acceleration and self-similar propagation with power-law dependence. In addition, it is seen that flamefront instability occurs at small value of  $R_{av}/\delta_L$  for  $H_2/O_2/Ar$  than  $H_2/O_2/He$  because the  $Le$  associated with  $H_2/O_2/Ar$  is smaller.

## 6.5 Concluding Remarks

In the present study, the extent of rigor in the various claims of self-similarity in previous studies of the self-acceleration of expanding spherical flames, particularly on the attainment of 1.5 for the power-law acceleration exponent, is first critically discussed. The conclusion is that the evidences presented in some of these prior

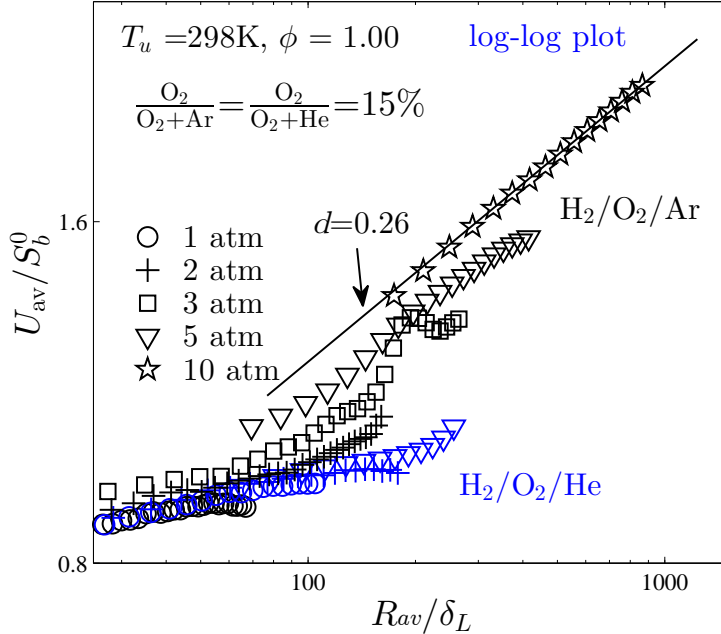


Figure 6.20: Experimental data  $U_{av}/S_b^0$ - $R_{av}/\delta_L$  for  $\text{H}_2/\text{O}_2/\text{He}$  and  $\text{H}_2/\text{O}_2/\text{Ar}$  at  $\phi = 1.00$  for various pressures, plotted in log-log scale.

studies were not rigorously interpreted, and as such the claim of the 1.5 exponent, motivated by the initial suggestion of Gostintsev *et al.* (1988) based on results of uncertain accuracy, and by the attractiveness of its potential implication on self-turbulization, is not justified.

Being mindful of the above concern, experiments with considerable caution and thoroughness have been designed, conducted and analyzed. The results suggest that self-acceleration definitely exists and self-similarity, subsequent to the initial transient, most likely exists. The power-law exponents measured in the present study, however, still seem to weakly depend on the system pressure and the intensity of the diffusional-thermal instability, and as such has not reached the hydrodynamic, flame-sheet limit.

The data of normalized flame speed  $U_{av}/S_b^0$  versus normalized flame radius

(Peclet number)  $R_{av}/\delta_L$  suggest three stages for propagation of cellular flames, *i.e.*, the stable flame propagation before instability occurs, the transient propagation stage with strong acceleration immediately following instability onset, and finally the self-similar propagation with power-law dependence.

# Chapter 7

## Turbulent Flame Speed Scaling For Expanding Flames

### 7.1 Introduction

In Chapters 3, 4 and 5, the study on laminar flame speeds using expanding flames has been presented, and in Chapter 6 the effects of flamefront cellular instabilities on propagation of expanding flames have also been presented. However, in almost all practical applications (perhaps except candle flames), the flow is turbulent since there is a need to increase the flow and burning rate. Therefore, understanding the interactions between flames and the turbulent flow field is crucial for developing predictive models for combustion applications.

In premixed turbulent combustion, understanding the overall burning rate, or, in other words, the turbulent flame speed, is an essential task. The problem has been addressed by the large volume of analytical ([Damköhler, 1940](#); [Clavin & Williams, 1979](#); [Yakhot, 1988](#); [Kerstein \*et al.\*, 1988](#); [Kerstein & Ashurst, 1992](#); [Lipatnikov &](#)

Chomiak, 2007; Kolla *et al.*, 2010), experimental (Abdel-Gayed *et al.*, 1987; Bradley *et al.*, 2011; Filatyev *et al.*, 2005; Kobayashi *et al.*, 1996, 2005; Venkateswaran *et al.*, 2011), computational (Bell *et al.*, 2005; Shim *et al.*, 2011) and review literature (Bradley, 1992; Peters, 2000; Driscoll, 2008; Lipatnikov & Chomiak, 2002, 2005; Pope, 1987). There is the interest to seek a unified scaling description of turbulent flame speeds, which not only enrich our fundamental understanding of the complex problem, but can also be utilized as a subgrid scale model for Large Eddy Simulations of combustion processes.

However, as discussed in Chapter 1, the problem is of considerable complexity and remains to be one of the most important unsolved problems in turbulent premixed combustion. Even under special conditions such as isotropic turbulence in upstream cold flow and negligible flame structure disturbance by the flow (*i.e.*, large Damkohler number, corrugated or flamelet regime), the measured turbulent flame speeds so far still show large scattering on any correlation curve and show strong geometry dependence (Driscoll, 2008), *i.e.*, the measurements on Bunsen flames (Kobayashi *et al.*, 1996, 2005; Venkateswaran *et al.*, 2011), V-flame (Smith & Gouldint, 1979), flat-flame (Shepherd & Cheng, 2001; Lawn & Schefer, 2006) and expanding flame (Abdel-Gayed *et al.*, 1987; Kido *et al.*, 2002; Bradley *et al.*, 2011) all show different characteristics. Therefore, in the literature review by Driscoll (2008), it is suggested that a preferable method is to first seek a unified understanding and scaling for one particular geometry.

Vessel II, described in Chapter 2, is a unique apparatus suitable for such an investigation on the expanding turbulent flame configuration for the following three reasons. First, the four symmetrically positioned fans generate a near isotropic turbulence, as will be shown next. This allows the flow field to be characterized by as few

parameters as possible, such as the root mean turbulent fluctuating velocity  $u_{\text{rms}}$ , the integral length scale  $L_I$  and Reynolds number. Second, the dual-chamber design of Vessel II allows for a pressure-release boundary condition at the chamber wall, such that the flame is propagating in a constant pressure flow, and the complicated couplings between the instantaneous pressure rise, flame propagation and chemical reactions are avoided. Finally, Vessel II allows us to vary the working pressure in a wide range so that the role of pressure on turbulent flame speeds can be clarified, which many previous experiments failed to do.

The present study has two major motivations. First, it aims to present an extensive experimental database of turbulent flame speeds using expanding turbulent flames. Vessel II is a unique apparatus, and the flow statistics of Vessel II have been measured and documented. Cold flow statistics were reported in [Chaudhuri \*et al.\* \(2012\)](#) and the reacting flow statistics will be reported in ([Chaudhuri \*et al.\*, 2014](#)). These data will be useful for validating both turbulent combustion models and potentially chemical kinetic models. Data for the following fuels are examined: hydrogen ( $\text{H}_2$ ), methane ( $\text{CH}_4$ ), ethylene ( $\text{C}_2\text{H}_4$ ), *n*-butane ( $\text{C}_4\text{H}_{10}$ ) and dimethylether (DME,  $\text{C}_2\text{H}_6\text{O}$ ), along with the *iso*-octane ( $\text{C}_8\text{H}_{18}$ ) data of ([Lawes \*et al.\*, 2012](#)), thereby forming a highly diverse group in terms of chemistry as well as distinct transport properties. Second, the present study aims to seek a unified scaling, at least for the special case of expanding turbulent flames propagating into near-isotropic turbulence. In the scaling, the roles of chemical kinetics, pressure, turbulence intensity, hydrodynamic length scale, and thermodiffusive transport will be clarified. It is recognized that the resulting scaling, although extensively tested against a wide range of data, is still to be verified and the boundaries of the applicable conditions need to be carefully quantified.

The results presented in this chapter have been previously published in the following two journal articles ([Chaudhuri \*et al.\*, 2012, 2013](#)):

- CHAUDHURI, S., WU, F., ZHU, D. & LAW, C. K. 2012 Flame speed and self-similar propagation of expanding turbulent premixed flames. *Physical review letters* **108**, 044503
- CHAUDHURI, S., WU, F. & LAW, C. K. 2013 Scaling of turbulent flame speed for expanding flames with Markstein diffusion considerations. *Physical Review E* **88**, 033005

## 7.2 Cold-flow Velocity Statistics

The experiments were conducted in Vessel II. During a flame experiment, fans continuously run with speed up to 8000 rpm, and generate turbulent fluctuating velocity  $u_{\text{rms}}$  up to 6 m/s. Cold-flow velocity statistics were measured, also with fans continuously running, in [Chaudhuri \*et al.\* \(2011\)](#) and recently in [Chaudhuri \*et al.\* \(2014\)](#) using high-speed PIV. The measurements were two-dimensional, taken in the center plane perpendicular to the center line of inner chamber. The measurement zone is a 40 mm  $\times$  40 mm box centered in the plane as shown in Figure 2.5. The area close to the electrodes was excluded from the PIV measurement to minimize the error due to reflection. From the measurement, the instantaneous velocity as a function of both space and time is obtained,  $u(x, y, t)$ . The spatial resolution is 0.28 mm and the time resolution is 0.25 ms. For each condition, a total of 3,000 snapshots were taken, corresponding to 750 ms.

The integral scale is estimated to be 4 mm in [Chaudhuri \*et al.\* \(2011\)](#) based on the measured two-point velocity correlation ([Pope, 2000](#)). The turbulent Reynolds

number,  $Re_T = u_{\text{rms}} L_I / \nu$  (where  $L_I$  is the integral scale while  $\nu$  the kinematic viscosity) based on the cold flow properties, varies from 0 to 16,000 for  $u_{\text{rms}}$  up to 6 m/s and pressure up to 10 atm. The Taylor Reynolds number,  $Re_\lambda = u_{\text{rms}} \lambda_g / \nu$  varies from 0 to 323, using the relation  $Re_\lambda = (20Re_T/3)^{1/2}$  (Pope, 2000), where  $\lambda_g$  is the transverse microscale.

The measured cold-flow velocity is adopted here to demonstrate the near isotropic cold-flow near the center of the inner chamber of Vessel II. The Reynolds averaged mean velocity  $U(x, y)$  and root-mean-square of the turbulent velocity fluctuations  $u_{\text{rms}}(x, y)$  can be calculated,

$$U(x, y) = \overline{u(x, y, t)} \quad (7.1)$$

and

$$u_{\text{rms}}(x, y) = \left[ \overline{(u - U)^2} \right]^{1/2} \quad (7.2)$$

where the over line means time average. To investigate the spatial dependence of  $U$  and  $u_{\text{rms}}$ , the following quantities are considered,

$$u_{\text{rms}}(r) = \langle u_{\text{rms}}(x, y) \rangle_\theta, \quad u_{\text{rms}}(\theta) = \langle u_{\text{rms}}(x, y) \rangle_r \quad (7.3)$$

$$U_r(r) = \langle U_r(x, y) \rangle_\theta, \quad U_r(\theta) = \langle U_r(x, y) \rangle_r \quad (7.4)$$

$$U_\theta(r) = \langle U_\theta(x, y) \rangle_\theta, \quad U_\theta(\theta) = \langle U_\theta(x, y) \rangle_r \quad (7.5)$$

where  $U_r(x, y)$  and  $U_\theta(x, y)$  are the radial and tangential components of the mean velocity  $U(x, y)$  at any coordinate  $(x, y)$ .  $\langle \cdot \rangle_r$  indicates the spatial average over a  $2\Delta r$  circular strip with mean radius  $r$  centering at the center of the chamber, *i.e.*,

any spatial points between  $r - \Delta r$  and  $r + \Delta r$ ; while  $\langle \cdot \rangle_\theta$  indicates the spatial average over a  $2\Delta\theta$  circular sector with mean angle  $\theta$  centering at the center of the chamber, *i.e.*, any spatial points between  $\theta - \Delta\theta$  and  $\theta + \Delta\theta$ .  $\Delta r$  and  $\Delta\theta$  are chosen to be 0.5 mm and  $\pi/6$ , respectively. Therefore, these averaged quantities indicate the  $r$  and  $\theta$  dependence of  $u_{\text{rms}}$ ,  $U_r$  and  $U_\theta$ .

Figure 7.1 plots the spatially averaged cold-flow  $u_{\text{rms}}$ ,  $U_r$  and  $U_\theta$  for two fan speeds: 2000 and 4000 rpm, with CH<sub>4</sub>/air at  $\phi = 0.9$  and 1 atm as the working fluid. It is seen that the values of  $u_{\text{rms}}$  are approximately constant with respect to both  $r$  and  $\theta$ , indicating that the turbulence intensity is near isotropic and homogenous near the center of the chamber. From the mean flow, it is seen that although the tangential velocity  $U_\theta$  is close to zero, there are negative values for  $U_r$  for all values of  $r$  and  $\theta$ . This means the stirring fans do cause an inward mean flow. However, from Figure 7.1, it is seen that the magnitude of  $U_r$  is only about 1/3 of  $u_{\text{rms}}$ . It increases with  $r$  but approximately constant with  $\theta$ .

From flow continuity, an inward mean  $U_r$  in the laser measurement plane suggests that there could also be a mean outward  $U_z$  ( $z$  is defined to be the coordinate in the direction of camera line of sight) from the center of the chamber. These information can be used for the mean flow correction of measured turbulent flame speeds. However, three-dimensional flow statistics is to be determined to further verify the mean flow and turbulence intensity throughout the inner chamber.

Finally, the cold-flow statistics could be different from the flow statistics when a flame is present. Recent measurements in Chaudhuri *et al.* (2014) on the flow statistics with presence of a flame show that the mean  $U_r$  is canceled out by the thermal expansion of the flame, but the turbulence intensity remains to be the same.

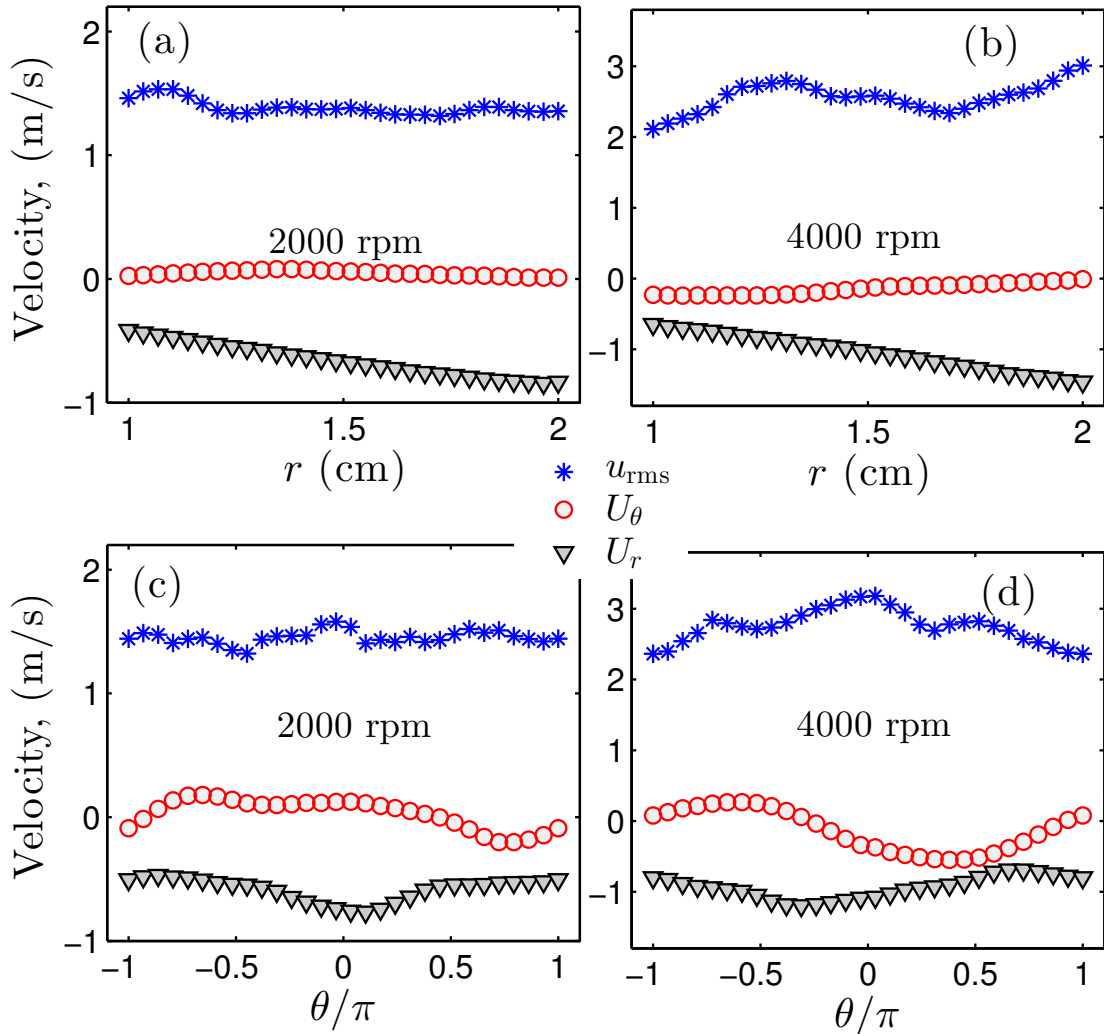


Figure 7.1: Spatially averaged cold-flow  $u_{\text{rms}}$ ,  $U_r$  and  $U_\theta$  as function of  $r$  and  $\theta$  for fan speed 2000 rpm and 4000 rpm, respectively. The gas mixture used is CH<sub>4</sub>/air at  $\phi = 0.9$  and 1 atm. The gas temperature is kept at 300 K. Data re-produced from the measurements in Chaudhuri *et al.* (2014).

### 7.3 Experimental Specifications

Figure 7.2 shows a set of Schlieren images of methane-air turbulent premixed flames at an equivalence ratio of  $\phi = 0.9$ , with different  $u_{\text{rms}}$  and pressures, and at nearly the same radius realized at different instants of their propagation. These images show that with increasing  $u_{\text{rms}}$ , the flame propagates faster on average, and finer scale structures emerge due to the reduction of the Kolmogorov length scale as the velocity integral length scale  $L_I$  is fixed. Furthermore, with increasing pressure, the flame also propagates faster, and the flame overall appears very different due to the emergence of very small scale structures. These fine structures indicate reduction of the thickness of the laminar flamelets with increasing pressure, which also allows flame surface wrinkling at progressively smaller scales. It is recognized that all these observations are not affected by any intrinsic flame instability as it was demonstrated by laminar flame propagation experiments that cover the pressure range studied in which essentially no Darrieus-Landau instability develops. Furthermore, since the mixture composition was selected such that its effective Lewis number ( $Le$ ) is close to unity, onset of diffusional-thermal instability is suppressed, and the effect of mean curvature on the mean propagation rate due to statistical sphericity of the flame should be negligible.

In the data reduction,  $\langle R \rangle$  is defined as  $\sqrt{A/\pi}$ , where  $A$  is the area enclosed by the flame edge tracked from the high-speed Schlieren imaging using tracking procedures described in Chapter 2. Even though the flames in Figure 7.2 are not symmetric for individual realizations, ensemble averaging at the same  $\langle R \rangle$  clearly produces near perfect symmetry, as shown in the 4th column of Figure 7.2.

The domain of validated data was chosen to be  $0.21 < \langle R \rangle / R_{\text{chamber}} < 0.38$ ,

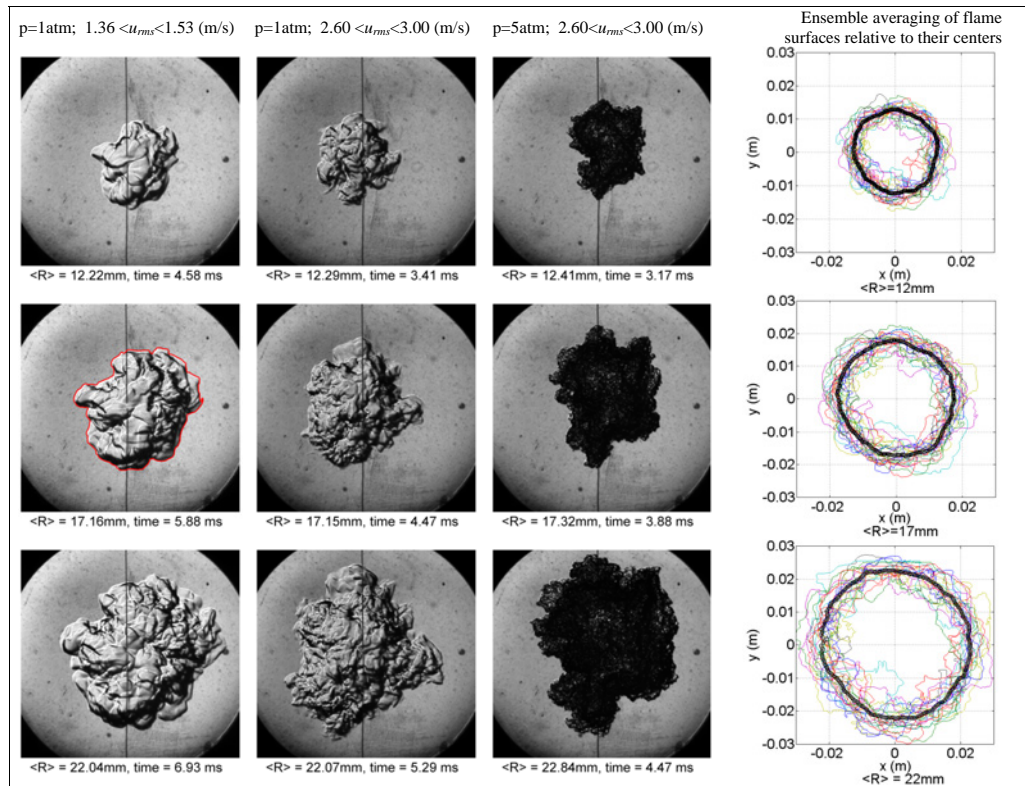


Figure 7.2: High speed Schlieren imaging at different  $u_{rms}$  and pressure, but at nearly same  $\langle R \rangle$ , showing the emergence of fine scale structures and associated increase in average propagation rate. The  $u_{rms}$  range specified above is the range experienced by the flame due to change in the largest length scale of the flame itself.

identified from laminar flame speed experiments to avoid ignition and wall effects at the initial and final stages of flame propagation. Here  $R_{\text{chamber}}$  is defined to be half of the inner cylinder diameter of Vessel II. This allowed measurements to initiate after an eddy turnover time of  $L_I/u_{\text{rms}}$ , with  $L_I$  fixed for all conditions in the present experiments.

The flame and flow properties as well as the symbols that designate each condition of the experiment in subsequent figures are given in Figure 7.3. For comparison and scaling purpose (shown later in this chapter), the recent experimental data for *iso*-octane from the University of Leeds ([Lawes \*et al.\*, 2012](#)) are also considered. The flame and flow properties of the Leeds data are listed in Figure 7.4. The fuel matrix constitutes a diverse range in the diffusive-reactive properties not only in terms of molecular diffusivity: from the light H<sub>2</sub> (Molecular Weight = 2) to the almost diffusionally neutral C<sub>2</sub>H<sub>4</sub> (28) relative to the abundant inert species N<sub>2</sub>, to the relatively heavy hydrocarbon *iso*-octane (114), but also in terms of chemical reactivity in that each of the fuel species embodies a specific kinetic feature that distinguishes it from the rest. Specifically, relative to *n*-C<sub>4</sub>H<sub>10</sub>, which can be considered as a typical paraffinic fuel, CH<sub>4</sub> is the only *n*-alkane constituted entirely by C-H bonds, rendering the initiation reaction more difficult; C<sub>2</sub>H<sub>4</sub> is the smallest alkene with a double, C=C, bond and having a high adiabatic flame temperature with correspondingly large laminar flame speeds; *iso*-octane has a branched structure that renders it knock resistant; and of course H<sub>2</sub> has a distinctively different chemistry than the hydrocarbons.

In addition to the above fuels, inclusion of DME adds further diversity to the fuel matrix under consideration in terms of fuel chemistry. DME has recently received considerable attention due to its fairly simple molecular structure yet intri-

Symbol	Fuel	Oxidizer	$\phi$	P (atm)	$T_u$ (K)	$S_u^0$ (cm/s)	$S_b^0$ (cm/s)	$\delta_L$ (cm)	$Ma_b$	$Le$
★	H <sub>2</sub>	air	4.00	5	298	113.0	544.9	0.0085	4.10	2.1
○	CH <sub>4</sub>	air	0.90	1	298	32.2	231.0	0.0480	1.18	1.0
○	CH <sub>4</sub>	air	0.90	2	298	25.0	183.0	0.0290	1.06	1.0
○	CH <sub>4</sub>	air	0.90	3	298	22.0	157.0	0.0220	0.95	1.0
●	CH <sub>4</sub>	air	0.90	5	298	17.0	122.5	0.0160	0.73	1.0
△	C <sub>2</sub> H <sub>4</sub>	15%O <sub>2</sub> +85%N <sub>2</sub>	1.30	2	298	18.0	115.0	0.0367	-1.10	1.1
▲	C <sub>2</sub> H <sub>4</sub>	15%O <sub>2</sub> +85%N <sub>2</sub>	1.30	5	298	11.0	75.0	0.0217	-0.83	1.1
▽	C <sub>2</sub> H <sub>4</sub>	air	1.30	1	298	60.9	501.0	0.0292	1.67	1.1
▽	C <sub>2</sub> H <sub>4</sub>	air	1.30	2	298	53.0	436.0	0.0161	1.72	1.1
▽	C <sub>2</sub> H <sub>4</sub>	air	1.30	3	298	47.9	395.0	0.0116	1.77	1.1
▽	C <sub>2</sub> H <sub>4</sub>	air	1.30	5	298	41.4	342.0	0.0078	1.87	1.1
◇	n-C <sub>4</sub> H <sub>10</sub>	air	0.80	5	298	18.0	118.0	0.0127	2.75	1.7
□	C <sub>2</sub> H <sub>6</sub> O	air	1.00	1	298	47.0	391.5	0.0324	2.69	1.3
□	C <sub>2</sub> H <sub>6</sub> O	air	1.00	5	298	29.0	244.3	0.0097	2.68	1.3
■	C <sub>2</sub> H <sub>6</sub> O	air	1.00	10	298	23.0	194.8	0.0060	2.78	1.3

Figure 7.3: Legends, laminar flame properties and turbulent intensity for all present experimental conditions. The flame thickness  $\delta_L$  is defined by Equation 3.10.  $\delta_L$  and the thermal expansion ratio  $S_u^0/S_b^0$  are obtained from Premix calculations within Chemkin II using the chemical kinetic models by Burke *et al.* (2012) for H<sub>2</sub>, Wang *et al.* (2007) (USC Mech II) for CH<sub>4</sub>, C<sub>2</sub>H<sub>4</sub> and n-C<sub>4</sub>H<sub>10</sub> and Zhao *et al.* (2007) for DME (C<sub>2</sub>H<sub>6</sub>O).  $S_u^0$  are determined from laminar expanding flame experiments. The burnt Markstein length  $Ma_b$  is obtained from laminar spherical flame experiments using Equation 3.8 as the extrapolation model.

Symbol	$\phi$	P (atm)	$T_u$ (K)	$S_u^0$ (cm/s)	$S_b^0$ (cm/s)	$\delta_L$ (cm)	$Le$	$Ma_b$
•	0.80	1	360	31.00	188.79	0.04	2.98	3.33
•	1.00	1	360	43.00	294.12	0.04	1.43	3.04
•	1.20	1	360	41.00	285.36	0.04	0.93	1.57
•	1.40	1	360	25.40	172.72	0.06	0.90	-1.38
•	0.80	5	360	21.00	128.31	0.01	2.98	3.96
•	0.90	5	360	25.00	164.75	0.01	2.94	3.03
•	1.00	5	360	28.00	194.60	0.01	1.43	2.77
•	1.10	5	360	29.00	204.45	0.01	0.94	2.33
•	1.20	5	360	28.00	195.72	0.01	0.93	1.88
•	1.40	5	360	24.00	163.20	0.02	0.90	NA
•	1.60	5	360	15.00	99.00	0.04	0.88	NA
•	1.80	5	360	7.30	46.65	0.05	0.86	NA
•	2.00	5	360	5.00	30.80	0.07	0.84	NA
•	0.80	10	360	16.00	97.92	0.01	2.98	3.78
•	1.00	10	360	23.00	160.77	0.01	1.43	2.49
•	1.20	10	360	24.00	168.00	0.01	0.93	NA
•	1.40	10	360	21.00	143.01	0.01	0.90	NA

Figure 7.4: Legends, laminar flame properties and turbulent intensity for all experimental conditions of *iso*-octane data from the University of Leeds (Lawes *et al.*, 2012). The  $S_b^0$  and  $Ma_b$  are obtained from experiments by Kelley *et al.* (2011b) (with  $T_u=353$  K) such that the nonlinear extrapolation technique used for other data sets in Figure 7.3 is consistent throughout. The flame thickness  $\delta_L$  and the thermal expansion ratio  $S_u^0/S_b^0$  are obtained from PREMIX calculations within Chemkin II using the chemical kinetic models by Chaos *et al.* (2007).

cate chemical effects. As such, acquisition of these turbulent flame speed data for further simulation studies employing DME chemistry is useful in its own right. It is significant to note from the onset that, in spite of the extensive range of fuel and flow conditions covered herein, the proposed scaling of this work approximately holds for all mixtures with positive Markstein number, irrespective of the fuel/air mixture, fuel chemistry, pressure and turbulence intensity.

Figure 7.5 plots the conditions of both the present experiments and the Leeds data in the regime diagram proposed by Peters *et al.* (2000). It is seen that many of the experimental conditions fall in the “thin reaction zone” regime, corresponding to the flame time scale ( $\delta_L/S_u^0$ ) larger than the Kolmogorov timescale ( $\tau_k$ ) *i.e.*,  $Ka = \delta_L/\tau_k S_u^0 > 1$ . However, even in such a regime, the flame structure may not be dominated by turbulent transport such that Lewis and Markstein number effects vanish since eddies of Kolmogorov length scale ( $\eta$ ) might not have sufficient momentum to transfer mass and heat in and out of the preheat zone. Figure 7.5 also plots the line  $Da = 1$  corresponding to  $\delta_L/S_u^0 = L_I/u_{rms}$ , as well as the line  $\delta_L = 13\eta$ , which is the characteristic length scale located at the centroid of the dissipation spectrum, suggested by Pope (1987). These two lines indicate the boundaries above which turbulent transport is expected to be predominant in the preheat zone. It is seen that most conditions considered are below these two lines. This indicates that the flamelet structure is at least partially preserved in the experimental conditions.

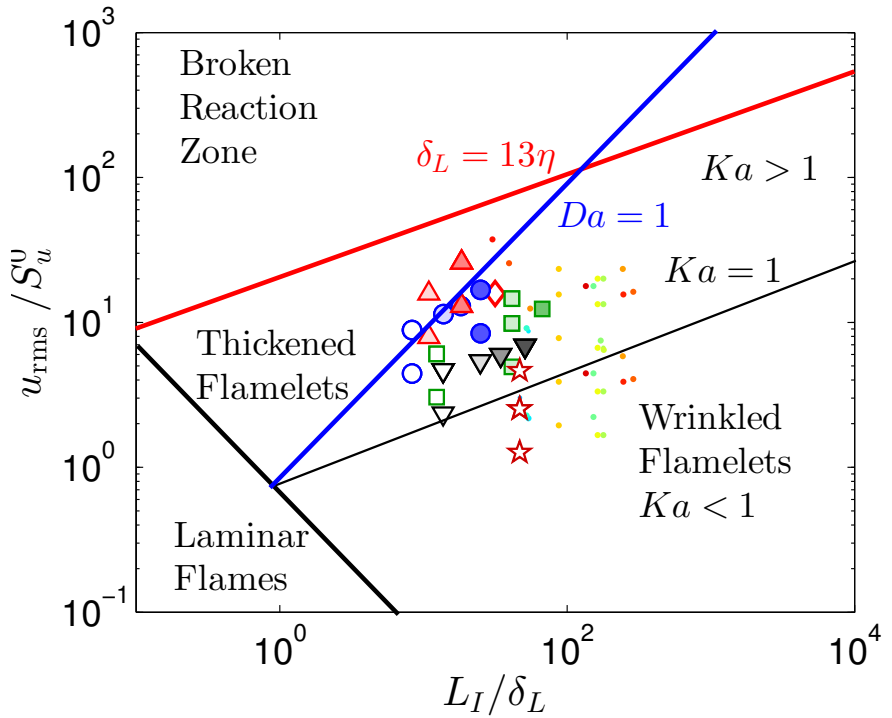


Figure 7.5: Regime Diagram with conditions of present experiments and those for *iso*-octane data from Lawes *et al.* (2012). The legends for present experimental conditions (symbols) and corresponding laminar flame and turbulence parameters could be found in Figure 7.3. The legends (dots), flame and flow parameters for the Leeds data (Lawes *et al.*, 2012) could be found in Figure 7.4.

## 7.4 Experimental Results

### 7.4.1 Raw Data and Random Error

First the raw data of all fuel/air mixtures used in the current study are plotted in Figures 7.6 and 7.7. In Figure 7.6  $\langle R \rangle$  vs. time ( $t$ ) is plotted, and in Figure 7.7  $d \langle R \rangle / dt$  vs.  $\langle R \rangle$  is plotted, where  $d \langle R \rangle / dt$  is obtained using a central difference scheme. From Figure 7.6 it is seen that all the  $\langle R \rangle$  versus  $t$  curves are concave upward, indicating flame acceleration. Figure 7.7 shows that although the values of  $d \langle R \rangle / dt$  for different mixtures vary from 2 m/s to 17 m/s, they all increase with

$\langle R \rangle$ . This means that acceleration is observed for all the expanding turbulent flames considered herein.

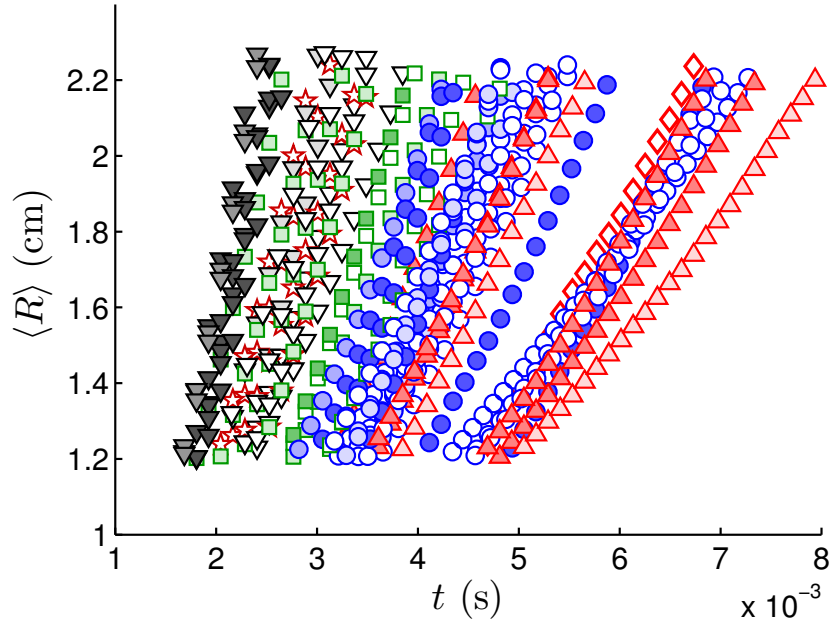


Figure 7.6:  $\langle R \rangle$  vs. time ( $t$ ) for all present experimental conditions listed in Figure 7.3.

To assess the random error of the  $d \langle R \rangle / dt$  data, the data for repeated experiments are fitted with a power-law, and the deviation of each data set from the fitted results is assessed. Figure 7.8 plots  $d \langle R \rangle / dt$  versus  $\langle R \rangle$  for seven repeated experiments for CH<sub>4</sub>/air mixtures with  $\phi = 0.9$ , 1 atm,  $u_{\text{rms}} \approx 2.85$  m/s. All the data from these seven repeated experiments were fitted as a power law, which yields  $d \langle R \rangle / dt \sim \langle R \rangle^{0.68}$ . The 95% confidence interval of this power-law fitting is  $\pm 0.73$  m/s, which is approximately  $\pm 15\%$ . Therefore, the random error of  $d \langle R \rangle / dt$  is considered to be  $\pm 15\%$ . It is noted that this 95% confidence interval does not change noticeably if other fitting equations are used, such as polynomial or rational equations.

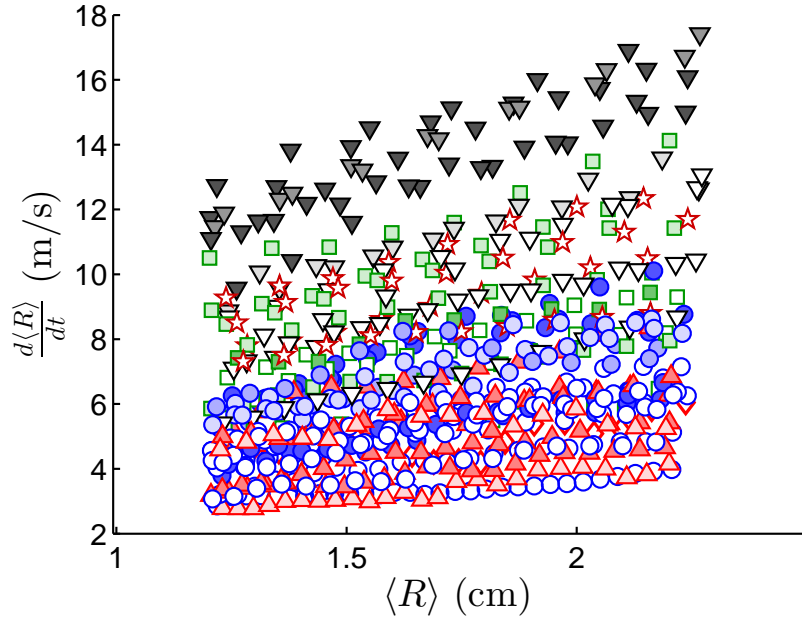


Figure 7.7:  $d \langle R \rangle / dt$  vs.  $\langle R \rangle$  for all present experimental conditions listed in Figure 7.3.

#### 7.4.2 Effective Turbulence Intensity

Previous studies have attempted to explain the acceleration of expanding turbulent flames as a consequence of the increased turbulence intensity the flame experiences as it expands (Abdel-Gayed *et al.*, 1987). Indeed, unlike a statistically stationary flame which experiences constant turbulence intensity, the effective turbulence intensity “experienced” by the expanding flame surface should be different at different stages of expansion. This is because only eddies smaller than the flame size are capable of wrinkling the flame surface, while the larger eddies would convect it.

In view of this consideration, the dependence of effective turbulence intensity on the flame size has been investigated. Consider a quantity

$$u'_{\text{eff}} = \left[ \frac{1}{2} \left( \left\langle (u_x - \langle u_x \rangle_R)^2 \right\rangle_R + \left\langle (u_y - \langle u_y \rangle_R)^2 \right\rangle_R \right) \right]^{1/2} \quad (7.6)$$

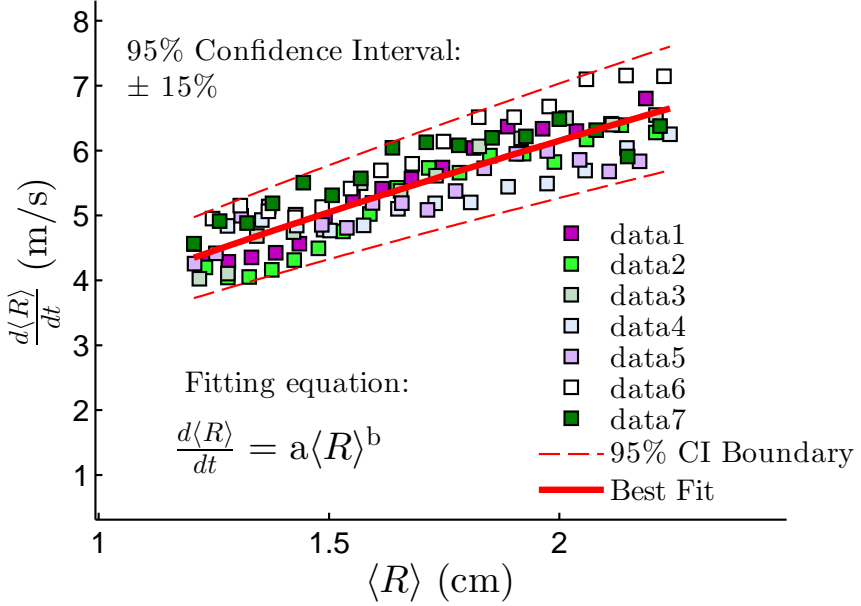


Figure 7.8: Data of  $d\langle R \rangle / dt$ - $\langle R \rangle$  and their corresponding ensemble average for 7 repeated experiments on CH<sub>4</sub>/air,  $\phi = 0.9$ , 1 atm,  $u_{rms} \approx 2.85$  m/s case. The inset text and the thick black line correspond to the best fit obtained by maximizing  $R^2$ .

where  $\langle \cdot \rangle_R$  means the spatial average over a 0.1 mm circular strip with mean radius  $R$  centering at the center of the chamber.  $u_x$  and  $u_y$  are the local velocity in the  $x$  and  $y$  directions respectively. Therefore,  $u'_{\text{eff}}$  only represent the effective turbulence fluctuation within a circular strip of radius  $R$ . It is also close to the turbulence fluctuation that an expanding flame experiences.

Figures 7.9 and 7.10 plot the instantaneous measured  $u'_{\text{eff}}$  for 2,000 time samplings for fan speed 2000 and 4000 rpm, respectively. First, it is seen that in average  $u'_{\text{eff}}$  increases with flame radius as expected. However, there is a large variation in  $u'_{\text{eff}}$  for different time samplings due to the chaotic nature of turbulence. Similar to the  $d\langle R \rangle / dt$  data, the instantaneous  $u'_{\text{eff}}$  were fitted as a power law. The 95% confidence interval of the power-law fitting shows that there is approximately  $\pm$

30% fluctuation in  $u'_{\text{eff}}$  for both fan speeds. It is believed that the fluctuation in  $u'_{\text{eff}}$  is the cause of the fluctuation in  $d \langle R \rangle / dt$ , if the relation  $d \langle R \rangle / dt \sim \sqrt{u'_{\text{eff}}}$  approximately holds, for  $1 \pm 15\% \approx \sqrt{1 \pm 30\%}$ .

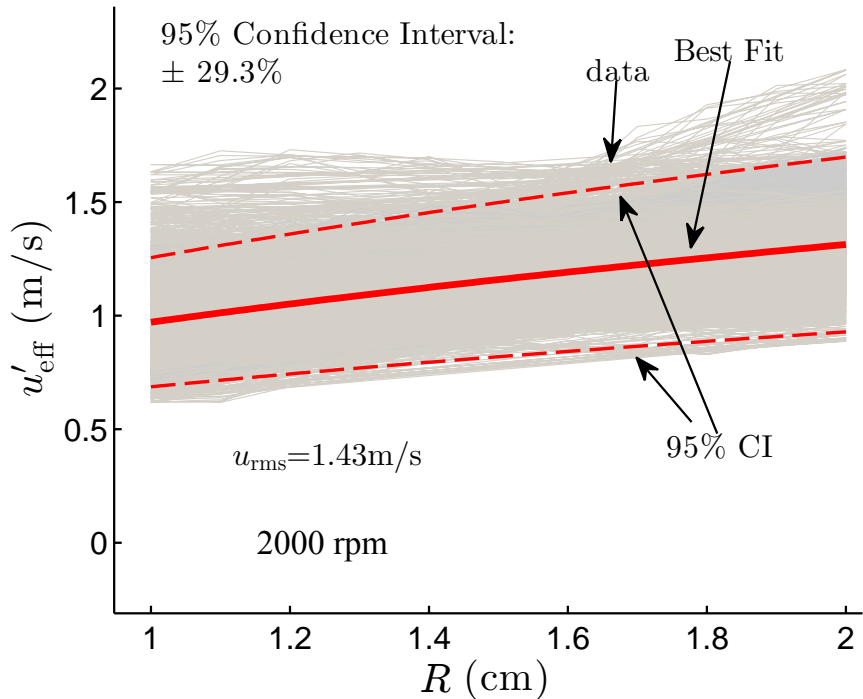


Figure 7.9: Instantaneous measurements of  $u'_{\text{eff}}$  for 2,000 time samplings for fan speed 2000 rpm. The figure is reproduced from the measurements conducted in [Chaudhuri et al. \(2014\)](#).

From the fitting, it was found that in the domain of the reported measurements, and fan speed ranging from 2000 to 8000 rpm,  $u'_{\text{eff}}$  can be approximately represented by the following correlation:

$$u'_{\text{eff}} = 0.002339 \times \text{rpm} \times \langle R \rangle^{0.33} \quad (7.7)$$

It is noted here that Equation 7.7 is slightly different from the original correlation

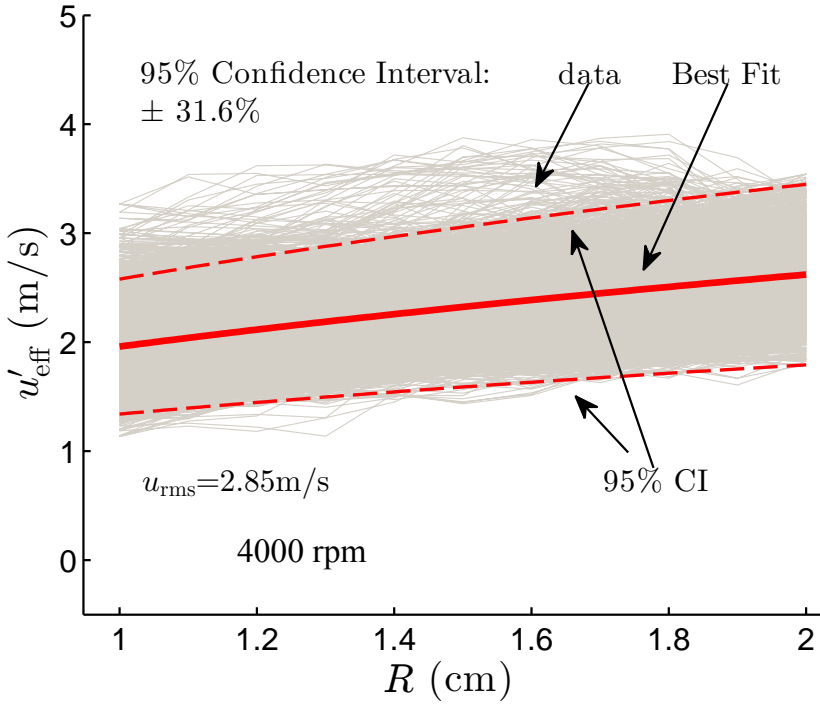


Figure 7.10: Instantaneous measurements of  $u'_{\text{eff}}$  for 2,000 time samplings for fan speed 4000 rpm. The figure is reproduced from the measurements conducted in [Chaudhuri et al. \(2014\)](#).

between fan speed and  $u'_{\text{eff}}$  published in [Chaudhuri et al. \(2013\)](#) because the PIV cold flow statistics was re-measured ([Chaudhuri et al., 2014; Wu et al., 2014c](#)) after a new close-loop fan speed control system was implemented. In addition, Equation 7.6 is also different from the definition given in [Chaudhuri et al. \(2013\)](#), which only considers the velocity fluctuation in the radial direction.

This dependence of  $u'_{\text{eff}}$  on  $\langle R \rangle$  by Equation 7.7 will introduce another dependence of the turbulent flame speed. However, as will be shown later, this dependence is too weak to explain the dependence of  $d \langle R \rangle / dt$  on  $\langle R \rangle$ . For example, as previous theoretical results show ([Chaudhuri et al., 2012](#)),  $u'_{\text{eff}}$  causes a dependence of  $d \langle R \rangle / dt$  on  $\sqrt{u'_{\text{eff}}} \sim \langle R \rangle^{0.115}$ . However, this power law dependence is clearly weaker

than the approximate  $\langle R \rangle^{0.5}$  dependence of  $d\langle R \rangle / dt$  shown in Figure 7.8.

## 7.5 Scaling of Turbulent Flame Speed

### 7.5.1 Theoretical Considerations

The pioneering work on turbulent premixed combustion by [Damköhler \(1940\)](#) was based on the assumption that reactions occur in a thin front, which is not influenced by the flow. As a result, there are two limits: small-scale and large-scale turbulence. For small-scale turbulence, if the largest flow eddy is smaller than the flame thickness so that  $A_T = A_L$ , but large enough so that reaction rates are not affected, then the effect of turbulence is only to change the molecular diffusivity to turbulent diffusivity. Based on the scaling of laminar flame speed ([Law, 2006](#)), [Damköhler \(1940\)](#) argued,

$$\frac{S_T}{S_u^0} = \left( \frac{D_T}{D} \right)^{0.5} \quad (7.8)$$

where  $D_T$  and  $D$  are the turbulent and molecular diffusivity, respectively. For large-scale turbulence, if the smallest flow eddy is still larger than the flame thickness (within which molecular diffusion and reactions occur) such that the local flame speed is unaffected (remains to be  $S_u^0$ ), then the turbulent flame speed  $S_T$  is entirely determined by the wrinkling of flamefront by turbulence, and  $S_T$  is only related with the effective flame surface area via,

$$\frac{S_T}{S_u^0} = \frac{A_T}{A_L} \quad (7.9)$$

where  $A_T$  is the effective total flame surface area and  $A_L$  is the projected area of  $A_T$  in the direction of flame propagation.

As shown, for example, in [Law \(2006\)](#), the turbulent diffusivity  $D_T = u_{\text{rms}} L_I$  while molecular diffusivity  $D = \delta_L S_u^0$ . Then in the small-turbulence limit, we have,

$$\frac{S_T}{S_u^0} = \left( \frac{D_T}{D} \right)^{0.5} = \left( \frac{u_{\text{rms}} L_I}{S_u^0 \delta_L} \right)^{0.5} \quad (7.10)$$

At the same time, for large-scale turbulence the value of  $A_T/A_L$  for statistically planar premixed flames propagating into homogeneous isotropic turbulence was recently analyzed theoretically by [Chaudhuri \*et al.\* \(2011\)](#), based on the spectral formulation of the G-equation ([Peters, 1992](#)) with turbulence imposing a  $k^{5/3}$  dependence on the flame surface fluctuation spectrum, where  $k$  is the wave number. By further assuming that the balance of dissipation by kinematic restoration and amplification by thermal expansion is due to their similar wave number dependence but with opposite signs ([Peters \*et al.\*, 2000](#)) and the dominant role of dissipation by Markstein diffusion occurs at large wave numbers, thereby retaining Markstein diffusion as the sole dissipation mechanism, the following relation was derived in [Chaudhuri \*et al.\* \(2011\)](#),

$$\frac{S_T}{S_u^0} = \frac{A_T}{A_L} \sim \left( \frac{u_{\text{rms}} L_I}{S_u^0 \delta_L \text{Ma}} \right)^{0.5} \quad (7.11)$$

It is noted that Equations 7.10 and 7.11 have the same dependence on  $u_{\text{rms}}$ ,  $L_I$ ,  $S_u^0$  and  $\delta_L$ , except that Equation 7.11 has Ma as an additional parameter. Therefore, the following equation is to be considered as the base line scaling relation,

$$\frac{1}{S_b^0} \frac{d \langle R \rangle}{dt} \sim \left( \frac{u'_{\text{eff}} L_I}{S_u^0 \delta_L} \right)^{0.5} \equiv Re_{L_I, \delta_L} \quad (7.12)$$

for a mixture with fixed Ma, where the LHS  $(1/S_b^0) d \langle R \rangle / dt$  is defined to be the

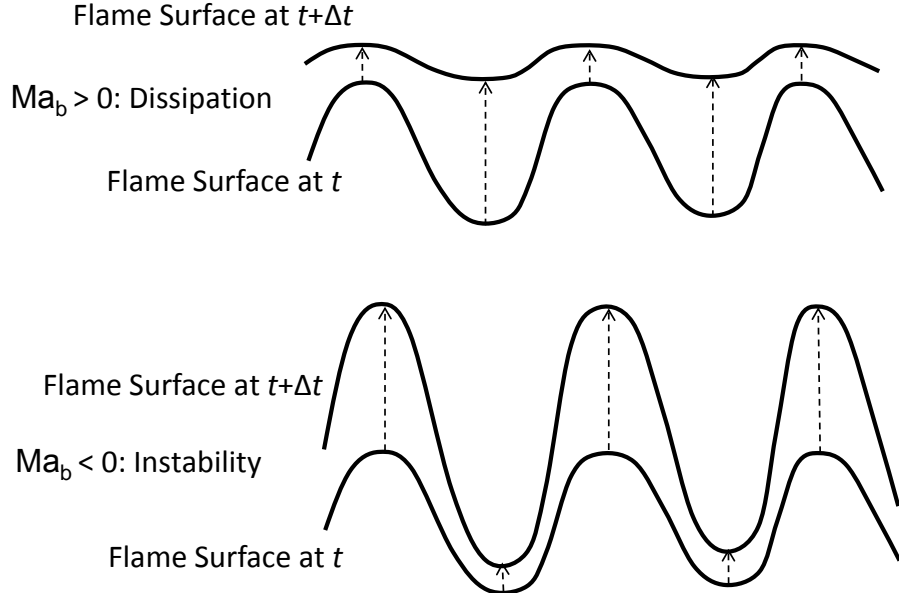


Figure 7.11: Schematic of flame surface fluctuation dissipation and amplification process by positive and negative Markstein numbers (Ma), respectively.

normalized displacement turbulent flame speed measured on the expanding flame configuration using the Schlieren technique.

In addition, from Equation 7.11, it is seen that increasing Ma (which increases with  $Le$ ) reduces the normalized turbulent flame speed. This is consistent with the effect of the dissipation property of flame surface on the total flame surface area. Such an argument is phenomenologically shown in Figure 7.11. Since for a laminar flamelet with  $Ma > 0$ , the local flame speed decreases for positive curvature (positive stretch) and increases for negative curvature (negative stretch), the flame surface fluctuation decreases because of Markstein diffusion. For  $Ma < 0$ , the effect is the opposite, *i.e.*, instability will develop due to Markstein (reverse-)diffusion.

The Markstein diffusion effect is also clearly observed from the flame surface morphology. It is noted from Equation 7.11 that the Markstein diffusivity  $D_{M,b} = S_b^0 L_b$  is the only parameter concerning the properties of the mixture. With the same

flow parameters,  $D_{M,b}$  plays a critical role in the dissipation of the flame wrinkles. To demonstrate this, Figure 7.12a and b show the Schlieren images of CH<sub>4</sub>/air at  $\phi = 0.9$ , 5 atm and fan speeds of 2000 and 4000 rpm, and Figure 7.12c and d show the Schlieren images of H<sub>2</sub>/air at  $\phi = 4.0$ , 5 atm and fan speeds of 4000 and 7500 rpm. Comparing the two CH<sub>4</sub>/air flames with the same Markstein length, it is seen that the flame at 4000 rpm shows evolution of finer scale structures as compared to the flame at 2000 rpm, which is due to the increased turbulence intensity. However, at the same and even higher turbulence intensities, the smallest scale structure for the two H<sub>2</sub>/air flames is much larger than that of the CH<sub>4</sub>/air flames. This cannot be explained by the flame thickness effect because  $\delta_L$  of the H<sub>2</sub>/air flames is about half of that of CH<sub>4</sub>/air flames. Rather, it can be explained by the Markstein length or Markstein diffusivity. Due to the high reactivity and large Lewis number of the rich H<sub>2</sub>/air flames, both  $S_b^0$  and  $L_b$  are much higher than those of CH<sub>4</sub>/air flames, leading to higher  $D_{M,b}$ . The large Markstein diffusivity prevents evolution of fine scale structures for the H<sub>2</sub>/air flames due to its inherent dissipative property at small scales, but a smaller Markstein diffusivity allows finer scale flame wrinkling for the CH<sub>4</sub>/air flames. Indeed, if Figure 7.12a and d are compared, which have nearly the same values of  $Re_{L_I,\delta_L}$ , 232 and 235, the flame in the former image shows much finer scales in comparison to the one in the latter. This means that  $Re_{L_I,\delta_L}$  itself is not enough to explain the difference. However, if one considers  $Re_{L_I,L_b}$ , the value is 49 for Figure 7.12d, which is much smaller than that of Figure 7.12a, being 146.

Given the dependence of the theoretical expression for Ma dependence of normalized turbulent flame speed and the Ma dependence on the experimental flame surface morphology, the following equation is considered to test the scaling of nor-

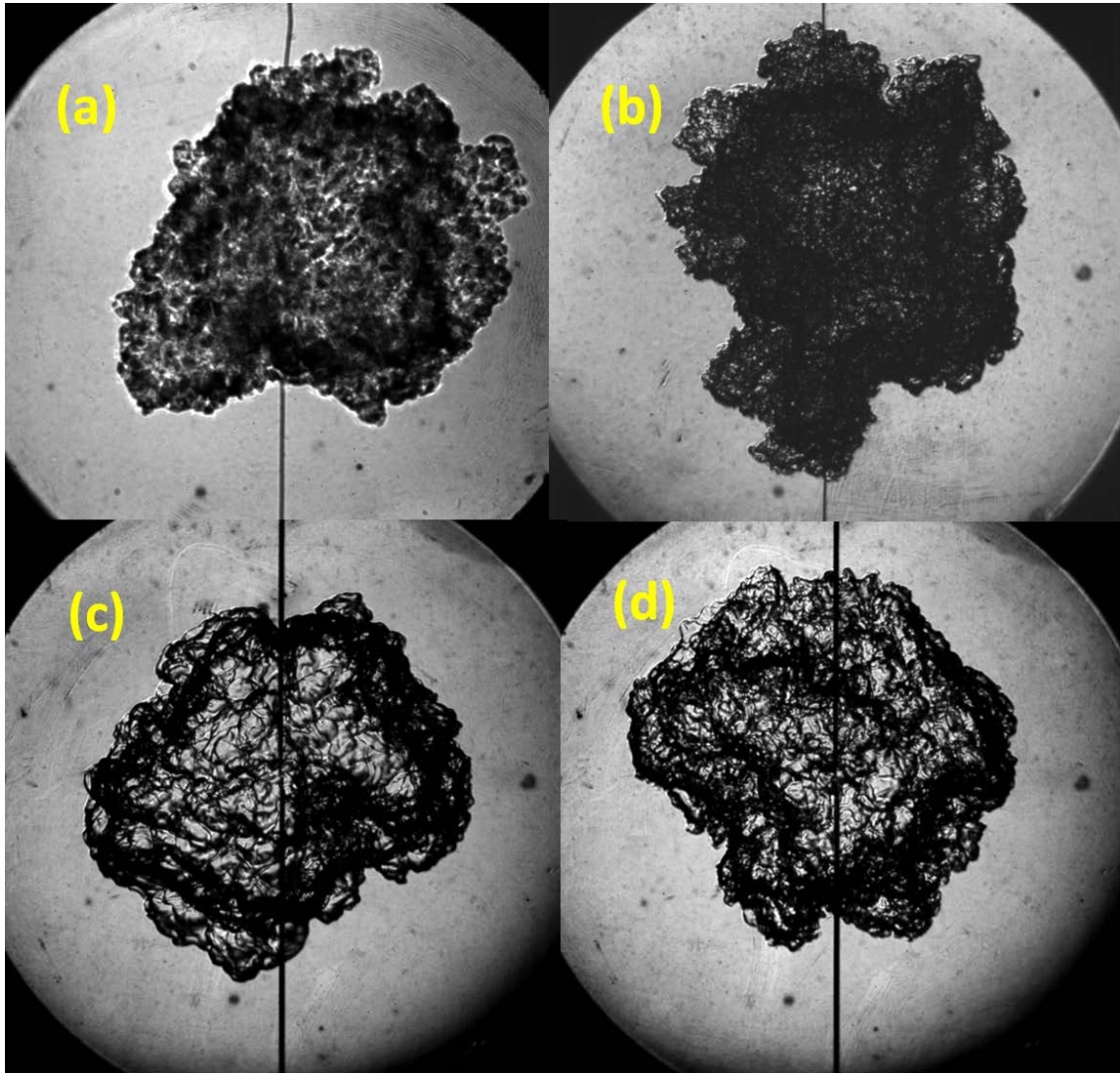


Figure 7.12: Effect of Markstein diffusivity on flame surface morphology. (a) CH<sub>4</sub>/air,  $\phi = 0.9$ , 5 atm, rpm = 2000,  $\delta_L = 0.16$  mm,  $L_b = 0.12$  mm,  $D_{M,b} = S_b^0 L_b = 1.43$  cm<sup>2</sup>/sec,  $Re_{L_I,\delta_L} = 232$ ,  $Re_{L_I,L_b} = 146$ ; (b) CH<sub>4</sub>/air,  $\phi = 0.9$ , 5 atm, rpm = 4000,  $\delta_L = 0.16$  mm,  $L_b = 0.12$  mm,  $D_{M,b} = S_b^0 L_b = 1.43$  cm<sup>2</sup>/sec,  $Re_{L_I,\delta_L} = 451$ ,  $Re_{L_I,L_b} = 284$ ; (c) H<sub>2</sub>/air,  $\phi = 4.0$ , 5 atm, rpm = 4000,  $\delta_L = 0.09$  mm,  $L_b = 0.35$  mm,  $D_{M,b} = S_b^0 L_b = 19.10$  cm<sup>2</sup>/sec,  $Re_{L_I,\delta_L} = 123$ ,  $Re_{L_I,L_b} = 26$ ; (d) H<sub>2</sub>/air,  $\phi = 4.0$ , 5 atm, rpm = 7500,  $\delta_L = 0.09$  mm,  $L_b = 0.35$  mm,  $D_{M,b} = S_b^0 L_b = 19.10$  cm<sup>2</sup>/sec,  $Re_{L_I,\delta_L} = 235$ ,  $Re_{L_I,L_b} = 49$ .

malized turbulent flame speeds of the experimental data for mixtures with different Ma,

$$\frac{1}{S_b^0} \frac{d \langle R \rangle}{dt} \sim \left( \frac{u'_{\text{eff}} L_I}{S_b^0 \text{Ma}_b \delta_L} \right)^{0.5} = \left( \frac{u'_{\text{eff}} L_I}{S_b^0 L_b} \right)^{0.5} \equiv Re_{L_I, L_b} \quad (7.13)$$

### 7.5.2 Scaling for Turbulence Intensity and Length Scale

As discussed above, the normalized turbulent flame speeds are largely influenced by the flame surface area ratio  $A_T/A_L$ , which in turn depends on both flame and flow parameters, such as the turbulence intensity  $u_{\text{rms}}$ , integral length scale  $L_I$ , laminar flame speed  $S_u^0$  and laminar flame thickness  $\delta_L$ . In addition,  $A_T/A_L$  is also influenced by the diffusion property of the flame surface, which is largely represented by Ma. Previous studies have shown that the thermodiffusive (Ma,  $Le$ ) effects modify the turbulent flame speeds significantly ([Lipatnikov & Chomiak, 2005](#)). Therefore, the Ma effects are first put aside, and first investigate the turbulent flame speed scaling for mixtures with constant Ma. As shown in previous chapters and flame theories on Markstein number, Ma is dominated by the value of  $Le$ , which is one of the properties of a combustible mixture and is weakly depends on pressure. Therefore, it is first aimed to seek a scaling that can explain the effects of turbulence intensity and pressure on the same mixture.

Equation 7.12 is the expected scaling for a statistically planar flame propagating into homogeneous isotropic turbulence for a particular combustible mixture. Figure 7.13 plots this  $Re_{L_I, \delta_L}$  scaling for CH<sub>4</sub>/air at  $\phi = 0.9$  and various turbulence intensity and pressure. It is seen from this log-log plot that the directions of increasing pressure and  $u_{\text{rms}}$  are parallel to the line  $y \sim x$  (where  $x$  and  $y$  indicate the x-axis and y-axis quantities). This means that this  $Re_{L_I, \delta_L}$  scaling can explain the dependence of  $u_{\text{rms}}$ ,  $S_b^0$  and  $\delta_L$  reasonably well. However, as seen from the figure that

the direction of increasing  $\langle R \rangle$  is different from that of  $y \sim x$  and that of increasing  $u_{\text{rms}}$  and pressure, which means this  $Re_{L_I, \delta_L}$  scaling is not enough to explain the  $\langle R \rangle$  dependence of turbulent flame speed.

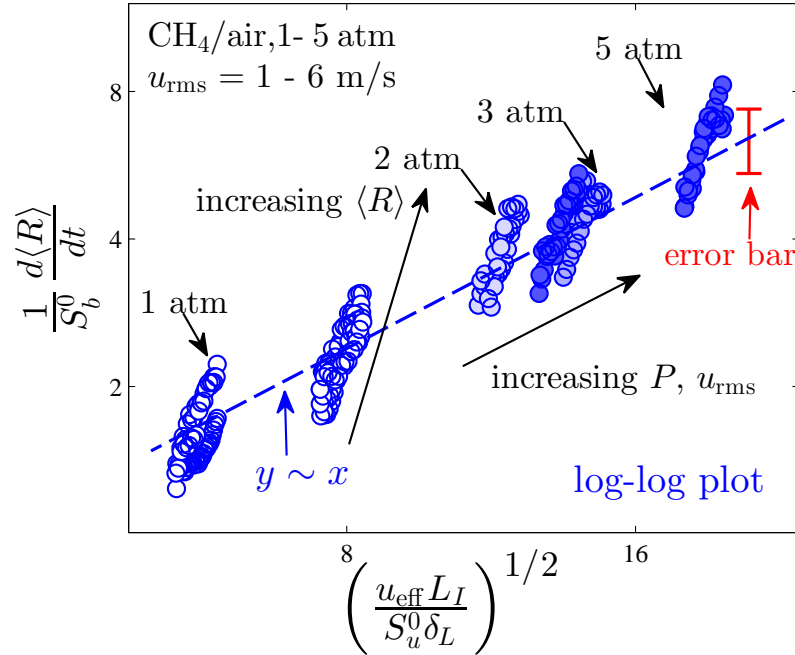


Figure 7.13: Plot of  $d\langle R \rangle / dt$  normalized by the laminar flame speed  $S_u^0$  against  $Re_{L_I,f}$  for  $\text{CH}_4/\text{air}$  at  $\phi = 0.9$ . The directions of variations of  $u_{\text{rms}}$ , pressure and flame radius  $\langle R \rangle$  are indicated with arrows in the figure.

However, the failure of Equation 7.12 is not surprising as it is only valid for statistically planar flames while the experimental data were collected with expanding flames. As suggested by recent review papers by [Bilger \*et al.\* \(2005\)](#) and [Driscoll \(2008\)](#), premixed flame wrinkling process by turbulent flows has very strong geometry dependence. An important difference between expanding turbulent flames and statistically planar flames is that the flame size of expanding flame continuously increases. As a result, the effective hydrodynamic length scale of the flame also

increases, which then leads to flame acceleration.

From the seven repeated CH<sub>4</sub>/air experiments at  $\phi = 0.9$  and 1 atm in Figure 7.8, it is seen that the acceleration follows approximately the power-law  $d \langle R \rangle / dt \sim \langle R \rangle^{0.68}$ . In Figure 7.8, the variation of  $\langle R \rangle$  is small, only from 1.2 cm to 2.2 cm, and as such the validity of this power-law dependence is not guaranteed. To verify this power dependence on  $\langle R \rangle$  for more conditions, Figure 7.14 plots the normalized speed  $(1/S_b^0) d \langle R \rangle / dt$  versus the normalized flame radius  $\langle R \rangle / \delta_L$  for CH<sub>4</sub>/air at  $\phi = 0.9$ . It is seen that all the dependence of  $d \langle R \rangle / dt$  is close to 1/2 for all conditions. It has also been verified that similar dependence is seen for mixtures at other conditions. It is noted that the difference between the  $\langle R \rangle^{0.68}$  dependence in Figure 7.8 and the  $\langle R \rangle^{0.5}$  dependence in Figure 7.14 maybe due to the weak dependence of  $u'_{\text{eff}}$  on  $\langle R \rangle$ , *i.e.*,  $u'_{\text{eff}} \sim \langle R \rangle^{0.33}$  (Equation 7.7).

It is seen that the normalized turbulent flame speeds have a square-root dependence on both  $Re_{L_I, \delta_L}$  and  $\langle R \rangle$ . This means a modified scaling relation can be considered by replacing the  $L_I$  by  $\langle R \rangle$ ,

$$\frac{1}{S_b^0} \frac{d \langle R \rangle}{dt} \sim \left( \frac{u'_{\text{eff}} \langle R \rangle}{S_u^0 \delta_L} \right)^{0.5} \equiv Re_{R, \delta_L} \quad (7.14)$$

However, the reason for replacing  $L_I$  by  $\langle R \rangle$  is empirical. This is related to the question as why the speed of turbulent expanding flames increases with its size. Previous studies on expanding turbulent flames by Bradley and co-workers explained the acceleration of expanding turbulent flames to be a consequence of the increased turbulence intensity the flame experiences as it expands (Abdel-Gayed *et al.*, 1987). However, as shown in Section 7.4.2, according to the calculation of the effective turbulence intensity  $u'_{\text{eff}}$  based on spatially and temporally resolved PIV

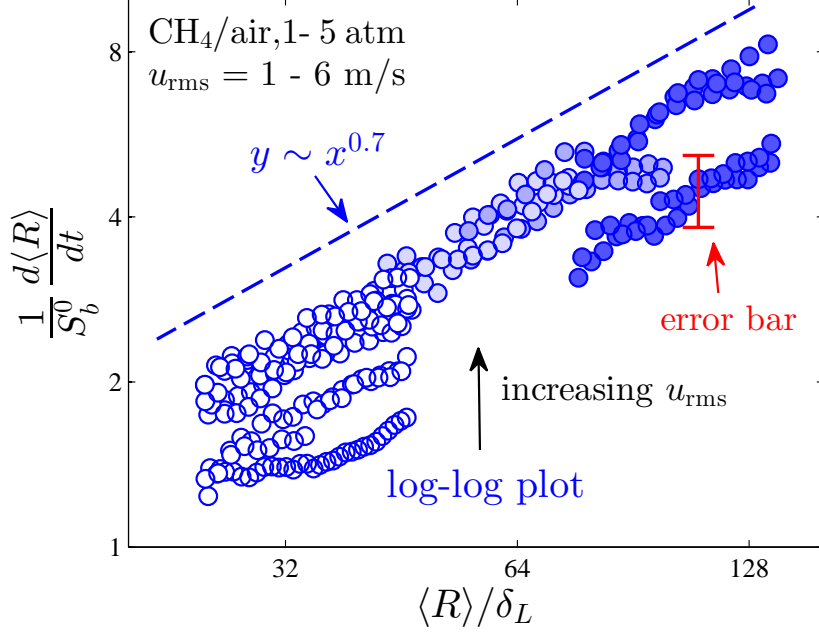


Figure 7.14: The normalized speed  $(1/S_u^0) d\langle R \rangle / dt$  versus the normalized flame radius  $\langle R \rangle / \delta_L$  for CH<sub>4</sub>/air at  $\phi = 0.9$  from 1 to 5 atm with  $u_{\text{rms}}$  from approximately 1 to 6 m/s

data,  $u'_{\text{eff}}$  has only a weak  $\langle R \rangle^{0.33}$  dependence, which has only  $\langle R \rangle^{0.16}$  dependence in Equation 7.12, much smaller than the  $\langle R \rangle^{0.5}$ .

Figures 7.15 and 7.16 plot this  $Re_{R,\delta_L}$  scaling for CH<sub>4</sub>/air at  $\phi = 0.9$  in linear and log-log scale, respectively. It is seen that now the scaling works reasonably well and the dependence of all the parameters on  $Re_{R,\delta_L}$  are captured. This means that, if the Markstein number (Ma) is kept the same, *i.e.*, the mixture compositions do not change, the  $Re_{R,\delta_L}$  scaling in Equation 7.14 is a good candidate to scale the flame speed of expanding turbulent flames to capture the dependence of  $u_{\text{rms}}$ , pressure and  $\langle R \rangle$ . The significance is that the dependence of turbulent flame speed on  $u_{\text{rms}}$ ,  $\langle R \rangle$  and  $\delta_L$  are all approximately 1/2, which suggest the fundamental mechanism of their effects on turbulent flame propagation is the same, *i.e.*, by increasing the total

flame surface area. The effect of increasing  $u_{\text{rms}}$  is to increase the turbulent kinetic energy spectrum and thus the conserved scalar spectrum. The effect of pressure is to decrease both the flame thickness  $\delta_L$ , molecular diffusivity and the Kolmogorov length scale, such that flame wrinkling can occur at smaller length scales at higher pressures, and thus the total flame surface area is increased.

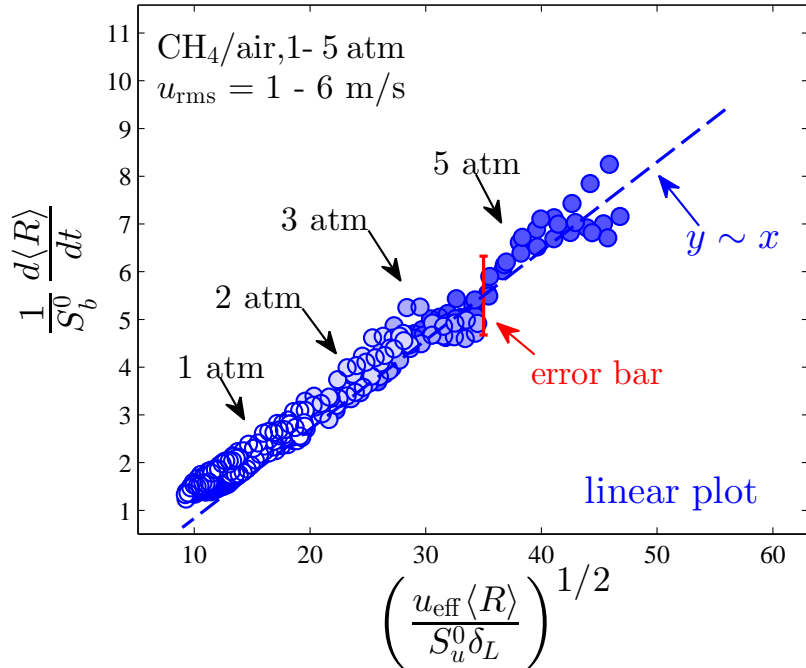


Figure 7.15: Plot of  $d\langle R \rangle / dt$  normalized by the laminar flame speed  $S_u^0$  against  $Re_{R,f}$  for CH<sub>4</sub>/air at  $\phi = 0.9$  in linear scale.

To further explain the  $\langle R \rangle^{0.5}$  of the speed of turbulent expanding flames, it is noted that an important assumption made in the analysis by Chaudhuri *et al.* (2011) on statistically planar flames is that the effective hydrodynamic scale of the flame (which can be represented by the turbulent brush thickness  $\delta_T$  defined, for example, in Lipatnikov & Chomiak (2002)), is equal to the integral scale  $L_I$ . This is why  $L_I$  explicitly appears in Equation 7.12. However, for expanding turbulent

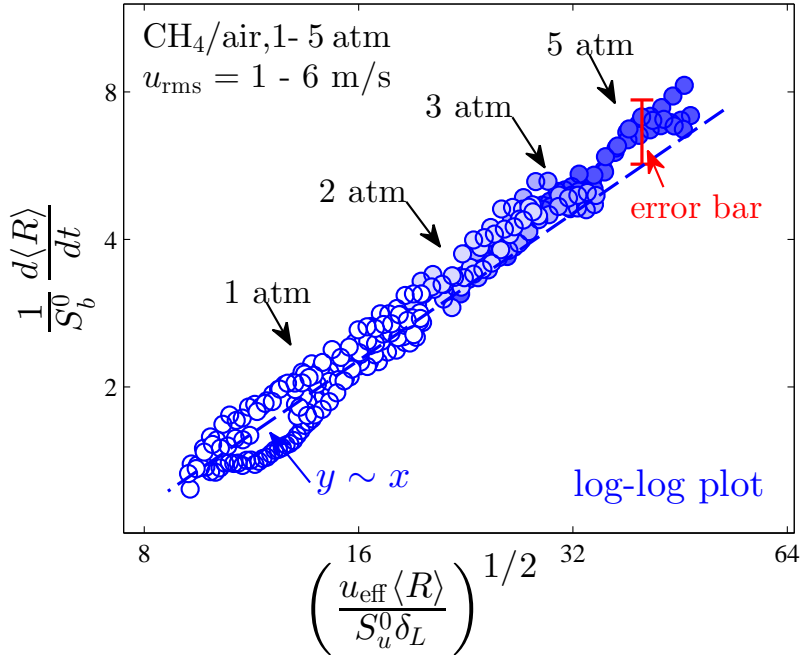


Figure 7.16: Plot of  $d\langle R \rangle / dt$  normalized by the laminar flame speed  $S_u^0$  against  $Re_{R,f}$  for CH<sub>4</sub>/air at  $\phi = 0.9$  in log-log scale.

flames this assumption is not appropriate. As an expanding turbulent flame grows in its size, its effective hydrodynamic length and hence  $\delta_T$  also increases. This is especially true for the cases in the present experiments where the size of the flame is instantaneously much smaller than the domain size.

To confirm the increase of the flame brush thickness  $\delta_T$ , Mie scattering experiments with flames were conducted in [Saha \*et al.\* \(2014\)](#) and [Chaudhuri \*et al.\* \(2014\)](#), to measure  $\delta_T$  for CH<sub>4</sub>/air at  $\phi = 0.9$  and n-C<sub>4</sub>H<sub>10</sub>/air at  $\phi = 0.9$ . Each of the several experimental conditions was repeated at least six times. Figure 7.17 plots the instantaneous and ensemble-averaged Mie scattering flame edges at three different flame radii. It can be seen that the scattering of flame edge does increase with flame size. The flame brush thickness  $\delta_T$  is estimated based on the standard derivation

of the fluctuating flame radius measured in Mie scattering image. In Figure 7.18, the standard deviation of the flame radius obtained from Mie scattering images is plotted with respect to the mean radius. From the measurements, it is seen that the standard derivation of the flame radius is approximately proportional to the mean flame radius, *i.e.*,  $\delta_T \sim \langle R \rangle$ . This therefore suggests that Equation 7.14 is an appropriate scaling relation for expanding turbulent flames.

Finally, the success of the scaling based on Equation 7.14 also suggests that for self-similar structure of expanding turbulent flames. This property is similar to the problem of self-acceleration of unstable flames due to the intrinsic flamefront cellular instabilities, presented in Chapter 6. In both problems,  $\langle R \rangle$  represents the hydrodynamic convection length scale (no matter the disturbance or wrinkling is caused by hydrodynamic instabilities or turbulence), while  $\delta_L$  represents the diffusion length scale.

### 7.5.3 Scaling for Thermodiffusive Effects

Although Equation 7.14 can scale turbulent flame speeds and capture the effects of turbulence intensity, length scale and pressure for mixtures with constant Ma, the dependence of turbulent flame speeds on Ma remains to be addressed. When the mixture composition changes such as  $\phi$  or inert, the thermodiffusive property variations change the turbulent flame speeds significantly. As reviewed by Driscoll (2008) and Lipatnikov & Chomiak (2005), the thermodiffusive effects on turbulent flame speed is strong and complex to understand. It is believed that this is still largely an open problem.

To obtain the dependence of Ma on turbulent flame speeds, scaling using Equation 7.14 for mixtures with different Ma is first investigated. Figures 7.19 and 7.20

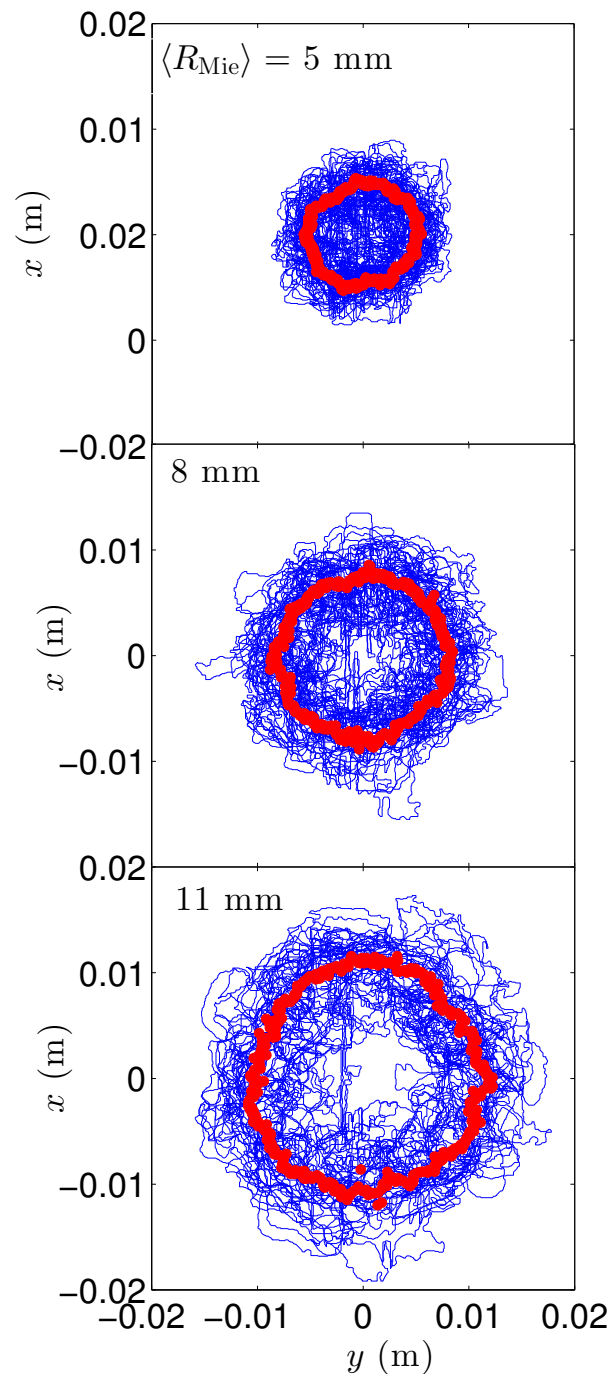


Figure 7.17: Instantaneous and ensemble-averaged Mie scattering flame edges at three different flame radii. The figure is reproduced from the measurements in Saha *et al.* (2014).

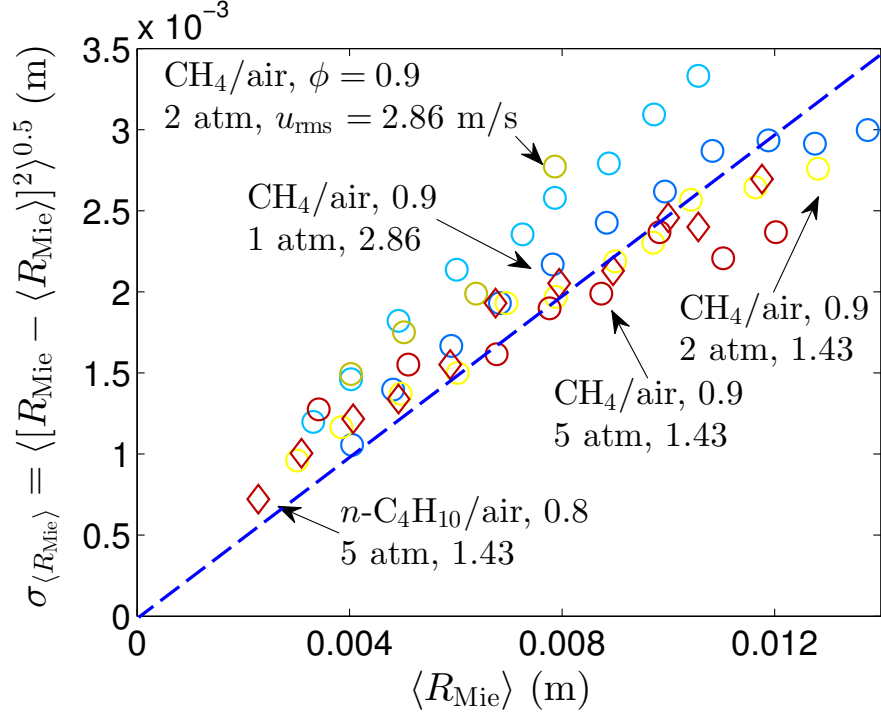


Figure 7.18: Standard deviation  $\sigma_{\langle R_{\text{Mie}} \rangle}$  of flame radius obtained from Mie scattering images, where  $\sigma_{\langle R_{\text{Mie}} \rangle} = \langle [R_{\text{Mie}} - \langle R_{\text{Mie}} \rangle]^2 \rangle^{0.5}$  and  $R_{\text{Mie}}$  is the flame radius from Mie scattering images. The data approximately suggest that the flame brush thickness  $\delta_T \sim \sigma_{\langle R_{\text{Mie}} \rangle} \sim \langle R_{\text{Mie}} \rangle$ .

plot Equation 7.14 scaling for all mixtures in linear and log-log scale, respectively. It is seen that each set of the data corresponding to a particular mixture collapses reasonably well on a single line, suggesting the general validity of Equation 7.14 for individual fuel/air mixtures. This further suggests that Equation 7.14 is general for all mixtures. At the same time, it can also be observed that for different mixtures the scaling lines based on Equation 7.14 have different slopes. Specifically, the slope decreases with increasing Ma. The  $\text{C}_2\text{H}_4$  mixtures ( $15\%\text{O}_2$ ,  $85\%\text{N}_2$ ,  $\phi = 1.3$ ), corresponding to negative Ma, has the largest slope, while the  $\text{H}_2/\text{air}$ ,  $\phi = 4.0$  mixture, corresponding to the highest Ma, has the smallest slope. In addition, Figures

[7.19](#) and [7.20](#) plot data obtained at the University of Leeds for *iso*-octane/air data ([Lawes et al., 2012](#)). The ensemble average is calculated based on instantaneous data taken from ([Lawes et al., 2012](#)). For *iso*-octane/air, Ma decreases from lean to rich and turbulent flame speed correspondingly increases from lean to rich. It is seen that the slope for Equation [7.14](#) scaling also decreases with increasing Ma.

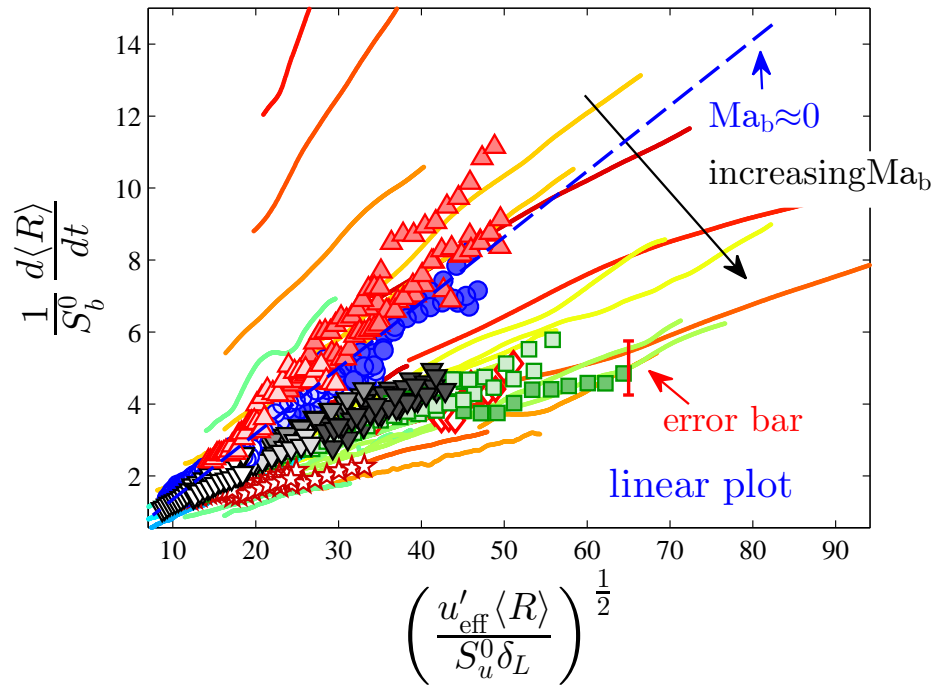


Figure 7.19: Linear plot of  $(1/S_b^0) d\langle R \rangle / dt$  against  $Re_{R,\delta_L}^{0.5}$  for all experimental conditions listed in Figures [7.3](#) (symbols) and [7.4](#) (lines). The *iso*-C<sub>8</sub>H<sub>18</sub> data were obtained from [Lawes et al. \(2012\)](#).

As discussed in Section [7.5.1](#), the effects of Markstein number can be considered as a modification of the diffusivity of the flame surface, because the Markstein diffusivity, a term proposed by [Peters \(1992\)](#), is defined to be  $S_u^0 \delta_L \text{Ma}$ . Therefore, the following equation is expected to be a potential scaling relation that captures

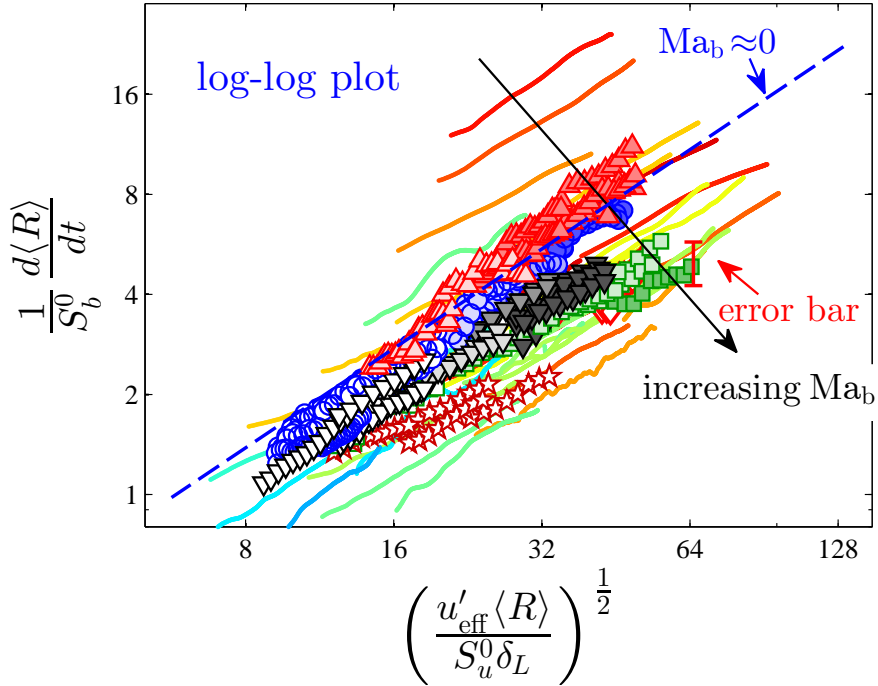


Figure 7.20: Log-log plot of  $(1/S_b^0) d\langle R \rangle / dt$  against  $Re_{R,\delta_L}^{0.5}$  for all experimental conditions listed in Figures 7.3 (symbols) and 7.4 (lines). The iso-C<sub>8</sub>H<sub>18</sub> data were obtained from Lawes *et al.* (2012).

the Ma dependence.

$$\frac{1}{S_b^0} \frac{d\langle R \rangle}{dt} \sim \left( \frac{u'_{\text{eff}} \langle R \rangle}{S_b^0 \text{Ma}_b \delta_L} \right)^{0.5} = \left( \frac{u'_{\text{eff}} \langle R \rangle}{S_b^0 L_b} \right)^{0.5} \equiv Re_{R,L_b} \quad (7.15)$$

where  $\text{Ma}_b$ , the burned gas Markstein number, is used because it is directly measurable from laminar expanding flame experiments. However, the problem is that if the thermodiffusive effects are purely considered to be a modification of the diffusivity, then the modified diffusivity has to be positive. When  $\text{Ma}_b < 0$ , the Markstein diffusivity becomes negative, and the entire formulation by Peters (1992) based on G-equation and Markstein diffusivity becomes ill-posed. In that case, the thermod-

iffusive effects on turbulent flame speeds is only purely through the modification of the diffusivity because flame cusps form, and perhaps the nonlinear couplings between turbulence, the chemical structure of flames and flamefront instability (induced by turbulence) need to be considered.

Figures 7.21 and 7.22 plot Equation 7.15 scaling in linear and log-log scale, respectively, for all mixtures with  $\text{Ma}_b > 0$ . It is seen that for the experimental conditions and fuels considered here, the data from various fuels, at different equivalence ratios, pressure and turbulence intensity indeed collapse rather well with Equation 7.15.

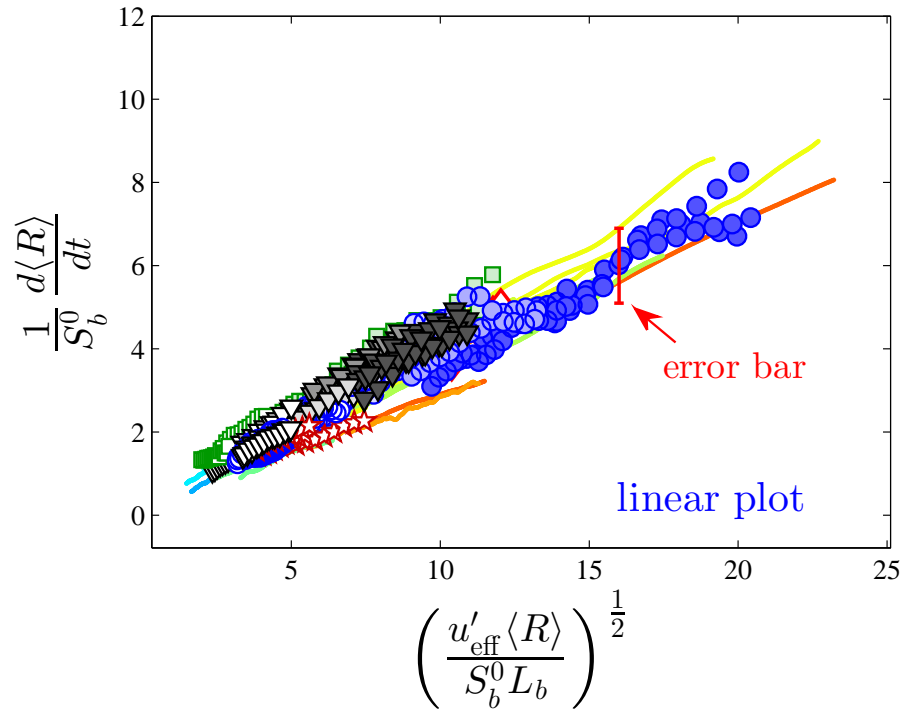


Figure 7.21: Linear plot of  $(1/S_b^0) d\langle R \rangle / dt$  against  $Re_{R,L_b}^{0.5}$  for all experimental conditions listed in Figures 7.3 (symbols) and 7.4 (lines). The *iso*-C<sub>8</sub>H<sub>18</sub> data were obtained from Lawes *et al.* (2012).

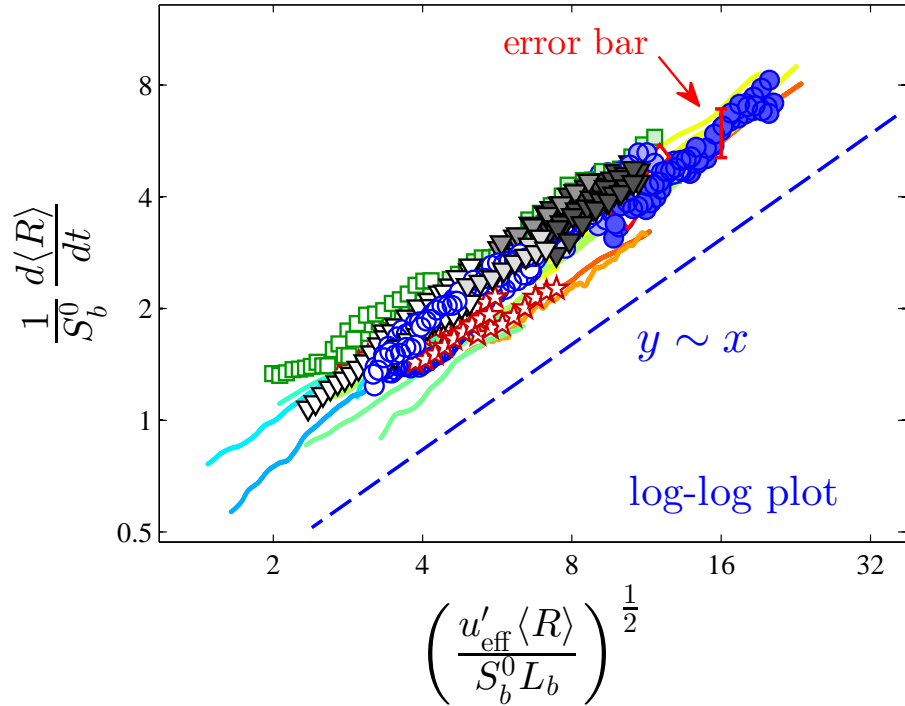


Figure 7.22: Log-log plot of  $(1/S_b^0) d\langle R \rangle / dt$  against  $Re_{R,L_b}^{0.5}$  for all experimental conditions listed in Figures 7.3 (symbols) and 7.4 (lines). The iso-C<sub>8</sub>H<sub>18</sub> data were obtained from Lawes *et al.* (2012).

## 7.6 Concluding Remarks

In this chapter, extensive experimental data on the flame speed of expanding turbulent flames are presented. Fuels considered include H<sub>2</sub>, CH<sub>4</sub>, C<sub>2</sub>H<sub>4</sub>, DME (C<sub>2</sub>H<sub>6</sub>O) and *n*-C<sub>4</sub>H<sub>10</sub>. Turbulence intensity varies from 1 to 6 m/s, and pressure varies from 1 to 10 atm. It has been shown that for a fixed combustible mixture with constant Markstein number, the normalized turbulent flame speed follows the  $Re_{\langle R \rangle, \delta_L}^{0.5}$  (Equation 7.14) scaling reasonably well, which captures the dependence of turbulence intensity, length scale and pressure. Experimental data shows thermodiffusive effect (Markstein number) significantly modifies turbulent flame speeds and as such

changes the slope of the  $Re_{\langle R \rangle, \delta_L}^{0.5}$  scaling for different mixtures. It is further shown that the  $Re_{\langle R \rangle, L_b}^{0.5}$  scaling (Equation 7.15) can capture the Markstein number effects reasonably well for mixtures with positive Markstein number, and therefore scale all the present data as well as the data for *iso*-C<sub>8</sub>H<sub>18</sub> from Lawes *et al.* (2012), irrespective of the fuel, pressure, and turbulence intensity as long as Markstein numbers are positive.

# Chapter 8

## Fuel Similarity and Local Extinction of Turbulent Flames

### 8.1 Introduction

Combustion chemistry of large practical fuels involves hundreds to thousands of compounds and even larger numbers of reactions (Lu & Law, 2009), which are difficult to track at the fundamental level. A simplified approach is based on the assumption that large fuels crack rapidly as compared to the subsequent oxidation of cracked intermediates (You *et al.*, 2009; Wang *et al.*, 2010). As a result, large fuels do not enter the active oxidation zone directly, and it is the oxidation of the cracked products that determines the rates of radical pool build-up and heat release. Consequently, a detailed description of the cracking process may not be necessary as long as the major cracked product distribution is well predicted. Such a concept has been explored for the global parameters of laminar flames (Ji *et al.*, 2010; Kelley *et al.*, 2011c; Wu *et al.*, 2012), particularly for *n*-alkanes (Wang *et al.*, 2010; Ji *et al.*,

2010; Kelley *et al.*, 2011c; Davidson *et al.*, 2010; Shen *et al.*, 2009; Davis & Law, 1998; Westbrook *et al.*, 2009; Ranzi *et al.*, 2005) which are important components in transportation fuels (Violi *et al.*, 2002; Pitz *et al.*, 2007a; Farrell *et al.*, 2007), demonstrating that the associated laminar flame speeds (Ji *et al.*, 2010; Kelley *et al.*, 2011c; Davis & Law, 1998), its sensitivity to stretch through the Markstein length (Kelley *et al.*, 2011c), laminar premixed flame and extinction strain rates (Ji *et al.*, 2010) largely assume similar values. This supports the use of similarity rules for rates of fuel-related reactions (Westbrook *et al.*, 2009).

In addition to the issue of fuel similarity, it is further noted that while there are a large number of measurements for the laminar flame speeds of large *n*-alkanes, well-defined measurements of turbulent flame speeds are rather scarce. Availability of such data would facilitate the study of turbulence-chemistry interactions (Chen *et al.*, 2011) because of the moderately well-established kinetic mechanisms of the *n*-alkanes, as well as the development and validation of turbulent combustion models such as that of Large Eddy Simulation (LES).

In the present study, the turbulent flame speeds of C<sub>4</sub>-C<sub>8</sub> *n*-alkanes were experimentally measured for expanding turbulent flames over a wide range of turbulence intensities and equivalence ratios, in the pressure range of 1 to 5 atm. The results provide useful data for further studies of the structure and modeling of turbulent flames, allow direct and consistent assessment of fuel similarity for *n*-alkanes under different flow and flame conditions, and yield useful observation on the occurrence of stretch-affected local extinction.

The results presented in this chapter have been previously published in the following journal article (Wu *et al.*, 2014c):

- Wu, F., SAHA, A., CHAUDHURI, S. & LAW, C. K. 2014c Propagation

speeds of expanding turbulent flames of C<sub>4</sub> to C<sub>8</sub> *n*-alkanes at elevated pressures: experimental determination, fuel similarity, and stretch-affected local extinction. *Proceedings of the Combustion Institute* **35**, in press

## 8.2 Experimental Conditions

The experiments were conducted in Vessel II. The present study reports data for four fuels: *n*-butane, *n*-pentane, *n*-hexane and *n*-octane at three different pressures, 1, 2 and 5 atm. The laminar flames in this pressure range do not exhibit intrinsic flamefront instabilities; therefore the interaction between turbulence and flamefront instabilities is removed. Figure 8.1 summarizes the mixture and flame properties of the conditions considered in this study, with *n*-hexane being an example. Due to fuel similarity, the values are similar for other fuels except for *Le*, which is separately listed in Figure 8.2. In addition to the stoichiometric condition at  $\phi = 1.0$ , lean mixtures at  $\phi = 0.8$  and rich mixtures at  $\phi = 1.4$  are selected because these flames have similar laminar flame speed  $S_u^0$  and laminar flame thickness  $\delta_L$ ; therefore the effect of differential diffusion can be independently studied.

The differential diffusion properties of a combustible premixture are characterized by the Lewis number *Le* and Markstein number *Ma*. In Figures 8.1 and 8.2, at  $\phi = 0.8$  *Le* is defined as *Le*<sub>Fuel</sub>, at  $\phi = 1.4$  *Le*<sub>O<sub>2</sub></sub>, and at  $\phi = 1.0$  0.5(*Le*<sub>Fuel</sub>+ *Le*<sub>O<sub>2</sub></sub>). *Ma*<sub>b</sub> is defined as *L*<sub>b</sub>/ $\delta_L$ . It is seen from Figure 8.1 that at  $\phi = 0.8$  and 1.0, *Le* > 1 and *Ma*<sub>b</sub> > 0, and at  $\phi = 1.4$ , *Le* < 1 and *Ma*<sub>b</sub> < 0.

The fan speeds vary from 2000 rpm to 7500 rpm, which results in cold flow turbulence intensity, *u*<sub>rms</sub>, varying from 1.4 m/s to 5.4 m/s. Figure 8.4 plots the conditions of the present experiments in the turbulent combustion regime diagram.

$P$ , atm	$\phi$	$T_{ad}$ , K	$S_u^0$ , cm/sec	$\delta_L$ , cm	$Ma_b$	$\Theta$
1	0.8	2115	35.6	0.044	2.55	6.27
1	1.0	2312	48.2	0.037	2.27	6.99
1	1.4	2080	33.3	0.046	-0.83	6.85
2	0.8	2119	30.2	0.025	2.76	6.27
2	1.0	2332	41.2	0.021	2.29	7.0
2	1.4	2078	25.4	0.029	N/A	6.86
5	0.8	2122	24.6	0.012	3.17	6.28
5	1.0	2356	32.7	0.010	1.80	7.1
5	1.4	2080	15.9	0.017	N/A	6.86

Figure 8.1: Laminar flame properties of *n*-hexane/air.  $S_u^0$  and Markstein number  $Ma_b$  are from experiments using the present vessel (Kelley *et al.*, 2011c; Kelley, 2011). N/A for  $Ma_b$  at  $\phi = 1.0$  and 1.4 at 2 and 5 atm means it cannot be measured due to flamefront instability.  $S_u^0$  at  $\phi = 1.4$  at 2 and 5 atm,  $T_{ad}$  and  $\delta_L$  are calculated using JetSurF 2.0 chemistry model (Wang *et al.*, 2010). The unburned gas temperature  $T_u$  is 353 K in all cases.

It is seen that most experiments fall in the so-called corrugated flamelet and “thickened” flamelet regimes.

## 8.3 Experimental Results

### 8.3.1 Laminar Flame Speeds

It has been shown in (Kelley *et al.*, 2011c) that laminar flame speeds for C<sub>4</sub>-C<sub>8</sub> *n*-alkanes flames are similar at the initial temperature 353 K and pressures from 1 - 20 atm. In Davis & Law (1998) it was also shown that C<sub>4</sub>-C<sub>8</sub> *n*-alkanes assumes similar flame speeds at 1 atm and an initial temperature of 298 K. To establish

$\phi$	<i>n</i> -butane	<i>n</i> -pentane	<i>n</i> -hexane	<i>n</i> -octane
0.8	1.7	1.9	2.0	2.3
1.0	1.4	1.5	1.6	1.8
1.4	0.9	0.9	0.9	0.9

Figure 8.2:  $Le$  of fuel/air mixtures calculated by the Chemkin II TRANSPORT package using the transport properties in the JetSurF 2.0 ([Wang et al., 2010](#)).  $Le$  does not change with pressure for ideal gases.

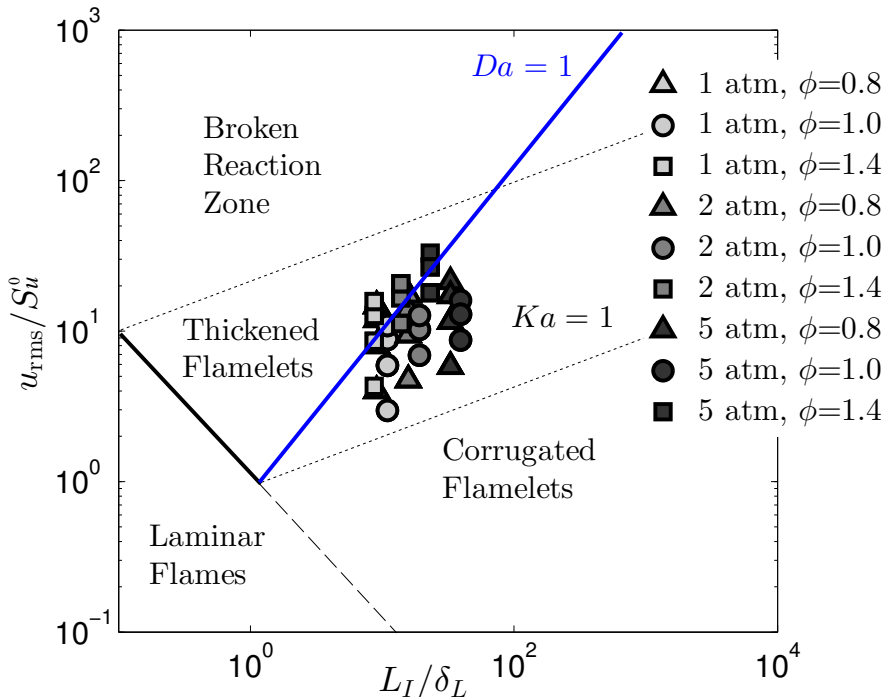


Figure 8.3: Regimes of the present experimental conditions on the premixed turbulent combustion regime diagram (Borghi diagram). To show the experimental conditions, laminar flame speeds and computed flame thickness of only *n*-hexane/air mixtures are used. Other C<sub>4</sub>-C<sub>8</sub> *n*-alkanes have almost the same laminar flame properties; therefore, their locations in the regime diagram overlap with those of *n*-hexane.

the laminar flame speeds for current experiments at 353 K and to complement the flame speed data of C<sub>5</sub>-C<sub>8</sub> *n*-alkanes at elevated temperatures reported in ([Kelley](#)

*et al.*, 2011c), here additional additional measurements on *n*-butane/air mixtures at 353 K for 1 - 5 atm were conducted. The results, plotted in Figure 8.4, show that *n*-butane indeed has similar flame speeds as the *n*-alkanes with longer carbon chain, and the difference is within typical experimental uncertainties.

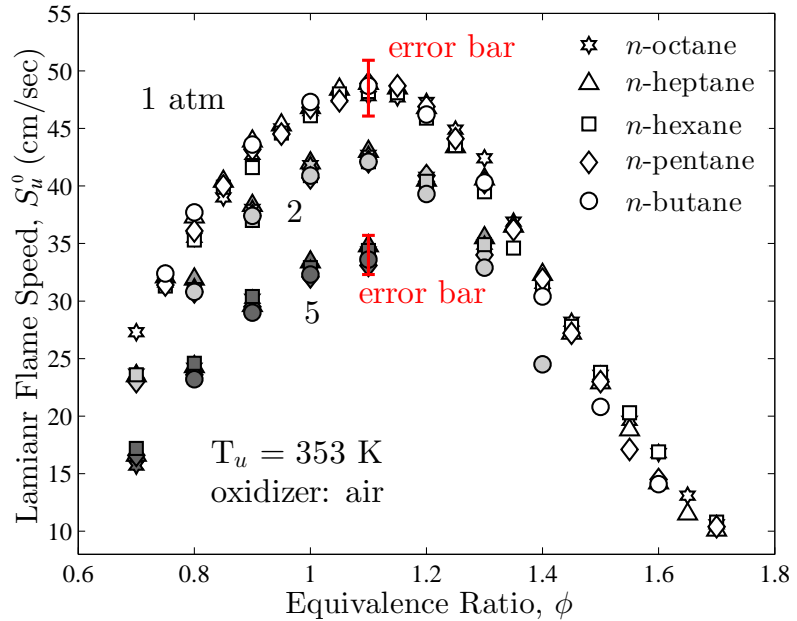


Figure 8.4: Measured laminar flame speeds for C<sub>4</sub>-C<sub>8</sub> *n*-alkanes. C<sub>5</sub>-C<sub>8</sub> data are taken from (Kelley *et al.*, 2011c; Kelley, 2011).

### 8.3.2 Turbulent Flame Speeds

In Chapter 7, it has been shown that the scaling based on  $Re_{(R),\delta_L}^{1/2}$  (Equation 7.14) holds for expanding turbulent flames for a wide range of conditions in the corrugated flamelet and “thickened” flamelet regimes. In the following, the fuel similarity of turbulent flame speeds for *n*-alkanes using this scaling will be presented.

Figure 8.5 shows the normalized turbulent flame speeds versus  $Re_{(R),\delta_L}^{1/2}$  for  $\phi =$

1.0 and 1.4 for *n*-butane, *n*-pentane, *n*-hexane and *n*-octane, respectively in log-log scale. The error bar represents  $\pm 15\%$  random uncertainty in  $d \langle R \rangle / dt$ , which is calculated based on the 95% confidence interval of seven repeated runs on stoichiometric CH<sub>4</sub>/air flames for a fixed experimental condition shown in Figure 7.8. To eliminate the influence of the effects of ignition and chamber wall, only data in the range of  $1.0 \text{ cm} < \langle R \rangle < 2.0 \text{ cm}$  were considered and plotted. While extensive experiments for *n*-hexane to obtain all possible conditions are conducted, only experimental conditions required for demonstrating the concept of fuel similarity at all possible  $Re_{\langle R \rangle, \delta_L}^{1/2}$  for other fuels were conducted.

In Figure 8.5(a), it is seen that all the data at  $\phi = 1.4$  also follow the  $Re_{\langle R \rangle, \delta_L}^{1/2}$  scaling well, but it has a much higher prefactor, resulting in uniformly higher normalized turbulent flame speeds than the data at  $\phi = 1.0$  in the log-log plots. From Figure 8.5(c-d), it is also observed that for the other three fuels, turbulent flame propagation approximately follows  $Re_{\langle R \rangle, \delta_L}^{1/2}$  scaling for each individual mixture, and the prefactor for data at  $\phi = 1.4$  is always higher than that of  $\phi = 1.0$ , which is because the Markstein number at  $\phi = 1.0$  is higher than at  $\phi = 1.4$ .

To test the concept of fuel similarity, Figure 8.6 shows all the data for *n*-butane, *n*-pentane, *n*-hexane and *n*-octane in terms of  $Re_{\langle R \rangle, \delta_L}^{1/2}$  scaling in one plot. It is seen that the data for different fuels collapse reasonably well for both small and large values of  $Re_{\langle R \rangle, \delta_L}^{1/2}$ . Consequently, the validity of fuel similarity for C<sub>4</sub>-C<sub>8</sub> *n*-alkanes is strongly suggested for such conditions, *i.e.*, stoichiometric and rich flames with air from 1 atm to 5 atm in corrugated and thickened flame regimes. In addition, Figures 8.7 and 8.8 also plots the absolute averaged propagation speed  $S_{T,\text{mean}}$  during each

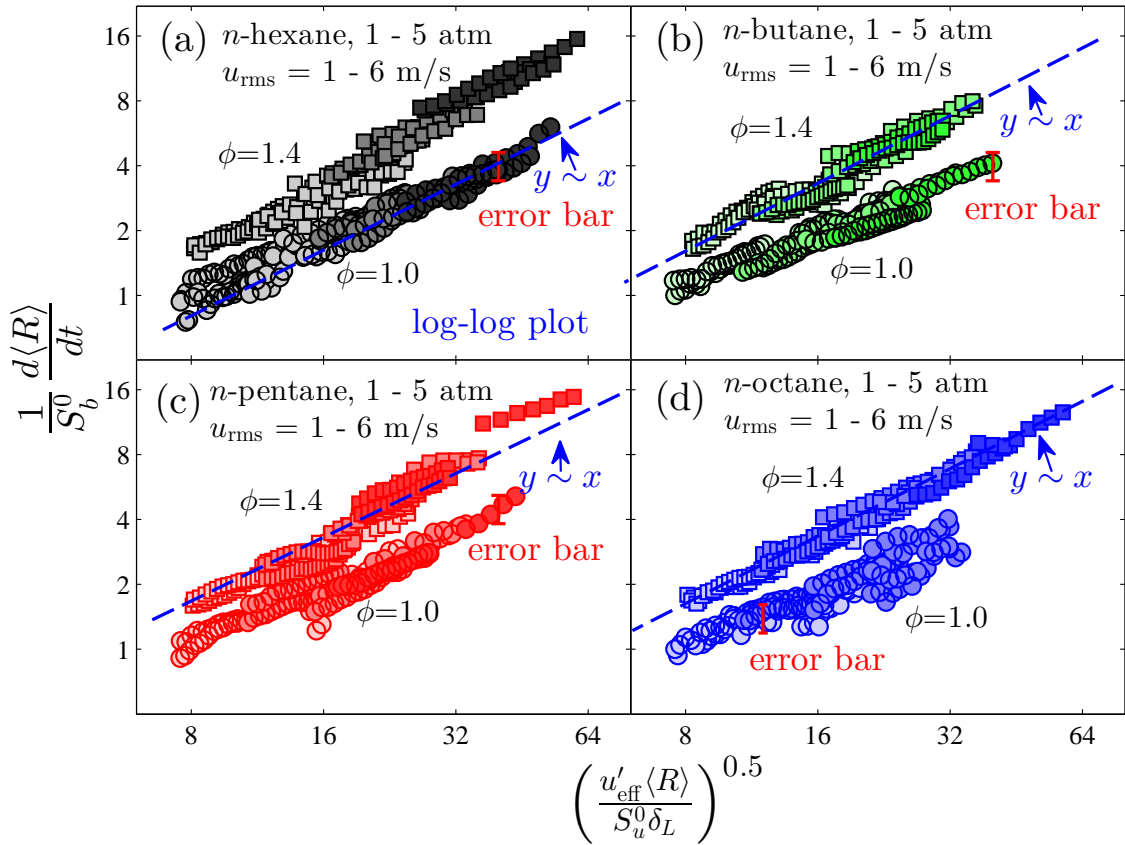


Figure 8.5: Normalized turbulent flame speeds for *n*-butane, *n*-pentane, *n*-hexane and *n*-octane plotted with  $Re_{\langle R \rangle, \delta_L}^{1/2}$ , for  $\phi = 1.0$  and 1.4 at various pressures and turbulent intensities.

run against pressure and  $u_{\text{rms}}$ , where  $S_{T,\text{mean}}$  is defined as,

$$S_{T,\text{mean}} = \frac{3 \int_{\langle R \rangle_1}^{\langle R \rangle_2} \langle R \rangle^2 \frac{d\langle R \rangle}{dt} d\langle R \rangle}{\Theta (\langle R \rangle_2^3 - \langle R \rangle_1^3)} \quad (8.1)$$

where  $\Theta$  is the thermal expansion ratio, and  $\langle R \rangle_1$  and  $\langle R \rangle_2$  are 1.0 and 2.0 cm respectively. It is seen that while laminar flame speeds decrease with pressure, turbulent flame speeds increase with pressure, and C<sub>4</sub>-C<sub>8</sub> *n*-alkanes have similar values for both.

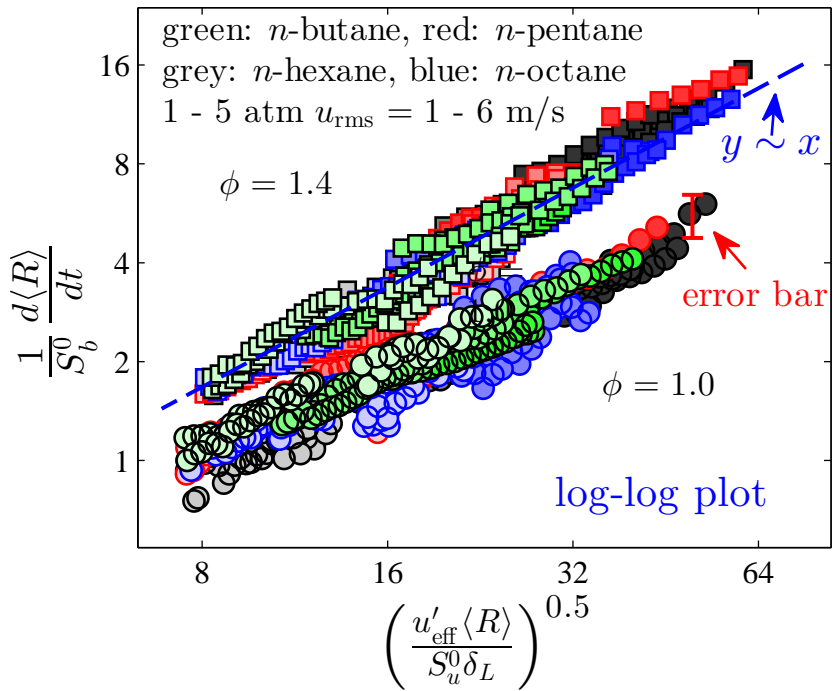


Figure 8.6: Normalized turbulent flame speeds for *n*-butane, *n*-pentane, *n*-hexane and *n*-octane plotted together for  $\phi = 1.0$  and  $1.4$  at various pressures and turbulent intensities.

### 8.3.3 Stretch-induced Local Extinction

Experiments at  $\phi = 0.8$  for a wide range of turbulence intensities and pressures have also been conducted. First, from the difference in the flame morphology between fuel-lean flames and stoichiometric and fuel-rich flames, as illustrated in Figure 8.9 for typical images of *n*-octane flames, that, while the flame images at  $\phi = 1.0$  and  $1.4$  show clear contours of the flamefront, those at  $\phi = 0.8$  on the contrary show that the flamefront locations cannot be sharply identified in extensive regions of the flame ensemble and the burning seems to spread out into multiple, loosely-connected, regions.

For  $\phi = 0.8$ , it is also observed local extinction as the flame propagates. Figure

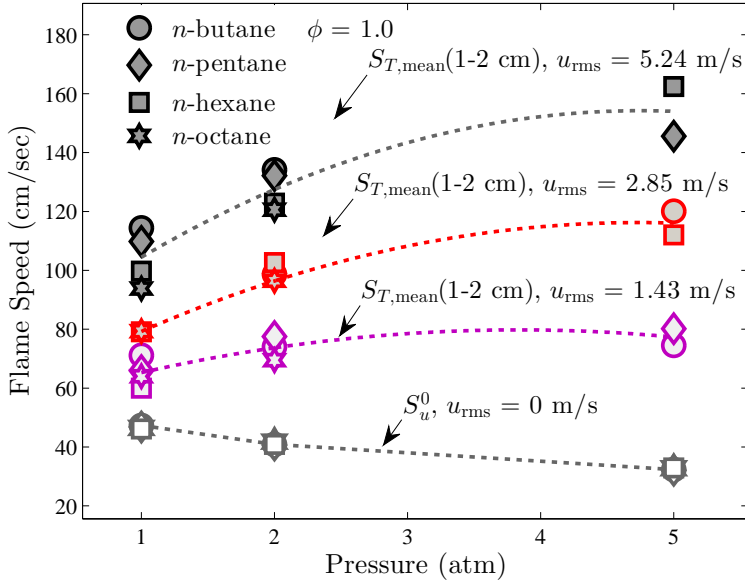


Figure 8.7: Absolute averaged propagation speed for  $\langle R \rangle$  from 1.0 to 2.0 cm,  $S_{T,\text{mean}}$  for each individual run as a function of pressure and  $u_{\text{rms}}$  at  $\phi = 1.0$ .

8.9 also shows a series of flame images for *n*-octane, where local extinction can be clearly identified at the marked zones. The occurrence of local extinction (as versus global extinction) over such a large region also suggests possible re-ignition since extinction leads to unburned hot fuel/air pockets which could re-ignite at another instant and location. Thus in spite of the fact that the conditions for  $\phi = 0.8$  fall at almost the same location as those for  $\phi = 1.0$  and 1.4 in the regime diagram, the nature of burning turns out to be quite distinct for these two cases. This observation implies that effects of nonequidiffusion need to be incorporated in a more generalized construction of the regime diagram to capture all possible effects.

It is further noted that local extinction and the blurry flame edge pose significant challenge in tracking or even defining the “flamefront” location. Nevertheless, tracking using the canny edge detection algorithm in MATLAB was still conducted,

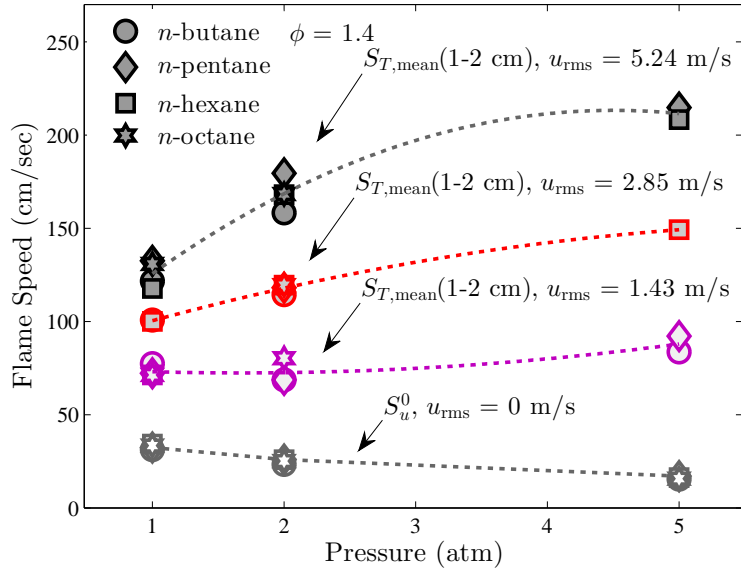


Figure 8.8: Absolute averaged propagation speed for  $\langle R \rangle$  from 1.0 to 2.0 cm,  $S_{T,\text{mean}}$  for each individual run as a function of pressure and  $u_{\text{rms}}$  at  $\phi = 1.4$ .

which can yield results with reasonably good consistency. In addition, multiple runs were repeated at the same condition to obtain more data for averaging. Figure 8.10 plots the normalized turbulent flame speed versus  $Re_{\langle R \rangle, \delta_L}^{1/2}$  at  $\phi = 0.8$  for *n*-butane, *n*-pentane, *n*-hexane and *n*-octane. First, it is seen that the data are more scattered than those for  $\phi = 1.0$  and  $\phi = 1.4$ , resulting in much higher random uncertainty, which makes it difficult to extract a clear trend from them. This causes a significant increase in the random uncertainty. Therefore, error bar 2 in Figure 8.10 represents  $\pm 80\%$  random uncertainty obtained from the 95% confidence interval from the four repeated experiments on *n*-hexane at  $\phi = 0.8$ .

To observe the trend of the mean flame speeds, Figure 8.11 plots linear fit of normalized turbulent flame speeds against  $Re_{\langle R \rangle, \delta_L}^{1/2}$  for each fuel at  $\phi = 0.8$ . The fitted results represent the mean value of experimental data. It is seen that on

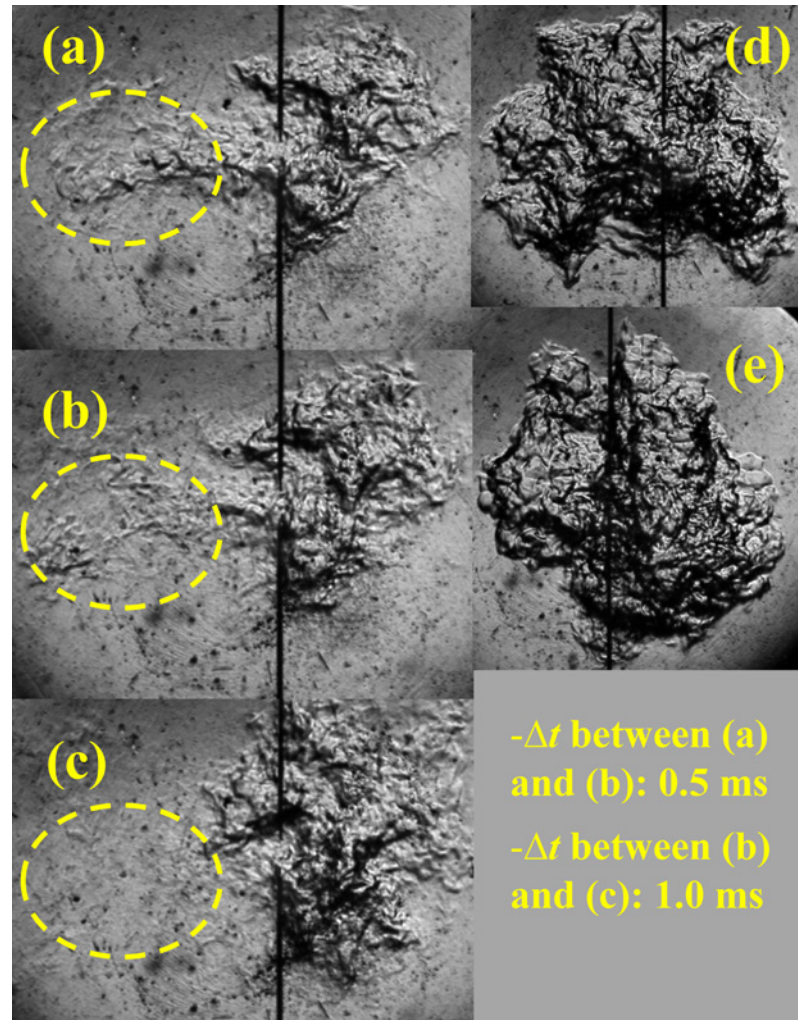


Figure 8.9: Schlieren images of *n*-octane/air flames at 1 atm with  $u_{\text{rms}} = 5.24 \text{ m/s}$  for (a-c)  $\phi = 0.8$ , (d)  $\phi = 1.0$ , (e)  $\phi = 1.4$  showing the large area of local extinction for  $\phi = 0.8$ , while other conditions do not show such events.

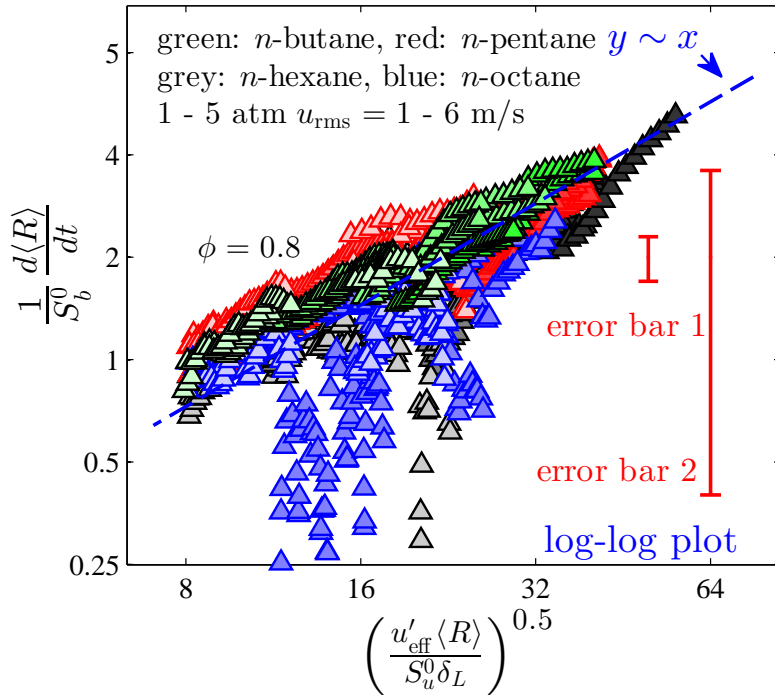


Figure 8.10: Normalized turbulent flame speeds for *n*-butane, *n*-pentane, *n*-hexane and *n*-octane plotted together for  $\phi = 0.8$  at various pressure and turbulent intensities.

average the turbulent flame speeds for *n*-octane are lower than *n*-hexane, which in turn are lower than *n*-pentane and *n*-butane. The trend seems to suggest that the turbulent flame speed decreases with the molecular size, although its validity is limited due to the increased uncertainty. In addition, from Schlieren images it is also found that local extinction for *n*-octane and *n*-hexane occurs in larger regions than *n*-butane and *n*-pentane. Finally, Figure 8.12 plots the linear fit of normalized turbulent flame speeds against  $Re_{\langle R \rangle, \delta_L}^{1/2}$  for all fuels and  $\phi$ . Again, it is seen that at  $\phi = 1.0$  and 1.4, the data for all four *n*-alkanes are almost the same.

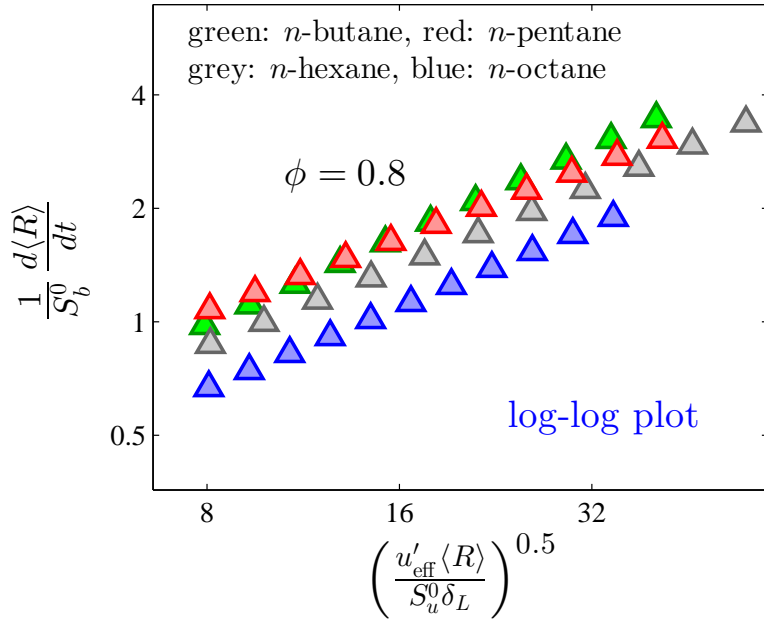


Figure 8.11: Linearly fitted results of normalized turbulent flame speeds against  $Re_{\langle R \rangle, \delta_L}^{1/2}$  for each fuel at  $\phi = 0.8$ .

## 8.4 Scaling of Turbulent Flame Speed

Finally, since new turbulent flame speed data on C<sub>4</sub>-C<sub>8</sub> *n*-alkanes have been measured, the scaling relations proposed for expanding turbulent flames proposed in Chapter 7 should be re-examined. Here only the data at  $\phi = 1.0$  and  $\phi = 1.4$  are considered, because as shown before there are severer local extinctions for flames of C<sub>4</sub>-C<sub>8</sub> *n*-alkanes at  $\phi = 0.8$ , which the scaling relations in Chapter 7 do not account for. In addition, for scaling of the thermodiffusive effects, only data at  $\phi = 1.0$  can be used, because flames of C<sub>4</sub>-C<sub>8</sub> *n*-alkanes at  $\phi = 1.4$  have negative Markstein numbers. Flame speed scaling for flames with negative Markstein number is a recognized challenge.

Figures 8.13 and 8.14 plot Equation 7.14 scaling for all experimental conditions

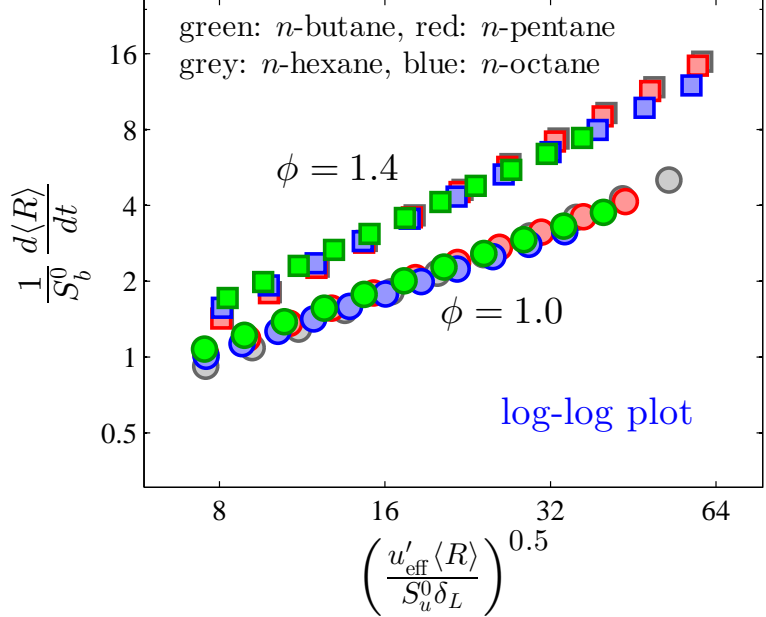


Figure 8.12: Linearly fitted results of normalized turbulent flame speeds against  $Re_{\langle R \rangle, \delta_L}^{1/2}$  for each fuel at  $\phi = 1.0$  and  $1.4$ .

presented in Chapter 7 and C<sub>4</sub>-C<sub>8</sub> *n*-alkanes at  $\phi = 1.0$  and  $\phi = 1.4$ , in linear and log-log scale, respectively. Again, it is seen that each set of the data corresponding to a particular mixture collapses reasonably well on a single line and the slope decreases with increasing Ma, the values of which are listed in Figures 7.3, 7.4 and 8.1.

Figures 8.15 and 8.16 plot Equation 7.15 scaling for all experimental conditions in Figures 8.13 and 8.14 which have positive Ma, in linear and log-log scale, respectively. It is seen that, compared to Figures 7.21 and 7.22, the new C<sub>4</sub>-C<sub>8</sub> *n*-alkane data at  $\phi = 1.0$  fall well in the band of the original plot, with the scattering having the same magnitude of the experimental random error, which suggests that Equation 7.15 is indeed quite general for the speed of expanding turbulent flames with

positive Markstein number.

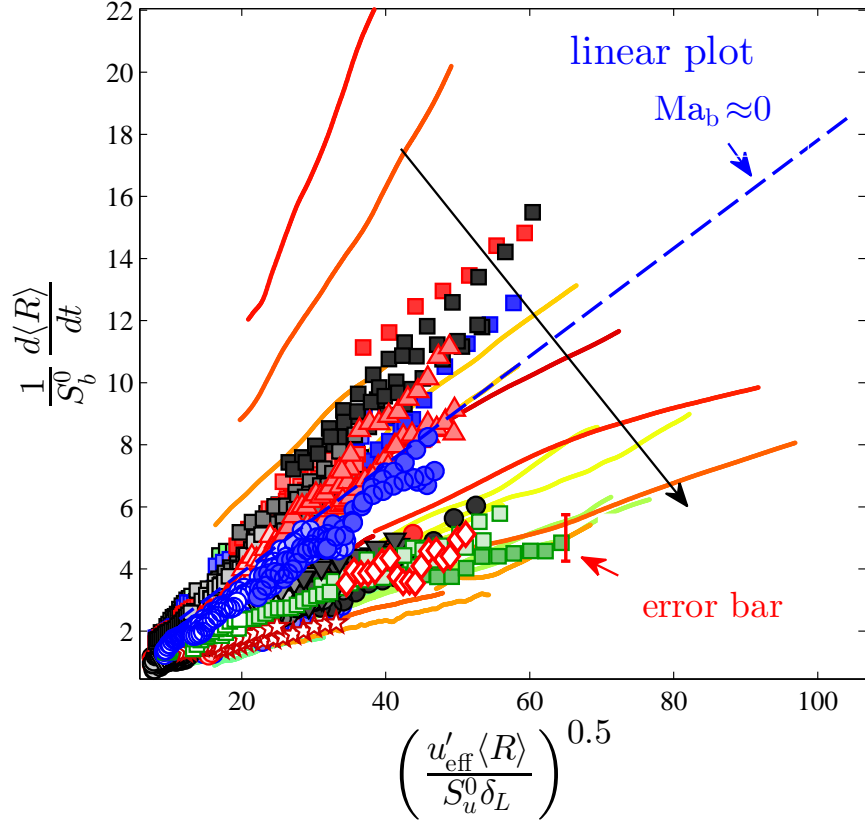


Figure 8.13: Linear plot of  $(1/S_b^0) d\langle R \rangle / dt$  against  $Re_{R,\delta_L}^{0.5}$  for experimental conditions listed in Figures 7.3 (symbols), 7.4 (lines) and 8.1 (symbols). The *iso-C<sub>8</sub>H<sub>18</sub>* data were obtained from Lawes *et al.* (2012).

## 8.5 Concluding Remarks

The present study reported turbulent flame speeds for *n*-butane, *n*-pentane, *n*-hexane and *n*-octane, from 1 atm to 5 atm and for a wide range of turbulence intensities and equivalence ratios, using expanding turbulent flames in a fan-stirred vessel. Results show that for stoichiometric and rich mixtures (near-unity *Le*, or

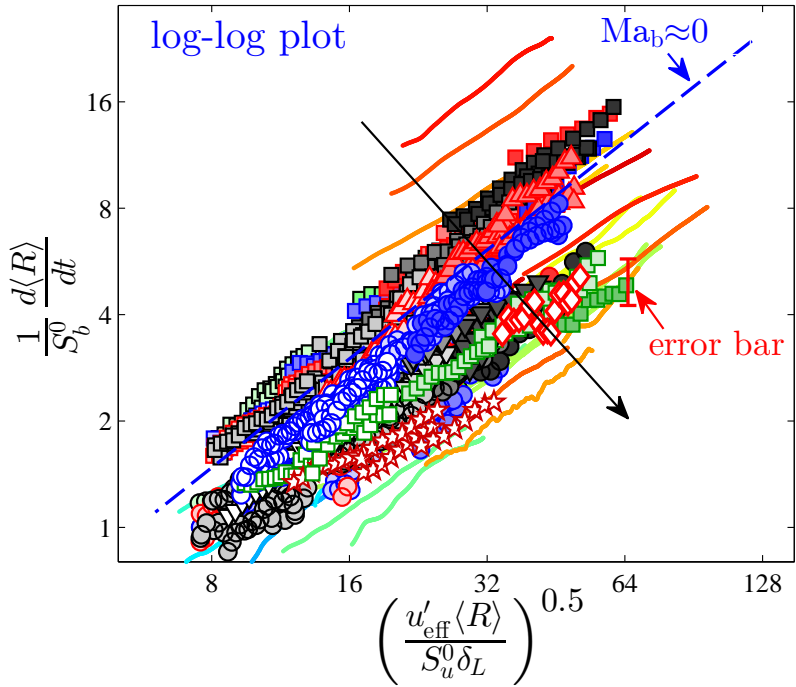


Figure 8.14: Log-log plot of  $(1/S_b^0) d\langle R \rangle / dt$  against  $Re_{R,\delta_L}^{0.5}$  for experimental conditions listed in Figures 7.3 (symbols), 7.4 (lines) and 8.1 (symbols). The *iso-C<sub>8</sub>H<sub>18</sub>* data were obtained from Lawes *et al.* (2012).

$Le < 1$ ), the normalized turbulent flame speeds of C<sub>4</sub>-C<sub>8</sub> *n*-alkanes are almost the same confirming the existence of flame speed similarity as observed for laminar flames. The similar flame speed also suggests that universally large chain *n*-alkanes break down to smaller species with similar reactivity before entering the reaction zone. The flame speed data for these conditions also shows  $Re_{\langle R \rangle, \delta_L}^{1/2}$  dependence.

The similarity in flame speeds, however, was not observed for lean mixtures ( $Le > 1$ ). The lean conditions were rather characterized by large regions of local extinction for almost all fuels as observed from the Schlieren images. Local extinctions and possible re-ignition results in large scatter in flame speed data. However, upon averaging, the data suggest that at lean conditions, the turbulent flame speeds

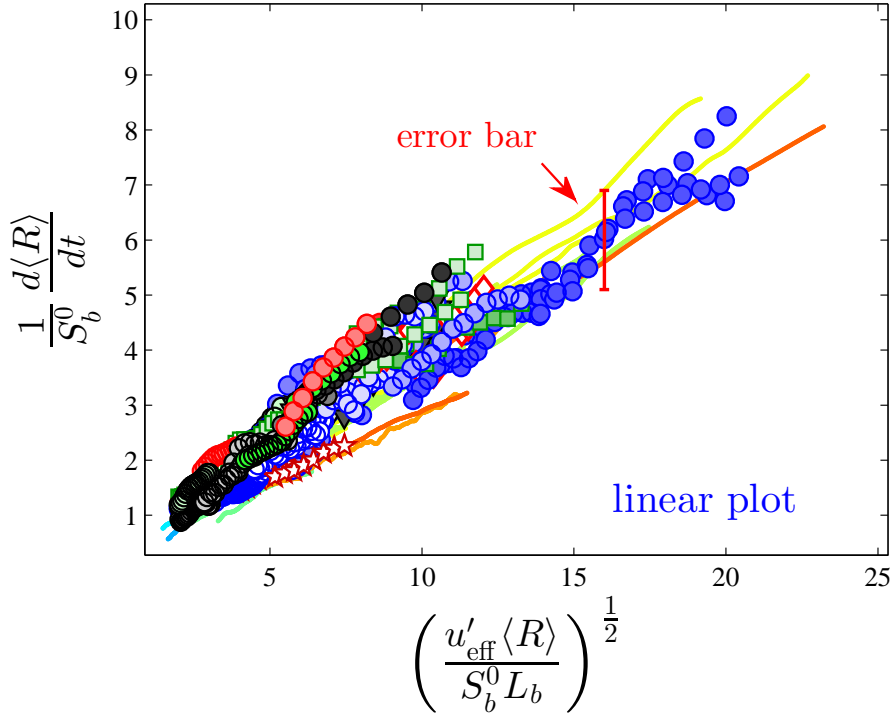


Figure 8.15: Linear plot of  $(1/S_b^0) d\langle R \rangle / dt$  against  $Re_{R,L_b}^{0.5}$  for experimental conditions listed in Figures 7.3 (symbols), 7.4 (lines) and 8.1 (symbols). The *iso-C<sub>8</sub>H<sub>18</sub>* data were obtained from Lawes *et al.* (2012).

decrease with the molecular weight of the fuel. The distinctively different behavior of turbulent flames at lean and rich mixtures at the same turbulence intensities and pressures strongly suggest inclusion of molecular diffusivity or  $Le$  in defining the regimes of turbulent flames.

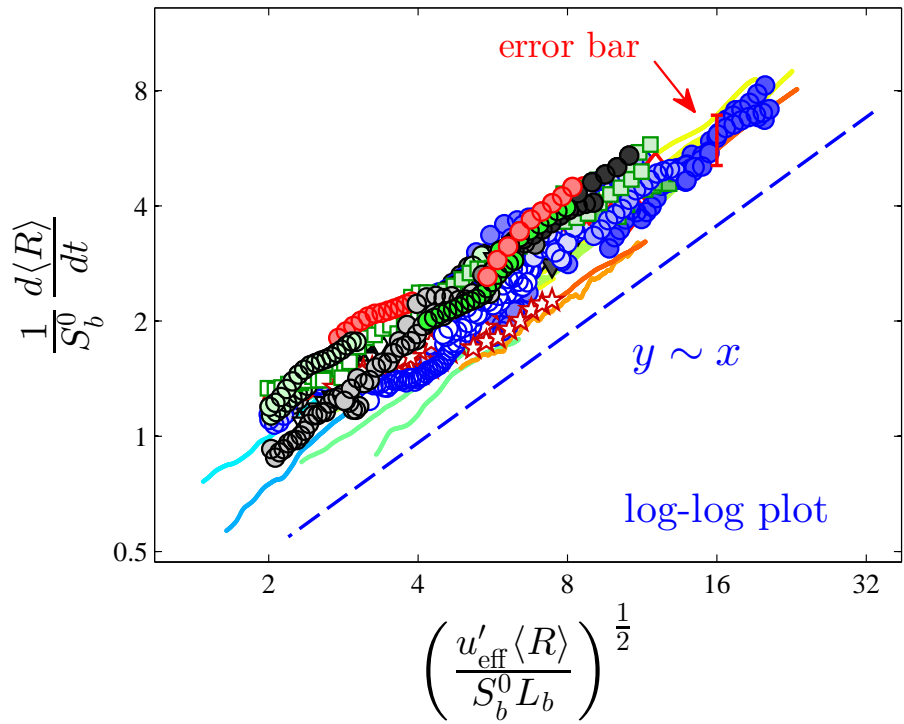


Figure 8.16: Log-log plot of  $(1/S_b^0) d\langle R \rangle/dt$  against  $Re_{R,L_b}^{0.5}$  for experimental conditions listed in Figures 7.3 (symbols), 7.4 (lines) and 8.1 (symbols). The iso-C<sub>8</sub>H<sub>18</sub> data were obtained from Lawes *et al.* (2012).

# Chapter 9

## Spark Ignition in Turbulent Flows

### 9.1 Introduction

Ignition of a combustible mixture by a stimulus kernel is of relevance to many terrestrial and extraterrestrial phenomena and applications, such as the various modes of engine operation and prevention of accidental explosions. Frequently, such ignition occurs in flows that are highly turbulent, involving a wide range of time and length scales. Previous studies have advocated that turbulence renders ignition more difficult (Ballal & Lefebvre, 1975, 1977; Kaminski *et al.*, 2000; Bradley *et al.*, 2004; Akindele *et al.*, 1982; Ahmed *et al.*, 2007; Ahmed & Mastorakos, 2006; Shy *et al.*, 2008b, 2010; Cardin *et al.*, 2013), based on the notion that turbulence increases the dissipation rate of the deposited kernel energy before an embryonic flame either has the time or is aerodynamically favorable to develop.

Such an argument, however, does not take into consideration the evolution and dynamics of the structure of the nascent flame kernel after it is formed. As discussed in previous chapters, particularly in Chapters 1 and 3, an expanding spherical flame

is subjected to positive stretch with the rate  $K = (2/R_f)dR_f/dt$  (Equation 3.3), where  $R_f$  and  $dR_f/dt$  are the flame radius and speed, respectively. Stretch modifies the flame temperature and thus flame speed due to the differential molecular diffusion of heat and mass. The controlling parameter is the Lewis number of a combustible mixture,  $Le$ . For  $Le > 1$ , the flame temperature and flame speed are reduced/increased if it is subjected to positive/negative stretch, and vice versa for  $Le < 1$ . For a nascent flame kernel with large  $Le$ , since the flame radius  $R_f$  is small and  $dR_f/dt$  is positive, it is subjected to extremely large positive stretch  $K$ , which significantly reduces the flame temperature and speed. Recent spark ignition experiments in quiescent gas (Kelley *et al.*, 2009) showed that for mixtures with large  $Le$  this stretch effect turns out to be the most limiting factor that prohibits spark ignition, and for successful ignition the deposited energy needs to be sufficient to maintain flame propagation until flame size surpasses a large value to diminish the stretch effect.

If ignition is not limited by the formation of the embryonic flame kernel but rather by the aerodynamic stretching on the kernel, an interesting question arises: what role does turbulence play in the morphology and thereby burning intensity of the embryonic flame? While the flame kernel in quiescent gas is spherical and subjected to positive stretch over its entire surface, wrinkling and even possibly breaking of the flame surface by eddies of wide-ranging scales in a turbulent flow could create flamelets with a wide range of stretch rates. For mixtures with large  $Le$ , the temperature and speed of the flamelets with small positive stretch and negative stretch can be locally enhanced. Since these locally facilitated flamelets can collectively ignite the entire mixture, it is possible that turbulence could promote ignition in conditions where ignition is not limited by the flame kernel formation

but rather its subsequent propensity to grow.

The present work aims to explore such a possibility, which may alter the traditional view on the criteria of ignition in turbulent flows, and as such highlighting the necessity to incorporate the dynamics of the embryonic flamelet structure into the description.

The results presented in this chapter have been previously published in the following journal article ([Wu et al., 2014b](#)):

- WU, F., SAHA, A., CHAUDHURI, S. & LAW, C. K. 2014*b* Facilitated ignition in turbulence through differential diffusion. *Physical Review Letters* **113**, 024503

## 9.2 Experimental Considerations

Tests were conducted in a Vessel II. Compared to previous experimental studies on spark ignition in turbulent flows ([Ballal & Lefebvre, 1975, 1977](#); [Kaminski et al., 2000](#); [Bradley et al., 2004](#); [Akindele et al., 1982](#); [Ahmed et al., 2007](#); [Ahmed & Mastorakos, 2006](#); [Shy et al., 2008b, 2010](#); [Cardin et al., 2013](#)), the advantage of Vessel II is that it creates a near isotropic turbulence in a constant pressure environment with small mean flow. As described in Chapter 2, the present ignition system was not designed and equipped for measuring and controlling the ignition energy with high accuracy. The ignition system was similar to those used in automotive engines, with slight modifications by replacing the spark plug by two tungsten wires of 250- $\mu\text{m}$  diameter and centered axially. The ignition energy is controlled by the voltage ( $U_{\text{ign}}$ ) across a discharging capacitor with capacitance  $C = 33 \mu\text{F}$ . Therefore, the total energy input from the discharging capacitor is  $E_{\text{ign}} = CU_{\text{ign}}^2/2$ . It is noted

that this energy is larger than the real energy supplied to the mixture due to losses in the electric circuit and heat losses to the two tungsten wires, which is difficult to quantify. The system suffices the goal of the present investigation, which is not to report ignition energy but to explore whether turbulence can enhance ignition under certain conditions with  $Le > 1$ .

In designing the matrix of the experimental investigation, it was noted that previous works on the interaction of turbulence and ignition kernel were limited to inhibited ignition, ostensibly due to the small deviations in  $Le$  from unity. Therefore, experiments to cover a wide range of  $Le$  were extended, with specially focus on mixtures with  $Le$  sufficiently greater than unity such that ignition could be limited by the extent of stretch that the flame kernel experiences. At the same time, mixtures with  $Le \approx 1$  or  $Le < 1$  were also considered, to provide a complete description of the phenomena.  $H_2/O_2$  mixtures have been selected for most of the investigation because it allows flexible variation of  $Le$  due to the drastic difference between the molecular weights of hydrogen and oxygen. This can be achieved by varying the  $H_2/O_2$  ratio, namely the equivalence ratio  $\phi$ , thereby changing the diffusivity of the deficient, hence controlling, reactant. Furthermore, since the  $H_2/O_2$  oxidation chemistry is relatively simple and also reasonably well established, the present data can be usefully adopted in further computational studies on issues of turbulence-chemistry interaction in general and of this practically relevant problem in particular.

### 9.3 Experimental Results

First, the distinctively different behaviors of flame kernel growth in quiescent gas for  $Le < 1$  and  $Le > 1$  cases respectively are demonstrated. Same as in Chapters 7 and 8, the flame radius in turbulent cases is defined as  $\langle R \rangle = \sqrt{A_S/\pi}$ , where  $A_S$  is the area enclosed by the flame edge tracked from the Schlieren image. When  $u_{\text{rms}} = 0$ ,  $\langle R \rangle = R_f$ .

Figure 9.1 plots the instantaneous propagation velocity  $d\langle R \rangle / dt$  for a lean H<sub>2</sub>/air mixture with  $Le < 1$ . It is seen from the solid line (the quiescent case, the cases with turbulent will be discussed later) that, for the quiescent situation of no turbulence,  $u_{\text{rms}} = 0$ , an  $Le (= 0.3) < 1$  flame will continuously propagate, with monotonically decreasing velocity, as long as sufficient ignition energy, controlled by the spark discharge voltage  $U_{\text{ign}}$ , is supplied. Figure 9.2 plots the instantaneous propagation velocity  $d\langle R \rangle / dt$  for a rich H<sub>2</sub>/air mixture with  $Le > 1$ . It is seen, again from the solid lines, that different from the lean case, the  $Le (= 2.3) > 1$  flame will extinguish if the ignition energy is not sufficient ( $U_{\text{ign}} = 80$  V), but with sufficient ignition energy ( $U_{\text{ign}} = 120$  V) will continuously propagate after having attained a minimum, critical radius.

Next, the possible enhancement of ignition by turbulence, through direct, time-resolved Schlieren images, with the fuel rich H<sub>2</sub>/air mixture of  $\phi = 5.1$  are demonstrated. The mixture has a large  $Le$  of 2.3 since the controlling, deficient reactant is O<sub>2</sub>, while the thermal diffusivity is controlled by that of H<sub>2</sub>. Figures 9.3A and B respectively show a successful and a failed ignition event in quiescent gas ( $u_{\text{rms}} = 0$ ), with an ignition voltage,  $U_{\text{ign}} = 120$  V and a smaller value of 80 V. These Schlieren images correspond to the solid lines shown in Figure 9.2.

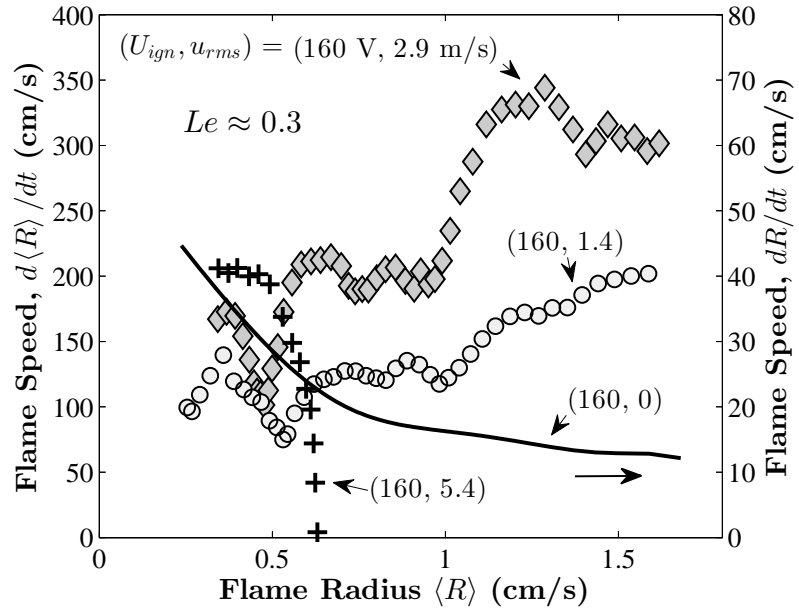


Figure 9.1: Flame speed versus flame radius for lean H<sub>2</sub>/air at  $\phi = 0.18$  at different ignition voltages and turbulent levels. The spark gap distance  $d_g$  is 0.30 mm.

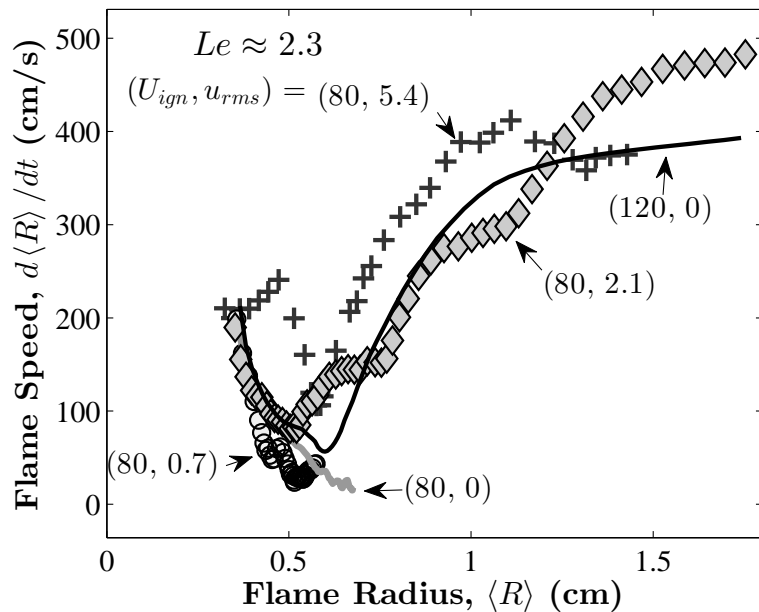


Figure 9.2: Flame speed versus flame radius for rich H<sub>2</sub>/air at  $\phi = 5.1$ , at different turbulent levels. The spark gap distance  $d_g$  is 0.58 mm.

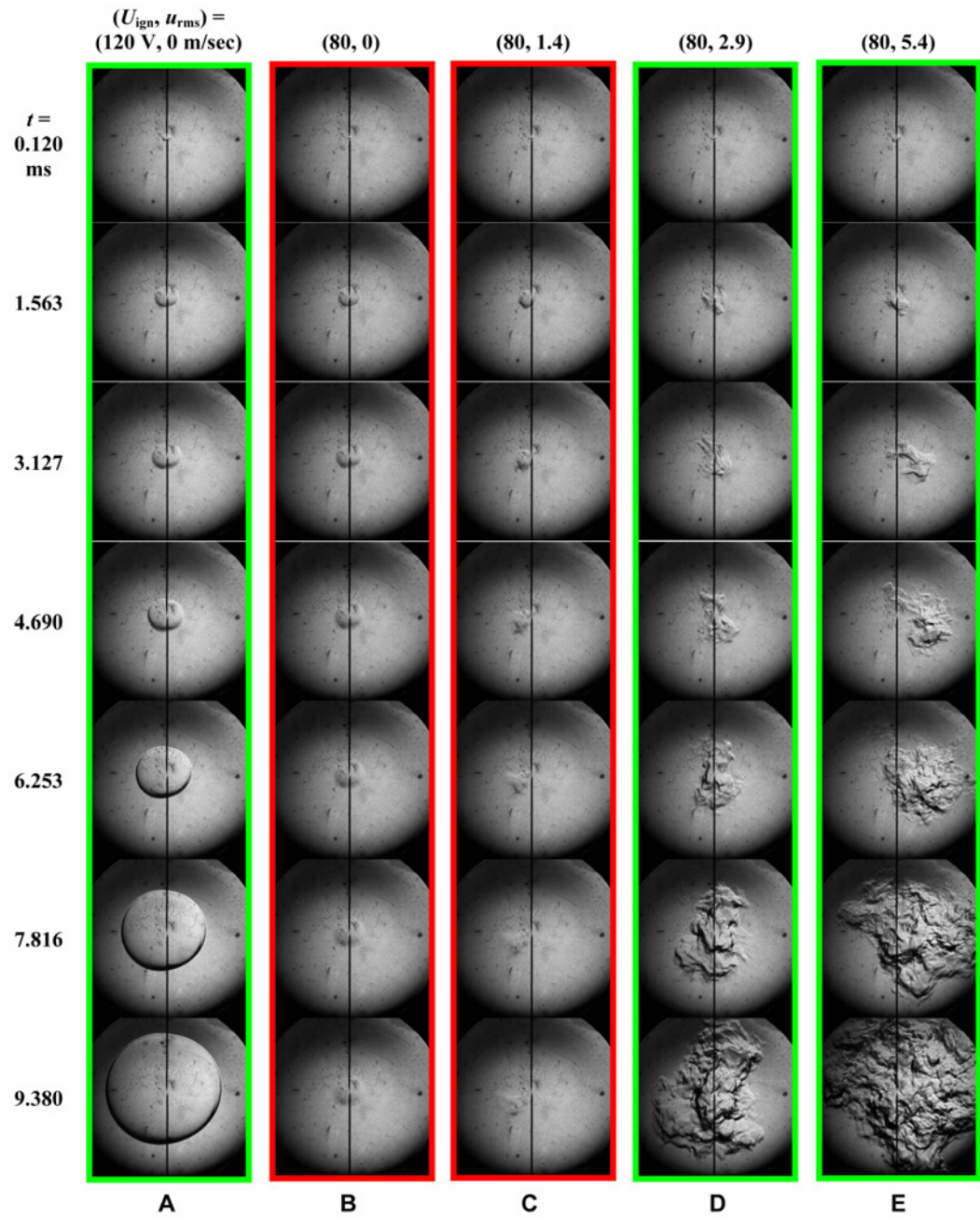


Figure 9.3: Sequential Schlieren images of flame kernel development for H<sub>2</sub>/air at  $\phi = 5.1$  ( $Le \approx 2.3$ ), at different turbulent levels. Schlieren imaging signal is proportional to the density gradient of the flow field, a good indicator of the flame front. The view for each image is 65 mm × 65 mm.  $t$  is time after discharge.

If the ignition voltage is maintained constant at 80 V but progressively increase the turbulence level, Figures 9.3B-E show that the structure of the flame kernel is changed from a positively stretched spherical surface to a multitude of wrinkled flamelets of both positive and negative curvatures, and that ignition is achieved at  $u_{\text{rms}} = 2.9$  m/s. This result therefore supports the notion that for  $Le > 1$ , a combustible mixture can be ignited in turbulence with an ignition energy that is not enough to ignite the same mixture in quiescent gas.

The ignition boundary for the  $\phi = 5.1$  mixture in terms of the turbulence intensity and the ignition energy have been extensively mapped out and summarized in Figure 9.4. It is found that the minimum discharge voltage required for successful ignition in the presence of moderate turbulence ( $u_{\text{rms}} = 2.9$  m/s) is 65 V, which is substantially reduced from the voltage required for ignition in quiescent gas (100 V). Based on the relation  $E_{\text{ign}} = CU_{\text{ign}}^2/2$ , this result implies that the minimum ignition energy can be lowered by a few factors with the presence of turbulence.

Having demonstrated the facilitating effect of turbulence on the  $Le > 1$ , rich H<sub>2</sub>/air mixtures, it is necessary to investigate the response of lean mixtures, whose  $Le$  is less than unity because the controlling, deficient reactant is now H<sub>2</sub> and the thermal diffusivity is dominated by those of O<sub>2</sub> and N<sub>2</sub>. As anticipated earlier, since a flame kernel with  $Le < 1$  is always facilitated by positive stretch in quiescent gas, ignition is expected to be successful as long as a flame kernel can be established. Turbulence, in this case, increases the dissipation rate of the deposited kernel energy and as such renders ignition progressively more difficult with increasing turbulence intensity, eventually leading to extinction. The results for lean H<sub>2</sub>/air ( $\phi = 0.12 - 0.2$ , Figure 9.4B and 9.4C) confirm this mechanistic interpretation and are also consistent with the conclusions of previous studies, which, as noted earlier, were

mostly based on  $Le \approx 1$  mixtures.

The possibility that the controlling ignition chemistry could be different for fuel rich and fuel lean mixtures, causing the observed phenomena, also needs to be ruled out. To remove such a possibility, the values of  $Le$  are manipulated by changing the inert bath gas from  $N_2$  to He, Ar or  $CO_2$ , with the fuel/oxygen ratio fixed such that the controlling lean-vs.-rich chemistry is not affected. It is seen (Figures 9.4D-H) that the facilitating effect of turbulence is again manifested only for  $Le > 1$  mixtures, and that the effect can be flipped from inhibiting to facilitating solely by changing the inert bath gas while  $\phi$  is fixed at unity. In particular, turbulence facilitates ignition with He, a light inert that substantially increases the thermal conductivity and thus  $Le$ , while, with heavier inerts such as  $CO_2$  and Ar,  $Le$  becomes less than or near unity and as a result inhibits ignition. These extensive sets of experiments therefore rule out the possibility that the distinct turbulence effects for fuel lean and fuel rich conditions are due to different chemical kinetics.

Finally, in order to provide even further substantiation of the phenomena and concept advanced herein, and for fuels other than  $H_2$ , the lean-vs.-rich aspect of the mixture by using *n*-butane ( $n\text{-C}_4\text{H}_{10}$ ) as the fuel has been flipped. The values of  $Le$  for *n*-butane are greater and smaller than unity for lean and rich mixtures because of the substantially larger molecular weight of *n*-butane relative to that of oxygen. Thus lean (rich) *n*-butane/air mixtures should exhibit behavior similar to those of rich (lean)  $H_2$ /air mixtures, respectively. Figures 9.4I-K summarizes the ignition test results for a lean and a rich *n*-butane/air mixture, with  $Le$  2.1 and 0.9 respectively. It is seen that ignition is indeed facilitated for the  $Le > 1$ , lean mixture. The above extensive results therefore demonstrate that ignition enhancement by turbulence for mixtures with large  $Le$  is of a general nature, irrespective of fuel,

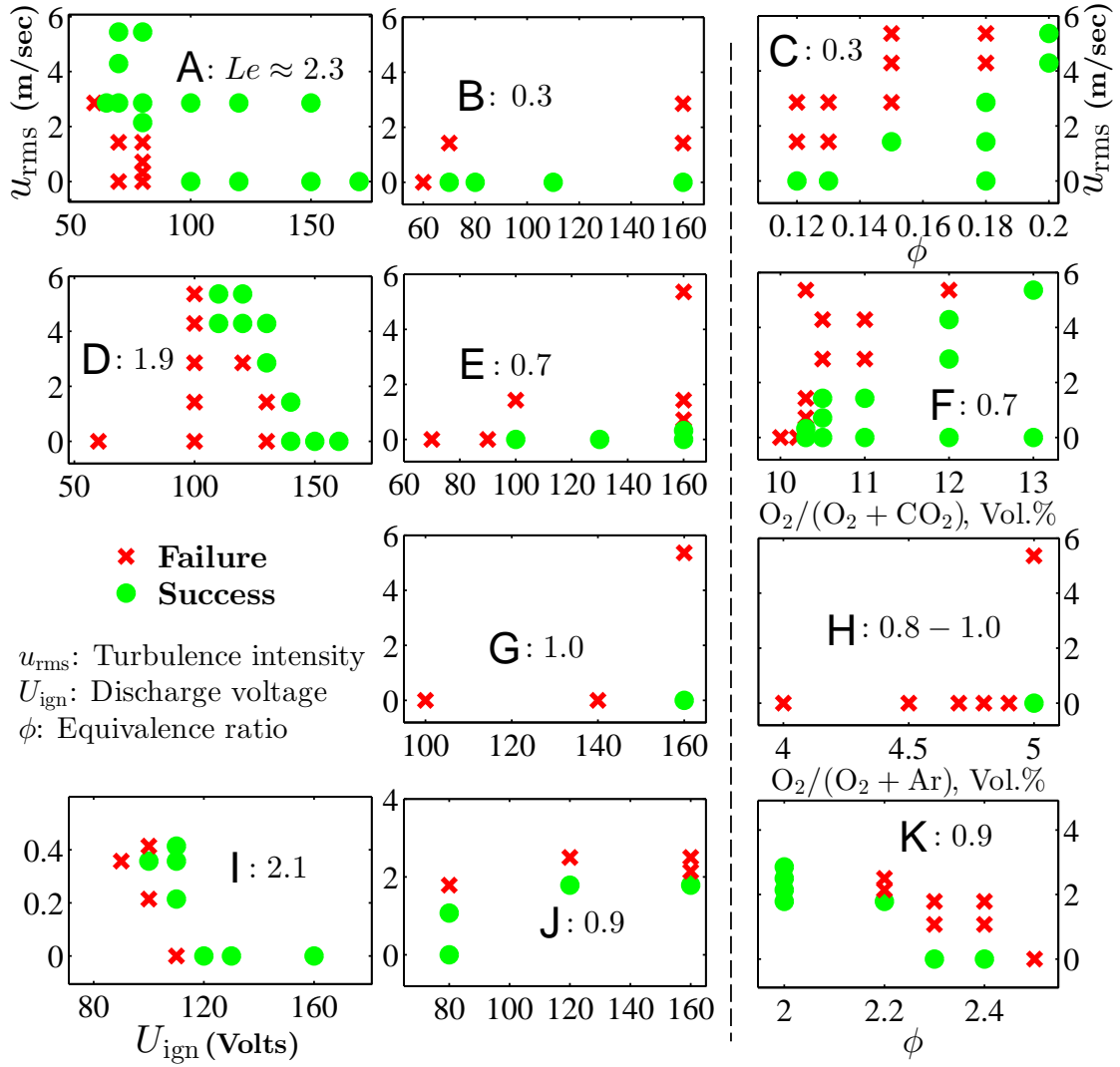


Figure 9.4: Ignition test results plotted against turbulence intensity and discharge voltage or mixture reactivity, represented by the  $H_2/O_2$  ratio or the amount of inert gas. (A)  $H_2$ /air at  $\phi = 5.1$  (B)  $H_2$ /air at  $\phi = 0.12$  (C)  $H_2$ /air for fixed  $U_{ign} = 160$  V. (D)  $H_2/O_2/He$  at  $\phi = 1.0$ ,  $O_2/(O_2+He)$  Vol.% = 8.0% (E)  $H_2/O_2/CO_2$  at  $\phi = 1.0$ ,  $O_2/(O_2+CO_2)$  Vol.% = 10.3% (F)  $H_2/O_2/CO_2$  at  $\phi = 1.0$  for fixed  $U_{ign} = 160$  V (G)  $H_2/O_2/Ar$  at  $\phi = 1.0$ ,  $O_2/(O_2+Ar)$  Vol.% = 5.0% (H)  $H_2/O_2/Ar$  at  $\phi = 1.0$  for fixed  $U_{ign} = 160$  V. (I)  $n\text{-C}_4\text{H}_{10}/\text{air}$  at  $\phi = 0.7$  (J)  $n\text{-C}_4\text{H}_{10}/\text{air}$  at  $\phi = 2.2$  (K)  $n\text{-C}_4\text{H}_{10}/\text{air}$  for fixed  $U_{ign} = 160$  V. Initial pressure and temperature for all tests are 1 atm and 298 K. The  $Le$  shown in figure is defined to be the effective Lewis number of a combustion mixture, based on theory in (Matalon *et al.*, 2003). The spark gap distance  $d_g$  is 0.58 mm for case A, 0.30 mm for cases B-H, and 0.80 mm for cases I-K.

equivalence ratio and inert.

## 9.4 Explanation and Analysis

The above extensive results therefore demonstrate clearly that ignition enhancement by turbulence for mixtures with large  $Le$  is universal irrespective of fuel, equivalence ratio and inert. A reasonable explanation is provided next.

As known from the experiments in quiescent gas, for mixtures with large  $Le$ , the flame kernel propagation is significantly suppressed by the positive stretch. The theory behind it and the relation between flame speed and stretch rate have been discussed in Chapter 3, in which it is shown that the relation between flame speed and stretch rate is largely nonlinear such that existing theoretically derived relations using asymptotic analysis all cause uncertainties when they are used for the extrapolation of laminar flame speeds. From those relations, it is shown that the following one can describe the situations with  $L_b K > 0$  qualitatively well,

$$\left(\frac{S_b}{S_b^0}\right)^2 \ln \left(\frac{S_b}{S_b^0}\right)^2 = -\frac{2L_b K}{S_b^0} \quad (3.5)$$

It can be re-written in the following form,

$$\left(\frac{S_b}{S_b^0}\right)^2 \ln \left(\frac{S_b}{S_b^0}\right)^2 = -2\text{Ma}_b \frac{\delta_L K}{S_b^0} \quad (9.1)$$

where  $\delta_L$  is the flame thickness, defined in Equation 3.10,  $\text{Ma}_b = L_b/\delta_L$  is the Markstein number defined based on the burned gas flame speed (see Chapter 7). In Equation 9.1, the relation is expressed in terms of the non-dimensional flame speed  $S_b/S_b^0$  and the non-dimensional stretch rate  $\delta_L K/S_b^0$ . Markstein number  $\text{Ma}_b$ , as a

parameter in Equation 9.1, embodies information regarding the transport properties of heat and mass, flame structure and sensitivity of reaction rate to temperature. Its value mainly depends on the sign of  $Le-1$ , *i.e.*, for  $Le > 1$   $Ma_b$  is greater than 0 and for  $Le < 1$   $Ma_b$  is less than 0. The explicit expression and the associated accuracy vary with the level of assumptions made in the asymptotic analyses (Matalon & Matkowsky, 1982; Pelce & Clavin, 1982; Bechtold & Matalon, 2001; Matalon *et al.*, 2003; Law, 2006; Clavin & Graña Otero, 2011). However,  $Ma_b$  can be determined by fitting experimental data of  $S_b/S_b^0$  and  $\delta_L K/S_b^0$  against Equation 9.1 with  $S_b^0$  and  $\delta_L$  computed from the one-dimensional planar flame using a predictive chemical kinetic model.

Two observations can be made from the above theoretical results. First, it can be shown that the linearized form of Equation 9.1 is,

$$S_b = S_b^0 \left( 1 - Ma_b \frac{\delta_L K}{S_b^0} \right) \quad (9.2)$$

which is equivalent to Equation 3.4. From Equation 9.2, it is apparent that the flame response is qualitatively affected by the sign of a combined, diffusivity-affected stretch term,  $Ma_b \delta_L K/S_b^0$ , weakened when it is greater than 0, and strengthened otherwise. Second, Equation 9.1 exhibits the dual-solution, extinction turning-point behavior, with flame extinction occurring at  $Ma_b \delta_L K/S_b^0 = e^{-1}$  and  $S_b/S_b^0 = e^{-1/2}$ , where  $e$  is the exponential constant.

From the experimental data,  $Ma_b$  is determined to be 3.8 for H<sub>2</sub>/air at  $\phi = 5.1$ . Then Equation 9.1 is plotted in Figure 9.5. It is seen that both  $S_b/S_b^0$  and its slope decreases with  $\delta_L K/S_b^0$ , and at  $\delta_L K/S_b^0 \approx 0.048$ , the slope of  $S_b/S_b^0$  becomes negative infinity, which means that the flame will be extinguished if  $\delta_L K/S_b^0$  is

further increased. Therefore, the condition  $\delta_L K / S_b^0 < 0.048$  defines the flammability limit.

Successful ignition depends on whether  $\delta_L K / S_b^0$  for a flame kernel is within the flammability limit when all the ignition energy is consumed. In quiescent gas, since the flame kernel is spherical, it is subjected to only one value of  $\delta_L K / S_b^0$ , *i.e.*, the probability density function (PDF) for  $\delta_L K / S_b^0$  is a delta function. The condition with the minimum velocity of a growing flame kernel approximately corresponds to the condition where ignition energy vanishes and from the experimental data (the quiescent case in Figure 9.2),  $\delta_L K / S_b^0$  is found to be 0.049, very close to the critical value 0.048 meaning the flame is close to be extinguished by the strong stretch. In turbulence, the flame kernel is subjected to a range of wrinkling and stretching by turbulent eddies, and thus the PDF for  $\delta_L K / S_b^0$  spans over a wide range of values. If the PDFs for  $\delta_L K / S_b^0$  in quiescent gas and turbulence are both assumed to be Gaussian, the turbulent  $\delta_L K / S_b^0$  PDF has a much larger standard deviation (a reasonable assumption based on measured stretch rate distribution of turbulent flames). Figure 9.5 also plots the assumed PDFs of  $\delta_L K / S_b^0$  in quiescent and turbulent cases. It is seen that the turbulence PDF covers much more flammable conditions, *i.e.*,  $\delta_L K / S_b^0 < 0.048$ . In addition, the PDF for  $S_b / S_b^0$  can also be calculated from the  $\delta_L K / S_b^0$  PDF and Equation 9.1, which is shown in Figure 9.6. It is seen that all possible values for  $S_b / S_b^0$  are greater than a critical value, and the  $S_b / S_b^0$  PDF in quiescent gas is located at values only slightly larger than this critical value, while the  $S_b / S_b^0$  PDF in turbulence spans over values that are much larger. It can also be calculated from the  $S_b / S_b^0$  PDFs that the mean values for  $S_b / S_b^0$  in turbulence is much larger than that in quiescent gas.

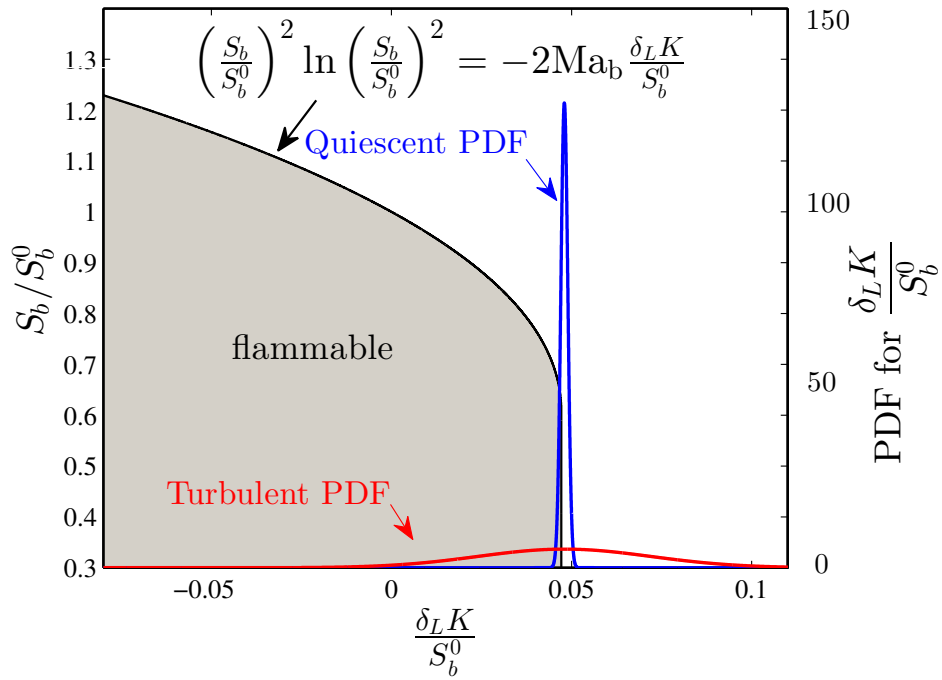


Figure 9.5: The relation between flame speed and stretch given by Equation 9.1 and the probability density function (PDF) of  $\delta_L K / S_b^0$  in quiescent and turbulent conditions for H<sub>2</sub>/air at  $\phi = 5.1$ . The Markstein number  $Ma_b = 3.8$  is extracted from the experimental data with  $U_{ign} = 120$  V and  $u_{rms} = 0$ . The thickness  $\delta_L = 0.06$  cm and speed (relative to burned gas velocity) of the unstretched flame  $S_b^0 \approx 500$  cm/sec are calculated using the Chemkin PREMIX code using the mechanism by Burke *et al.* (2012). The PDFs of  $\delta_L K / S_b^0$  in quiescent and turbulent conditions is assumed to be Gaussian, with mean value 0.049, which is calculated based on the conditions at the minimum speed in the experiment  $U_{ign} = 120$  V and  $u_{rms} = 0$ , *i.e.*,  $\langle R \rangle \approx 0.5$  cm and  $d \langle R \rangle / dt \approx 100$  cm/sec. The standard deviation for the quiescent case is assumed to be 0.001, to mimic the delta function, while the standard deviation for the turbulence case is assumed to be 0.03, much larger than the quiescent case.

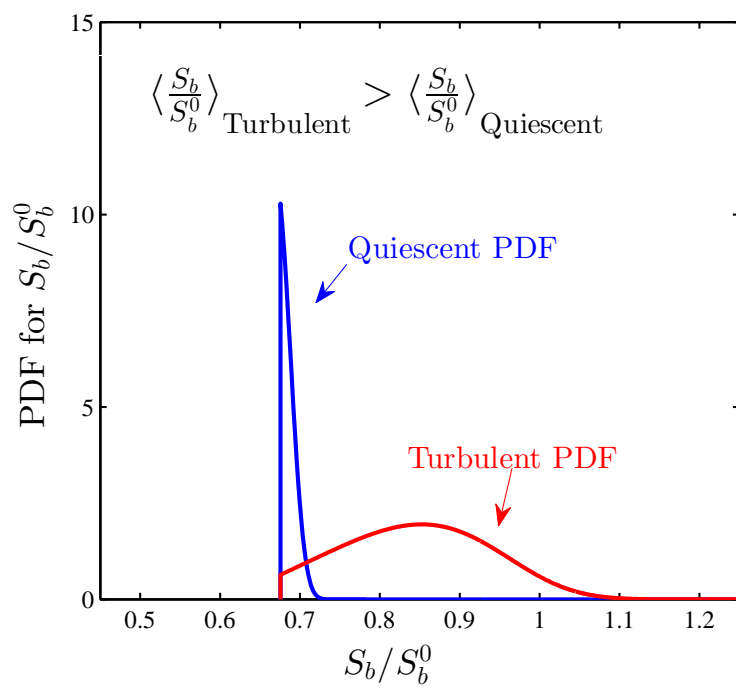


Figure 9.6: The PDF for  $S_b/S_b^0$  calculated from PDF for  $\delta_L K/S_b^0$  and Equation 9.1, for conditions outside the flammability limit,  $S_b/S_b^0$  is set to be 0 due to extinction.

## 9.5 Concluding Remarks

In this chapter, it was experimentally shown that, while turbulence is usually believed to suppress ignition due to the enhanced dissipation of localized ignition energy, it can actually facilitate ignition under conditions where ignition is limited by the difficulty of the flame kernel to transition into an expanding flame. This is possible through an embryonic flamelet structure consisting of segments subjected to both positive and negative stretch, while quiescent ignition generates only positive stretch through the positive curvature over the expanding, smooth flame surface. Such an understanding is of both practical and scientific significance. For example, explosion tests in quiescent gas may underestimate the risk of accident, while engine flows can also be optimized to reduce misfire for ultra-lean, clean, fuel-efficient operations, recognizing that engine fuels are large hydrocarbons such that their lean burning corresponds to  $Le > 1$  situations. Furthermore, while studies of supernova explosions have always assumed the initial existence of a flame that subsequently transitions to a detonation wave, perhaps it would be of interest to also investigate situations for which the establishment and sustenance of such a flame may not be possible in the first place, recognizing the fact that the  $Le$  for supernovae is exceedingly large, of the order of  $10^4$ . Finally, the potential implication on the ignition and reactions of liquid-phase and supercritical systems for various technological applications such as materials synthesis, is also of interest because they are also characterized by extremely large values of  $Le$ .

# **Chapter 10**

## **Conclusions and Recommendations**

### **10.1 Conclusions**

Recognizing the challenges of combustion science, particularly the nonlinear, multi-variable and multi-scale nature in both chemical kinetics and fluid mechanics, the present investigation has focused on two topics: measurements of laminar flame speeds and dynamics of premixed flames. Experimentation on the expanding flame configuration is the main technique of the study. Since each chapter contains its own conclusions, the following summary is presented as a brief overview of the results.

A unique dual-chamber, high-pressure, fan-stirred, preheated combustion vessel was developed for studying both laminar and turbulent flames. The dual-chamber and symmetric fan design provides well-defined initial and boundary conditions, such as constant-pressure during flame propagation and near isotropic turbulence. They also allow high operating pressures up to 30 atm.

The uncertainty associated with stretch extrapolation of laminar flame speeds from expanding spherical flames is quantified using numerical simulations. Results showed large extrapolation error for flames with Lewis number largely deviating from unity at atmospheric pressures. This systematic uncertainty explained the discrepancies in many previous measurements on hydrogen and heavy hydrocarbons, and provided a useful method and criterion to correct previous measurements as well as to minimize uncertainty of future ones.

High fidelity laminar flame speed data on cyclo-alkanes, butanol isomers, toluene, *o*-xylene and mixtures of H<sub>2</sub> with C<sub>1</sub>-C<sub>4</sub> hydrocarbons have been acquired for a wide range of pressures (1-20 atm). The data at high pressures are particularly valuable for validating and developing chemical kinetic models. These studies also resulted in important insights on the dependence of flame speeds on fuel molecular structure and bond energies.

High pressure up to 40 atm experiments on hydrogen flames have been conducted for studying intrinsic flamefront instabilities. Since the flame thickness decreases with pressure substantially, this is a novel method to study “large-scale” flames in a laboratory-scale apparatus because the Peclet numbers (flame size normalized by flame thickness, which is around 5000 at 40 atm) are in the same range as atmospheric flames of 5 to 10 meters in size. Effects of the flamefront instabilities on burning rate are accurately quantified. A transient period with strong acceleration immediately following the instability onset and subsequent acceleration in a self-similar fashion have been identified.

High pressure and high turbulent Reynolds number (up to 10,000 based cold flow properties and integral length scale) turbulent flames propagating in near isotropic turbulence have been studied. Unique features of expanding turbulent flames have

been determined. First, it is found that all expanding flames in turbulence are subjected to strong acceleration as the flame size increases, which is believed to due to the increase of flame hydrodynamic length scale. Second, for a wide range of conditions in the wrinkled and thickened flamelet regime, the accelerating turbulent flame speeds can be scaled by a Reynolds number defined on the properties of the corresponding laminar flame and the flow, which includes both the effect of hydrodynamic scale, turbulence intensity, pressure and chemistry. At the same time, recent measurements on hydrocarbon flame at lean-burn conditions, which show large area of stretch-induced local extinction, does not follow this Reynolds number scaling.

Based on the consideration of the stretch dynamics of a flame kernel, it has been conjectured and later experimentally verified with extensive evidence that ignition of a combustible mixture by a high-energy kernel can actually be facilitated by turbulence for mixtures whose thermal diffusivity sufficiently exceeds its mass diffusivity. This result is contrary to the general belief that turbulence always renders ignition more difficult. The present results demonstrate the crucial role of molecular differential diffusion in multi-component reacting turbulent flows. Such a new physical understanding is interesting in a broad range of problems, such as engine ignition, mine safety, supernovae and liquid phase material synthesis.

## 10.2 Recommendations

Six years of graduate research is by no means adequate to resolve all the problems in expanding flames. Major challenges in combustion science remain to be solved and the expanding flame as a canonical configuration will continue to play an important

role in solving problems in chemical kinetics and turbulent combustion. Listed in the following are recommendations and new avenues which might be promising to implement and to explore.

### 10.2.1 Combustion Vessel Design

Vessels I and II are originally designed to measure laminar flame speeds. For flame speed measurements, there is no need to increase the vessel size as most flames will exhibit instabilities as they grow to a large radius anyway, particularly for flames at elevated pressures. However, for studying self-accelerating flames due to flamefront instabilities and turbulent flames, since the flame speed continues to increase with the flame size, data on larger flames are needed to investigate whether the self-similar flame acceleration continues at larger size. As the flame speed increases, a relevant question is whether deflagration-to-detonation transition can be triggered. To answer all these questions, the size of the combustion vessel needs to be increased. For studying turbulent combustion, more than four fans are recommended to achieve a turbulent flow that is closer to homogenous isotropic turbulence in a larger volume.

### 10.2.2 Flame Speed Extrapolation

It is shown in Chapter 3 that none of the existing stretch extrapolation models are accurate when the  $Le$  significantly deviate from unity, particularly at  $Le < 1$  conditions. These models are mostly derived from asymptotic theories with various assumptions. The reasons for their inaccuracy and which assumption is to be blamed need to be investigated. These can be identified by conducting numerical simulations in which each assumption made in the theories are turned on or off. For example,

whether one-step chemistry is the cause can be studied by simulating an expanding spherical flame with one-step chemistry but holding other parameters same as those in detailed simulations.

For future laminar flame speed studies, if the goal is only to study chemical kinetics, it is recommended that expanding flame simulations be conducted and the results are directly compared with measured stretched flame speeds, rather than extrapolated ones. This way the uncertainties in stretch extrapolation are avoided. This practice will become more and more feasible as the computation power increases.

If the unstretched flame speed has to be obtained, the ultimate extrapolation should come from both theory and computational results. This is because the governing equations of combustion systems are highly nonlinear, and analytical solution without assumptions that deviate from reality are difficult to obtain. Equation 3.14 is a good starting point since from theory we know  $MaKa$  is the governing parameter for the stretch effects but the specific correction coefficients should come from detailed simulations. More expanding flame simulations are needed to verify Equation 3.14, or to arrive at a better one.

### 10.2.3 Expanding Laminar Flames

In the present work and many previous studies, the laminar expanding flame is only used to measure the laminar flame speed. Although laminar flame speed is one of the most fundamental combustion properties, it only provides constraints to a small set of reactions at most conditions. Therefore, conducting experiments at more conditions for more fuels perhaps cannot help the study of combustion chemistry. One can add kinetically sensitive species into the test mixture to tune

the sensitivity of flame speed to certain reactions that we know less accurately. The additives, for example, can be formaldehyde ( $\text{HCHO}$ ), hydrogen peroxide ( $\text{H}_2\text{O}_2$ ), ozone ( $\text{O}_3$ ), which can all be used to tune the sensitivity. The challenge is how to deliver these additives into the test chamber since they are thermodynamically not quite stable.

Laminar flame speed only gives the global information about the combustion chemistry. With high-speed optical and laser diagnostics, more detailed information can be obtained from expanding laminar flame experiments. One possible diagnostic that can be made is the integrated speciation measurement across the reaction zone and the burned gas of an expanding spherical flame, using the laser absorption technique. The idea is similar to the laser absorption measurements in shock tubes, except that in shock tubes the mixture is approximately homogeneous while there is large species gradient in the reaction and post-flame zone of spherical expanding flame. Although laser absorption measurements will not resolve the spatial distribution of species, it gives the integrated quantity of a particular species across the reaction and the burned gas zone. This integrated quantity can be obtained at different times, which then can be compared with the computed results using 1-D or 2-D spherical expanding flames.

Another possible avenue that can be explored is the quantification of soot formation in the post-flame zone for fuel rich conditions. In the present work, soot formation is observed both by eyes and from the Schlieren images (Figure 10.1) for rich conditions of sooting fuels, such as toluene and acetylene. From Figure 10.1, it is seen that soot formation occurs at a much later time after ignition compared to the flame travel time. This means that soot formation has a long triggering time. First of all, this time can be quantified through experiment. Since the burned gas

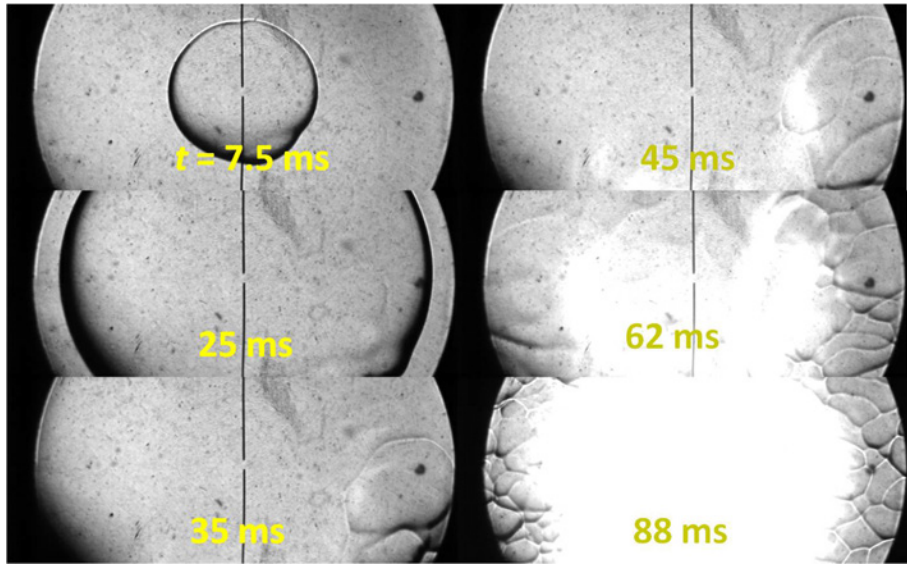


Figure 10.1: Series of Schlieren images showing the soot formation (white color) in the burned gas of a spherical expanding flame. Experimental conditions: toluene/air,  $\phi = 1.6$ ,  $P = 1$  atm. The width of each image is approximately 78 mm.  $t$  in images indicate time after ignition. The color of light radiated by soot is white in the images because the Phantom camera is black-and-white.

conditions of expanding spherical flames can be easily obtained from computation, the data is well defined. Second, quantitative information, such as soot particle size and number density, can also be measured using techniques such as the three-color method and laser induced incandescence.

#### 10.2.4 Flamefront Instabilities

The present work on self-accelerating flames due to flamefront instabilities only covered H<sub>2</sub>/O<sub>2</sub> mixtures. Experiments on other fuels can be conducted to verify whether the self-similar acceleration also applies. However, one problem using fuels other than H<sub>2</sub> is that they have much larger flame thicknesses due to lower reactivity. As a result, the  $Pe$  that can be reached is small. One solution to this is the use mixtures with high concentration of O<sub>2</sub> or use pure O<sub>2</sub> as the oxidizer.

Another investigation that needs to be conducted is to separate the influence of Lewis number and thermal expansion ratio. For the data presented in Chapter 6 on H<sub>2</sub>/air mixtures, both the thermal expansion ratio and Lewis number vary with the equivalence ratio. Future experiments can be conducted with varying Lewis number but fixed thermal expansion ratio, or the other way around to separate the influence of the two. This can be implemented by adjusting the two parameters with inerts, such as He, Ar, N<sub>2</sub> or CO<sub>2</sub>.

The highest  $Pe$  reached in the present work is less than 3,600 and only around 1,000 for stoichiometric mixtures. Future experiments can be conducted to further increase  $Pe$  by increasing the vessel size or pressure. The interest is to explore the possible values for the acceleration exponent  $\alpha$  for high- $Pe$  flames, whether self-turbulization and transition to detonation are indeed possible.

### 10.2.5 Expanding Turbulent Flames

Study on turbulent expanding flames can continue to validate or invalidate the scaling relations demonstrated in Chapter 7 by conducting experiments at higher pressures and for mixtures with very large or small Markstein numbers. The highest pressure in the data of the present work is 10 atm, for the stoichiometric DME/air flames. Vessel II has been tested to hold 30 atm. Therefore, there is room to explore high-pressure conditions. In the present work, it is found that at high-pressure turbulent flame conditions, the mass flow rate passing through the pressure-release holes between inner and outer chambers is so high that the sealing o-rings are often blown off from designed position. This causes inconvenience since each time this occurs many components of the vessel needs to be taken apart to install new o-rings. This problem needs to be solved before high-pressure turbulent conditions can be

effectively explored.

The scaling relation demonstrated in Chapter 7 is only shown to work for conditions with positive Markstein numbers. Work is needed to achieve a reliable scaling for conditions with negative Markstein numbers. In addition to theoretical efforts to resolve the issue, systematic experiments can be conducted to isolate the influence of individual parameters, such as turbulence intensity, laminar flame speeds, flame size, laminar flame thickness and Markstein number. An empirical scaling relation can be first obtained from these experimental data, which can provide insights to finally achieve a scaling relation with a theoretical basis.

One interesting avenue to explore on expanding turbulent flames is the combined effect of the turbulent flow field and flamefront instabilities on the flame speeds. It has been shown that both turbulence and flamefront instabilities accelerate the flame with speed proportional to power laws of flame radius. It is of interest to investigate in the presence of both turbulence and instabilities, whether the effects of the two acceleration mechanisms can be simply additive or there are strong couplings between the two.

### 10.2.6 Flame Ignition Study

The discovery that turbulence can enhance spark ignition for  $Le > 1$  conditions is a good starting point for a series of future studies to extend the findings. In the present work, the ignition energy was controlled by the voltage on the capacitor that provides the electric energy that causes the discharge. However, the exact value of the ignition energy has not been measured. The total electric energy on the capacitor is  $0.5CU_{\text{ign}}^2$ ; however, due to inevitable electric and heat losses, the actual energy that is used to ignite the test mixture is significantly smaller. A better way

to quantify the ignition energy is to measure the voltage and current time history of the spark during discharge. However, the current ignition system has an ignition coil (134:1 turns ratio) between the controlling capacitor and the spark gap. This will cause complexity in how the voltage and current profile is interpreted. Therefore, it is recommended that future quantitative studies on ignition energy should adopt an ignition pulse generator that can better control the spark. Once the ignition energy can be measured, parametric studies can be conducted to quantify the ignition enhancement by turbulence for more conditions. At the same time, theoretical and computational studies can also be conducted to eventually reach a closure of the problem.

# Bibliography

- ABDEL-GAYED, R. G. & BRADLEY, D. 1977 Dependence of turbulent burning velocity on turbulent Reynolds number and ratio of laminar burning velocity to r.m.s turbulent velocity. *Proceedings of the Combustion Institute* **16**, 1725–1735.
- ABDEL-GAYED, R. G., BRADLEY, D., HAMID, M. N. & LAWES, M. 1984 Lewis number effects on turbulent burning velocity. *Proceedings of the Combustion Institute* **20**, 505–512.
- ABDEL-GAYED, R. G., BRADLEY, D. & LAWES, M. 1987 Turbulent burning velocities: a general correlation in terms of straining rates. *Proceedings of the Royal Society A* **414**, 389–413.
- ADDABBO, R., BECHTOLD, J. K. & MATALON, M. 2002 Wrinkling of spherically expanding flames. *Proceedings of the Combustion Institute* **29**, 1527–1535.
- AHMED, S.F., BALACHANDRAN, R. & MASTORAKOS, E. 2007 Measurements of ignition probability in turbulent non-premixed counterflow flames. *Proceedings of the Combustion Institute* **31**, 1507–1513.
- AHMED, S. & MASTORAKOS, E. 2006 Spark ignition of lifted turbulent jet flames. *Combustion and Flame* **146**, 215–231.

- AKINDELE, O. O., BRADLEY, D. & MAK, P. W. 1982 Spark ignition of turbulent gases. *Combustion and Flame* **47**, 129–155.
- ALDREDGE, R. & ZUO, B. 2001 Flame acceleration associated with the Darrieus-Landau instability. *Combustion and Flame* **127**, 2091–2101.
- ALLEN, J. W., GOLDSMITH, C. F. & GREEN, W. H. 2012 Automatic estimation of pressure-dependent rate coefficients. *Physical chemistry chemical physics : PCCP* **14**, 1131–55.
- ASHURST, W. T. 1997 Darrieus-Landau instability, growing cycloids and expanding flame acceleration. *Combustion Theory and Modelling* **1**, 405–428.
- ASPDEN, A. J., DAY, M. S. & BELL, J. B. 2011 Turbulence-flame interactions in lean premixed hydrogen: transition to the distributed burning regime. *Journal of Fluid Mechanics* **680**, 287–320.
- ATTILI, A., BISSETTI, F., MUELLER, M. E. & PITTSCH, H. 2014 Formation, growth, and transport of soot in a three-dimensional turbulent non-premixed jet flame. *Combustion and Flame* **161**, 1849–1865.
- BALLAL, D. R. & LEFEBVRE, A. H. 1975 The influence of flow parameters on minimum ignition energy and quenching distance. *Proceedings of the Combustion Institute* **15**, 1473–1481.
- BALLAL, D. R. & LEFEBVRE, A. H. 1977 Ignition and flame quenching in flowing gaseous mixtures. *Proceedings of the Royal Society A* **357**, 163–181.
- BECHTOLD, J. K. & MATALON, M. 1987 Hydrodynamic and diffusion effects on the stability of spherically expanding flames. *Combustion and Flame* **67**, 77–90.

- BECHTOLD, J. K. & MATALON, M. 1999 Effects of stoichiometry on stretched premixed flames. *Combustion and Flame* **119**, 217–232.
- BECHTOLD, J. K. & MATALON, M. 2001 The dependence of the Markstein length on stoichiometry. *Combustion and Flame* **127**, 1906 –1913.
- BELL, J. B., DAY, M. S., SHEPHERD, I. G., JOHNSON, M. R., CHENG, R. K., GRCAR, J. F., BECKNER, V. E. & LIJEWSKI, M. J. 2005 Numerical simulation of a laboratory-scale turbulent V-flame. *Proceedings of the National Academy of Sciences of the United States of America* **102** (29), 10006–10011.
- BILGER, R. W. 2000 Future progress in turbulent combustion research. *Progress in Energy and Combustion Science* **26**, 367–380.
- BILGER, R. W., POPE, S. B., BRAY, K. N. C. & DRISCOLL, J. F. 2005 Paradigms in turbulent combustion research. *Proceedings of the Combustion Institute* **30**, 21–42.
- BLACK, G., CURRAN, H. J., PICHON, S., SIMMIE, J. M. & ZHUKOV, V. 2010 Bio-butanol: Combustion properties and detailed chemical kinetic model. *Combustion and Flame* **157**, 363–373.
- BLINNIKOV, S. I. & SASOROV, P. V. 1996 Landau-Darrieus instability and the fractal dimension of flame fronts. *Physical Review E* **53** (5), 4827–4841.
- BONHOMME, A., SELLE, L. & POINSOT, T. J. 2013 Curvature and confinement effects for flame speed measurements in laminar spherical and cylindrical flames. *Combustion and Flame* **160**, 1208–1214.

- BORGHI, R. 1988 Turbulent combustion modelling. *Progress in Energy and Combustion Science* **14**, 245–292.
- BOSSCHAART, K. J. & DE GOEY, L. P. H. 2003 Detailed analysis of the heat flux method for measuring burning velocities. *Combustion and Flame* **132**, 170–180.
- BRADLEY, D. 1992 How fast can we burn? *Proceedings of the Combustion Institute* **24**, 247–262.
- BRADLEY, D. 1999 Instabilities and flame speeds in large-scale premixed gaseous explosions. *Philosophical Transactions of the Royal Society of London* **357**, 3567–3581.
- BRADLEY, D., CRESSWELL, T. M. & PUTTOCK, J. S. 2001 Flame acceleration due to flame-induced instabilities in large-scale explosions. *Combustion and Flame* **124**, 551–559.
- BRADLEY, D., HAQ, M. Z., HICKS, R. A., KITAGAWA, T., LAWES, M., SHEPPARD, C. G. W. & WOOLLEY, R. 2003 Turbulent burning velocity, burned gas distribution, and associated flame surface definition. *Combustion and Flame* **133**, 415–430.
- BRADLEY, D. & HARPER, C. M. 1994 The development of instabilities in laminar explosion flames. *Combustion and Flame* **99**, 562–572.
- BRADLEY, D., LAWES, M., LIU, K. & MANSOUR, M. S. 2013 Measurements and correlations of turbulent burning velocities over wide ranges of fuels and elevated pressures. *Proceedings of the Combustion Institute* **34**, 1519–1526.

- BRADLEY, D., LAWES, M. & MANSOUR, M. S. 2009 Explosion bomb measurements of ethanol-air laminar gaseous flame characteristics at pressures up to 1.4 MPa. *Combustion and Flame* **156**, 1462–1470.
- BRADLEY, D., LAWES, M. & MANSOUR, M. S. 2011 Correlation of turbulent burning velocities of ethanol-air, measured in a fan-stirred bomb up to 1.2 MPa. *Combustion and Flame* **158**, 123–138.
- BRADLEY, D., SHEPPARD, C. G. W., SUARDJAJA, I. M. & WOOLLEY, R. 2004 Fundamentals of high-energy spark ignition with lasers. *Combustion and Flame* **138**, 55–77.
- BRADLEY, D., SHEPPARD, C. G. W., WOOLLEY, R., GREENHALGH, D. A. & LOCKETT, R. D. 2000 The development and structure of flame instabilities and cellularity at low Markstein numbers in explosions. *Combustion and Flame* **122**, 195–209.
- BUCKMASTER, J., CLAVIN, P., LIÑÁN, A., MATALON, M., PETERS, N., SIVASHINSKY, G. I. & WILLIAMS, F. A. 2005 Combustion theory and modeling. *Proceedings of the Combustion Institute* **30**, 1–19.
- BURKE, M. P., CHAOS, M., DRYER, F. L. & JU, Y. 2010 Negative pressure dependence of mass burning rates of H<sub>2</sub>/CO/O<sub>2</sub>/diluent flames at low flame temperatures. *Combustion and Flame* **157**, 618–631.
- BURKE, M. P., CHAOS, M., JU, Y., DRYER, F. L. & KLIPPENSTEIN, S. J. 2012 Comprehensive H<sub>2</sub>/O<sub>2</sub> kinetic model for high-pressure combustion. *International Journal of Chemical Kinetics* **44** (7), 444–474.

- BURKE, M. P., CHEN, Z., JU, Y. & DRYER, F. L. 2009 Effect of cylindrical confinement on the determination of laminar flame speeds using outwardly propagating flames. *Combustion and Flame* **156**, 771–779.
- BYCHKOV, V. V. & LIBERMAN, M. A. 1996 Stability and the fractal structure of a spherical flame in a self-similar regime. *Physical Review Letters* **76** (15), 2814–2817.
- CARDIN, C., RENOU, B., CABOT, G. & BOUKHALFA, A. M. 2013 Experimental analysis of laser-induced spark ignition of lean turbulent premixed flames: New insight into ignition transition. *Combustion and Flame* **160**, 1414–1427.
- CAVALLOTTI, C., ROTA, R., FARAVELLI, T. & RANZI, E. 2007 Ab initio evaluation of primary cyclo-hexane oxidation reaction rates. *Proceedings of the Combustion Institute* **31**, 201–209.
- CHAOS, MARCOS, KAZAKOV, ANDREI, ZHAO, ZHENWEI & DRYER, FREDERICK L. 2007 A high-temperature chemical kinetic model for primary reference fuels. *International Journal of Chemical Kinetics* **39**, 399–414.
- CHAUDHURI, S., AKKERMANN, V. & LAW, C. K. 2011 Spectral formulation of turbulent flame speed with consideration of hydrodynamic instability. *Physical Review E* **84**, 026322.
- CHAUDHURI, S., SAHA, A. & LAW, C. K. 2014 On flame-turbulence interaction in constant-pressure expanding flames. *Proceedings of the Combustion Institute* **35**, in press.

- CHAUDHURI, S., WU, F. & LAW, C. K. 2013 Scaling of turbulent flame speed for expanding flames with Markstein diffusion considerations. *Physical Review E* **88**, 033005.
- CHAUDHURI, S., WU, F., ZHU, D. & LAW, C. K. 2012 Flame speed and self-similar propagation of expanding turbulent premixed flames. *Physical review letters* **108**, 044503.
- CHEN, J. H. 2011a Petascale direct numerical simulation of turbulent combustion - fundamental insights towards predictive models. *Proceedings of the Combustion Institute* **33**, 99–123.
- CHEN, Z. 2010 Effects of radiation and compression on propagating spherical flames of methane/air mixtures near the lean flammability limit. *Combustion and Flame* **157**, 2267–2276.
- CHEN, Z. 2011b On the extraction of laminar flame speed and Markstein length from outwardly propagating spherical flames. *Combustion and Flame* **158**, 291–300.
- CHEN, Z., BURKE, M. P. & JU, Y. 2009a Effects of compression and stretch on the determination of laminar flame speeds using propagating spherical flames. *Combustion Theory and Modelling* **13**, 343–364.
- CHEN, Z., BURKE, M. P. & JU, Y. 2009b Effects of Lewis number and ignition energy on the determination of laminar flame speed using propagating spherical flames. *Proceedings of the Combustion Institute* **32**, 1253–1260.

- CHEN, Z., BURKE, M. P. & JU, Y. 2011 On the critical flame radius and minimum ignition energy for spherical flame initiation. *Proceedings of the Combustion Institute* **33**, 1219–1226.
- CHEN, Z. & JU, Y. 2007 Theoretical analysis of the evolution from ignition kernel to flame ball and planar flame. *Combustion Theory and Modelling* **11**, 427–453.
- CHEN, Z., QIN, X., XU, B., JU, Y. & LIU, F. 2007 Studies of radiation absorption on flame speed and flammability limit of CO<sub>2</sub> diluted methane flames at elevated pressures. *Proceedings of the Combustion Institute* **31**, 2693–2700.
- CHU, S. & MAJUMDAR, A. 2012 Opportunities and challenges for a sustainable energy future. *Nature* **488**, 294–303.
- CIA 2014 CIA World Fact Page, <https://www.cia.gov/library/publications/the-world-factbook/geos/xx.html>.
- CLAVIN, P. 1985 Dynamic behavior of premixed flame fronts in laminar and turbulent flows. *Progress in Energy and Combustion Science* **11**, 1–59.
- CLAVIN, P. & NICOLI, C. 1985 Effect of heat losses on the limits of stability of premixed flames propagating downwards. *Combustion and Flame* **60**, 1–14.
- CLAVIN, P. & GRAÑA OTERO, J. C. 2011 Curved and stretched flames: the two Markstein numbers. *Journal of Fluid Mechanics* **686**, 187–217.
- CLAVIN, P., PELCE, P. & GARCIA, P. 1983 Stability limits of planar premixed flames. *Annals of New York Academy of Sciences* **404**, 221–223.
- CLAVIN, P. & WILLIAMS, F. A. 1979 Theory of premixed-flame propagation in large-scale turbulence. *Journal of Fluid Mechanics* **90**, 589–604.

- CLAVIN, P. & WILLIAMS, F. A. 1982 Effects of molecular diffusion and of thermal expansion on the structure and dynamics of premixed flames in turbulent flows of large scale and low intensity. *Journal of Fluid Mechanics* **116**, 251.
- COLKET, M., EDWARDS, T., WILLIAMS, S., CERNANSKY, N. P., MILLER, D. L., EGOLFOPOULOS, F. N., LINDSTEDT, P., SESHADRI, K., DRYER, F. L., LAW, C. K., FRIEND, D., LENHERT, D. B., PITSCH, H., SAROFIM, A., SMOOKE, M. & TSANG, W. 2007 Development of an experimental database and kinetic models for surrogate jet fuels. In *American Institute of Aeronautics and Astronautics*, pp. Paper 2007–770.
- Cox, D.R. & HINKLEY, D.V. 1974 *Theoretical Statistics*. Chapman and Hall.
- CUOCI, A., FRASSOLDATI, A., FARAVELLI, T. & RANZI, E. 2011 Open SMOKE: numerical modeling of reacting systems with detailed kinetic mechanisms. In *XXXIV meeting of the Italian Section of the Combustion Institute, Rome (Italy)*.
- DAGAUT, P. & CATHONNET, M. 2006 The ignition, oxidation, and combustion of kerosene: A review of experimental and kinetic modeling. *Progress in Energy and Combustion Science* **32**, 48–92.
- DAMKÖHLER, G. 1940 Der Einfluss der Turbulenz auf die Flammengeschwindigkeit in Gasgemischen. *Z. Elektrochem* **46**, 601–652.
- DARRIEUS, G. 1938 Propagation dun front de flame. *La Technique Moderne* **30**, No. 18.
- DAVIDSON, D. F., RANGANATH, S. C., LAM, K. Y., LIAW, M., HONG, Z. & HANSON, R. K. 2010 Ignition delay time measurements of normal alkanes and simple oxygenates. *Journal of Propulsion and Power* **26** (2), 280–287.

- DAVIS, S. G. & LAW, C. K. 1998 Determination of and fuel structure effects on laminar flame speeds of C<sub>1</sub> to C<sub>8</sub> Hydrocarbons. *Combustion Science and Technology* **140**, 427–449.
- DESHMUKH, K. V., MODEST, M. F. & HAWORTH, D. C. 2008 Direct numerical simulation of turbulence-radiation interactions in a statistically one-dimensional nonpremixed system. *Journal of Quantitative Spectroscopy and Radiative Transfer* **109**, 2391–2400.
- DOWDY, D. R., SMITH, D. B. & WILLIAMS, A. 1990 The use of expanding spherical flames to determine burning velocities and stretch effects in hydrogen/air mixtures. *Combustion and Flame* **23**, 325–332.
- DRISCOLL, J. 2008 Turbulent premixed combustion: Flamelet structure and its effect on turbulent burning velocities. *Progress in Energy and Combustion Science* **34**, 91–134.
- DUBOIS, T., CHAUMEIX, N. & PAILLARD, C. E. 2009 Experimental and modeling study of *n*-propylcyclohexane oxidation under engine-relevant conditions. *Energy & Fuels* **23**, 2453–2466.
- EGOLFOPOULOS, F. N., HANSEN, N., JU, Y., KOHSE-HÖINGHAUS, K., LAW, C. K. & QI, F. 2014 Advances and challenges in laminar flame experiments and implications for combustion chemistry. *Progress in Energy and Combustion Science* **43**, 36–67.
- EHRLICH, P. R., KAREIVA, P. M. & DAILY, G. C. 2012 Securing natural capital and expanding equity to rescale civilization. *Nature* **486**, 68–73.

- FARRELL, J. T., CERNANSKY, N. P., DRYER, F. L., FRIEND, D. G., HERGART, C. A., LAW, C. K., MCDAVID, R. M., MUELLER, C. J., PATEL, A. K. & PITSCHE, H. 2007 Development of an experimental database and kinetic models for surrogate diesel fuels. In *SAE Paper*, pp. Paper 2007-01-0201.
- FARRELL, J. T., JOHNSTON, R. J. & ANDROULAKIS, I. P. 2004 Molecular structure effects on laminar burning velocities at elevated temperature and pressure. In *SAE Paper*, pp. 2004-01-2936.
- FILATYEV, S. A., DRISCOLL, J. F., CARTER, C. D. & DONBAR, J. M. 2005 Measured properties of turbulent premixed flames for model assessment, including burning velocities, stretch rates, and surface densities. *Combustion and Flame* **141**, 1–21.
- FILYAND, L., SIVASHINSKY, G. I. & FRANKEL, M. L. 1994 On self-acceleration of outward propagating wrinkled flames. *Physica D* **72**, 110–118.
- FRANKEL, M. L. & SIVASHINSKY, G. I. 1983 On effects due to thermal expansion and Lewis number in spherical flame propagation. *Combustion Science and Technology* **31**, 131–138.
- FURSENKO, R., PAN, K. & MINAEV, S. 2008 Noise influence on pole solutions of the Sivashinsky equation for planar and outward propagating flames. *Physical Review E* **78**, 056301.
- GALANTI, B., KUPERVASSER, O., OLAMI, Z. & PROCACCIA, I. 1998 Dynamics and wrinkling of radially propagating fronts inferred from scaling laws in channel geometries. *Physical Review Letters* **80** (11), 2477–2480.

- GICQUEL, L.Y. M., STAFFELBACH, G. & POINSOT, T. J. 2012 Large eddy simulations of gaseous flames in gas turbine combustion chambers. *Progress in Energy and Combustion Science* **38**, 782–817.
- GOSTINTSEV, Y. A., FORTOV, V. E. & SHATSKIKH, Y. V. 2004 Self-similar propagation law and fractal structure of the surface of a free expanding turbulent spherical flame. *Physical Chemistry* **397** (1), 141–144.
- GOSTINTSEV, Y. A., ISTRATOV, A. G. & FORTOV, V. E. 1997 On fractal structure of turbulent spherical flame. *Doklady Akademii Nauk* **353** (1), 55–56.
- GOSTINTSEV, Y. A., ISTRATOV, A. G., KIDIN, N. I. & FORTOV, V. E. 1999 Autoturbulization of gas flames: analysis of experimental results. *High Temperature* **37** (2), 306–312.
- GOSTINTSEV, Y. A., ISTRATOV, A. G. & SHULENIN, Y. V. 1988 Self-similar propagation of a free turbulent flame in mixed gas. *Combustion Explosion and Shock Waves* **24** (5), 63–70.
- GRANATA, S., FARAVELLI, T. & RANZI, E. 2003 A wide range kinetic modeling study of the pyrolysis and combustion of naphthenes. *Combustion and Flame* **132**, 533–544.
- GROFF, E. G. 1982 The cellular nature of confined spherical propane-air flames. *Combustion and Flame* **48**, 51–62.
- GU, X., HUANG, Z., LI, Q. & TANG, C. 2009 Measurements of laminar burning velocities and Markstein lengths of *n*-butanolair premixed mixtures at elevated temperatures and pressures. *Energy & Fuels* **23**, 4900–4907.

- GU, X., HUANG, Z., WU, S. & LI, Q. 2010 Laminar burning velocities and flame instabilities of butanol isomers-air mixtures. *Combustion and Flame* **157**, 2318–2325.
- GU, X., LI, Q. & HUANG, Z. 2011a Laminar burning characteristics of diluted *n*-butanol/air mixtures. *Combustion Science and Technology* **183**, 1360–1375.
- GU, X., LI, Q., HUANG, Z. & ZHANG, N. 2011b Measurement of laminar flame speeds and flame stability analysis of *tert*-butanol/air mixtures at elevated pressures. *Energy Conversion and Management* **52**, 3137–3146.
- GUPTA, A., HAWORTH, D. C. & MODEST, M. F. 2013 Turbulence-radiation interactions in large-eddy simulations of luminous and nonluminous nonpremixed flames. *Proceedings of the Combustion Institute* **34**, 1281–1288.
- HALTER, F., TAHTOUH, T. & MOUNAÏM-ROUSSELLE, C. 2010 Nonlinear effects of stretch on the flame front propagation. *Combustion and Flame* **157**, 1825–1832.
- HAMLINGTON, P. E., POLUDNENKO, A. Y. & ORAN, E. S. 2011 Interactions between turbulence and flames in premixed reacting flows. *Physics of Fluids* **23**, 125111.
- HANSEN, N., HARPER, M. R. & GREEN, W. H. 2011 High-temperature oxidation chemistry of *n*-butanol -experiments in low-pressure premixed flames and detailed kinetic modeling. *Physical Chemistry Chemical Physics* **13**, 20262–74.
- HANSON, R. K. 2011 Applications of quantitative laser sensors to kinetics, propulsion and practical energy systems. *Proceedings of the Combustion Institute* **33**, 1–40.

- HAQ, M. Z. 2005 Correlations for the onset of instabilities of spherical laminar premixed flames. *Transactions of the ASME* **127**, 1410–1415.
- HARPER, M. R., VAN GEEM, K. M., PYL, S. P., MARIN, G. B. & GREEN, W. H. 2011 Comprehensive reaction mechanism for *n*-butanol pyrolysis and combustion. *Combustion and Flame* **158**, 16–41.
- HEYWOOD, J. B. 1988 *Internal Combustion Engine Fundamentals*. McGraw-Hill Science/Engineering/Math.
- IPCC 2007 Fourth assessment report of the intergovernmental panel on climate change. *Tech. Rep.*. Intergovernmental Panel on Climate Change.
- IPCC 2011 IPCC special report on carbon dioxide capture and storage summary for policymakers. *Tech. Rep.*. Intergovernmental Panel on Climate Change.
- JAYACHANDRAN, J., ZHAO, R. & EGOLFOPOULOS, F. N. 2014 Determination of laminar flame speeds using stagnation and spherically expanding flames: Molecular transport and radiation effects. *Combustion and Flame* .
- JI, C., DAMES, E., SIRJEAN, B., WANG, H. & EGOLFOPOULOS, F. N. 2011 An experimental and modeling study of the propagation of cyclohexane and mono-alkylated cyclohexane flames. *Proceedings of the Combustion Institute* **33**, 971–978.
- JI, C., DAMES, E., WANG, H. & EGOLFOPOULOS, F. N. 2012a Propagation and extinction of benzene and alkylated benzene flames. *Combustion and Flame* **159**, 1070–1081.

- JI, C., DAMES, E., WANG, Y. L., WANG, H. & EGOLFOPOULOS, F. N. 2010 Propagation and extinction of premixed  $C_5$ - $C_{12}$  *n*-alkane flames. *Combustion and Flame* **157**, 277–287.
- JI, C., SARATHY, S. M., VELOO, P. S., WESTBROOK, C. K. & EGOLFOPOULOS, F. N. 2012b Effects of fuel branching on the propagation of octane isomers flames. *Combustion and Flame* **159**, 1426–1436.
- JOMAAS, GRUNDE 2008 Propagation and stability of expanding spherical flames. Phd, Princeton University.
- JOMAAS, G., BECHTOLD, J. K. & LAW, C. K. 2007a Spiral waves in expanding hydrogen-air flames: experiment and theory. *Proceedings of the Combustion Institute* **31**, 1039–1046.
- JOMAAS, G. & LAW, C. K. 2010 Observation and regime classification of pulsation patterns in expanding spherical flames. *Physics of Fluids* **22**, 124102.
- JOMAAS, G., LAW, C. K. & BECHTOLD, J. K. 2007b On transition to cellularity in expanding spherical flames. *Journal of Fluid Mechanics* **583**, 1–26.
- JOMAAS, G., ZHENG, X. L., ZHU, D. L. & LAW, C. K. 2005 Experimental determination of counterflow ignition temperatures and laminar flame speeds of  $C_2$ - $C_3$  hydrocarbons at atmospheric and elevated pressures. *Proceedings of the Combustion Institute* **30**, 193–200.
- JOULIN, G. & CLAVIN, P. 1979 Linear stability analysis of nonadiabatic flames: diffusional-thermal model. *Combustion and Flame* **35**, 139–153.

- KAMINSKI, C. F., HULT, J., ALDÉN, M., LINDENMAIER, S., DREIZLER, A., MAAS, U. & BAUM, M. 2000 Spark ignition of turbulent methane/air mixtures revealed by time-resolved planar laser-induced fluorescence and direct numerical simulations. *Proceedings of the Combustion Institute* **28**, 399–405.
- KARLIN, V. & SIVASHINSKY, G. I. 2006 The rate of expansion of spherical flames. *Combustion Theory and Modelling* **10** (4), 625–637.
- KARLIN, V. & SIVASHINSKY, G. I. 2007 Asymptotic modelling of self-acceleration of spherical flames. *Proceedings of the Combustion Institute* **31**, 1023–1030.
- KARLOVITZ, B., DENNISTON, D. W., KNAPSCHAEFER, D. H. & WELLS, F. E. 1953 Studies on Turbulent flames. *Proceedings of the Combustion Institute* **4**, 613–620.
- KARPOV, V.P., SEMENOV, E. S. & SOKOLIK, A. S. 1959 Turbulent burning in closed volume. *Doklady Akademii nauk SSSR* **128**, 1220–1223.
- KEE, R. J., GRCAR, J. F., MILLER, J. A., MEEKS, E. & SMOKE, M. D. 1985 Premix: A Fortran program for modeling steady laminar one-dimensional premixed flames. Sandia report 85-8240. *Tech. Rep.* Sandia National Laboratories.
- KELLEY, A. P. 2011 Dynamics of expanding flames. PhD thesis, Princeton University.
- KELLEY, A. P., BECHTOLD, J. K. & LAW, C. K. 2011a Premixed flame propagation in a confining vessel with weak pressure rise. *Journal of Fluid Mechanics* **691**, 26–51.

- KELLEY, A. P., JOMAAS, G. & LAW, C. K. 2009 Critical radius for sustained propagation of spark-ignited spherical flames. *Combustion and Flame* **156**, 1006–1013.
- KELLEY, A. P. & LAW, C. K. 2009 Nonlinear effects in the extraction of laminar flame speeds from expanding spherical flames. *Combustion and Flame* **156**, 1844–1851.
- KELLEY, A. P., LIU, W., XIN, Y. X., SMALLBONE, A. J. & LAW, C. K. 2011b Laminar flame speeds, nonpremixed stagnation ignition, and reduced mechanisms in the oxidation of *iso*-octane. *Proceedings of the Combustion Institute* **33**, 501–508.
- KELLEY, A. P., SMALLBONE, A. J., ZHU, D. L. & LAW, C. K. 2011c Laminar flame speeds of C<sub>5</sub>–C<sub>8</sub> *n*-alkane at elevated pressures: Experimental determination, fuel similarity, and stretch sensitivity. *Proceedings of the Combustion Institute* **33**, 963–970.
- KERSTEIN, A. R. & ASHURST, W. T. 1992 Propagation rate of growing interfaces in stirred fluids. *Physical Review Letters* **68** (7), 934–937.
- KERSTEIN, A. R., ASHURST, W. T. & WILLIAMS, F. A. 1988 Field equation for interface propagation in an unsteady homogeneous flow field. *Physical Review A* **37** (7), 2728–2731.
- KIDO, H., NAKAHARA, M., NAKASHIMA, K. & HASHIMOTO, J. 2002 Influence of local flame displacement velocity on turbulent burning velocity. *Proceedings of the Combustion Institute* **29**, 1855–1861.

- KIM, H. H., WON, S. H., SANTNER, J., CHEN, Z. & JU, Y. 2013 Measurements of the critical initiation radius and unsteady propagation of *n*-decane/air premixed flames. *Proceedings of the Combustion Institute* **34**, 929–936.
- KLIPPENSTEIN, S. J., PANDE, V. S. & TRUHLAR, D. G. 2014 Chemical kinetics and mechanisms of complex systems: a perspective on recent theoretical advances. *Journal of the American Chemical Society* **136**, 528–546.
- KNUDSEN, E., KOLLA, H., HAWKES, E. R. & PITSCHE, H. 2013 LES of a premixed jet flame DNS using a strained flamelet model. *Combustion and Flame* **160**, 2911–2927.
- KOBAYASHI, H., SEYAMA, K., HAGIWARA, H. & OGAMI, Y. 2005 Burning velocity correlation of methane/air turbulent premixed flames at high pressure and high temperature. *Proceedings of the Combustion Institute* **30**, 827–834.
- KOBAYASHI, H., TAMURA, T., MARUTA, K., NIIOKA, T. & WILLIAMS, F. A. 1996 Burning velocity of turbulent premixed flames in a high-pressure environment. *Proceedings of the Combustion Institute* **26**, 389–396.
- KOLLA, H., ROGERSON, J. W. & SWAMINATHAN, N. 2010 Validation of a turbulent flame speed model across combustion regimes. *Combustion Science and Technology* **182**, 284–308.
- KWON, O. C., ROZENCHAN, G. & LAW, C. K. 2002 Cellular instabilities and self-acceleration of outwardly propagating spherical flames. *Proceedings of the Combustion Institute* **29**, 1775–1783.

- KWON, S., TSENG, L. & FAETH, G. M. 1992 Laminar burning velocities and transition unstable flames in H<sub>2</sub>/O<sub>2</sub>/N<sub>2</sub> and C<sub>3</sub>H<sub>8</sub>/O<sub>2</sub>/N<sub>2</sub>. *Combustion and Flame* **90**, 230–246.
- LANDAU, L. D. 1944 On the theory of slow combustion. *Acta Physiocochemical URSS* **19**, 77–85.
- LAW, C. K. 2006 *Combustion Physics*. New York: Cambridge University Press.
- LAW, C. K. 2007 Combustion at a crossroads: status and prospects. *Proceedings of the Combustion Institute* **31**, 1–29.
- LAW, C. K., JOMAAS, G. & BECHTOLD, J. K. 2005 Cellular instabilities of expanding hydrogen/propane spherical flames at elevated pressures: theory and experiment. *Proceedings of the Combustion Institute* **30**, 159–167.
- LAW, C. K. & KWON, O. C. 2004 Effects of hydrocarbon substitution on atmospheric hydrogen-air flame propagation. *International Journal of Hydrogen Energy* **29**, 867–879.
- LAW, C. K. & SUNG, C. J. 2000 Structure, aerodynamics, and geometry of premixed flamelets. *Progress in Energy and Combustion Science* **26**, 459–505.
- LAWES, M., ORMSBY, M. P., SHEPPARD, C. G. W. & WOOLLEY, R. 2012 The turbulent burning velocity of iso-octane/air mixtures. *Combustion and Flame* **159**, 1949–1959.
- LAWN, C. J. & SCHEFER, R. W. 2006 Scaling of premixed turbulent flames in the corrugated regime. *Combustion and Flame* **146**, 180–199.

- LEFKOWITZ, J. K., HEYNE, J. S., WON, S. H., DOOLEY, S., KIM, H. H., HAAS, F. M., JAHANGIRIAN, S., DRYER, F. L. & JU, Y. 2012 A chemical kinetic study of tertiary-butanol in a flow reactor and a counterflow diffusion flame. *Combustion and Flame* **159**, 968–978.
- LEFKOWITZ, J. K., WON, S.H., FENARD, Y. & JU, Y. 2013 Uncertainty assessment of species measurements in acetone counterflow diffusion flames. *Proceedings of the Combustion Institute* **34**, 813–820.
- LEWIS, B. & VON ELBE, G. 1934 Determination of the speed of flames and the temperature distribution in a spherical bomb from time-pressure explosion records. *Journal of Chemical Physics* **2**, 283–290.
- LIBBY, P. A. & WILLIAMS, F. A. 1994 *Turbulent Reacting Flows*. Academic Press.
- LIBERMAN, M. A., IVANOV, M. F., PEIL, O. E., VALIEV, D. M.. & ERIKSSON, L. E. 2004 Self-acceleration and fractal structure of outward freely propagating flames. *Physics of Fluids* **16** (7), 2476–2482.
- LIEUWEN, T. C. 2012 *Unsteady Combustor Physics*. Cambridge University Press.
- LIND, C. D. & WHITSON, J. C. 1977 Explosion hazards associated with spills of large quantities of hazardous materials, phase II. *Tech. Rep.*. Naval Weapons Center.
- LIPATNIKOV, A. N. & CHOMIAK, J. 2002 Turbulent flame speed and thickness: phenomenology, evaluation, and application in multi-dimensional simulations. *Progress in Energy and Combustion Science* **28**, 1–74.

- LIPATNIKOV, A. N. & CHOMIAK, J. 2005 Molecular transport effects on turbulent flame propagation and structure. *Progress in Energy and Combustion Science* **31**, 1–73.
- LIPATNIKOV, A. N. & CHOMIAK, J. 2007 Global stretch effects in premixed turbulent combustion. *Proceedings of the Combustion Institute* **31**, 1361–1368.
- LIU, W., KELLEY, A. P. & LAW, C. K. 2011a Non-premixed ignition, laminar flame propagation, and mechanism reduction of *n*-butanol, *iso*-butanol, and methyl butanoate. *Proceedings of the Combustion Institute* **33**, 995–1002.
- LIU, W., KOCH, J. A. & LAW, C. K. 2011b Nonpremixed ignition of C<sub>7</sub>–C<sub>16</sub> normal alkanes in stagnating liquid pool. *Combustion and Flame* **158**, 2145–2148.
- LU, T. & LAW, C. K. 2009 Toward accommodating realistic fuel chemistry in large-scale computations. *Progress in Energy and Combustion Science* **35**, 192–215.
- MANDELBROT, B. B. 1974 Intermittent turbulence in self-similar cascades: divergence of high moments and dimension of the carrier. *Journal of Fluid Mechanics* **62**, 331–358.
- MANDELBROT, B. B. 1975 On the geometry of homogeneous turbulence, with stress on the fractal dimension of the iso-surfaces of scalars. *Journal of Fluid Mechanics* **72**, 401–416.
- MANTON, J., VON ELBE, G. & LEWIS, B. 1952 Nonisotropic Propagation of Combustion Waves in Explosive Gas Mixtures and the Development of Cellular Flames. *The Journal of Chemical Physics* **20**, 153–157.

- MARKSTEIN, G. H. 1951 Experimental and theoretical studies of flame-front stability. *Journal of the Aeronautical Sciences* **18**, 199–209.
- MARKSTEIN, G. H. 1964 *Nonsteady Flame Propagation*. New York: Pergamon Press.
- MATALON, M., CUI, C. & BECHTOLD, J. K. 2003 Hydrodynamic theory of premixed flames: effects of stoichiometry, variable transport coefficients and arbitrary reaction orders. *Journal of Fluid Mechanics* **487**, 179–210.
- MATALON, M. & MATKOWSKY, B. J. 1982 Flames as gasdynamic discontinuities. *Journal of Fluid Mechanics* **124**, 239–259.
- MATKOWSKY, B. J., PUTNICK, L. J. & SIVASHINSKY, G. I. 1980 A nonlinear theory of cellular flames. *SIAM Journal on Applied Mathematics* **38** (3), 489–504.
- METCALFE, W. K., DOOLEY, S. & DRYER, F. L. 2011 Comprehensive detailed chemical kinetic modeling study of toluene oxidation. *Energy* **25**, 4915–4936.
- METGHALCHI, M. & KECK, J. C. 1980 Laminar burning velocity of propane-air mixtures at high temperature and pressure. *Combustion and Flame* **38**, 143–154.
- MILLER, J. A., PILLING, M. J. & TROE, J. 2005 Unravelling combustion mechanisms through a quantitative understanding of elementary reactions. *Proceedings of the Combustion Institute* **30**, 43–88.
- MITSOS, A., OXBERRY, G. M., BARTON, P. I. & GREEN, W. H. 2008 Optimal automatic reaction and species elimination in kinetic mechanisms. *Combustion and Flame* **155**, 118–132.

- MITTAL, V., COOK, D. J. & PITSCHE, H. 2012a An extended multi-regime flamelet model for IC engines. *Combustion and Flame* **159**, 2767–2776.
- MITTAL, VARUN, PITSCHE, HEINZ & EGOLFOPOULOS, FOKION 2012b Assessment of counterflow to measure laminar burning velocities using direct numerical simulations. *Combustion Theory and Modelling* **16**, 419–433.
- MOSS, J. T., BERKOWITZ, A. M., OEHLSCHLAEGER, M. A., BIET, J., WARTH, V., GLAUDE, P. A. & BATTIN-LECLERC, F. 2008 An experimental and kinetic modeling study of the oxidation of the four isomers of butanol. *Journal of Physical Chemistry A* **112**, 10843–10855.
- MUKAIYAMA, KENJI, SHIBAYAMA, SHIMON & KUWANA, KAZUNORI 2013 Fractal structures of hydrodynamically unstable and diffusive-thermally unstable flames. *Combustion and Flame* **160**, 2471–2475.
- NIGAM, P. S. & SINGH, A. 2011 Production of liquid biofuels from renewable resources. *Progress in Energy and Combustion Science* **37**, 52–68.
- OLAMI, Z., GALANTI, B., KUPERVASSER, O. & PROCACCIA, I. 1997 Random noise and pole dynamics in unstable front propagation. *Physical Review E* **55** (3), 2649–2663.
- OLAMI, Z., PROCACCIA, I. & ZEITAK, R. 1995 Interface roughening in systems with quenched disorder. *Physical Review E* **52** (4), 3402–3414.
- PALM-LEIS, A. & STREHLOW, A. 1969 On the propagation o turbulent flames. *Combustion and Flame* **13**, 111–129.

- PAN, K. L. & FURSENKO, R. 2008 Characteristics of cylindrical flame acceleration in outward expansion. *Physics of Fluids* **20**, 094107.
- PELCE, P. & CLAVIN, P. 1982 Influence of hydrodynamics and diffusion upon the stability limits. *Journal of Fluid Mechanics* **124**, 219–237.
- PETERS, N. 1984 Laminar diffusion flamelet models in non-premixed turbulent combustion. *Progress in Energy and Combustion Science* **10**, 319–339.
- PETERS, N. 1992 A spectral closure for premixed turbulent combustion in the flamelet regime. *Journal of Fluid Mechanics* **242**, 611–629.
- PETERS, N. 2000 *Turbulent Combustion*. Cambridge: Cambridge University Press.
- PETERS, N. 2009 Multiscale combustion and turbulence. *Proceedings of the Combustion Institute* **32**, 1–25.
- PETERS, N., WENZEL, H. & WILLIAMS, F. A. 2000 Modification of the turbulent burning velocity by gas expansion. *Proceedings of the Combustion Institute* **28**, 235–243.
- PILLING, M. J. 2009 From elementary reactions to evaluated chemical mechanisms for combustion models. *Proceedings of the Combustion Institute* **32**, 27–44.
- PILLING, M. J. 2013 Reactions of hydrocarbon radicals and biradicals. *The Journal of Physical Chemistry A* **117**, 3697–3717.
- PITZ, W. J., CERNANSKY, N. P., DRYER, F. L., EGOLFOPOULOS, F. N., FARRELL, J. T. & FRIEND, D. G. 2007a Development of an experimental database and chemical kinetic models for surrogate gasoline fuels. In *SAE Paper*, pp. 2007-01-0175.

- PITZ, W. J., NAIK, C. V., MHAOLDÚIN, T. N., WESTBROOK, C. K., CURRAN, H. J., ORME, J. P. & SIMMIE, J. M. 2007b Modeling and experimental investigation of methylcyclohexane ignition in a rapid compression machine. *Proceedings of the Combustion Institute* **31**, 267–275.
- POINSOT, T. J. & VEYNANTE, D. 2005 *Theoretical and Numerical Combustion*, 2nd edn. Philadelphia, PA: Edwards Pub.
- POLUDNENKO, A. Y. & ORAN, E. S. 2010 The interaction of high-speed turbulence with flames: Global properties and internal flame structure. *Combustion and Flame* **157**, 995–1011.
- POPE, S. B. 1987 Turbulent Premixed Flames. *Annual Review of Fluid Mechanics* **19**, 237–270.
- POPE, S. B. 2000 *Turbulent Flows*. Cambridge University Press.
- POPE, S. B. 2013 Small scales, many species and the manifold challenges of turbulent combustion. *Proceedings of the Combustion Institute* **34**, 1–31.
- QI, F. 2013 Combustion chemistry probed by synchrotron VUV photoionization mass spectrometry. *Proceedings of the Combustion Institute* **34**, 33–63.
- QIN, X. & JU, Y. 2005 Measurements of burning velocities of dimethyl ether and air premixed flames at elevated pressures. *Proceedings of the Combustion Institute* **30**, 233–240.
- RANZI, E. 2006 A wide-range kinetic modeling study of oxidation and combustion of transportation fuels and surrogate mixtures. *Energy & Fuels* **20**, 1024–1032.

- RANZI, E., FRASSOLDATI, A., GRANA, R., CUOCI, A., FARAVELLI, T., KELLEY, A. P. & LAW, C. K. 2012 Hierarchical and comparative kinetic modeling of laminar flame speeds of reference fuels and their mixtures. *Progress in Energy and Combustion Science* **38**, 468–501.
- RANZI, E., FRASSOLDATI, A., GRANATA, S. & FARAVELLI, T. 2005 Wide-range kinetic modeling study of the pyrolysis, partial oxidation, and combustion of heavy *n*-alkanes. *Industrial & Engineering Chemistry Research* **44**, 5170–5183.
- REITZ, R. D. 2013 Directions in internal combustion engine research. *Combustion and Flame* **160**, 1–8.
- RONNEY, P. D. & SIVASHINSKY, G. I. 1989 A theoretical study of propagation and extinction of nonsteady flame fronts. *SIAM Journal on Applied Mathematics* **49** (4), 1029–1046.
- ROZENCHAN, G., ZHU, D. L., LAW, C. K. & TSE, S. D. 2002 Outward propagation, burning velocities, and chemical effects of methane flames up to 60 atm. *Proceedings of the Combustion Institute* **29**, 1461–1470.
- RUBIN, E. S., MANTRIPRAGADA, H., MARKS, A., VERSTEEG, P. & KITCHIN, J. 2012 The outlook for improved carbon capture technology. *Progress in Energy and Combustion Science* **38**, 630–671.
- SAHA, A., CHAUDHURI, S. & LAW, C. K. 2014 Flame surface statistics of constant-pressure turbulent expanding premixed flames. *Physics of Fluids* **26**, 045109.

- SANTNER, J., DRYER, F. L. & JU, Y. 2013 The effects of water dilution on hydrogen, syngas, and ethylene flames at elevated pressure. *Proceedings of the Combustion Institute* **34**, 719–726.
- SANTNER, J., HAAS, F. M., JU, Y. & DRYER, F. L. 2014 Uncertainties in interpretation of high pressure spherical flame propagation rates due to thermal radiation. *Combustion and Flame* **161**, 147–153.
- SARATHY, S. M., THOMSON, M. J., TOGBÉ, C., DAGAUT, P., HALTER, F. & MOUNAIM-ROUSSELLE, C. 2009 An experimental and kinetic modeling study of *n*-butanol combustion. *Combustion and Flame* **156**, 852–864.
- SARATHY, S. M., VRANCKX, S., YASUNAGA, K., MEHL, M., OSSWALD, P., METCALFE, W. K., WESTBROOK, C. K., PITZ, W. J., KOHSE-HÖINGHAUS, K., FERNANDES, R. X. & CURRAN, H. J. 2012 A comprehensive chemical kinetic combustion model for the four butanol isomers. *Combustion and Flame* **159**, 2028–2055.
- SHEN, H. S., STEINBERG, J., VANDEROVER, J., OEHLSCHLÄGER, M. A., DECEMBER, R. V, RE, V, RECEI, MANUSCRIPT & FEBRUARY, V 2009 A shock tube study of the ignition of *n*-heptane , *n*-decane , *n*-dodecane , and *n*-tetradecane at elevated pressures. *Energy & Fuels* **23**, 2482–2489.
- SHEPHERD, I. G. & CHENG, R. K. 2001 The burning rate of premixed flames in moderate and intense turbulence. *Combustion and Flame* **127**, 2066–2075.
- SHER, E. & OZDOR, N. 1992 Laminar burning velocities of *n*-butane/air mixtures enriched with hydrogen. *Combustion and Flame* **89**, 214–220.

- SHIM, Y., TANAKA, S., TANAHASHI, M. & MIYAUCHI, T. 2011 Local structure and fractal characteristics of H<sub>2</sub>-air turbulent premixed flame. *Proceedings of the Combustion Institute* **33**, 1455–1462.
- SHY, S. S., CHEN, Y. C., YANG, C. H., LIU, C. C. & HUANG, C. M. 2008a Effects of H<sub>2</sub> or CO<sub>2</sub> addition, equivalence ratio, and turbulent straining on turbulent burning velocities for lean premixed methane combustion. *Combustion and Flame* **153**, 510–524.
- SHY, S. S., LIU, C. C. & SHIH, W. T. 2010 Ignition transition in turbulent premixed combustion. *Combustion and Flame* **157**, 341–350.
- SHY, S. S., SHIH, W. T. & LIU, C. C. 2008b More on minimum ignition energy transition for lean premixed turbulent methane combustion in flamelet and distributed regimes. *Combustion Science and Technology* **180**, 1735–1747.
- SILKE, E. J., PITZ, W. J., WESTBROOK, C. K. & RIBAUCOUR, M. 2007 Detailed chemical kinetic modeling of cyclohexane oxidation. *Journal of Physical Chemistry A* **111**, 3761–3775.
- SILVA, G., KIM, C. H. & BOZZELLI, J. W. 2006 Thermodynamic properties (enthalpy, eond energy, entropy, and heat capacity) and internal rotor potentials of vinyl alcohol, methyl vinyl ether, and their corresponding radicals. *Journal of Physical Chemistry A* **110**, 7925–7934.
- SIVASHINSKY, G. I. 1977a Diffusional-thermal theory of cellular flames. *Combustion Science and Technology* **15**, 137–145.
- SIVASHINSKY, G. I. 1977b Nonlinear analysis of hydrodynamic instability in laminar flames-derivation of basic equations. *Acta Astronautica* **4**, 1177–1206.

- SIVASHINSKY, G. I. 1979 On selfturbulization of a laminar flame. *Acta Astronautica* **6**, 569–591.
- SIVASHINSKY, G. I. 1983 Instabilities, pattern formation, and turbulence in flames. *Annual Review of Fluid Mechanics* **15**, 179–199.
- SIVASHINSKY, G. I. 2002 Some developments in premixed combustion modeling. *Proceedings of the Combustion Institute* **29**, 1737–1761.
- SIVASHINSKY, G. I., LAW, C. K. & JOULIN, G. 1982 On stability of premixed flames in stagnation-point flow. *Combustion Science and Technology* **28**, 155–159.
- SMITH, K. O. & GOULDINT, F. C. 1979 Turbulence effects on flame speed and flame structure. *AIAA Journal* **17** (11), 1243–1251.
- SMOOKE, M. D. 2013 The computation of laminar flames. *Proceedings of the Combustion Institute* **34**, 65–98.
- SOKOLIK, A. S., KARPOV, V.P. & SEMENOV, E. S. 1967 Turbulent combustion of gases. *Combustion, Explosion, and Shock Waves* **3**, 36–45.
- SREENIVASAN, K. R. & MENEVEAU, C. 1986 The fractal facets of turbulence. *Journal of Fluid Mechanics* **173**, 357–386.
- SREENIVASAN, K. R. & PRASAD, R. R. 1989 New result on the fractal and multifractal structure of the large Schmidt number passive scalars in fully turbulent flows. *Physica D* **38**, 322–329.
- SREENIVASAN, K. R., RAMSHANKER, R. & MENEVEAU, C. 1989 Mixing , entrainment and fractal dimensions of surfaces in flows turbulent. *Proceedings of the Royal Society A* **A421**, 79–108.

- SUN, C. J. & LAW, C. K. 2000 On the nonlinear response of stretched premixed flames. *Combustion and Flame* **121**, 236–248.
- SUN, C. J., SUNG, C. J., HE, L. & LAW, C. K. 1999 Dynamics of weakly stretched flames: quantitative description and extraction of global flame parameters. *Combustion and Flame* **118**, 108–128.
- SUN, H., YANG, S. I., JOMAAS, G. & LAW, C. K. 2007 High-pressure laminar flame speeds and kinetic modeling of carbon monoxide/hydrogen combustion. *Proceedings of the Combustion Institute* **31**, 439–446.
- TANG, C., HUANG, Z. & LAW, C. K. 2011 Determination, correlation, and mechanistic interpretation of effects of hydrogen addition on laminar flame speeds of hydrocarbon-air mixtures. *Proceedings of the Combustion Institute* **33**, 921–928.
- TIEN, J. & MATALON, M. 1991 On the burning velocity of stretched flames. *Combustion and Flame* **84**, 238–248.
- TRISJONO, P., KLEINHEINZ, K., PITSCHE, H. & KANG, S. 2013 Large Eddy Simulation of Stratified and Sheared Flames of a Premixed Turbulent Stratified Flame Burner Using a Flamelet Model with Heat Loss. *Flow, Turbulence and Combustion* **92**, 201–235.
- TSE, S. D., ZHU, D. L. & LAW, C. K. 2000 Morphology and burning rates of expanding spherical flames in  $H_2/O_2$ /inert mixtures up to 60 atmospheres. *Proceedings of the Combustion Institute* **28**, 1793–1800.
- TSE, S. D., ZHU, D. L. & LAW, C. K. 2004 Optically accessible high-pressure combustion apparatus. *Review of Scientific Instruments* **75** (1), 233–239.

- VAGELOPOULOS, C. M., EGOLFOPOULOS, F. N. & LAW, C. K. 1994 Further considerations on the determination of laminar flame speeds with the counterflow twin-flame technique. *Proceedings of the Combustion Institute* **25**, 1341–1347.
- VAN GEEM, K. M., PYL, S. P., MARIN, G. B., HARPER, M. R. & GREEN, W. H. 2010 Accurate high-temperature reaction networks for alternative fuels : butanol isomers. *Industrial & Engineering Chemistry Research* **49**, 10399–10420.
- VELOO, P. S. & EGOLFOPOULOS, F. N. 2011 Flame propagation of butanol isomers/air mixtures. *Proceedings of the Combustion Institute* **33**, 987–993.
- VELOO, P. S., WANG, Y. L., EGOLFOPOULOS, F. N. & WESTBROOK, C. K. 2010 A comparative experimental and computational study of methanol, ethanol, and *n*-butanol flames. *Combustion and Flame* **157**, 1989–2004.
- VENKATESWARAN, P., MARSHALL, A., SHIN, D. H., NOBLE, D., SEITZMAN, J. & LIEUWEN, T. C. 2011 Measurements and analysis of turbulent consumption speeds of H<sub>2</sub>/CO mixtures. *Combustion and Flame* **158**, 1602–1614.
- VIOLI, A., YAN, S., EDDINGS, E. G., SAROFIM, A. F., GRANATA, S., FARVELLI, T. & RANZI, E. 2002 Experimental formulation and kinetic model for JP-8 surrogate mixtures. *Combustion Science and Technology* **174**, 339–417.
- VRANCKX, S., HEUFER, K. A., LEE, C., OLIVIER, H., SCHILL, L., KOPP, W. S., LEONHARD, K., TAATJES, C. S. & FERNANDES, R. X. 2011 Role of peroxy chemistry in the high-pressure ignition of *n*-butanol experiments and detailed kinetic modelling. *Combustion and Flame* **158**, 1444–1455.
- WANG, H. 2011 Formation of nascent soot and other condensed-phase materials in flames. *Proceedings of the Combustion Institute* **33**, 41–67.

- WANG, H., DAMES, E., SIRJEAN, B., SHEEN, D. A., TANGKO, R., VIOLI, A., LAI, J. Y. W., EGOLFOPOULOS, F. N., DAVIDSON, D. F., HANSON, R. K., BOWMAN, C. T., LAW, C. K., CERNANSKY, N. P., MILLER, D. L. & LINDSTEDT, R. P. 2010 A high-temperature chemical kinetic model of *n*-alkane (up to *n*-dodecane), cyclohexane, and methyl-, ethyl-, *n*-propyl and *n*-butyl-cyclohexane oxidation at high temperatures.
- WANG, H., YOU, X., AMEYA, V. J., DAVIS, S. G., LASKIN, A., EGOLFOPOULOS, F. N. & LAW, C. K. 2007 High temperature combustion reaction model of H<sub>2</sub>/CO/C<sub>1</sub> – C<sub>4</sub> compounds.
- WANG, Y., HOLLEY, A., JI, C., EGOLFOPOULOS, F. N., TSOTSISS, T. & CURRAN, H. 2009 Propagation and extinction of premixed dimethyl-ether/air flames. *Proceedings of the Combustion Institute* **32**, 1035–1042.
- WESTBROOK, C. K. 2013 Biofuels combustion. *Annual review of physical chemistry* **64**, 201–19.
- WESTBROOK, C. K., PITZ, W. J., HERBINET, O., CURRAN, H. J. & SILKE, E. J. 2009 A comprehensive detailed chemical kinetic reaction mechanism for combustion of *n*-alkane hydrocarbons from n-octane to *n*-hexadecane. *Combustion and Flame* **156**, 181–199.
- WILLIAMS, F. A. 1985 *Combustion Theory*. The Benjamin/Cummings Publishing Company, Inc.
- WON, S. H., WINDOM, B., JIANG, B. & JU, Y. 2014 The role of low temperature fuel chemistry on turbulent flame propagation. *Combustion and Flame* **161**, 475–483.

- WRANGHAM, R. 2010 *Catching Fire: How Cooking Made Us Human*. Basic Books.
- WU, C. K. & LAW, C. K. 1984 On the determination of laminar flame speeds from stretched flames. *Proceedings of the Combustion Institute* **20**, 1941–1949.
- WU, F., JOMAAS, G. & LAW, C. K. 2013 An experimental investigation on self-acceleration of cellular spherical flames. *Proceedings of the Combustion Institute* **34**, 937–945.
- WU, F., KELLEY, A. P. & LAW, C. K. 2012 Laminar flame speeds of cyclohexane and mono-alkylated cyclohexanes at elevated pressures. *Combustion and Flame* **159**, 1417–1425.
- WU, F., KELLEY, A. P., TANG, C., ZHU, D. & LAW, C. K. 2011 Measurement and correlation of laminar flame speeds of CO and C<sub>2</sub> hydrocarbons with hydrogen addition at atmospheric and elevated pressures. *International Journal of Hydrogen Energy* **36**, 13171–13180.
- WU, F. & LAW, C. K. 2013 An experimental and mechanistic study on the laminar flame speed, Markstein length and flame chemistry of the butanol isomers. *Combustion and Flame* **160**, 2744–2756.
- WU, F., LIANG, W., CHEN, Z., JU, Y. & LAW, C. K. 2014a Uncertainty in stretch extrapolation of laminar flame speed from expanding spherical flames. *Proceedings of the Combustion Institute* **35**, in press.
- WU, F., SAHA, A., CHAUDHURI, S. & LAW, C. K. 2014b Facilitated ignition in turbulence through differential diffusion. *Physical Review Letters* **113**, 024503.

- WU, F., SAHA, A., CHAUDHURI, S. & LAW, C. K. 2014c Propagation speeds of expanding turbulent flames of C<sub>4</sub> to C<sub>8</sub> *n*-alkanes at elevated pressures: experimental determination, fuel similarity, and stretch-affected local extinction. *Proceedings of the Combustion Institute* **35**, in press.
- YAKHOT, V. 1988 Propagation velocity of premixed turbulent flames. *Combustion Science and Technology* **60**, 191–214.
- YOO, C. S., LU, T., CHEN, J. H. & LAW, C. K. 2011 Direct numerical simulations of ignition of a lean *n*-heptane/air mixture with temperature inhomogeneities at constant volume: Parametric study. *Combustion and Flame* **158**, 1727–1741.
- YOU, X., EGOLFOPOULOS, F. N. & WANG, H. 2009 Detailed and simplified kinetic models of *n*-dodecane oxidation: The role of fuel cracking in aliphatic hydrocarbon combustion. *Proceedings of the Combustion Institute* **32**, 403–410.
- YU, G., LAW, C. K. & WU, C. K. 1986 Laminar flame speeds of hydrocarbon + air mixtures with hydrogen addition. *Combustion and Flame* **63**, 339–347.
- ZÁDOR, J., TAATJES, C. A. & FERNANDES, R. X. 2011 Kinetics of elementary reactions in low-temperature autoignition chemistry. *Progress in Energy and Combustion Science* **37**, 371–421.
- ZHANG, H. R., EDDINGS, E. G. & SAROFIM, A. F. 2007 Criteria for selection of components for surrogates of natural gas and transportation fuels. *Proceedings of the Combustion Institute* **31**, 401–409.

- ZHANG, P., KLIPPENSTEIN, S. J. & LAW, C. K. 2013 Ab initio kinetics for the decomposition of hydroxybutyl and buoxy radicals of *n*-butanol. *The Journal of Physical Chemistry A* **117**, 1890–906.
- ZHAO, P., YUAN, W., SUN, H., LI, Y., KELLEY, A. P. & ZHENG, X. 2014 Laminar Flame Speeds , counterflow Ignition , and kinetic modeling of the butene isomers. *Proceedings of the Combustion Institute* **35**, in press.
- ZHAO, Z., CHAOS, M., KAZAKOV, A. & DRYER, F. L. 2007 Reaction and a comprehensive kinetic model of dimethyl ether. *International Journal of Chemical Kinetics* **40**, 1–18.